

# **Analysis of the Influence of Network Structures on the Stability of Modern Power Systems**

A thesis submitted to The University of Manchester for the degree of  
**Doctor of Philosophy**  
in the Faculty of Science and Engineering

**2022**

**Mr. Jaime L. Trivino Bustamante**

**Department of Electrical and Electronic Engineering**



# Table of Contents

<b>Table of Contents</b> .....	<b>3</b>
<b>List of Figures</b> .....	<b>7</b>
<b>List of Tables</b> .....	<b>10</b>
<b>List of Abbreviations</b> .....	<b>11</b>
<b>Abstract</b> .....	<b>14</b>
<b>Declaration</b> .....	<b>15</b>
<b>Copyright Statement</b> .....	<b>16</b>
<b>Acknowledgements</b> .....	<b>17</b>
<b>1 Introduction</b> .....	<b>19</b>
1.1 Motivation.....	19
1.2 Power system stability .....	21
1.2.1 Rotor angle stability .....	23
1.2.1.1 Small signal stability .....	24
1.2.1.2 Transient stability.....	25
1.2.2 Frequency stability.....	26
1.2.3 Voltage stability .....	27
1.2.4 Resonance stability .....	28
1.2.5 Converter-driven stability .....	28
1.3 Essential concepts of transient stability .....	29
1.3.1 Classical model of synchronous generators.....	29
1.3.2 Single machine infinite bus.....	30
1.3.3 Power angle equation.....	31
1.3.4 Equal Area Criterion .....	31
1.3.5 Critical Clearing Time .....	34
1.3.6 Synchronising power coefficient .....	35
1.3.7 Generator embedded controllers influencing transient stability .....	36
1.3.8 Transient stability in multimachine systems.....	38
1.4 Literature review .....	39
1.4.1 Industry practices involving topological changes.....	39
1.4.2 Optimal transmission switching.....	40
1.4.3 Optimal topology control.....	43
1.4.4 Controlled islanding.....	46
1.4.5 Transient stability constrained optimal power flow.....	48
1.4.6 Network topology assessments based on graph theory.....	50
1.4.7 Summary of past work.....	51

1.5	Research aims and objectives .....	53
1.6	Main contributions.....	54
1.7	Thesis overview .....	55
<b>2</b>	<b>Modelling of Power System Components, Analysis Techniques and Computational Tools.....</b>	<b>59</b>
2.1	Modelling of power system components.....	60
2.1.1	Synchronous generators.....	60
2.1.2	Generator excitation systems.....	62
2.1.2.1	DC excitation .....	62
2.1.2.2	Static excitation .....	63
2.1.3	Power system stabilisers.....	64
2.1.4	Transmission lines .....	65
2.1.5	Transformers.....	66
2.1.6	Loads .....	66
2.2	Network representation and impedance-based distance metrics .....	67
2.2.1	Admittance and impedance matrices.....	67
2.2.2	Weighted graphs .....	68
2.2.3	Impedance-based distance metrics .....	70
2.2.3.1	Thevenin impedance and electrical distance .....	70
2.2.3.2	Shortest path length or geodesic distance .....	71
2.3	Short circuit and line-switching modelling techniques .....	72
2.3.1	Short circuit modelling using admittance matrices .....	72
2.3.2	Short circuit modelling in simulation environments .....	74
2.3.3	Line-switching modelling using admittance matrices.....	75
2.4	Power system optimisation techniques.....	76
2.4.1	Optimal power flow.....	77
2.4.2	Dynamic optimisation and optimal control .....	78
2.4.3	Genetic algorithms.....	81
2.5	Overview of computational tools .....	82
2.6	Summary.....	83
<b>3</b>	<b>Assessment of the Impact of Line-Switching Actions on Transient Stability .....</b>	<b>85</b>
3.1	Effect of line-switching actions between generators and fault location on transient stability .....	85
3.1.1	SMIB test system.....	85
3.1.2	Considerations for the analysis based on the SMIB test system with the classical model of SG.....	87
3.1.3	Preliminary analysis using the EAC and CCT based on the SMIB system .....	89
3.1.4	Impedance between a generator and fault location .....	96
3.1.5	Analysis of the effect of ZFG with the aid of EAC.....	98
3.1.6	Verification of the effect of ZFG with the aid of TDS.....	101



3.2	Effect of line-switching between generators on transient stability .....	105
3.2.1	AF9B modified test system and test cases .....	105
3.2.2	Impedance between generators .....	108
3.2.3	Analysis of ZBG based on AF9B with the aid of TDS.....	111
3.2.4	Verification of the effect of ZBG with the aid of TDS.....	114
3.3	Summary .....	118
<b>4</b>	<b>Modelling Framework for Transient Stability Preventive Control via Rescheduling and Switching .....</b>	<b>121</b>
4.1	Classical multi-machine model for transient stability analysis.....	122
4.1.1	Network modelling and reduction .....	123
4.1.2	Classical multi-machine model with network reduction .....	124
4.2	Classical multi-machine model for transient stability with structure-preserving network and switching .....	125
4.2.1	Structure-preserving network model.....	126
4.2.2	Security, fault and switching modelling .....	127
4.2.3	Classical multi-machine model with structure-preserving network and line switching.....	128
4.3	Study of time-domain transient stability indicators for constraint modelling.....	131
4.4	General transient stability and security constrained optimal power flow with switching actions .....	134
4.4.1	Condensed formulation of the general problem.....	136
4.4.2	Detailed formulation of preventive TSSC-OPFwS.....	138
4.4.2.1	Power flow constraints .....	140
4.4.2.2	Dynamic and binary constraints .....	142
4.4.2.3	Objective functional .....	143
4.5	Summary .....	144
<b>5</b>	<b>Transient Stability Preventive Control with Generation Dispatching and Network Optimisation .....</b>	<b>147</b>
5.1	IEEE68 bus test system.....	148
5.2	Solution of TSSC-OPFwS by topology optimisation for transient stability .....	149
5.3	Topology optimisation for transient stability .....	153
5.4	Study of impact factors on transient stability.....	154
5.4.1	Impact of network structure .....	156
5.4.2	Impact of initial generation loading .....	159
5.4.3	Impact of rotor angle separation .....	161
5.4.4	Impact of inertia reduction.....	164
5.4.5	Impact of network topology metrics .....	166
5.4.5.1	Distance between Fault and Generators .....	168
5.4.5.2	Distance Between Generators .....	171
5.5	Robustness metric for transient stability optimisation.....	173

5.5.1	Nodal robustness .....	174
5.5.2	Network robustness .....	176
5.5.3	Composite transient stability robustness metric .....	177
5.6	Assessment of switching solutions based on proposed CTSRMs .....	178
5.6.1	Assessment of CTSRMs with stable base-case .....	179
5.6.2	Network topology optimisation with unstable base-case .....	181
5.6.3	Network topology optimisation with load curtailments .....	184
5.6.4	Computation times.....	185
5.7	Summary.....	185
<b>6</b>	<b>Conclusions and Future Work .....</b>	<b>189</b>
6.1	Conclusions .....	189
6.1.1	Optimisation framework TSSC-OPFwS .....	191
6.1.2	Two-stage solution of TSSC-OPFwS.....	193
6.1.3	Study of TS nodal impact factors .....	194
6.1.4	Study of TS topological impact factors .....	195
6.1.5	Definition of TS robustness metrics .....	196
6.2	Future work.....	197
	<b>References .....</b>	<b>201</b>
	<b>Appendix A: Network Data.....</b>	<b>215</b>
A.1	SMIB network.....	215
A.2	Modified AF9B network.....	216
A.2.1	Branch impedances.....	216
A.2.2	Load flow data.....	216
A.2.3	Generator dynamic data.....	217
A.3	Modified IEEE 68-bus test network .....	218
A.3.1	Branch impedances.....	218
A.3.2	Load flow data .....	219
A.3.3	Generator dynamic data.....	221
A.3.4	Optimal power flow data .....	222
	<b>Appendix B: List of Author's Thesis Based Publications .....</b>	<b>223</b>
B.1	International Journal Publications.....	223
B.2	International Conference Publications .....	223

*Word Count: 54854*

# List of Figures

Figure 1.1: Classification of power system stability [17][18].	23
Figure 1.2: Effect of synchronising and damping torque ( $TS$ and $TD$ ) [20] with constant field voltage (a), and with excitation control (b).	24
Figure 1.3: Time frame of power system dynamics [21].	25
Figure 1.4: National Grid frequency response requirements (a), and operational and statutory limits (b) of system frequency for the UK power network [25].	27
Figure 1.5: Circuit (a) and phasor diagram (b) of the classical representation of a SG; armature resistance neglected [21].	30
Figure 1.6: SMIB system (a) and impedance diagram (b).	31
Figure 1.7: EAC for a SMIB system considering pre-fault and during fault curves (adapted from [20]).	32
Figure 1.8: Power-angle characteristic for a SMIB system. (a) Stable case and (b) unstable case (adapted from [20]).	33
Figure 1.9: Transient synchronising power coefficient and power-angle characteristic (adapted from [21]).	36
Figure 1.10: Influence of the AVR in (a) power-angle characteristic SMIB system, and (b) backswing effect [21].	37
Figure 2.1: Simplified functional relationship diagram of SG, AVR and PSS [155].	62
Figure 2.2: Simplified block diagram of the IEEE Type 1 DC exciter [17].	63
Figure 2.3: Simplified block diagram of the IEEE Type DC1A DC exciter [155].	63
Figure 2.4: Simplified block diagram of the IEEE Type ST1A ST exciter [26].	64
Figure 2.5: Simplified block diagram of a PSS [155].	65
Figure 2.6: Equivalent $\pi$ circuit of a medium length transmission line [23].	65
Figure 2.7: Equivalent $\pi$ circuit a two-winding transformer [20].	66
Figure 2.8: Resistive circuit (a) and graph representation (b) (adapted from [164]).	69
Figure 2.9: Thevenin equivalent impedance seen from node $k$ (a) and between node $k$ and $j$ (b) (adapted from [23]).	70
Figure 2.10: Impedance-based circuit (a) and geodesic path between nodes 1 and 7 (b) (adapted from [164]).	72
Figure 2.11: Simplified topology with a fault on a busbar of a transmission network	73
Figure 2.12: Simplified topology for single circuit (a) and double circuit (b) with faults in the middle (50% of line length) of transmission lines.	74
Figure 2.13: Simplified topology representing a switching-off action of a transmission line.	76
Figure 2.14: Simplified flow chart of a GA (Adapted from [176]).	81
Figure 2.15: Simplified flow chart of data for the proposed topology optimisation.	83
Figure 3.1: SMIB test system (100KM-SMIB) with double circuit transmission lines	86
Figure 3.2: SMIB test system variant (50KM-SMIB) with double circuit transmission lines	87
Figure 3.3: Impedance diagram of cases type A (a) and B (b) of the 100KM-SMIB test system with 8 and 2 parallel lines.	90

Figure 3.4: Power angle characteristics of cases type A (a) and B (b) of the 100KM-SMIB test system with 8 and 2 parallel lines. ....	92
Figure 3.5: Impedance diagram of cases type A (a) and B (b) of the 50KM-SMIB test system with 8 and 2 parallel lines. ....	93
Figure 3.6: Power angle characteristics (in scale) of cases type A and B of the 100KM (a) and 50KM (b) SMIB test systems with 8 and 2 parallel lines. ....	95
Figure 3.7: Transfer impedance ratio of cases type A of the 100KM-SMIB and 50KM-SMIB test systems. ....	97
Figure 3.8: <i>ZFG</i> of cases type A (a) and B (b) of the 100KM-SMIB and 50KM-SMIB test systems. ....	98
Figure 3.9: CCT factors and <i>ZFG</i> of cases type A (a)(c) and B (b)(d) of SMIB-based test systems with 2, 4, 6 and 8 parallel lines. ....	100
Figure 3.10: CCT-based stability level of cases type A (a)(c) and B (b)(d) of SMIB-based test systems with 2, 4, 6 and 8 parallel lines. ....	102
Figure 3.11: Generator rotor angles of cases type A (a)(c) and B (b)(d) of SMIB-based test systems with 2, 4, 6 and 8 parallel lines. ....	103
Figure 3.12: Generator active power output of cases type A (a)(c) and B (b)(d) of SMIB-based test systems with 2, 4, 6 and 8 parallel lines. ....	104
Figure 3.13: Modified AF9B test system. ....	105
Figure 3.14: Impedance diagram of types A, B and C of the AF9B test system with 5 lines. ....	107
Figure 3.15: Impedance diagram of cases type A of the AF9B test system with 5, 4 and 3 lines. ....	108
Figure 3.16: Impedance-based proximity metrics between generators: <i>ZBG(SPL)</i> , <i>ZBG(ED)</i> , and impedance between busbars 7 and 9 of the AF9B test system. ....	110
Figure 3.17: Impedance-based proximity metrics between generators and fault location: <i>ZFG</i> from G2, <i>ZFG</i> from G3, and impedance between busbars 5 and 7 of the AF9B test system. ....	110
Figure 3.18: <i>ZBG(ED)</i> and <i>ZBG(SPL)</i> for cases with 3 Lines (a) and 5 Lines (b) between busbars 7 and 9 of the AF9B test system. ....	111
Figure 3.19: Transient synchronising power coefficient and power-angle characteristic (adapted from [21]) ....	112
Figure 3.20: <i>ZBG(SPL)</i> (a) and <i>ZFG</i> (b) of test cases of the AF9B test system. ....	113
Figure 3.21: Simulation-based CCTs of test cases type A(a), B(b), and C(c) of the AF9B test system. ....	115
Figure 3.22: Generator rotor angles of cases type A (a)(b) and C (c)(d) of the AF9B-based test systems with 3, 4, and 5 lines. ....	116
Figure 3.23: P-delta curves of G2 and G3 for test cases type A (a)(b) and C (c)(d) of AF9B-based test systems with 3, 4, and 5 lines between busbars 7 and 9. ....	117
Figure 4.1: Multi-machine system with network reduction (adapted from [17]) ....	122
Figure 4.2: Multi-machine system with structure-preserving network (adapted from [17]) ....	127
Figure 4.3: Partial representation of a power system with structure-preserving network ....	131
Figure 4.4: Components of the optimisation framework ....	135
Figure 5.1: IEEE68 Bus Test System [148][149]. ....	148
Figure 5.2: Two-stage solution procedure. ....	150
Figure 5.3: Flow chart of the pre-fault (steady state) data elaboration process ....	151

Figure 5.4: Flow chart of the transient stability verification process using TDS .....	151
Figure 5.5: Flow-chart of topology optimisation for transient stability. ....	152
Figure 5.6: IEEE 68 bus test network showing line switching (purple and green), fault locations (red), and generation subject to inertia reduction (light blue) (adapted from [148][149]). ....	156
Figure 5.7: TSI results for different faults (y-axis) and switching scenarios (x-axis) of the IEEE68 Bus test system with clearing time of 100 ms. ....	157
Figure 5.8: TSI difference between single-switching scenarios and SWL0 for the IEEE68 Bus test system with clearing time of 100 ms. ....	158
Figure 5.9: Generator pre-fault (steady state) load angles $\text{fipol}$ (a) and $\text{fipol}$ differences against base-case SWL0 (b) of IEEE68 test switching scenarios. ....	160
Figure 5.10: Box plot of pre-fault generator load angles. ....	161
Figure 5.11: RAS difference (a) and TSI difference (b) between test switching scenarios and the base-case SWL0. ....	162
Figure 5.12 Bar plots of pre-fault RAS difference (a) with a different colour for each SG. TSI evaluations (b) where each colour represents a different fault location with $t_{cl}=100$ ms. ....	163
Figure 5.13: Pre-fault (a) and maximum (b) RAS coherence for a fault on Line8 with $t_{cl}=100$ ms. ....	165
Figure 5.14: Average DFG impedance means of better and worse TSI groups with 95% confidence intervals based on shortest path (a), two shortest paths (b) and electrical distances (c). ....	170
Figure 5.15: Average DBG impedance mean of better and worse TSI groups with 95% confidence intervals based on shortest path (a), mean of shortest paths (b) and electrical distances (c). ....	172
Figure 5.16: Generator inertia impact factor IFM2. ....	175
Figure 5.17: Fitness comparison of test switching scenarios for a fault on Line8 based on FF1 (a)(b) and FF2(c)(d). ....	179
Figure 5.18: Box plots of fitness differences between all switching scenarios and SWL0 based on FF1 (a) and FF2 (b). Means of the fitness difference for evaluations using FF1 (c) and FF2 (d). ....	181
Figure 5.19: TSI results: switching scenarios with SWL33 as baseline (x-axis); fault locations on Line24, Line25, and Line27 (y-axis). ....	182
Figure 5.20: Normalised $FF1_{nor}$ (blue), $FF2_{nor}$ (red) and their affine combination (yellow). The x-axis contains switching scenarios with fault conditions FC-A (a) and FC-B(b). ....	183

# List of Tables

---

Table 3.1 Transfer impedances of the 100KM-SMIB Cases A-B with 8 and 2 parallel lines....	89
Table 3.2 CCT factors of the 100KM-SMIB Cases A-B with 8 and 2 parallel lines.....	92
Table 3.3 Transfer impedances of the 50KM-SMIB Cases A-B with 8 and 2 parallel lines.....	94
Table 3.4 CCT factors of the 50KM-SMIB Cases A-B with 8 and 2 parallel lines.....	94
Table 3.5 Test cases Type A and B of SMIB-Based test systems .....	96
Table 3.6 Test cases type A, B, and C of the AF9B test system.....	106
Table 3.7 ZBG and ZFG of test cases type A, B, and C of the AF9B test system.....	114
Table 4.1 Time-domain transient stability indicators .....	132
Table 4.2 Spearman correlation coefficient of transient stability indicators .....	133
Table 5.1 Studies of impact factors on transient stability .....	155
Table 5.2 Impact of switching scenarios based on TSI.....	158
Table 5.3 Comparison of test switching scenarios based on summation of pre-fault load angle differences and TSI results for faults on Line8 and Line47.....	160
Table 5.4 Network topology metrics.....	167
Table 5.5 Spearman correlation coefficient between transient stability indicators and network topology metrics.....	168
Table 5.6 Spearman correlation coefficients between DFG metrics and transient stability indicators.....	170
Table 5.7 Spearman correlation coefficients between DBG metrics and transient stability indicators.....	173
Table 5.8 Spearman correlation coefficients of objective functions and transient stability indicators.....	180
Table 5.9 Evaluation of FF1 and FF2 for double-switching scenarios with SWL33 as base-case .....	183
Table 5.10 Stability outcomes with load curtailment for total load increase of 7% and 10%..	184
Table 5.11 Median computational time (seconds) for TDS and CTSRM using FF1 (5.16).....	185
Table 6.1 List of contributions.....	191
Table A.1 Branch data for the modified AF9B test network .....	216
Table A.2 Load flow data for the modified AF9B test network .....	216
Table A.3 Generator dynamic data for the modified AF9B test network (1) .....	217
Table A.4 Generator dynamic data for the modified AF9B test system (2) .....	217
Table A.5 Branch data for the modified IEEE 68-bus test network .....	218
Table A.6 Load flow data for the modified IEEE 68-bus test network .....	219
Table A.7 Generator dynamic data for the modified IEEE 68-bus test network (1) .....	221
Table A.8 Generator dynamic data for the modified IEEE 68-bus test system (2) .....	221
Table A.9 Data for optimal power flow solution for the IEEE 68-bus test system .....	222

## List of Abbreviations

---

AC	Alternating Current
ACPF	Alternating Current Power Flow
ACOPF	Alternating Current Optimal Power Flow
AF9B	Anderson and Fouad 9 Bus test system
AGC	Automatic Generation Control
API	Application Programme Interface
AVR	Automatic Voltage Regulator
CCT	Critical Clearing Time
CI	Controlled Islanding
CIG	Converter Interfaced Generation
COI	Centre of Inertia
CSF	Critical Switching Flow
CTSRM	Composite Transient Stability Robustness Metric
DAEs	Differential-Algebraic Equations
DBG	Impedance-based Distance Between Generators
DC	Direct Current
DCPF	Direct Current Power Flow
DFG	Impedance-based Distance between Fault and Generators
DFIG	Doubly-Fed Induction Generator
DNE	Do-Not-Exceed
EAC	Equal Area Criterion
ED	Economic Dispatch
EMF	Electromotive Force
ENTSO-E	European Network Transmission System Operators for Electricity
FACTS	Flexible AC Transmission Systems
FCC	Full Converter Connected
FES	Future Energy Scenarios
GA	Genetic Algorithm
GB	Great Britain
HV	High Voltage
HVDC	High Voltage Direct Current
IEC	International Electrotechnical Commission

IEEE	Institute of Electrical and Electronic Engineers
ISGA	Integral of Squared Rotor Angles
KCL	Kirchhoff's Current Law
KVL	Kirchhoff's Voltage Law
LV	Low Voltage
NGESO	National Grid Electricity System Operator
MC	Monte Carlo
MILP	Mixed-Integer Linear Programming
MINLP	Mixed-Integer Non-Linear Programming
MISOCP	Mixed-Integer Second-Order Cone Programming
MV	Medium Voltage
NETS	New England Test System
NYPS	New York Power System
OPF	Optimal Power Flow
OTS	Optimal Transmission Switching
OTC	Optimal Topology Control
p.f.	Power Factor
PC	Personal Computer
PDF	Probability Density Function
PJM	Pennsylvania-New Jersey-Maryland RTO
PMU	Phasor Measurement Unit
POC	Point of Connection
PSS	Power System Stabiliser
PTDF	Power Transfer Distribution Factors
PV	Photovoltaic
RAS	Rotor Angle Separation
RES	Renewable Energy Sources
RTO	Regional Transmission Operator
RTS	Reliability Test System
SG	Synchronous Generator
SIME	Single Machine Equivalent
SMIB	Single Machine Infinite Bus
SPL	Shortest Path Length
SSR	Sub-Synchronous Resonance
TDS	Time Domain Simulation



TEF	Transient Energy Function
TS	Transient Stability
TSC-OPF	Transient Stability Constrained OPF
TSSC-OPFwS	Transient Stability and Security Constraint Optimal Power Flow with Switching
TSI	Transient Stability Index
TSO	Transmission System Operator
UC	Unit Commitment
UN	United Nations
WAMS	Wide Area Measurement Systems
WECC	Western Electricity Coordinating Council
WP	Wind Power
WTG	Wind Turbine Generator
ZFG	Impedance from Fault to Generators
ZBG	Impedance Between Generators

# Abstract

---

*Analysis of the Influence of Network Structures on the Stability of Modern Power Systems*

**Mr. Jaime L. Trivino Bustamante, The University of Manchester, September 2022.**

Power systems are integrating a significant portion of converter interfaced generation at a growing rate, driven by major commitments to remove carbon emissions in producing electrical energy. Though the current generation landscape is changing, in developing countries generation is still dominated by conventional units; therefore, synchronous generators will continue to be relevant assets in the future. Furthermore, from a network perspective, the connection between systems is expanding; hence, the integration of distant areas will require significant transmission network reinforcements. Nevertheless, additional infrastructure will face growing environmental and budget restrictions; therefore, new approaches are needed to design flexible and cost-effective solutions, like using transmission lines as flexible assets, so that the network can adjust its structure to operate under an estimated condition.

This work contributes to power systems stability research; particularly, it reveals how discrete topological changes can positively impact transient stability. A comprehensive study of the effect of line-switching actions on the impedance between generators and fault locations, and between generators, with further implications on transient stability was performed. Results based on small and realistic test systems revealed the impact of line-switching actions on transient stability behaviour. A novel optimisation method called transient stability and security constraint optimal power flow with switching was proposed. The optimisation method is based on a new multi-machine model with a structure-preserving network and line switching; moreover, the proposed method combines network metrics and other transient stability impact factors on a composite transient stability robustness metric, which serves as a fitness function to be used on an optimisation approach using a genetic algorithm. The main research output is given by the definition and comprehensive assessment of network metrics capable of quantifying the topological influence of the network structure on the first-swing transient stability behaviour of power systems. The undertaken research is relevant because it focuses not only on improving the flexibility of the current infrastructure but also addresses the transient stability problem, which is likely to remain one of the key stability areas in the following years.

## **Declaration**

---

No portion of the work referred to in this thesis has been submitted in support of an application for another degree or qualification of this or any other university or other institutes of learning.

## Copyright Statement

---

The author of this thesis (including any appendices and/or schedules to this thesis) owns certain copyright or related rights in it (the “Copyright”) and s/he has given The University of Manchester certain rights to use such Copyright, including for administrative purposes.

Copies of this thesis, either in full or in extracts and whether in hard or electronic copy, may be made only in accordance with the Copyright, Designs and Patents Act 1988 (as amended) and regulations issued under it or, where appropriate, in accordance with licensing agreements which the University has from time to time. This page must form part of any such copies made.

The ownership of certain Copyright, patents, designs, trademarks and other intellectual property (the “Intellectual Property”) and any reproductions of copyright works in the thesis, for example graphs and tables (“Reproductions”), which may be described in this thesis, may not be owned by the author and may be owned by third parties. Such Intellectual Property and Reproductions cannot and must not be made available for use without the prior written permission of the owner(s) of the relevant Intellectual Property and/or Reproductions.

Further information on the conditions under which disclosure, publication and commercialisation of this thesis, the Copyright and any Intellectual Property and/or Reproductions described in it may take place is available in the University IP Policy (see <http://documents.manchester.ac.uk/DocuInfo.aspx?DocID=24420>), in any relevant Thesis restriction declarations deposited in the University Library, The University Library’s regulations (see <http://www.library.manchester.ac.uk/about/regulations/>) and in the University’s policy on Presentation of Theses.

---

# Acknowledgements

---

Firstly, I praise my Lord Jesus Christ because he has been my refuge. During the highs and lows of my journey, He has sustained me. My Lord has provided all I need; I will trust in him and not be disappointed.

I would like to express my gratitude to my supervisor Dr Victor Levi for his guidance, support, constructive comments, and empathy throughout these years. Without his contribution of time and ideas, I could not have completed this research work. His commitment to excellence and patience with which he has reviewed this thesis and the work contained within it has been inspirational.

This thesis also benefited from the friendly advice and support provided by Dr Juan Morales, to whom I must also express my gratitude. I found his insight into the field of transient stability invaluable. He also helped me by guiding me on the usage of PowerFactory software.

I would also like to thank Prof. Andrew Sherry for his mentoring and christian friendship. He encouraged me to move forward, even in those days when it was very difficult to make relevant progress on my research project.

At last, to my beautiful family, my wife Angelica and my children Luciana and Santiago; they brought happiness and laughter to my life and I am grateful for them every day. Thank you for your love, patience and relentless support throughout all these years. Furthermore, I extend this expression of gratitude to my parents, Carmen and Jaime, and my sisters Sandra and Lorena, who prayed for me so faithfully during the time of my PhD program.

*“But because of his great love for us, God, who is rich in mercy, made us alive with Christ even when we were dead in transgressions — it is by grace you have been saved.”*

*Ephesians 2:4-5*

*To my wife, Angelica*

*and my children*

*Luciana and Santiago*

# 1 Introduction

---

## 1.1 Motivation

The UK was among the first countries to recognise that climate change is not only an environmental issue but also an economic and political challenge. Proof of the commitment to address this problem was the Climate Change Act, passed in 2008. The main objective of the regulation was to set the goal of the reduction of greenhouse emissions by at least 80% by 2050, compared with 1990 levels. Additionally, a gradual approach was set by five-year checkpoints of reduction called “Carbon Budgets”. This early action allowed the UK to play a critical role in global efforts to tackle climate change. Actually, the five-year cap was replicated by the UN in the Paris Agreement [1].

According to the UK Energy Research Centre, energy efficiency and demand reduction will be critical to reach the emission goals by 2050. However, transitioning to a low-carbon system may imply a trade-off between security and decarbonisation [2]. This concern is evident in the declaration of energy security stated in the “Clean Growth Strategy” because it defines flexibility, adequacy and resilience as cornerstone features of the plan [1]. Remarkably, the security risk can be mitigated by flexibility, which implies the increase of measures like demand-side response and energy storage [2].

Similar conclusions are stated by National Grid Electricity System Operator (NGESO) in its projections made in Future Energy Scenarios FES 2019 [3]. To reach net-zero carbon levels, the electricity system will have to operate using only low-carbon generation while simultaneously delivering negative emissions. In parallel, energy consumption needs to be reduced by increasing the thermal efficiency of houses and buildings. Moreover, electric vehicles will help decarbonise the transport and energy

supply in the UK. Charging 35 million electric vehicles will provide flexibility to increase penetration and reduce the curtailment of renewable energy sources (RES) [3]. Recently, the FES 2021 [4] deepened the focus on flexibility; it considers the integration of large-scale energy storage based on hydrogen to reach the net zero scenario. Hydrogen production is crucial to reach carbon budgets; hence, the selection of production processes must be carefully assessed. Low-carbon hydrogen, like green hydrogen, requires energy from renewable sources for the electrolysis; therefore, effects on the transmission system must be considered due to the large-scale production required to make a meaningful impact.

The concerns about the transition to a low-carbon energy system are shared worldwide [5]; the transition to a net-zero carbon emission electrical system will require a sustained investment in low-carbon energy systems, where the conversion to electric heat and transport services will require a substantial innovation effort [2][3][6]. An attempt to improve power systems has been proposed by the Systems & Control community in its research agenda for the year 2030 [7]. As power systems have been classified as critical infrastructure systems, the impact of disruption due to failures, intentional disturbance [8], or natural disasters [9] is noteworthy. Therefore, future operation and planning require a significant enhancement in managing and monitoring the infrastructure to make it more secure and reliable. This challenge represents a major task in modelling and control because new algorithms will have to consider multiple distributed data elements [7].

Though the current scenario is changing, power generation in developing countries is still dominated by synchronous generators (SGs) and is primarily centralised in conventional power plants [10]. The change is driven by the cost reduction of Converter Interfaced Generation (CIGs), especially Photovoltaics (PVs) [11]. This cost reduction will increase the participation of CIG, decentralising the generation and shifting to a converter-dominated grid [12][13]. In a converter-dominated grid, the inertia provided by SGs will decrease; however, it is not likely that SGs will completely disappear. Therefore, what are the possible effects of a scenario with a large proportion of geographically decentralised CIG? Benefits are related to reducing network losses and congestion due to having a potentially more reliable network with more decentralised sources [14]. From the network perspective, to reduce the curtailment of CIG and effectively transport the generated power, the transmission network needs to change, so several investments must be made to improve its efficiency. For instance, the



Pennsylvania-New Jersey-Maryland RTO declared in [15] that the total congestion costs increased by US\$466.6 million between 2020 and 2021, which indicates that improving the efficiency of the network is an urgent matter.

In summary, future power systems will need to accommodate a significant portion of CIG [12][13], which implies a reduction in the inertia of the system [14]. Besides, integrating geographically distant areas and markets will require significant transmission network reinforcements [6]. Thus, to deliver flexible and cost-effective solutions, there is a need to explore new approaches, such as using transmission lines as a dispatchable asset, so that the system may change its structure under foreseeable operating conditions. However, how these changes in network structure are going to impact the stability of the system? Moreover, is it possible to relate the structure of a network with its ability to endure severe disturbances? Potential positive effects derived from network structure and reconfiguration on the system's stability need to be studied and assessed to enhance the system's flexibility as a whole. In particular, this research will answer these questions by introducing the analysis of network structures from the transient stability perspective.

## 1.2 Power system stability

To understand the power system stability phenomenon, there is a need to understand what is involved in the stable operation of a power system. Formally, power system stability is the ability of an electric power system, for a given operating condition, to regain a state of operating equilibrium after being subjected to a physical disturbance, with most system variables bounded so that the behaviour of the system is similar to the pre-disturbance [16]. This definition relies on the concept of stability in the sense of Lyapunov, where it is assumed that the system has an attractive equilibrium point, and the trajectories approach a single “stable point” as time approaches infinity. A similar definition has been given in [17] and considers the condition of damping the oscillatory behaviour after the disturbance and settling down to new steady state operating conditions in finite time. The damping of oscillations, i.e., asymptotic stability, is an essential requirement for power systems because sustained oscillations can cause damage to physical assets.

The successful operation of a power system must guarantee reliable and uninterrupted service to the loads [17]. Reliable operation implies that the voltages and frequency must always be maintained close to reference values to ensure the safe and satisfactory

operation of the customer's equipment. Notably, there are two major reliability requirements for electrical power systems. Firstly, SGs must work in parallel with adequate capacity to supply the power required by the loads. This requisite suggests that the loss of synchronism of a generator may induce voltage and frequency excursions away from the reference points; a significant deviation will trigger the protection devices to trip equipment with further undesired effects. Secondly, the integrity of the power network must be maintained; this requirement indicates that the means to transport the generated power to the load centres must have enough redundancy to avoid service interruptions due to single outages.

According to [16], a conceptual relationship exists between reliability, security and stability. The reliability of power systems is the probability of their satisfactory operation over an extended period. High reliability suggests that the power system delivers a suitable electric service over an extended period with only a few exceptions (service interruptions). Comparably, security is the degree of risk in its ability to survive disturbances without service interruptions. It relates to the system's capability to withstand the effect of disturbances and remain stable, also known as robustness. Security and robustness depend on the level of risk, which varies due to internal factors like operating conditions and external elements like the probability and severity of contingencies [16]. Remarkably, there is a causality relationship between reliability and security because a system must endure a set of predefined contingencies. When the robustness is high, the system will provide an almost continuous service that will enable high availability, which indicates that the system is reliable. Indeed, power system stability is a cornerstone of security and reliability; it affects the continuous operation after a disturbance and depends on the operating conditions and the nature of the disturbance, e.g. location, duration, and size [17]. Detailed definitions of different stability areas are included in sections 1.2.1-1.2.5.

The nature of a disturbance is a critical element in the power system stability; different types of disturbances have made the problem more complex to analyse with a single approach. Consequently, stability problems can be classified considering the nature of the system variables, the magnitude of the disturbance, and the time span of the effects. Recently, as a result of the increased penetration of CIG, the classification included in [16] has been extended in [17][18]. Figure 1.1 illustrates an overview of the classification of power system stability. The work presented in this thesis focus on rotor angle stability, particularly in transient stability; other types of issues like resonance, converter-driven

voltage and frequency stability are out of the scope of this work. Different areas of power system stability are described below.

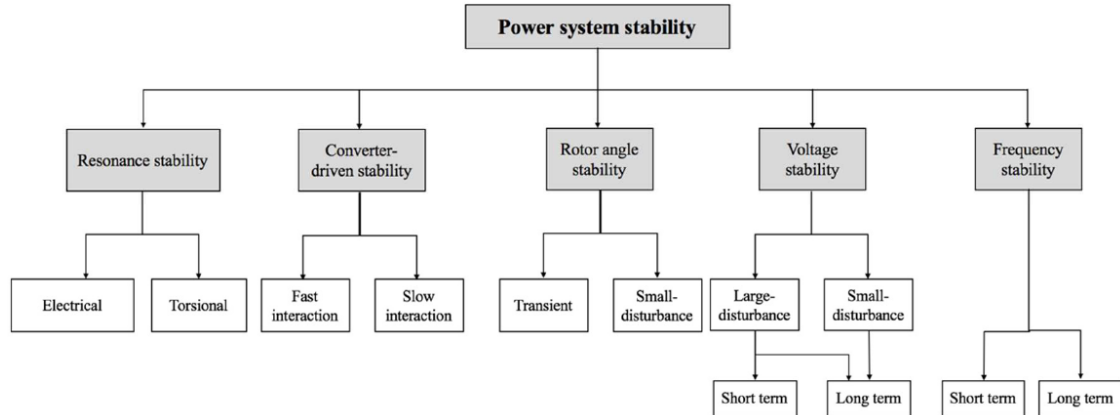


Figure 1.1: Classification of power system stability [17][18].

### 1.2.1 Rotor angle stability

Rotor angle stability is the ability of interconnected SGs of a power system to remain in synchronism after being subjected to a disturbance. The stability depends on the balance between the mechanical torque provided by the prime mover and the electromagnetic counter-torque induced by the currents flowing in the armature windings of the machines [15][19]. Under the steady state condition, the electromagnetic and mechanical torques are equal, and the angular velocity of the rotor is constant; as a result, the rotor angle also remains constant. In steady-state operation, there is a magnetic link between the rotor field and the stator field. Both fields run in synchronism under system frequency (reference), and the magnetic link between them remains stable [21]. When the torque balance is disturbed, generators will accelerate (or decelerate), resulting in a relative change in the angular separation of different generators. Due to the acceleration, one or several rotors will rotate faster than others, increasing the angle difference between them.

In practical terms, system stability after a disturbance depends on the change in the electrical torque of SGs; in fact, synchronising and damping components of the electrical torque are essential, and they are needed to restore the stable condition. In particular, the synchronising torque component is in phase with the rotor angle perturbation [20]; moreover, the synchronising torque relies on the change of electrical power output due to the change in rotor angle [16][21]. Similarly, the damping torque component is in phase with the speed deviation [20] and combines the effect of generator damper windings with rotor angle. Figure 1.2 illustrates the effect of synchronising and damping torque ( $T_S$  and  $T_D$ ); particularly, Figure 1.2(a) and Figure 1.2(b) show the effect with constant field voltage and excitation control, respectively. Unstable behaviour can be

seen as aperiodic drift when the synchronising torque is negative or with growing oscillations when the damping torque is negative. On the contrary, stable behaviour can be seen for the combination of positive synchronising and damping torque; in this case, oscillations die out, and the rotor angle settles to a constant value. An extended analysis of synchronising power coefficients is provided later in Section 1.3.6.

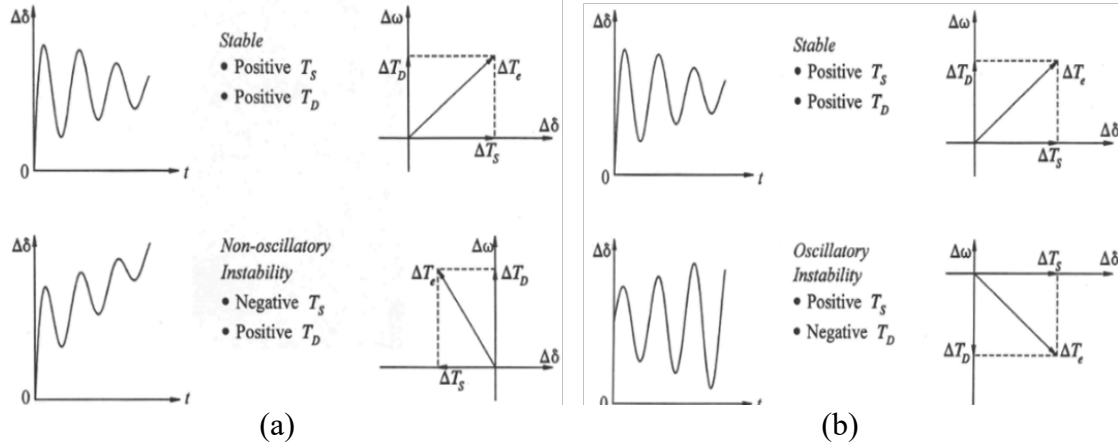


Figure 1.2: Effect of synchronising and damping torque ( $T_s$  and  $T_D$ ) [20] with constant field voltage (a), and with excitation control (b).

### 1.2.1.1 Small signal stability

According to [16], rotor angle stability can be classified by the size of disturbances in small-disturbance stability, also known as small-signal stability, and large-disturbance, commonly known as transient stability. Small-disturbance stability relates to the capability of a power system to remain in synchronism under small-size disturbances. In this case, the disturbances are sufficiently small that it is possible to analyse the system's behaviour by linearising the governing equations [16]. Furthermore, due to the linearisation, the analysis of small-signal stability can be performed by the spectral analysis of the system matrix, also known as modal analysis.

Small disturbances occur all the time and are related to minor variations in load or generation. Besides, restoring the system to a stable condition depends on several factors, such as operating conditions before the disturbance, transmission system strength, and generator excitation controls [20]. System parameters affect the system's performance under small disturbances, where instability may arise in the form of a steady increment of rotor angle or the increase of oscillation amplitude, as seen in the previous section.

### 1.2.1.2 Transient stability

Significant disturbances are those where linearised equations cannot describe a power system; therefore, a non-linear system of differential equations needs to be used. Transmission system faults, sudden and significant load changes, loss of generating units, and switching lines can be considered in this type [23]. Related to the nature of large disturbances, the transient stability of a power system is “the ability to maintain synchronism when subjected to severe transient disturbances” [20]; the effect of those disturbances causes large excursion in generator rotor angles, terminal voltage drops, a significant increase of currents due to faults, among others [16].

Instability arises if the system cannot absorb the kinetic energy accumulated in the generators after a severe disturbance [16]. The increasing angle separation causes the loss of synchronism of one or several machines, also known as “falling out of step” with the rest of the system, due to the increase (or decrease) of angular velocity. The asynchronous operation or “pole slip” occurs when the rotor field and stator field lose the magnetic link, which happens when the load angle, i.e., the angle between the rotor field and stator field, is beyond the stable point [21]. The “slip” of the rotor field from the stator field produces large oscillations in power output, current, and voltage; this situation is harmful, and protection devices in the generators are activated, disconnecting the machines from the rest of the system [20].

Usually, for transient stability studies, the period under analysis is the first few seconds when the electromechanical phenomenon is taking place. According to Figure 1.3, electromechanical transients are fast phenomena lasting from milliseconds to a few seconds. In this time frame, transient stability depends primarily on the initial conditions, i.e., operating conditions at the time of disturbance, and the severity of the disturbance, among others [20].

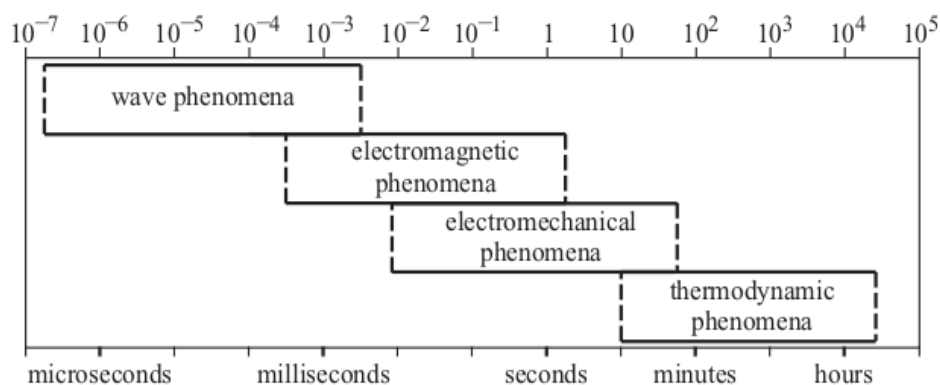


Figure 1.3: Time frame of power system dynamics [21].

### 1.2.2 Frequency stability

Frequency stability is the ability of a power system to maintain a steady frequency after a severe disturbance, which significantly disrupts the balance between generation and demand [16]. The definition indicates the need to maintain the active power balance between the generation and load within the system. Hence, the loss of generating units, or sudden and significant increase (or decrease) in the load, may result in substantial frequency excursions with further disconnection of loads (or generators).

As explained in [20], the frequency of a power system depends directly on the active power balance between generation and load, and it is a common factor throughout the system; a deviation from the system reference (synchronous) frequency reveals the presence of an imbalance, e.g., a total load higher than system's generation produces a frequency decay. In particular, the primary purpose of frequency control is to maintain the frequency of the system within a narrow band, i.e., as stable and close as possible to a reference value. Besides, maintaining a constant speed is a crucial factor that impacts the performance and reliability of the power system.

The classification of frequency stability by time frame in [16] is implicitly related to the control action in place to restore the system's frequency to a reference value. In the UK, NGESO is responsible for maintaining an adequate level of reserves to maintain the frequency within the statutory limit of  $\pm 1\%$  of 50 Hz., considering emergency limits of  $+4\%$  and  $-6\%$ ; nevertheless, the usual operating limits are  $\pm 0.4\%$  [24] as shown in Figure 1.4(b). The time frame of control actions, also known as frequency response, and its effect on the system frequency can be seen in Figure 1.4(a), considering the following elements [21][25]:

- i. Inertial response: It is a characteristic inherent to the size of SGs that allows them to absorb kinetic energy; this effect occurs almost immediately after a disturbance and contributes to arresting the frequency excursion.
- ii. Primary frequency control: Available a few seconds after the disturbance up to thirty seconds; in this control action, generator governors adjust the mechanical power input to stop the frequency excursion.
- iii. Secondary frequency control: Available from thirty seconds to thirty minutes after the disturbance. The control adjusts the load reference set point of the generators allowing the generation to increase their output to restore the

frequency to the nominal value; it can be realised in a centralised or decentralised way.

- iv. Tertiary frequency control: This is the slowest frequency control action compared to primary and secondary control, and it is activated when they are not enough to restore the frequency to the reference value. This control is mainly centralised and introduces changes in operating points and reserves.
- v. Emergency frequency control: If the frequency deviation exceeds emergency limits, the under-frequency load shedding activates circuit breakers and disconnects loads.

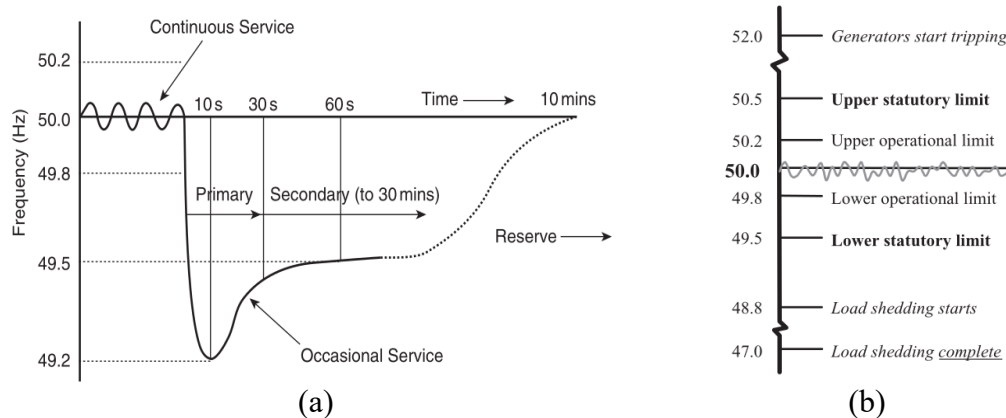


Figure 1.4: National Grid frequency response requirements (a), and operational and statutory limits (b) of system frequency for the UK power network [25].

### 1.2.3 Voltage stability

Voltage stability is the ability of a power system to maintain steady voltages in all system buses following a disturbance [16]. This ability depends on the system's capacity to provide reactive power for a given active power demand [21]; therefore, the ability is related to the maximum power transfer of the network, and active and reactive power flows through inductive reactances [19]. In practical terms, voltage stability issues are intrinsically related to the fact that a system cannot supply the reactive power demand. The criterion presented in [16] establishes that the system is voltage stable if reactive power injection increases the bus voltages in all buses; on the contrary, if one bus reduces its voltage under reactive power injection, then the system is unstable. The unstable condition is inherently local, i.e., it can affect only one bus; however, that condition can cause a widespread effect known as voltage collapse. Voltage collapse is a complex phenomenon that combines a sequence of events that results in a low voltage profile on a significant area of the system [19]; in those cases, the local injection of reactive power has been exhausted, and transformers tap changers have reached their boost limit. Voltage and rotor angle stability issues can be related under high loading conditions

involving pre-fault active and reactive power flows. For instance, voltage instability can occur due to the loss of synchronism, which causes rapid voltage drops; conversely, rotor angle stability can arise from degraded operating conditions under voltage instability [19].

The classification of voltage stability by time frame is related to the load type and the control action of converter-based sources. For example, short-term voltage stability can be influenced within a second or less by stalled induction motors consuming large starting currents; or HVDC systems connected to weak AC systems [18]. For time frames of minutes, long-term voltage stability is influenced by the limited voltage support from slow-acting devices or SGs reaching their limits [19].

#### **1.2.4 Resonance stability**

Recently formally introduced in [19], resonance stability is intrinsically related to Sub-Synchronous Resonance (SSR) and can be associated with electromechanical or purely electrical resonance. The resonance manifests as significant increases in voltage, currents, or torques magnitudes; resonance instability arises when those magnitudes grow beyond acceptable limits. A further classification of resonance stability includes torsional and electrical resonance [18]. On the one hand, torsional resonance affects SGs when SSR appears due to the torsional interaction of series compensated lines and the turbine-generator mechanical shaft. On the other hand, electrical resonance involves SSR between induction generators and series compensation, like in the case of Doubly-Fed Induction Generators (DFIG).

#### **1.2.5 Converter-driven stability**

Converter-driven stability has become more relevant with the growth of CIG to harness power from RES, like wind and solar, and so it has been introduced formally as a new type of stability [16]. The power converters of CIG rely on fast sampling and control actions (switching) to provide the desired output. Those control loops may interfere with electromechanical dynamics of SGs or electromagnetic transients from the network; the interaction between power converters and SGs can lead to instability in a wide range of frequencies. A further classification based on the frequency range of interactions includes fast and slow converter-driven stability [18]. Fast interaction converter-driven stability involves a frequency range from tens of Hz up to several kHz; stability issues are related to the fast dynamic interaction between control loops of power electronics of



CIG, HVDC, flexible AC transmission systems (FACTS) with fast response components of the system like stator dynamics of SGs, transmission network and other power electronic interfaced devices [19]. On the contrary, slow interaction converter-driven stability involves a frequency range around tens of Hz; instability arises due to the interaction of electromechanical dynamics and controllers of SGs with slow dynamics of controllers of CIG devices [18]. Slow-interaction instability is typically associated with CIG connected to weak AC grids, i.e., long transmission lines with high equivalent impedance.

### 1.3 Essential concepts of transient stability

This section introduces the essential concepts associated with transient stability based on a simplified representation of a power system. The purpose is to describe analytical tools to analyse the transient stability problem highlighting the effect of the network structure.

#### 1.3.1 Classical model of synchronous generators

As stated in Section 1.2.1.2, the analysis of transient stability studies in power systems involves the study of the effects of large disturbances in the relative rotor angle deviation among SGs; therefore, linearised system equations are not suitable for this purpose [23]. The SG is a sophisticated machine with complex geometries that influence the magnetic coupling in the air gap between the rotor and stator. Nevertheless, the work presented in this thesis concentrates on the dynamics of SGs during the first swing, which is the early stage of electromechanical phenomena (see Figure 1.3). Within the first second after a fault, the rotor angle of an SG increases with respect to the pre-fault value; this first oscillation is known as first-swing [26].

The classical model of an SG in (1.1), which is mainly based on the swing equation, provides the mathematical basis to identify if a system is first swing stable. Assuming constant flux linkage and neglecting generator transient saliency, i.e., direct and quadrature axis reactances are equal [20][21], the SG is represented by a constant EMF  $E' \angle \delta'$  behind the direct axis transient reactance  $x'_d$ , (see Figure 1.5) with constant mechanical power input. The EMF  $E' \angle \delta'$  is the induced voltage on the stator with a constant magnitude  $E'$  and angle  $\delta'$ , where  $\delta'$  is the phase shift between the internal voltage and the voltage reference (infinite bus) representing the spatial angle between synchronously rotating rotors [21], also known as rotor angle. This model does not

consider rotational loss (damping) [21]; however, excitation control and turbine governing can be integrated.

$$\begin{aligned} \frac{2H}{\omega_r} \frac{d\Delta\omega'}{dt} &= P_M - P_E \\ \frac{d\delta'}{dt} &= \Delta\omega' = \omega' - \omega_r \end{aligned} \quad (1.1)$$

Model (1.1) specifies the dynamics of an SG in p.u.; the rotor variables are  $\delta'$  and  $\Delta\omega'$  representing the rotor angle position in electrical radians and rotor speed deviation in electrical radians per second, respectively. Parameters are the inertia constant  $H$  of the generator in seconds, and the reference speed of the system  $\omega_r$  in electrical radians per second.  $P_M$  and  $P_E$  are the turbine mechanical power and electrical power output of the synchronous generator in per unit, respectively.

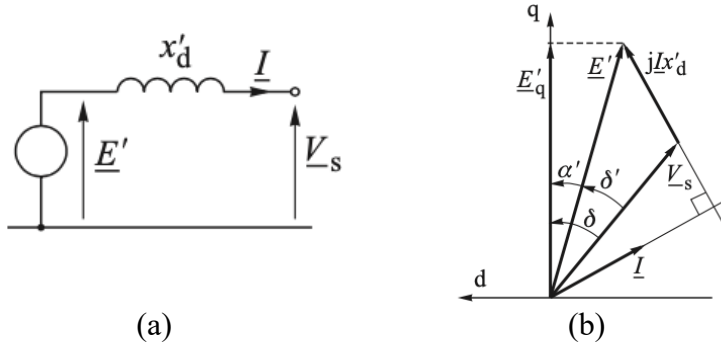


Figure 1.5: Circuit (a) and phasor diagram (b) of the classical representation of a SG; armature resistance neglected [21].

The classical model has been extensively used for transient stability assessment using transient energy function methods [27][28] or time-domain simulation (TDS) [29][30]. Interestingly, for TDS, the classical model provides pessimistic results compared to more sophisticated models, like the sixth-order model; in practice, the classical model provides more conservative results, making it suitable for preliminary analyses [21].

### 1.3.2 Single machine infinite bus

In practical terms, an SG is connected to a power system comprising a large number of loads and several generators connected by a transmission network. In particular, the combination of SGs can be represented by an ideal voltage source, also known as infinite busbar [21]. This type of network is typically known as Single Machine Infinite Bus (SMIB) system (see Figure 1.6). SMIB is highly used for testing purposes due to its versatility; the infinite bus absorbs all active and reactive power output of an SG whilst maintaining constant voltage and frequency. For simplicity, the SMIB is usually purely reactive, i.e., armature losses and resistive components are neglected.

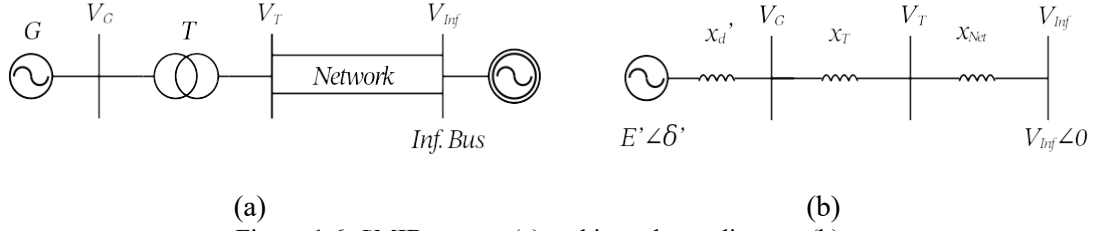


Figure 1.6: SMIB system (a) and impedance diagram (b).

### 1.3.3 Power angle equation

As stated in Section 1.3.1, the mechanical power output  $P_M$  is constant in the classical model (1.1); therefore, the electrical power output  $P_E$  determines the acceleration experienced by the SG. The transient power-angle characteristic  $P_E(E', \delta')$  given in equation (1.2) is a function of the transient EMF  $E'$  and power angle  $\delta'$ , also known as the power angle equation. In this thesis equation (1.2) is also referred as power-angle characteristic.

$$P_E = \frac{E' \times V_{Inf}}{x_{Eq}} \sin \delta' \quad (1.2)$$

Notably, under the classical SG model, the angle  $\delta'$  has a dual purpose; it represents the relative rotor angle position with respect to the reference machine and the power angle defining the flow of active power between the SG and the infinite bus [21]. For the SMIB system of Figure 1.6, the equivalent impedance  $x_{Eq}$  between the SG and the infinite bus is the sum of impedances of the network  $x_{Net}$ , step-up transformer  $x_T$ , and generator internal transient reactance  $x_d'$ . This fact implies that characteristics of the network, in terms of structure and parameters, has a key effect on the maximum active power transfer capability; this effect will be highlighted in the sections below.

### 1.3.4 Equal Area Criterion

The power-angle characteristic (1.2) enables the analysis of the effect of a large disturbance on the SMIB system. As described in Section 1.2.1.2, a large disturbance can produce the loss of synchronism of an SG, i.e., an unstable system, which results from multiple factors such as SG parameters, system operation, fault characteristics or network structure. By focusing on the clearing time, the Equal Area Criterion (EAC) defines the condition where a SMIB system is able to remain stable, which depends on the maximum energy that the system can dissipate after a fault; in practical terms, it specifies the critical clearing angle  $\delta_{cr}$ , which is the one that makes the accelerating area equal to the decelerating area. For a three-phase self-clearing fault in one of the two transmission

lines of SMIB (see Figure 1.6), Figure 1.7 illustrates the EAC by highlighting  $\delta_{cr}$ . In the figure the area  $A_1$  represents the accelerating area where the SG accumulates kinetic energy during the fault; conversely, in the decelerating area  $A_2$  the system dissipates the accumulated energy decreasing the rotor speed. The direct (or second) Lyapunov's method, which is also known as the Transient Energy Function (TEF) method [20][30], provides insight into the meaning of the areas. The area  $A_1 + A_3$  in Figure 1.7 is the total energy of the system accumulated during the fault, which is composed by the kinetic energy  $A_1$  and the potential energy  $A_3$ . Similarly,  $A_2 + A_3$  is the total potential energy at the unstable equilibrium  $\delta_{lim}$ , also called the critical energy, which is the one that the system is able to absorb. If the accumulated energy is larger than the potential energy  $A_1 + A_3 > A_2 + A_3$  the system is unstable.

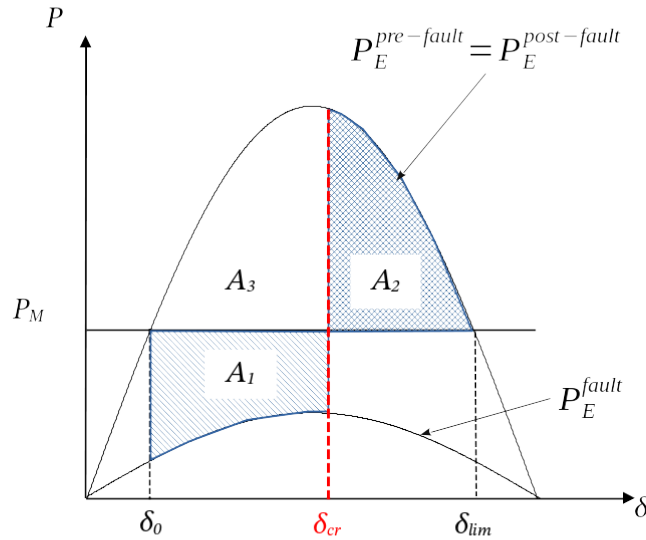


Figure 1.7: EAC for a SMIB system considering pre-fault and during fault curves (adapted from [20]).

Figure 1.8 illustrates the behaviour of the rotor angle for stable and unstable cases. Initially, in steady state  $P_M$  is equal to  $P_E$  and the system is in a stable equilibrium with a pre-fault rotor angle  $\delta_0$ , shown as point 1 in Figure 1.8 (a). During the fault, the SG continues transferring power to the infinite bus through the remaining line; the rotor angle  $\delta$  follows the power angle characteristic  $P_E^{Fault}$  along the segment 2-3 in Figure 1.8 (a). Under fault condition  $P_M > P_E$ , hence the SG absorbs kinetic energy and its rotor angle starts to increase. From the clearing time, given by the clearing angle  $\delta_{cl}$ ,  $P_E$  changes instantaneously to point 5, following  $P_E^{Post-Fault}$  with decelerating power  $P_E > P_M$ ; here, the rotor angle  $\delta$  increases up to point 6 where the kinetic energy is depleted. At point 6 the system has dissipated the kinetic energy gained during the fault, and the SG rotor angle starts to decrease; it oscillates around point 1 due to the inertia, but it will remain stable. As seen in Figure 1.8(a), the decelerating area of the post-fault system  $A_2 + A_4$  is larger than the kinetic energy accumulated during the fault  $A_1$ ; therefore, the

rotor angle oscillates around  $\delta_0$  and the system remains stable. On the contrary, Figure 1.8(b) shows an unstable scenario. Due to the delayed fault clearing, the system is not able to dissipate the kinetic energy gained during the fault; Figure 1.8(b) reveals that  $A_1 > A_2$ . After the fault clearing,  $P_E > P_M$  and the system decelerates; however, the system cannot dissipate all the kinetic energy and the rotor angle increase continues. Beyond the unstable equilibrium  $\delta_{lim}$ ,  $P_M > P_E$  which accelerates the SG again; the acceleration increases the rotor angle excursion even further, and the system becomes unstable, as shown in Figure 1.8(b).

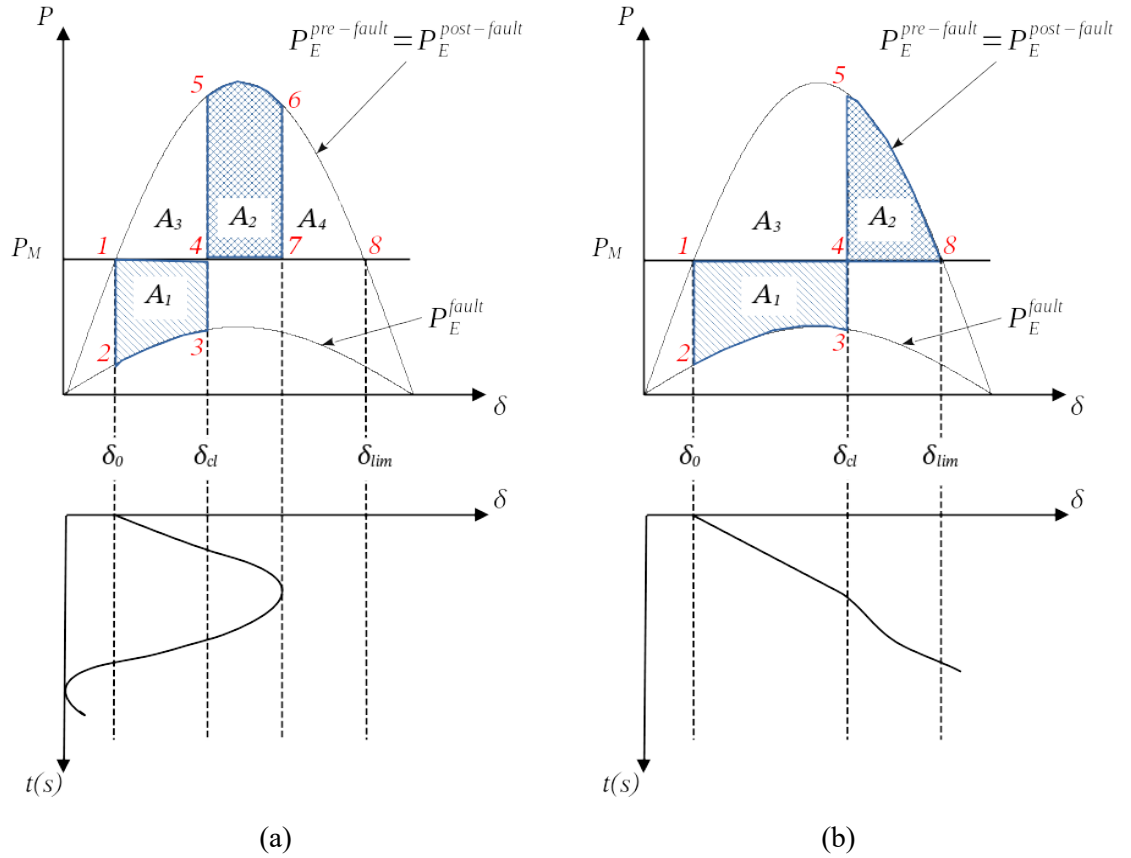


Figure 1.8: Power-angle characteristic for a SMIB system. (a) Stable case and (b) unstable case (adapted from [20]).

From the network structure viewpoint, the network plays a role in the maximum electrical power output during and after the fault altering the power angle characteristic. The effect of modifying  $x_{Net}$  will increase (or decrease)  $x_{Eq}$  reducing (or increasing) the peak of  $P_E^{Fault}$  and  $P_E^{Post-Fault}$ . For the post-fault network, the increase of  $x_{Eq}$  would decrease the power angle characteristics, and at first glance, it would decrease the decelerating area, negatively affecting the stability; this is true, especially for faults making  $P_E = 0$ . However, for faults in which the network structure allows some power transfer during the fault, such an effect can be positive towards transient stability, as it will be thoroughly studied later in chapters 3 and 5.

### 1.3.5 Critical Clearing Time

A method for transient stability assessment is the Critical Clearing Time (CCT) [21], [31]. The CCT is the longest fault clearing time for which an SG remains stable; in comparison, a system with a longer CCT implies that a system is more stable, whilst a shorter CCT suggests a more fragile system. The CCT is intrinsically related to the critical clearing angle  $\delta_{cr}$ , which is the angle that makes  $A_1 + A_3 = A_2 + A_3$  (see Figure 1.7). A common practice to obtain  $\delta_{cr}$  is calculating definite integrals of  $A_1$  and  $A_2$ , with integration limits  $\delta_0 \rightarrow \delta_{cr}$  and  $\delta_{cr} \rightarrow \delta_{lim}$ , respectively.

Regarding the stability level, the used CCT formula can be derived from model (1.1).; rewritten here as a second-order differential equation in p.u.

$$\frac{2H}{\omega_r} \frac{d^2 \delta}{dt^2} = P_M - P_E \quad (1.3)$$

With a negligible effect of the governor during a fault condition, the mechanical power input is considered constant in the accelerating power  $P_A = P_M - P_E$ . Assuming constant  $P_A$ , with initial conditions  $\delta(t=0) = \delta_0$  and  $\frac{d\delta_0}{dt} = 0$ , allows the solution of (1.3) as follows:

$$\begin{aligned} \int_{\omega_0}^{\omega} d\omega &= \frac{\omega_r}{2H} (P_M - P_E) \int_{t_0=0}^t dt \rightarrow \omega = \frac{\omega_r}{2H} (P_M - P_E) t \\ \frac{d\delta}{dt} &= \frac{\omega_r}{2H} (P_M - P_E) t \rightarrow \int_{\delta_0}^{\delta} d\delta = \int_0^t \frac{\omega_r}{2H} (P_M - P_E) t dt \\ (\delta - \delta_0) &= \frac{\omega_r}{2H} (P_M - P_E) \frac{t^2}{2} \rightarrow t = \sqrt{\frac{4H(\delta - \delta_0)}{\omega_r (P_M - P_E)}} \end{aligned} \quad (1.4)$$

An analytical expression of the CCT in seconds is given by equation (1.5). Here, the selected MVA base is the MVA rating of the SG; therefore,  $H$  and  $\omega_r$  are the SG inertia constant in seconds and rated speed in radians per second, respectively.  $P_M$  and  $P_E$  are in p.u., normalised using the SG MVA rating.

$$CCT = \sqrt{\frac{4H(\delta_{cr} - \delta_0)}{\omega_r (P_M - P_E)}} \quad (1.5)$$

An analysis of equation (1.5) can be done considering the ratio  $4H/\omega_r$  constant. A stability increase, i.e., longer CCT, requires either an increase of  $(\delta_{cr} - \delta_0)$  or a

reduction of  $(P_M - P_E)$ . From a topological perspective, the structure of the network during the fault can positively affect the CCT by increasing  $P_{E,max}^{fault}$ , which will reduce  $(P_M - P_E)$  in (1.5). The post-fault network also has an impact on CCT, an increase  $P_{E,max}^{post-fault}$  due to a lower equivalent impedance  $x_{Eq}$ , which can boost the decelerating area. The effect of the network will be described in detail in Section 3.1.3.

### 1.3.6 Synchronising power coefficient

Also introduced in Section 1.2.1, the synchronising torque is the electrical torque component that helps to avoid aperiodic drifts [20]. For the classical model (1.1), the synchronising effect is related to the electrical power output of the SG given in (1.2). Assuming constant flux linkage and neglecting rotor transient saliency  $x'_d \approx x'_q$ , the increase of the pre-fault rotor angle  $\delta'_0$  by  $\Delta\delta'$  produces a change in the electrical power output in phase with the rotor angle deviation, known as the transient synchronising power  $P_S = K_S \Delta\delta'$  [21]. Here, the transient synchronising power coefficient in equation (1.6) is the slope of the power-angle characteristic (1.2) evaluated at the stable equilibrium point  $\delta'_0$ .

$$K_S = \left. \frac{\partial P_{E'}}{\partial \delta'} \right|_{\delta'=\delta'_0} = \frac{E' \times V_{Inf}}{x_{Eq}} \cos \delta'_0 \quad (1.6)$$

The transient synchronising power coefficient  $K_S$ , is the change in the electrical power output of the SG due to a change in the angle between the machine's internal EMF and the infinite bus [17][22]. The provision of synchronising power  $P_S = K_S \Delta\delta'$  depends on the internal EMF, the infinite bus voltage, the steady state rotor angle, and the equivalent impedance between the SG and the infinite bus. In particular,  $K_S$  is sensitive to the initial condition  $\delta'_0$ ; as seen in Figure 1.9, an increase in active power dispatch will increase the steady state rotor angle reducing the synchronising coefficient  $K_S$ . Similarly, from the network viewpoint, the power-angle and synchronising power coefficient curves share the same maximum given by  $E' \times V_{Inf}/x_{Eq}$ ; thus, an increase of network impedance  $x_{Net}$  will lower the peak of the power-angle characteristic and synchronising power curve, reducing the magnitude of  $K_S$ . Either the increase of  $\delta'_0$  or  $x_{Net}$  reduce  $K_S$ , which can be seen as detrimental for transient stability because it diminishes the ability to return to the stable equilibrium.

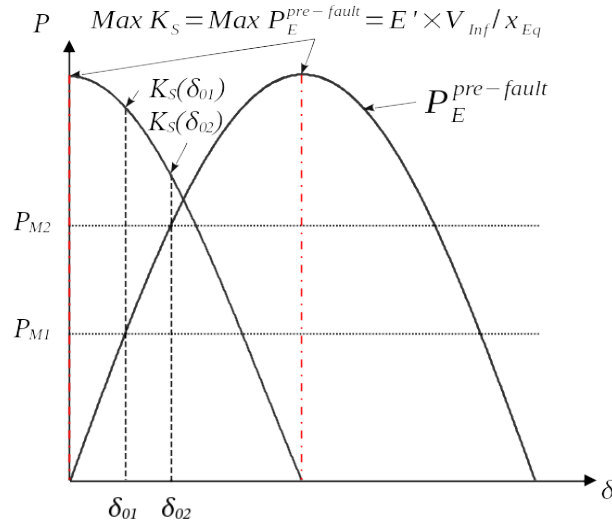


Figure 1.9: Transient synchronising power coefficient and power-angle characteristic (adapted from [21])

### 1.3.7 Generator embedded controllers influencing transient stability

In principle, the purpose of generator controllers is to improve the stability of a power system by changing the dynamic response of SGs; the most common generator controllers are the Automatic Voltage Regulator (AVR), Power System Stabiliser (PSS) and governor. The classical model of SG has been extensively used to describe the transient stability problem based on the SMIB system due to its simplicity. However, for more accurate transient stability studies, the most used model is the sixth-order dynamical model of an SG [20][21][31], which will be described in Chapter 2, along with the detail of generator controllers used in the present work. Compared with the sixth-order model, the classical model provides pessimistic results that can be used for preliminary assessments [21].

From the rotor angle stability viewpoint, whilst the AVR's primary effect is during the first swing, the effect of the PSS focus beyond the first swing [21]. In particular, the AVR provides voltage regulation at the SG terminals by controlling the DC current in the stator field winding, i.e., excitation current [25]. For that purpose, the AVR monitors the SG terminal voltage and compares it with a reference; the voltage error is usually amplified and fed to an exciter, which controls the excitation current so that the voltage error can be eliminated [21]. Particularly, after a fault occurs, the voltage in generator terminals falls, which provides a large error signal to the AVR. The AVR will increase the field current according to its gain and time constant parameters, but the transient EMF will react according to the field winding time constant [21].



The resulting action of the AVR produces a boost on  $E'$  increasing the peak power-angle characteristic during the fault and post-fault condition, which creates a family of curves, as shown in Figure 1.10(a). The benefits of the AVR are twofold; firstly, the reduction of the accelerating area  $A_1$  during the fault; secondly, the increase of decelerating area  $A_2$  after the fault clearing, with the former being the most important due to the time constants involved in the dynamic response. Even though the benefit of the AVR is clear for the first swing, it can introduce negative damping, increasing the second and further swings. The latter effect depends on system parameters and dynamic characteristics of the AVR and SG [21]. For instance, if the SG is connected through a weak link, i.e., a large impedance, the voltage level at clearing time will continue to produce a large voltage error. The AVR will continue to increase the excitation due to the voltage error; hence, the back swing of the rotor angle will be larger, as illustrated in Figure 1.10(b). Another source of negative damping is the interaction between the currents induced in the direct axis damper winding due to the change in field voltage, opposing the current induced by the change in speed deviation. This negative damping effect can increase due to large generator loads, gain in AVR controllers, and network reactances [21].

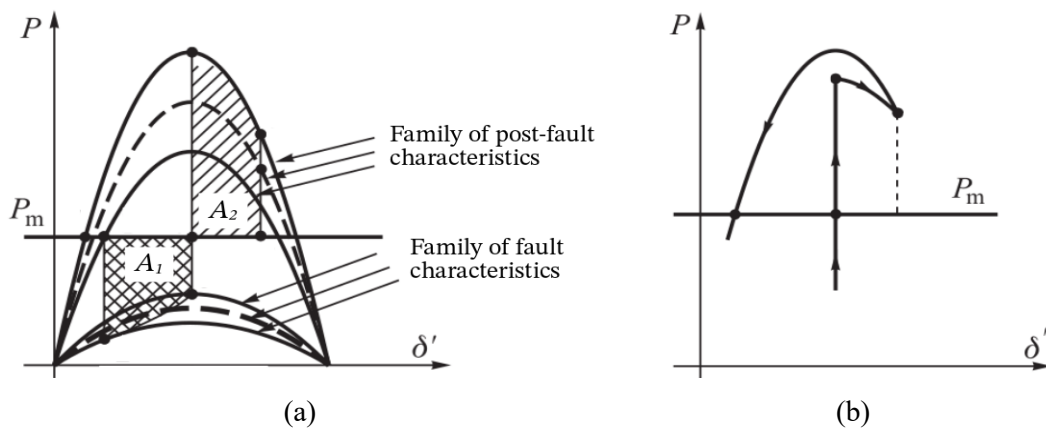


Figure 1.10: Influence of the AVR in (a) power-angle characteristic SMIB system, and (b) backswing effect [21].

To reduce the effect of negative damping, the PSS increases the damping of rotor angle oscillations by injecting an auxiliary stabilizing signal to the AVR [20]. The purpose of the PSS is to increase the damping torque in phase to the speed deviation during the transient state. For that purpose, the auxiliary signal is zero during the steady state to avoid voltage regulation distortion. On the contrary, when a fault occurs, a large auxiliary voltage signal is added opposing the voltage error; the resultant voltage error will introduce positive damping in phase with the speed deviation. Traditionally, PSSs are tuned to provide damping instead of synchronising torque; thus, its effect focus beyond the first swing, whilst its effect on the first swing can be neglected [21].

From the frequency stability perspective, the governor monitors changes in rotor speed and acts by increasing (or reducing) the flow in the prime mover to increase (or decrease) the mechanical torque [25]. The prime mover thermal dynamics are slow in comparison to the electromechanical phenomena (see Figure 1.3); therefore, the governor action does not affect the mechanical torque during the transient period [32], which is considered constant for transient stability studies [20][21][31]. Though the governor's influence is out of the scope of this thesis, governor control is included in the test systems of this thesis to provide realistic dynamic responses.

### **1.3.8 Transient stability in multimachine systems**

Electricity is a highly flexible form of energy that can be transported and transformed into other forms of energy; these features have made it one of the most widely used energies [25]. In this context, real power systems can be characterised as large and meshed networks connecting generating plants with load centres. Although the SMIB system is a valuable tool to assess the stability of a power system, it is limited to a single machine; the stability analysis of multi-machine systems requires a different approach because the interaction of different SGs has a significant impact on the stability outcome.

For SMIB systems, the reference is the infinite bus, whereas for multi-machine systems, the reference can be defined arbitrarily. Typically, the SG with the largest inertia and far away from the fault location is selected as the system reference [21]; thus, all other rotor angles can be measured with respect to the rotor angle of the reference SG. Another method is to measure the rotor angles with respect to the Centre of Inertia (COI), also known as the COI synchronous reference frame. The COI is derived from the centre of angles; it was introduced in [33][34] for the analysis of transient energy [22]. In simple terms, the COI represents the collective behaviour of the SGs connected to the system. In the COI framework, the inertia weighted average of all rotor angles in the system, i.e., the centre of angles [35], is the reference and represents the position of the rotor of the collective representation. This approach has been used as a tool in several dynamic security studies, e.g., [36][37].

In the context of multi-machine systems, disturbances affect SG in different degrees of severity, especially considering the relative location of loads and SGs. Particularly, the relative location of SGs with respect to the fault location can produce different dynamic responses; similarly, the relative location of loads or other SGs might result in a different

stability outcome. In summary, a severe disturbance can generate instability in a multimachine system, depending on the relative location of the fault, as follows [21]:

- i. The SG closest to the fault location loses synchronism without showing synchronous swings; other SGs can be affected by the fault experiencing rotor angle oscillations, but they remain stable, returning to synchronous operation. The SMIB system can represent this case because the effect of the fault is not severe enough to produce instability in other SGs; the SG nearest to the fault location is likely to become unstable during the initial swings.
- ii. The SG, or several SGs, close to the fault location, loses synchronism experiencing rotor angle oscillations. In this case, the SG nearest to the fault may be first swing stable, but it may become unstable in later swings because of the synchronising effect of other relatively close SGs severely affected by the disturbance.
- iii. The SG close to the fault location loses synchronism, which produces instability in other SGs. This case of multimachine instability is pervasive; if an SG loses stability, it is highly likely that relatively close SGs will also lose synchronism.
- iv. The SG or several SGs, close to the fault location remain stable after experiencing rotor angle oscillations; however, one or more SGs relatively far away from the fault may lose synchronism. This case is related to the lack of damping torque of weakly connected SGs; although an SG far from the fault may be first swing stable, it can lose synchronism due to negative damping.

## 1.4 Literature review

The role of the network structure on the transient stability of power systems is the central theme of this thesis. Therefore, the reviewed literature considers industry practices involving changes in the network structure and optimisation techniques such as optimal transmission switching, optimal topology control, controlled islanding, and transient stability constrained optimal power flow. Furthermore, as network metrics can characterise the topology, the survey also includes graph theory results applied to network assessments.

### 1.4.1 Industry practices involving topological changes

In 2005 [38], in the context of Regional Transmission Operators (RTOs), the concept of dispatchable transmission element included any transmission element that can be

operated at more than one level, e.g., discrete states like On/Off; with this definition, authors in [38] specified transmission dispatch in a similar way as for generation assets. Though technologies to interrupt the flow of power, like circuit breakers, are already mature [39] with negligible operational costs, \$10 per switching operation cycle according to [40], traditionally computational methods and operational protocols used by Transmission System Operators (TSOs) do not harness the flexibility of transmission assets and use a fixed network topology. Even though most TSOs do not implement systematic methodologies to assess the benefits of switching transmission components, industry practices already take advantage of changing the topology of the network by ad-hoc procedures like Pennsylvania-New Jersey-Maryland (PJM) RTO [41] and Elia Belgian TSO [42]. In practice, TSOs switch transmission components to improve voltage profiles and transfer capabilities during lightly loaded hours [43][44], as corrective or special protection schemes under contingencies [45][46], for seasonal load changes [47], for scheduled maintenance [41][48], and to mitigate congestion on transmission lines [41][43]. Most ad-hoc practices are based on historical data or expert knowledge about the specific transmission network [49]. These practices are prescribed as procedures for system operators instead of being included in optimisation methods [50]; though they are effective, their efficiency can be questioned.

Mitigating transmission congestion has been one of the main drivers for implementing measures to improve power transfer capabilities; in fact, PJM declared in the state of the market report 2021 [15] that the total congestion costs increased 88.2% from \$528.7 million in 2020 to \$995.3 million in 2021. Power flow control technologies like FACTS devices can be successfully used to tackle the problem [51][52]; however, the major advantage of topological changes implemented by circuit breakers is that they do not require expensive or sophisticated hardware [39][47]. Therefore, methods using circuit breakers offer better comparative advantages in terms of reliability [39] and cost [40].

### **1.4.2 Optimal transmission switching**

From a broad perspective, Optimal Transmission Switching (OTS) encloses methodologies, like optimisation techniques, that rely on the status (On/Off) of transmission assets, traditionally transformers and lines, to provide a control measure to improve the operating condition of a power system [53]. When focused on transmission congestion in power systems [54], OTS has the potential to use the available transfer capability to transmit more power from lower-cost generating units to meet the demand

[54]. However, even considering potential benefits, the challenges in adopting OTS from the industry described in [47] are related to long computational time, effective AC performance, stability of switching actions, and limited understanding of performance on a realistic large-scale power system. Furthermore, the reviewed literature shows that transmission switching focuses mainly on overloading and voltage violations, with virtually non-existent work related to transient stability issues that switching actions may trigger.

According to [55], branch switching was introduced in 1980 to reduce overloads and load shedding. For the past 40 years, researchers and engineers have been using transmission switching to relieve branch overloads [56]–[60], mitigating voltage violations [57][58][61][62], generation cost reduction [63][64][67], reducing transmission line losses [65][61], security enhancement [39][61][66], and integration of RES [67]. A corrective OTS method to reduce generation costs was introduced in 2008 [64][68]. The authors extended a DC power flow (DCPF) formulation to include active power line flow constraints with binary variables (On/Off). Results based on the 118-Bus test system provide evidence of a 25% cost reduction in [64]; the reason behind the cost reduction is that the planned (fixed) topology is designed for long-term use based on reliability considerations, whereas the OTS focus on cost reduction given a specific load profile [64]. Further extensions to the OTS formulation were implemented as Mixed-Integer Linear Programming (MILP) considering contingency analysis [50] and co-optimisation of unit commitment and N-1 reliability [69].

Different heuristics have been used to solve OTS problems to reduce system losses [70] and generation costs [54], [71]–[74]. Authors of [70] solved the problem using the branch and bound method and included overloading and security costs in the fitness function of a genetic algorithm (GA). In [71], the MILP computation is improved by ranking heuristics based on an economic congestion charge parameter; highly congested lines are removed from the solution space. Two screening heuristics proposed in [54] are based on line outage and power transfer distribution factors (PTDF); results based on the IEEE300 test system show approximately 70 times faster computation in comparison with regular MILP solutions in [54]. Based on the results of the RTS-96 test system, the authors of [72] state that limiting the number of switching operations by screening branches can provide near-optimal results; the analysis of single switching suggests that only a small number of line switching produce significant cost savings. Though previous work was mainly derived from DCPF, the OTS method proposed in [73] was one of the

first to use an AC power flow (ACPF) formulation to define a Mixed Integer Non-linear Programming (MINLP) problem. The authors state that methods based on DCPF frequently violate voltage limits, which may produce system collapse; thus, the proposed OTS as ACOPF provides more secure switching options. The ranking heuristic proposed in [71] based on DCPF was later improved in [74] by using the ACPF formulation. The authors in [74] concluded that under high load scenarios, the heuristic based on ACPF is more accurate than the one based on DCPF; the authors also found that DCPF-based heuristics provide switching candidates that increase the cost [74].

Heuristics have also been proposed to solve corrective OTS to reduce generation cost, avoid component overloading [47], [75]–[79], maximise load served with security [39], and minimize load shedding [80]. The heuristic proposed to improve the computation of the MINLP problem in [75] was one of the first to use the shortest path length within the procedure; the proposed method in [75] provided corrective switching solutions in less than a minute, reducing post contingency violations in 70% of cases. Tested on IEEE-118, sequential and simultaneous heuristic methods proposed in [39] show a load shedding reduction of at least 24%; though counter-intuitive, the authors in [39] found that corrective OTS adds flexibility to the system enhancing operations efficiency and reliability. In [47], real-time contingency analysis defines a list of switching candidates; the switching solutions are ranked by their shortest path length to the overloaded asset or to the asset under active contingency. The results show in [47] that substantial reductions in post-contingency violations are observed in 56%-83% of the cases; results reveal significant savings due to the reduced need for expensive reliability-motivated generation redispatch and commitment [47]. Mixed Integer Second Order Cone Programming (MISOCP) approaches were proposed in [76][77]; in standard IEEE test cases, the second-order cone relaxation in [76][77] provides consistent improvements with up to 20% cost reduction with 50% reduction of computation time in comparison with MILP approaches. Authors of [78] proposed a decentralised OTS problem to reduce the operational cost of a multi-area power system; they found that subproblems related to each area can be fully decoupled to facilitate parallel computation using an augmented Lagrangian relaxation. Recently, an enhanced energy management system proposed in [79] combines real-time contingency analysis with corrective OTS as input to a DC security-constrained economic dispatch problem; the authors in [79] state that the method can reduce at least 80% of congestion cost with computation time below one second. Moreover, the method's performance enables online applications to enhance topology

flexibility, relieve network congestion, and significantly reduce congestion costs [79]. A linear approximation for AC OTS is proposed in [80] in the form of MILP to avoid load shedding; in comparison with previous approaches, the proposed method reduces computational time by at least 80%.

From the stability of power systems viewpoint, most of the literature on transmission switching is related primarily to asset overloading, voltage violation and reduction of operational costs, with only a small fraction focusing on transient stability. Though the methods proposed in [47][75] perform transient stability verification for the optimal switching solution, only a few addressed transient stability issues as their primary objective [81][82]. The authors of [81] proposed a switching scheme for long transmission circuits connecting SGs to distant loads through long parallel transmission circuits. The stabilizing idea behind the scheme was the isolation of the accelerated units during fault conditions; at fault clearing, other SGs are connected, providing synchronising power and reducing the acceleration of the critically accelerated machines. The drawback of this approach is the network topology; the structure is highly regular, representing a long transmission circuit, and all generators are equally and strongly connected. Also related to transient stability, the authors of [82] proposed an OTS method to reduce generation cost and short circuit currents (SCC); the heuristic proposed to solve the MILP was one of the first to use an electrical distance ranking based on graph theory. Though the reduction of SCCs can be beneficial for transient stability, the main purpose of the method proposed in [82] is to avoid overloading due to high SCC; particularly, the authors found that the larger the electrical distance between generators and fault location, the smaller the short circuit current is. Moreover, including the SCC constraints significantly improves the computational time with at least six times better performance than previous formulations.

### 1.4.3 Optimal topology control

Optimal Topology Control (OTC) focuses on changing the status of transmission assets as a means of control, which is similar to OTS; however, in OTC literature, topological changes include not only transmission assets like transformers and lines [41] but also splitting and merging busbars [83][84], and the operation of phase-shifting transformers [85]. One of the main drivers for OTC is that long-term transmission planning focus on optimising costs over the years, which can significantly diverge, and may collide, from real-time operation goals; in practice, lines built to relieve a specific constraint may cause

economic inefficiencies under rapidly changing operating scenarios [86]. The classic economic dispatch (ED) problem minimizes the generation cost subject to transmission constraints where the topology is commonly fixed, but by dispatching an optimal topology [38], along with generation, high congestion costs are reduced [86]. Based on a realistic large-scale system with RES, the analysis in [87] suggests that the benefits of OTC increase under high production from RES and low demand; this indicates that OTC becomes especially promising given the ambitious targets of RES integration, which are expected to reduce the net load in the following years [3][4]. In the case of networks with a high share of wind generation, like the Danish and German networks, authors of [88]–[90] have shown that OTC is a useful congestion management tool to improve the integration of RES.

Previous work related to the optimisation of network topology focused on avoiding component overloading and voltage stability [56], generation cost reduction [48][83][84][86][91]–[94], load shed recovery [95][96], reduction unit commitment (UC) costs [87][97], and reduction of PTDFs [85]. The seminal work in [56] proposed an OTC problem as linear programming where nodal current injections simulated the switching actions to reduce the current flowing in a line to zero. Authors of [83][84] included busbar splitting and merging in OTC problems formulated as MILP; whilst [83] used Fuzzy C-means as a clustering technique based on location marginal process to partition large systems, [84] addressed not only the line opening but also line closing as available circuit breaker control actions. Paper [91] proposed an OTC method based on ACOPF with N-1 reliability constraints formulated as a semi-definite programming (SDP); based on IEEE-30, the authors [91] found OTC solutions provide at least 5% cost reduction maintaining the N-1 reliability criterion. In [92][94], probabilistic OTC methods included the integration of RES generation and risk-based assessment for switching transmission lines; OTC solutions have considerable economic benefits with low risk in 22 out of the 24-hour period. The work in [93] consists of a robust topology control method for integration of RES by enhancing Do-Not-Exceed (DNE) limits; using a rank heuristic based on the active power flowing on lines to solve the MILP problem, the authors found that DNE limits can be increased by ~24% using OTC actions. For emergency conditions, authors of [95][96] proposed an OTC method for load shed recovery formulated as a MIP; whilst [95] solves the problem by a combination of MIP and a heuristic, testing single line switching at a time, the approach in [96] implements a binary switching tree tool. Comparing solutions with and without OTC on IEEE118 test



system, results from [95][96] indicate that OTC increases load shed recovery between 14% and 33%. Paper [87] proposed a OTC co-optimisation of UC and ED in two stages tested on a European Network Transmission System Operators for electricity (ENTSO-E) test system. OTC results in [87] show cost savings between 0.3% to 2% of total cost; large proportion of cost reduction is achieved by 1 or 2 switching actions. Authors of [97] proposed an stochastic UC with OTC method where the optimal topology control can provide benefits to reduce the need of large reserves due to the variability of renewable generation. Based on a representation of the Central Western European system [98], results show that the flexibility provided by OTC enables economic benefit between 0.3 and 1.87 million euros; this effect is due to the congestion reduction given by transmission switching that enables the commitment of cheaper units [97]. Paper [85] proposes an OTC method to avoid parallel flows, formulated as a large scale MIP and solved by a genetic algorithm; based on a large-scale representation of the European electric system, the power transfers distribution factor across the France–Switzerland interconnection can be decreased 95% by implementing topology changes.

The review of past work in OTC shows significant advantages like congestion reduction and facilitating the integration of RES; however, transient stability issues derived from the switching actions have not been studied in detail. Only a limited amount of relevant literature includes transient stability considerations in OTC [99]–[104]. Early 90's work in [99] proposed control strategies based on topological changes to reduce rotor angle deviation using sliding mode control. Similarly, an optimal reconfiguration of transmission networks was proposed in [100]; however, [99][100] were tested only in a small test system without verifying the proposed approaches in realistic systems. Corrective stabilizing switching has also been addressed within OTC. Authors of [101] proposed a corrective OTC by stabilizing switching where the objective function includes the transient kinetic energy of the centre of inertia and the steady state voltage of SGs. The solution of the OTC relies on offline TDS [101]; therefore, the actual implementation requires a fast real-time topological state estimation and centralised control action, which is not realistic for large systems. The work in [102] provides an assessment tool for the impact of corrective OTC on a system with a high share of RES. Authors in [102] found that switching actions close to wind plants can produce negative damping; similarly, the evidence showed sustained oscillations in hydropower plants due to interaction with excitation controls. Though the tool [102] can analyse the effect of a single corrective OTC under a given fault condition, the switching solution must be

verified for voltage, small signal and transient stability. The latest advance in OTC was presented in [103][104] as a method of preventive stabilizing switching. The authors introduced a Critical Switching Flow (CSF) index to assess the effect of switching actions on transient stability based on a TEF method; the CSF is the maximum real power flow allowed on a given transmission line so that the system is stable after switching off the particular line. Though the method [103][104] is promising, a drawback is that CFS requires the system's state in an unstable equilibrium. The authors also proposed a Monte Carlo (MC) Day-ahead probabilistic assessment for CFS calculation, which is computationally intensive. Due to the required computational load, the evidence shows scalability issues; for instance, the increase in computation time between IEEE118 and Texas2000 test systems is of 899% [104].

#### **1.4.4 Controlled islanding**

Controlled Islanding (CI) is a special control scheme that uses changes in the network topology to avoid catastrophic scenarios caused by slow propagating dynamics, like undamped oscillations, overloads, voltage and frequency instability, or fast propagating dynamics such as transient instability [105][106]. Frequently, islanding actions are triggered by the detection of critical conditions and consider line switching, load shedding and generator output adjustments to avoid frequency instability. Islanding limits cascading failures by intentionally splitting a transmission system into smaller independent subnetworks called islands [105]. Islanding is a highly complex problem that requires the preservation of system stability (rotor angle, frequency, and voltage) whilst minimizing the load shedding; hence, timing and location are essential for the success of the islanding strategy [106]. In this thesis, the focus is on the effect of the network's topology; therefore, the review concentrates on the location of islanding actions.

The literature on CI can be classified by the objective of the islanding method, such as minimal load shedding, whilst the graphs-based [107]–[111] and optimisation-based [106][112][113] methods are used to define groups of generators and corresponding cut sets, i.e., set of lines switching actions to split the system into islands. The work in [107][108] introduced an ordered binary decision diagram to define the islanding solution; the definition of cut sets is based on synchronisation, power balance and rating limits criteria. Authors of [109] proposed a multi-objective graph partitioning method for emergency control considering the real and reactive power generation. The emergency

control method stops the propagation of disturbances; however, it does not consider coherency between generators, which may lead to unstable islands. The method in [110] includes the definition of a graph where edge weights are the active power flow on branch elements; further graph simplification and identification of minimum spanning trees provide the islanding solution. Paper [111] proposes a real-time identification of coherent generators based on phasor measurement units. The ratio between synchronising power coefficient and inertia are used as edge weights for the graph; these are used by a community detection method to identify coherent generators [111]. Also reducing the amount of load shedding, but based on optimisation, the work in [112] introduced an optimisation problem based on a piecewise approximation of AC power flow equations (PWLAC); the comparison between MILP based on DC and PWLAC solutions shows that PWLAC increases the load shedding, but it is more accurate, which improves the voltage feasibility of the islanding solution. Authors of [106][113] proposed an optimal splitting strategy to minimise load shedding by solving the MILP using benders decomposition. Results based on IEEE118 show a significant increase in generation output and load shedding to maintain frequency stability within each island [106]; besides, benders decomposition provides a 60% faster solution than traditional MILP computations [113].

Focused on minimal power flow disruption, hybrid approaches combining graph theory and optimisation techniques were recently proposed in [114]–[117]. For instance, authors of [114][115] proposed a two-step spectral-based clustering controlled islanding algorithm; the method relies on the eigenvector of the Laplacian of a graph built using synchronising power coefficients. Later, they introduced eigenvalue and eigenvector sensitivities to calculate the impact of the change of inertia of SGs [115]. In [116], the authors also proposed a method based on eigenvectors of the Laplacian, but the graph representation used the average active power flow injections at end nodes of transmission branches; results in [116] based on a reduced GB network show an average of 2% quality improvements in comparison to previous methods. Paper [117] introduces a scheme that uses a wide area monitoring, protection and control to define a weighted time-varying graph structure of the network; graph edges are defined by the affine combination of active and reactive power flow on branches per unit of length. Based on a representation of the Iranian power network results in [117] show that the method provides stable islands avoiding blackouts for a set of fault conditions.

Slow coherency theory, introduced in the early 2000s, was one of the earliest and most consistently used strategies for CI [107], [108], [119], [120], [109]–[111], [114]–[118]; the theory is intrinsically related to transient stability because it identifies groups of SGs which rotor angles remain relatively close after a disturbance. In particular, after a severe disturbance, rotor angle oscillations of electrically close SGs decay, whilst oscillations between different areas continue; generators swinging together are coherent with regard to the slow modes, i.e., they are in the same slow coherency group [110]. Slow coherency uses linearised dynamics equation of SGs, based on the classical model, to find groups of slow electromechanical modes; whilst slow coherency depends heavily on machine parameters, it also depends on initial conditions and fault location to a much lesser extent. In particular, the work in [118] presents an adaptive islanding approach considering load shedding; it includes a two-level load shedding scheme combined with slow coherency islanding. Similarly, in [119], the islanding strategy combines the grouping of generators and the identification of the weakest links, where slow coherency identifies the most fragile connections among generators. Later in [120], the approach's effectiveness was demonstrated in a realistic scenario; simulation results showed that for the August 2003 blackout scenario, slow coherency-based islanding significantly reduced disturbance impacts preventing cascading failures.

#### **1.4.5 Transient stability constrained optimal power flow**

Since early 1998, optimisation techniques focused on generation dispatch with transient stability considerations have received considerable attention as a preventive approach [121]–[123]. Introduced in 2000 [122], the Transient Stability Constrained Optimal Power Flow (TSC-OPF) is an optimisation problem consisting of a standard OPF problem, extended by TS constraints using differential-algebraic equations (DAEs) representing the generator's dynamics. Over the last few years, several approaches have been proposed to define and solve TSC-OPF. Regarding the techniques to include transient stability constraints, the TSC-OPF traditional method was proposed in [122], which consists of discretising DAEs using the implicit trapezoidal method. Several adaptations of the traditional method have been introduced where multi-contingency scenarios have been addressed [124], and computational performance has been improved by focusing on integration errors [125] and relaxation of DAEs [126]. Derivations from previous approaches focus on sensitivity analysis, like rotor angle sensitivity with respect to the dispatch change [127], directional derivative [128], and energy sensitivity [129]. Another way to define stability constraints is the TSC-OPF direct method, where

dynamic constraints are enforced on generator responses based on TDS. Even though the approach is computationally efficient, it may result in near-optimal solutions due to the use of Single Machine Equivalent (SIME) and the sequential nature of the algorithms [130][131]. SIME-based direct methods, including dynamic loads [132], and a combination of kinetic energy sensitivity analysis [129], have also been proposed. The TSC-OPF problem can be written as a nonlinear programming (NLP) with dynamics constraints; successful techniques used to solve the problem range from evolutionary algorithms like differential evolution [133], genetic algorithms [134], and search heuristics like particle swarm optimisation [135]. The more mathematically tractable technique to solve TSC-OPF problems is the interior point method, which has been used as a main computation technique in [122][124][125].

TSC-OPF approaches use different ways to quantify the stability level. In particular, TSC-OPF direct methods rely on TDS to evaluate the transient stability level to assess a given OPF solution; in this case, the transient stability constraint is based on the computation of the stability margin based on the equal area criterion, where the generators are represented using the SIME method [129][130][131][132]. Even though the inclusion of only one transient stability constraint is efficient, the TDS can increase the computational load if a large number of contingencies is considered. Another approach is used in the TSC-OPF traditional method. The transient stability constraints come in the form of the rotor angle deviation with respect to the Centre of Inertia (COI) with a threshold angle of 100-150 degrees [122][124][125][126]; a recently proposed method quantifies the stability level by the square of the rotor angle with respect to the COI [128]. Transforming DAEs into algebraic equations increases the number of constraints [122]; particularly, differential equations are replaced by difference equations.

A further possible extension of the TSC-OPF model is the introduction of discrete variables to represent the switching of transmission branches; it should be noted that in the revised literature, the network topology modification (i.e., transmission switching) has never been modelled as available control mean in the context of TSC-OPF. Moreover, the TSC-OPF can also be improved to account not only for the behaviour of an aggregated representation of SGs (SIME method). Though the scope of this thesis does not consider improving the representation of SGs, more sophisticated transient stability metrics such as the coherence index [36], dot-products [36], Integral of Squared Rotor Angles (ISGA) [136], Transient Stability Index (TSI) [137], as well as CCT-based

stability margin [138] can be used as transient stability constraints to verify the behaviour of each SG.

#### **1.4.6 Network topology assessments based on graph theory**

Network theory can provide tools to evaluate different features of network topologies, like size, connectivity, and robustness. For instance, the concept of synchronisation, known as coherency of rotor angles in power system literature [36], has related structural properties of the network with the ability to reach and maintain coherency [139][140][141][142]. In particular, the structure of a network can be characterised by topology metrics such as node degree [143], shortest path length [144], efficiency [145], betweenness centrality [146], algebraic connectivity [147][148], among others; thus, these can be used to quantify the influence of the structure on different processes, like electromechanical transients.

In power systems, the role of the network structure in cascading failures has been extensively studied [149][150]; in this context, network robustness is related to the structural strength of a system to survive perturbations and failures [150]. Particularly, weighted node degree and efficiency metrics have been used in [151][149] to assess vulnerabilities of power systems with embedded communication infrastructure. For example, authors in [152] used the line betweenness centrality and efficiency to identify vulnerabilities in the IEEE39 and IEEE118 test systems against random and targeted attacks. From a network robustness perspective, paper [153] demonstrates the effect of the network structure in cascading failures using the average shortest path length on the IEEE118 test system; the authors also evaluate the topologies using the average effective resistance (distance) between generators and load nodes on the Northern European Grid. Similarly, the authors of [154] defined robustness based on five network metrics, considering the average degree, betweenness, closeness, efficiency, and shortest path length between generators; based on the IEEE118 test system, the proposed method in [154] defines an optimal topology using simulated annealing that improves the total robustness in 65%. In particular, the review of the literature where network theory has been used in the context of power systems is scarce; besides, the transient stability problem has not been analysed using graph-based methods.

### 1.4.7 Summary of past work

Several research aspects have been identified in the literature review presented in this thesis, which previous researchers have not addressed. These are summarised below:

- i. Industry practices already take advantage of changing the topology of the network by ad-hoc procedures based on historical data or expert knowledge to improve voltage profiles and transfer capabilities during lightly loaded hours, as special protection schemes under contingencies, for seasonal load changes, for scheduled maintenance, and to mitigate congestion on transmission lines. However, most TSOs do not apply systematic methodologies to harness the flexibility benefits of switching transmission components to reduce or eliminate overloads.
- ii. The challenges adopting Optimal Transmission Switching (OTS) in industry, like long computational time, effective AC performance, and understanding of performance on large-scale power systems, have been addressed to a certain extent by power system researchers. However, the reviewed literature shows that OTS focus mainly on power system security, that is, asset overloading, voltage violations, and reduction of operational costs, with only a small fraction focusing on transient stability. Furthermore, the OTS literature that indirectly addresses transient stability focuses only on a regular topology or includes restrictions on short circuit currents rather than generator rotor angles.
- iii. Similar to OTS, the reviewed literature concerning Optimal Topology Control (OTC) shows significant advantages in congestion reduction and facilitating the integration of RES; however, transient stability within OTC has only been addressed by a few authors. Among the works considering transient stability, it is possible to find corrective approaches based on transient energy functions; nonetheless, a drawback is the complexity and scalability of the proposed methodologies. For instance, the controllable unstable equilibrium point method would require finding the unstable point for each potential network structure.
- iv. Notably, the use of network theory in the form of graph-based metrics is almost absent from the reviewed literature on optimisation techniques used in OTS and OTC. In particular, graph theory was used in two papers as part of heuristic methods; interestingly, the authors found beneficial effects in short circuit reduction by increasing graph-based electrical distance between generators and

fault location; this suggests that graph theory can be a useful tool in the context of transient stability assessment.

- v. Controlled Islanding (CI) methods based on slow coherency help address long-term dynamic problems, like voltage and frequency stability; however, their application to short-term dynamics, like transient stability, is questionable because slow coherency does not fully reflect the impact of fault characteristics, like disturbance size, or pre-fault operating conditions. Another drawback of CI is that it introduces significant topological changes because it was designed as a last resource corrective measure to prevent widespread catastrophic events; though effective, less aggressive preventive topology-based measures with or without corrective capabilities can be used to tackle transient stability issues maintaining the system integrity.
- vi. Transient stability inequality constraints have been added to the TSC-OPF models; however, discretised DAEs cannot be avoided leading to potential convergence problems, modelling of limited-size networks and non-scalable feature of the model. It is reasonable to assume that modelling discrete network switching within a TSC-OPF model would amplify scalability and complexity issues. The entire TSC-OPF would need to be solved for each network switching configuration defined by the binary vector of branch statuses; this indicates that a non-simulation-based TS approach can be an alternative way, which would be capable of generating not only optimum but ranked suboptimal solutions as well. To this end, quantification of the network topology impact, or network robustness with respect to transient stability, needs to be developed; recent results from network theory can be adapted for this purpose.
- vii. The network structure, also known as topology, has a relevant role in dynamical processes; however, the influence of the structure in transient stability assessments has not been addressed in detail by power system researchers. Though several topology metrics have been developed within network theory, the potential application in power system processes has mainly been studied for robustness against cascading failures and controlled islanding. In the reviewed literature, topology metrics designed to assess the impact of the topology on the dynamic behaviour of SG during electromechanical transients are practically non-existent; therefore, specific network topology metrics need to be further investigated. This also includes properties of the node where an SG is connected and some SG characteristics.



## 1.5 Research aims and objectives

This thesis aims to address several issues identified in the current body of research. The main aim of the research project is to investigate the impact of the structure of transmission networks on transient stability. The network topology is defined by the statuses (i.e., on/off) of switching devices that can change the service condition of the transmission lines; the switching actions introduce instantaneous step changes in the network configuration and are considered large disturbances. Understanding the effects of network structure on the stability of power systems can be considered a prerequisite to a potentially valid pathway to improve network flexibility. Therefore, once effects are understood, it will be possible to define control methods to maximise the network transient stability, using not only “standard controls” (e.g., economic dispatch, AVR settings) but also the network as a dispatchable asset as well. In order to achieve the main aim, the following research objectives have been defined:

- i. To summarise and critically assess the existing literature reporting contributions linking changes in network structure to stability areas of power systems. In particular, focus on the previous work related to transient stability to establish this research topic's state of the art.
- ii. To investigate the impact of discrete changes on transmission networks, such as line-switching actions, on the transient stability response of power systems. In particular, verify the mechanisms affected by network parameters that drive the transient stability behaviour.
- iii. To develop the general dynamic optimization model that uses generation active power dispatch and network switching as available controls. The model will consider both transient stability and network security.
- iv. To develop a simplified optimization procedure that will maximise transient stability without using the transient stability differential-difference equations.
- v. To propose robustness metrics that capture the essential impact factors on transient stability; this includes the influence of the network structure on the behaviour of generators during the early stage of the transient period.
- vi. To develop a solution procedure for the simplified optimisation method capable of identifying the best network structure to improve the security and transient stability response of power systems.
- vii. To draw conclusions by using several test network models.

## 1.6 Main contributions

The work presented in this thesis contributes to the general area of power system stability research by investigating and modelling the effect of network structure, defined by line-switching actions (line disconnections or connections), on the first swing transient stability. The primary outcome of this research work is the definition and comprehensive assessment of network metrics and generator features capable of quantifying the topological influence of the network structure on the transient stability behaviour of power systems. Furthermore, the assessment was used to propose a non-simulation-based optimisation framework for using line-switching actions as a preventive control measure to improve transient stability.

The points below summarise the main contributions of this research.

- i. A novel optimization framework was proposed, which integrates transient stability and network security aspects with line switching as an available control. The transient stability block uses the classical multi-machine model with structure-preserving network and line switching, as well as an inequality constraint based on TSI. The combination of security and transient stability constraints defines the general dynamic optimisation problem called Transient Stability and Security Constraint Optimal Power Flow with Switching (TSSC-OPFwS).
- ii. A two-stage methodology was defined to solve the proposed TSSC-OPFwS problem, combining SC-OPF and topology optimisation for transient stability based on a general network robustness metric. The proposed solution decouples the power flow (security) constraints from the dynamic and binary (transient stability) constraints; moreover, using a transient stability robustness metric within the topology optimisation reduces the complexity of solving the dynamical models in time domain.
- iii. A study of transient stability nodal (generator) impact factors evaluating single line-switching scenarios revealed three main findings related to switching actions. Firstly, pre-fault variables like generator loading and rotor angles can give invaluable insight into the potentially unstable generators. Secondly, line-switching actions defining different network topologies can positively impact transient stability. Finally, a higher inertia level does not always guarantee more

stable results and vice versa; a harmful factor is the combination of inertia reduction and increased rotor angle separation.

- iv. The definition and study of two impedance-based proximity metrics, in the context of small test systems, to evaluate the effect of line-switching actions on the structure of a transmission network and how those discrete changes impact the transient stability behaviour of power systems. The analysis based on a realistic test system suggested that impedance-based distance between generators and a fault location (DFG), and between nearby generators (DBG), offer higher accuracy in discriminating between network structures with a better or worse performance from the transient stability point of view. In particular, the confirmation of the effects of DFG and DBG on transient stability based on a realistic test system, originally revealed on two small test systems, leads to the conclusion that the findings based on network topology metrics are general.
- v. Within the proposed topology optimisation for transient stability, two network robustness metrics in the form of fitness functions were designed to be used in a GA-based optimisation method. In particular, the proposed robustness metrics are called Composite Transient Stability Robustness Metrics (CTSRMs), which serve as proxy functions to predict, to a certain extent, the transient stability behaviour of a power system for a given set of faults. The introduction of proxy functions replaced the solution of the multimachine model and verification of transient stability constraints in the time domain, reducing the complexity of solving the TSSC-OPFwS problem.

## 1.7 Thesis overview

This thesis consists of six chapters in total. The five chapters that follow this introductory chapter are outlined below:

### **Chapter 2 – Modelling of Power System Components, Techniques and Computational Tools**

This chapter describes the model of power system components and techniques, which are already established in the literature and used in research and industry. Firstly, the mathematical models of relevant components are described. Secondly, the modelling of the network, including discrete changes like line-switching actions and short circuits, is defined through simple procedures. Thirdly, fundamental concepts of optimisation

techniques are introduced. Finally, the computational environment used to perform the studies is also described.

### **Chapter 3 - Assessment of the Impact of Line-Switching Actions on Transient Stability**

This chapter introduces the assessment of the effect of line-switching actions on the structure of transmission networks. In particular, the assessment of switching actions is done by two impedance-based proximity metrics using two small test systems. The chapter includes two parts. Firstly, an in-depth analysis, using theoretical and simulation tools, of the effect of line-switching actions changing the impedance between generators and fault locations. Secondly, a detailed analysis of line-switching actions affecting circuits connecting SGs using simulation results.

### **Chapter 4 – Modelling Framework for Transient Stability Preventive Control via Rescheduling and Switching**

This chapter presents an optimisation framework to minimise generation production costs whilst meeting stability and security constraints. Within the framework, line-switching actions are used as binary (discrete) controls to change the topology and improve the transient stability response of the system in the presence of large disturbances. The chapter includes four parts. Firstly, the description of the classical multi-machine model with the reduced network for transient stability analysis. Secondly, a detailed explanation of a new model for transient stability analysis called the classical multi-machine model with structure-preserving network and network switching. Thirdly, a study of transient stability indicators to determine the most suitable to define stability limits. Finally, a general dynamic optimisation model is proposed as an optimum power flow with transient stability and security constraints.

### **Chapter 5 – Transient Stability Preventive Control with Generation Dispatching and Network Optimisation**

This chapter introduces a methodology to solve the TSSC-OPFwS problem described in the previous chapter. The proposed approach is a two-stage method; the first stage is the solution of an SC-OPF for fixed network topology, whilst the second stage is a network topology optimisation to find the network structure with the best transient stability response considering a set of credible faults. The chapter includes four parts. Firstly, the description of the IEEE68 bus test system. Secondly, a detailed description of the two-

stage solution method highlights the computational processes. Thirdly, a comprehensive study of impact factors relating the topological effect, given by a network structure, to transient stability. Finally, the network robustness metric is defined in the form of two fitness functions; the functions are assessed to verify their accuracy in mapping combinations of switching scenarios and fault conditions to TDS-based stability results.

## **Chapter 6 – Conclusions and Future Work**

In this chapter, the main conclusions of the undertaken research are summarised. Furthermore, suggestions are made for future improvements and expansion of the studies and methods presented within this work.



## **2 Modelling of Power System Components, Analysis Techniques and Computational Tools**

---

Commercial tools are available for engineers to perform tasks such as power system modelling and analysis; those tools implement mature and testing models, which are mathematical representations of power system components. Furthermore, the modelling of power system components enables their use in dynamic or quasi-dynamic simulation engines, which allows the analysis of different effects to support decision-making processes in the industry.

Particularly, this chapter describes the model of power system components and analysis techniques, which are already established in the literature and used in research and industry. Firstly, the mathematical models of relevant components include synchronous generators (SGs), automatic voltage regulators (AVRs), excitation systems, power system stabilizers (PSSs), transformers, transmission lines, and loads. Secondly, as the network structure is the main focus of the work presented in this thesis, modelling the network, including discrete changes like line-switching actions and short circuits, is described in detail. Thirdly, fundamental concepts of optimisation techniques are introduced. Finally, the computational environment used to perform the studies is also described. The computational tools are used in an integrated fashion enabling the automation of computational processes, which provided results used throughout this thesis.

## 2.1 Modelling of power system components

This section includes the modelling of essential power system components; these components have been integrated into test systems and implemented in computational tools to obtain TDS results. In particular, the components of the power system are modelled using single-phase representation, assuming that all three phases are balanced [21].

### 2.1.1 Synchronous generators

The synchronous generator (SG) has been the essential plant to transform different forms of energy, such as nuclear, chemical (coal, oil, and gas), and hydro, into electrical energy in modern electrical power systems [25]. In many parts of the world, generation is primarily centralised in power plants where SGs transform mechanical energy into electrical energy. Though the adoption of inertialess converter interfaced generation (CIG) may seem to be rapidly changing the current scenario [10][11], the simplicity and versatility of the SG will ensure that it will remain one of the fundamental components of power systems in many years to come. The most straightforward mathematical representation of the SG is the second-order model (1.1) [17][20], also known as the classical model; in this framework, the SG can be represented as a constant voltage source behind a transient reactance. The model (1.1) enables the explanation of electromechanical phenomena in the easiest possible way; it has been used by many researchers [14][17][18][20] in the development of power system dynamics and control theory.

For more realistic simulations, a more sophisticated mathematical representation of the SG can be used, like the sixth-order model [17][20][23], also known as the standard model; derivation and description of the algebraic and differential equation of the standard model can be found in several textbooks [14][17][20][23]. The first-order differential equations of the sixth-order model are given by equations (2.1)-(2.6); the notation of equations is consistent with [23][148][149]. In the equations below, electrical quantities are in p.u., time in seconds, rotor angle in electrical radians, and rotor speed in electrical radians per second. Subscripts  $d$  and  $q$  are related to the stator  $d$  and  $q$  axes, whereas  $fd$  is related to the rotor field winding. In particular (2.1)-(2.6) are the derivatives with respect to time of the stator transient EMFs  $E'_d$  and  $E'_q$ , rotor circuit flux linkages  $\psi_{1d}$  and  $\psi_{2q}$ , rotor speed deviation  $\Delta\omega_r$ , and rotor angle  $\delta$ ; in this model  $E'_d$ ,



$E'_q$ ,  $\psi_{1d}$ ,  $\psi_{2q}$ ,  $\Delta\omega_r$ , and  $\delta$  are state variables. Generator parameters are synchronous reactances  $X_d$  and  $X_q$ , transient reactances  $X'_d$  and  $X'_q$ , sub-transient reactances  $X''_d$  and  $X''_q$ , transient open circuit time constants  $T'_{d0}$  and  $T'_{q0}$ , sub-transient open circuit time constants  $T''_{d0}$  and  $T''_{q0}$ , stator leakage reactance  $X_{lk,s}$ , inertia constant  $H$ , damping factor  $D$  and nominal (synchronous) speed  $\omega_0$ . Variables in the model are the rotor speed  $\omega_r$ , and stator voltages  $E_d$  and  $E_q$  with  $E_t$  as the resultant voltage, which depend on stator currents  $I_d$  and  $I_q$ . The mechanical power  $P_M$  is a parameter and the electrical power  $P_E$  is a dependent variable.

$$\frac{d}{dt}E'_d = \frac{1}{T'_{q0}} \left[ -E'_d + (X_q - X'_q) \left\{ I_q - \frac{X'_q - X''_q}{(X'_q - X_{lk,s})^2} (\psi_{2q} + (X'_q - X_{lk,s})I_q + E'_d) \right\} \right] \quad (2.1)$$

$$\begin{aligned} \frac{d}{dt}E'_q = \frac{1}{T'_{d0}} \left[ -E'_q - (X_d - X'_d) \left\{ I_d - \frac{X'_d - X''_d}{(X'_d - X_{lk,s})^2} (\psi_{1d} + (X'_d - X_{lk,s})I_d + E'_q) \right\} \right. \\ \left. + E_{fd} \right] \end{aligned} \quad (2.2)$$

$$\frac{d}{dt}\psi_{1d} = \frac{1}{T''_{d0}} [-\psi_{1d} + E'_q - (X'_d - X_{lk,s})I_d] \quad (2.3)$$

$$\frac{d}{dt}\psi_{2q} = \frac{1}{T''_{q0}} [-\psi_{2q} - E'_d - (X'_q - X_{lk,s})I_q] \quad (2.4)$$

$$\frac{d}{dt}\Delta\omega_r = \frac{1}{2H} [P_M - P_E - D\Delta\omega_r] \quad (2.5)$$

$$\frac{d}{dt}\delta = (\omega_r - \omega_0) = \Delta\omega_r \quad (2.6)$$

Algebraic equations below describe stator voltages (2.7)-(2.9) and electrical power (2.10), assuming negligible generator armature resistance. The electrical power  $P_E$  is obtained by combining (2.7) and (2.8) in (2.10), which is in turn plugged in (2.5).

$$E_d = \frac{X''_q - X_{lk,s}}{X'_q - X_{lk,s}} E'_d - \frac{X'_q - X''_q}{X'_q - X_{lk,s}} \psi_{2q} + X''_q I_q \quad (2.7)$$

$$E_q = \frac{X''_d - X_{lk,s}}{X'_d - X_{lk,s}} E'_q + \frac{X'_d - X''_d}{X'_d - X_{lk,s}} \psi_{1d} - X''_d I_d \quad (2.8)$$

$$E_t = \sqrt{E_d^2 + E_q^2} \quad (2.9)$$

$$P_E = E_d I_d + E_q I_q \quad (2.10)$$

### 2.1.2 Generator excitation systems

The purpose of an excitation system is to provide direct current to the SG field winding. Figure 2.1 illustrates the functional relationship between the SG and controllers like AVR and PSS. The figure shows that the excitation system controls the field voltage  $E_{fd}$ , and also the field current of the stator winding, contributing to power system stability [20]. The control action is performed by the AVR, the upper closed loop in Figure 2.1, which manipulates  $E_{fd}$  to reduce the error between the generator terminal voltage  $E_t$  and the terminal voltage reference set-point  $E_t^{ref}$ ; in practical terms, the AVR's purpose is to maintain  $E_t$  close to the reference  $E_t^{ref}$  providing voltage control and contributing to first-swing stability. As described in Section 1.3.7, AVR's effect can increase the oscillatory behaviour of the system, especially for those with large impedance; a PSS may be included to ensure the damping of oscillations beyond the first swing. Figure 2.1 also shows the integration of the PSS voltage signal  $E_{PSS}$  as an extra input to the AVR. A comprehensive review of AVR types can be found in [156]; the AVR implementations used in this dissertation are described below.

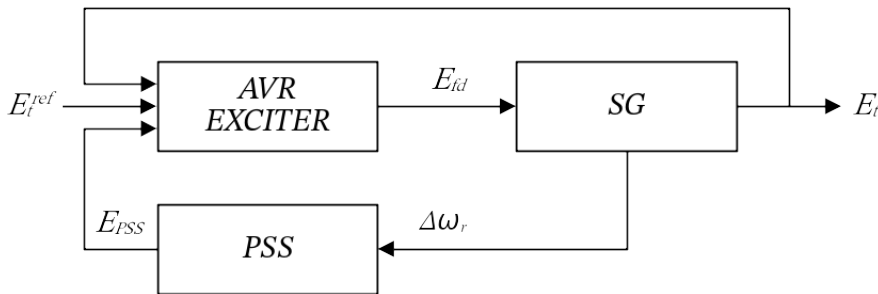


Figure 2.1: Simplified functional relationship diagram of SG, AVR and PSS [155].

#### 2.1.2.1 DC excitation

DC excitation systems date back to the 1920s, which have been replaced due to the introduction of AC exciters in the mid-1960s [20]; however, there still are several SGs in service with this type of excitation system [156]. DC excitation systems use DC generators as a source of excitation power to provide current to the SG rotor through slip rings, and they can be self or separately excited; from the dynamic viewpoint, this type of excitation is slow, which is reflected by longer time constants [20]. In particular, Figure 2.2 shows a simplified block diagram of the Mag-A IEEE Type 1 [17] exciter used in Chapter 3 within time domain simulations (TDS) using the IEEE68 Bus test system. The system considers a transducer delay block to represent the measuring of the SG terminal voltage  $E_t$ , an AVR block to amplify the error signal, a feedback

compensation with gain  $K_F$  and time constant  $T_F$  to improve the dynamic performance of the excitation system, and the exciter block which combines the gain  $K_E^{ex}$ , time constant  $T_E^{ex}$  and an exponential saturation function. Here the regulated voltage  $E_R$  is the input to the exciter with upper and lower limits  $E_R^{max}$  and  $E_R^{min}$ , respectively.

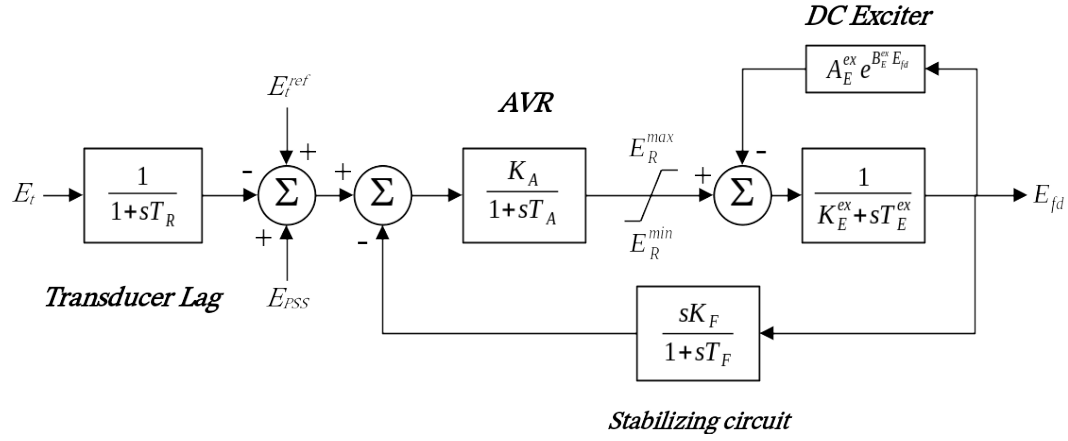


Figure 2.2: Simplified block diagram of the IEEE Type 1 DC exciter [17].

For the Anderson and Fouad Test system, a simplified version of the IEEE-type DC1A excitation system [155] used in Chapter 5 for TDS can be seen in Figure 2.3. A separately excited DC1A exciter has been implemented without considering the stabilizing feedback loop. In particular, the output of the AVR is not limited; however, the output of the exciter is limited by  $E_{fd}^{max}$  and  $E_{fd}^{min}$ .

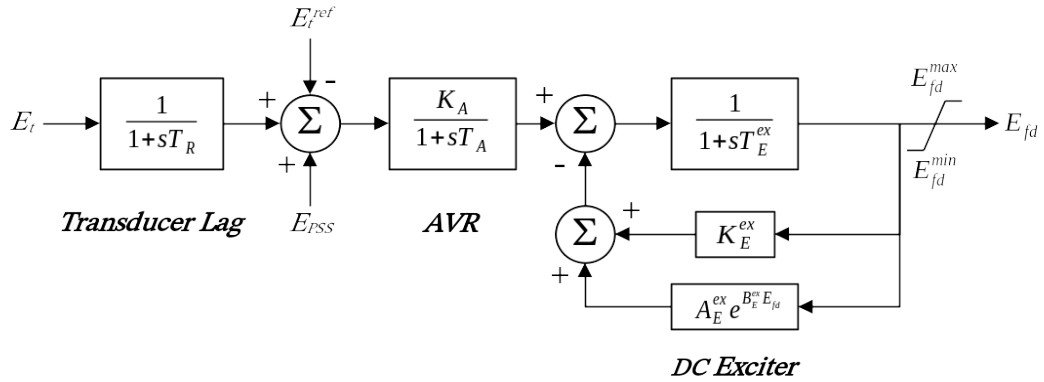


Figure 2.3: Simplified block diagram of the IEEE Type DC1A DC exciter [155].

### 2.1.2.2 Static excitation

In static (ST) excitation systems, the voltage is transformed to DC form of an appropriate level by controlled or uncontrolled rectifiers, which supply the excitation current directly to the field winding through slip rings [20]. A difference between ST and DC or AC exciters is that the ST type has lower time constants, which means that they can act very fast; therefore, the stabilizing feedback loop is not required [156]. Figure 2.4 illustrates a simplified version of the IEEE type ST1A excitation system [26] used in Chapter 5 for

TDS; it considers a voltage delay transducer block and the exciter gain without time constant; moreover, it does not include lead-lag blocks to reduce or increase the transient gain. The output of the ST exciter has upper and lower limits,  $E_{fd}^{max}$  and  $E_{fd}^{min}$ , which bound the field voltage  $E_{fd}$ .

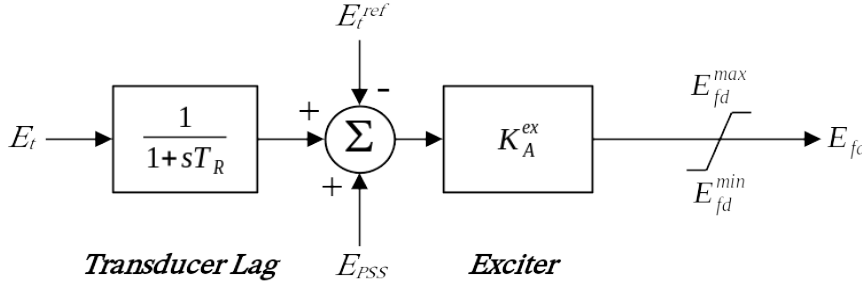


Figure 2.4: Simplified block diagram of the IEEE Type ST1A ST exciter [26]

### 2.1.3 Power system stabilisers

Commonly, PSSs are tuned to damp small-disturbance oscillations using linearised power systems models; nevertheless, they can improve transient stability if adequately tuned [26]. Briefly discussed in Section 1.3.7, the control action provided by the combination of AVR and PSS during the first rotor oscillation can be characterised by a sharp increase of the excitation voltage to its upper limit  $E_{fd}^{max}$  where the synchronising torque is maximised by the AVR. In parallel, since the rotor speed deviation  $\Delta\omega$  is not zero during a fault, the PSS signal  $E_{PSS}$  (see Figure 2.3) is added to the voltage error input to the AVR. The resulting net voltage error  $E_{PSS} - \Delta V$  leads the rotor speed deviation, and the quadrature component of the transient EMF reinforce the natural damping by introducing a positive damping torque in phase with the speed deviation [21]. Though the integration of the PSS reduces the voltage error reducing the AVR effect on the first swing, this negative effect has a small magnitude and can be neglected; however, the positive effect of the PSS becomes more influential beyond the first swing reducing the net voltage error and the magnitude of the rotor angle oscillations [21]. Since the main focus of this work is on first-swing stability, the effect of PSSs will not be assessed in detail. Particularly, the PSS modelling is incorporated because they are integrated into generating units which are part of the test system used in Chapter 5 within TDS.

In general, the PSS takes an input signal, and after the filter, phase compensation and amplification processes, it passes the resultant voltage signal  $E_{PSS}$  to the AVR modifying the net voltage error. One of the most common types of PSS uses the rotor speed  $\Delta\omega_r$  as

input [21] and is the one used in this thesis. In particular, a simplified block diagram of a single-input PSS [155] used in Chapter 5, similar to the generic PSS in [21], can be seen in Figure 2.5. The figure shows a washout filter with a time constant  $T_W$ , which eliminates an offset from the input signal to ignore steady state changes; later, a combination of lead-lag compensating blocks ensures that the introduced electrical damping torque is in phase with the rotor angle speed deviation. The gain  $K_{PSS}$  amplifies the filtered and compensated signal to maximise the damping, which is later passed through a limiter; the auxiliary signal limits  $E_{PSS}^{max}$  and  $E_{PSS}^{min}$  can be asymmetric to avoid harmful effects due to component failure [155]. Though considered in [21], a low pass-pass filter is not included in Figure 2.5 because the potential interactions between torsional mechanical modes and high-frequency output of the PSS are not in the scope of this work.

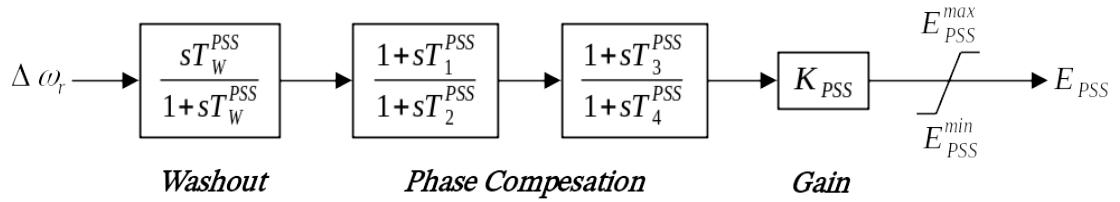


Figure 2.5: Simplified block diagram of a PSS [155].

#### 2.1.4 Transmission lines

Throughout the work presented in this dissertation, the main model representing transmission lines is the lumped parameter model with nominal  $\pi$  representation [23]. The test systems used in Chapters 3 and 5 include lines short enough to be considered medium-length transmission lines; therefore, the use of distributed parameters is not required [23]. Figure 2.6 shows a circuit representing a medium-length transmission line, suitable to model lines between 80 and 240 kms long [23]. The model considers a series impedance composed of total resistance and reactance  $r$  and  $x$ , and the total capacitance between conductors  $c$ ; particularly, the shunt admittance  $y = c/2$  is placed as the sending and receiving ends of the line.

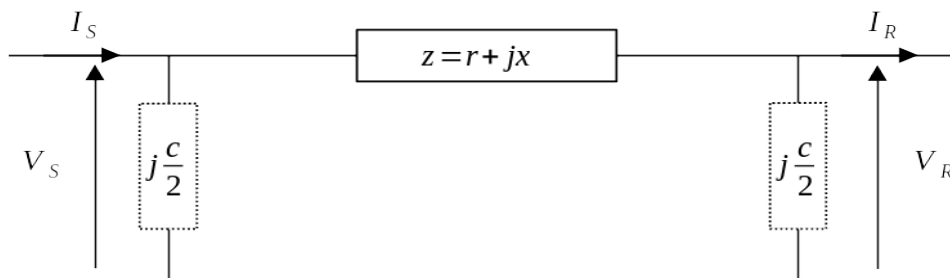


Figure 2.6: Equivalent  $\pi$  circuit of a medium length transmission line [23].

### 2.1.5 Transformers

The equivalent  $\pi$  representation is used to model a two-winding transformer shown in Figure 2.7, considering the single-phase representation of power system components. In the figure,  $Y_{eq}$  is the reciprocal of the leakage reactance of the transformer  $Z_{eq}$ , and  $c = 1/ONR$  is the reciprocal of the off-nominal turns ratio (ONR) of the transformer [20]. The series resistance, originating from active power losses, is ignored.

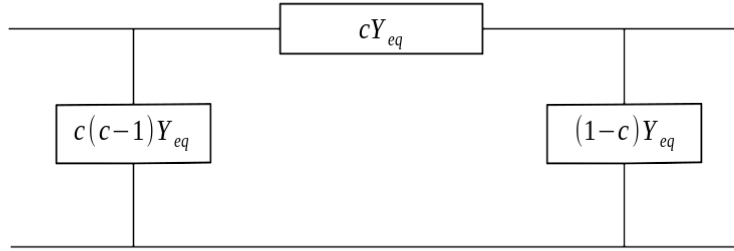


Figure 2.7: Equivalent  $\pi$  circuit of a two-winding transformer [20].

### 2.1.6 Loads

The modelling of power system loads can significantly impact the accuracy of simulation results for stability studies. Since bus voltages usually drop in the presence of a large disturbance, the power consumed by the loads will impact the imbalance between generation and load; the load change affects the magnitude of rotor angle oscillations and the first swing stability of the system [157]. In particular, electromechanical oscillations can significantly affect voltage magnitudes and system frequency across the network; therefore, frequency and voltage dependant loads require more detailed models to guarantee accurate stability results [158]. A comprehensive description of load models can be found in [151][153].

A study of international load modelling practices reveals that about 70% of utilities and system operators use static load models in power system stability studies [160]. In particular, two load models are included in this thesis. Firstly, in the constant impedance load model (2.11) [17], which is considered suitable for exploratory stability studies [21], loads are represented by equivalent shunt admittances using the load-flow solution of the pre-fault condition, i.e., steady state. Secondly, the constant power load model represents a load at node  $m$  as constant active power  $P_m$  and reactive power  $Q_m$  demands; this model has been used in the context of transient stability analysis with structure-preserving network modelling [161]. The main difference between models is that the constant impedance load can be easily integrated into the network admittance matrix to perform first-swing stability studies [17], while the constant power load can be used in

stability studies where structural aspects of the network are more relevant [162]. In this thesis, the constant impedance model was used in the context of network reduction methods in Section 4.1, whilst the constant power demand model was used in modelling structure-preserving networks in Section 4.2.

$$Y_m = \frac{P_m - jQ_m}{V_m^2} \quad (2.11)$$

## 2.2 Network representation and impedance-based distance metrics

This section introduces the representation of a multimachine system for transient stability studies focusing on the structure of the transmission system. Particularly, the network representation is treated from basic circuit theory and graph theory, providing the background for two methods to quantify the proximity between nodes; those methods are relevant to describe the effect of topological changes in the network structure. Commonly, all physical quantities are related to the positive-sequence network for transient stability studies because they consider the worst-case scenario, three-phase faults [22].

### 2.2.1 Admittance and impedance matrices

It is possible to represent a network of  $N$  buses as a combination of all transmission lines, transformers, and loads, depending on the load model used. A mathematical representation of the network is the admittance matrix, also known as  $Y_{bus}$ . The  $Y_{bus}$  matrix, shown in equation (2.12), can be built using the following rules [23]:

- i. A diagonal element  $Y_{ii}$ , also known as self-admittances, is equal to the sum of the admittances of all branches directly connected to node  $i$ . All shunt admittances  $Y_{i0}$  representing a load at node  $i$  are also added.
- ii. An off-diagonal element  $Y_{ij}$ , also known as mutual admittance between bus  $i$  and  $j$ , is equal to the negative of the branch admittance connected between node  $i$  and  $j$ . If there is no line connecting the nodes  $Y_{ij} = 0$ .

$$Y_{bus} = \begin{bmatrix} Y_{1,2} + \dots + Y_{1,N} + Y_{1,0} & -Y_{1,2} & \dots & -Y_{1,N} \\ -Y_{2,1} & \ddots & & -Y_{2,N} \\ \vdots & & \ddots & \vdots \\ -Y_{N,1} & -Y_{N,2} & \dots & Y_{N,1} + Y_{N,2} + \dots + Y_{N,N-1} + Y_{N,0} \end{bmatrix} \quad (2.12)$$

The  $Y_{bus}$  matrix can be used to construct the algebraic equation of the network, also known as the nodal network equation (2.13), which is based on the first and second Kirchhoff's law. For stability studies, the Kron method [23] can be used to reduce the dimension of (2.13), eliminating all buses with zero current injection [17]; this lowers the computational burden of power system analyses.

$$\begin{bmatrix} I_1 \\ \vdots \\ I_i \\ \vdots \\ I_N \end{bmatrix} = \begin{bmatrix} Y_{11} & \dots & Y_{1i} & \dots & Y_{1N} \\ \vdots & \ddots & \vdots & \ddots & \vdots \\ Y_{i1} & \dots & Y_{ii} & \dots & Y_{iN} \\ \vdots & \ddots & \vdots & \ddots & \vdots \\ Y_{N1} & \dots & Y_{Ni} & \dots & Y_{NN} \end{bmatrix} \begin{bmatrix} V_1 \\ \vdots \\ V_i \\ \vdots \\ V_N \end{bmatrix} \text{ or } \mathbf{I} = \mathbf{YV} \quad (2.13)$$

The inverse of the  $Y_{bus}$  is the bus impedance matrix, or  $Z_{bus}$ , which is also a well-known network representation [163]. Although both network matrices are symmetrical, a key difference is that the  $Z_{bus}$  is not a sparse matrix, i.e., it is not likely to have elements equal to zero. Particularly, an element of the main diagonal  $Z_{ii}$ , called self (or driving point) impedance of node  $i$ , is equal to the ratio between the voltage at the node and the injected current  $V_i/I_i$ , not having other active current injections, i.e., all other node current sources are open-circuited. Moreover, an off-diagonal element  $Z_{ij}$ , called mutual (or transfer) impedance between node  $i$  and  $j$ , is the ratio between the voltage at node  $i$  and the current injected at node  $j$  without current injections at any other node. Another difference between network matrices is their actual use; the  $Y_{bus}$  is mainly employed for load flow related computations whereas the  $Z_{bus}$  provides key information for fault analysis [23]. Within this thesis, elements of the  $Z_{bus}$  are used in impedance-based proximity metrics.

### 2.2.2 Weighted graphs

From network theory, an electrical circuit can also be represented by a simple graph  $G(\Omega_n, \Omega_l)$ . The simple graph of a network is defined by a set of vertices  $\Omega_n$  with  $n = 1, 2, \dots, N$ , and a set of edges  $\Omega_l$  connecting vertices with  $l = 1, 2, \dots, L$ . In network literature [164], nodes and vertices are considered interchangeable terms; moreover, links and edges are considered identical concepts. Similarly, in power systems literature [23], vertices and edges can be understood as buses and branch elements. The adjacency matrix  $A$  is the mathematical representation of a graph; for simple graphs, the elements of  $A$  are binary values (*On/Off*) which contains the information related to the connection between nodes. For instance, if nodes  $i$  and  $j$   $i \neq j$  are connected with a branch, then  $A_{ij} = 1$ ; otherwise  $A_{ij} = 0$  [164].



A weighted graph is a generalization of the simple graph where the components of the adjacency matrix represent the weight  $w$ , also called “strength”, of the connection between nodes. Hence, for weighted graphs, if nodes  $i$  and  $j$  ( $i \neq j$ ) are connected with a branch, then  $A_{ij} = w_{ij}$ , with  $w_{ij} > 0$ , otherwise  $A_{ij} = 0$  [164]. An example of the relationship between graphs and electrical circuits is shown for the circuit in Figure 2.8(a); the figure illustrates a purely resistive circuit with identical resistances  $R$  and nodes representing the junctions between them. Currents flow in the circuit obeying Kirchhoff’s current law (KCL), and there is a voltage source between nodes 1 and 7; KCL can be expressed for each node in terms of the components of the adjacency matrix  $A_{ij}$  according to (2.14), where  $I_i$  represents the external current injection at node  $i$ .

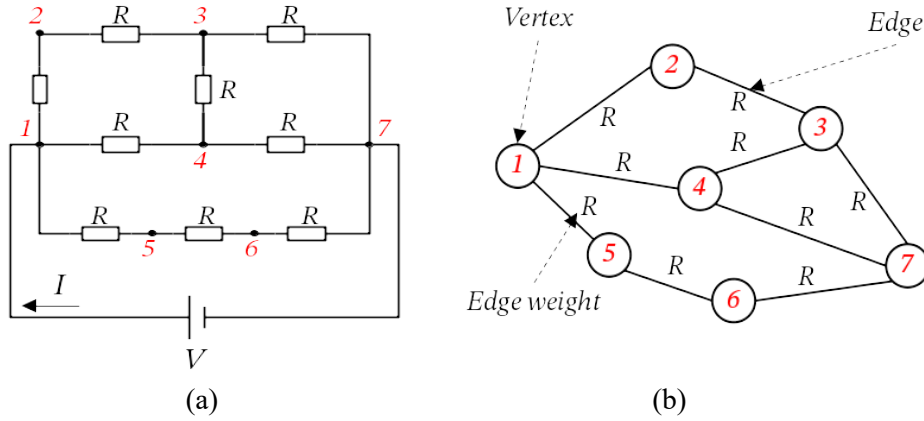


Figure 2.8: Resistive circuit (a) and graph representation (b) (adapted from [164])

$$\sum_j^N \frac{A_{ij}(V_j - V_i)}{R} + I_i = 0, i = 1, 2, \dots, N \quad (2.14)$$

The adjacency matrix of the example defines the connectivity between nodes and provides the basis for the weighted graph representation of the circuit, illustrated in Figure 2.8(b). The benefit of graph representation is the use of network theory tools to analyse the network. The focus of network theory is to analyse the topological features of complex networks, such as the relative importance of a vertex, also known as degree centrality [164]. For instance, a node's connectivity measure is node strength, which is the sum of the weights of edges connected to a node [144][143]. In the above example, nodes 1, 3, 4, and 7 have a strength of  $3R$ , whereas nodes 2, 5 and 6 are less important because they have a strength of  $2R$ . In practical terms, a failure in a node with high strength can cause large current and voltage changes within the network; those changes may cause a violation of operational limits of other assets leading to cascading failures [165].

### 2.2.3 Impedance-based distance metrics

The concept of transient stability in multimachine systems, introduced in Section 1.3.8, described a qualitative severity analysis under specific scenarios [21]. In particular, the analysis highlighted the effect of the relative “proximity” between SGs and fault locations on the transient stability behaviour. The following sections describe two methods to provide proximity metrics in the form of impedance-based distance; circuit theory defines the context for the first metric, whilst graph theory provides the basis for the second. The main difference between metrics is the number of paths considered in the calculation; the first metric includes all paths between two buses, whilst the second includes only the path with the smallest opposition to the current flow.

#### 2.2.3.1 Thevenin impedance and electrical distance

A measure of proximity based on the impedance between two network nodes is the Thevenin equivalent impedance between them or Electrical Distance (ED). The bus impedance matrix  $Z_{bus}$  is an open-circuit network description where each column contains the impedances corresponding to a given node current injection, i.e., all other node current sources are open-circuited [163]. Using Thevenin’s theorem, all the complexity of the structure of a network can be reduced to an open circuit voltage and an impedance connected in series, as shown in Figure 2.9(a) [23]. In particular, having the open circuit voltage at a given bus  $k$  and a change in current injection  $\Delta I_k$ , the voltage at the bus is  $V_k = V_k^0 + Z_{kk}\Delta I_k$ , where the driving point impedance  $Z_{kk}$  is also the Thevenin equivalent impedance of the network seen from node  $k$ . In fact, the diagonal elements of the  $Z_{bus}$  contain the network equivalent representations seen from each bus, which is useful for different studies like the analysis of short circuit currents at each bus.

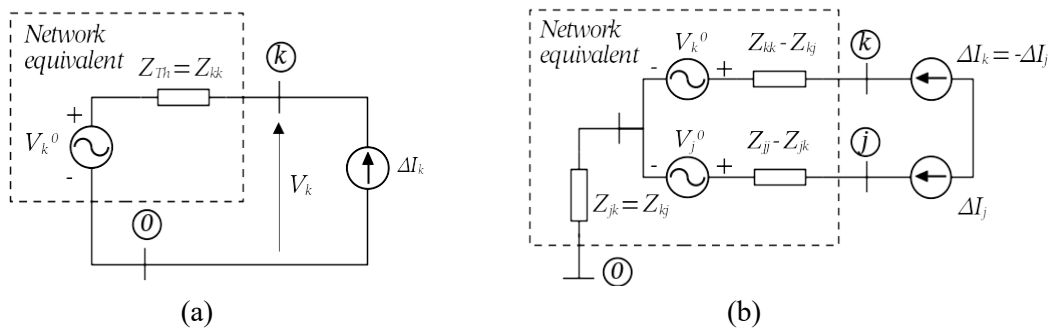


Figure 2.9: Thevenin equivalent impedance seen from node  $k$  (a) and between node  $k$  and  $j$  (b) (adapted from [23])

Using the concept of Thevenin equivalent impedance is also possible to find the equivalent impedance between any pair of buses, also known as the electrical distance.

In this case, the equivalent system seen from an external connection to nodes  $k$  and  $j$  is illustrated in Figure 2.9(b) [23]. The Thevenin equivalent impedance is given by (2.15)

$$ED_{kj} = |Z_{kk} + Z_{jj} - 2Z_{kj}| \quad (2.15)$$

Here, the electrical distance  $ED_{kj}$  is the magnitude of the complex impedance opposing the flow of the short circuit current between nodes and includes the driving point ( $Z_{kk}$  and  $Z_{jj}$ ) and mutual impedances ( $Z_{kj}$ ) of the corresponding nodes. In particular,  $ED_{kj}$  includes the impedances of all available parallel circuits between nodes  $k$  and  $j$ , which makes it highly sensitive to topological changes.

### 2.2.3.2 Shortest path length or geodesic distance

Another measure of proximity based on impedance can be derived using a graph representation of a network called shortest path length (SPL), also known as geodesic distance. Frequently, graph-based representation of transmission systems [166]–[168] assumes that transmission lines can be represented by total series impedances, i.e., short-length transmission lines [23]. For instance, the graph representation of the network illustrated in Figure 2.10 uses the magnitude of the impedance of the lines  $|z|$  as weights of the edges.

From network theory, a path is a sequence of vertices from a starting node  $k$  to an ending node  $j$ , such that every consecutive pair of nodes  $a$  and  $b$  in the path are connected by an edge [164]. For weighted graphs, if a path connects two nodes, the distance between the starting and ending nodes is the sum of the weights of the edges in the path. In particular, the geodesic path, also called the shortest path (SP), is the path with the lowest edge weights sum among all possible paths between two selected starting and ending nodes. The actual summation of the edge weights of the geodesic path is the SPL (2.16).

$$SPL_{k,j} = \min_{paths\ k,j} \left\{ \sum_{ab \in path\ k,j} w_{ab} \right\} \quad (2.16)$$

Here the  $k$  and  $j$  are the starting and ending nodes, respectively;  $w_{ab}$  is the weight of the branch connecting nodes  $a$  and  $b$ , with both nodes in the SP. In this thesis, the weight of the edge  $w_{ab}$  is the modulus of the series impedance connecting nodes  $a$  and  $b$ . Figure 2.10(b) illustrates an example of  $SPL$  between nodes  $k = 1$  and  $j = 7$ . The figure shows that there are multiple paths connecting nodes 1 and 7; however, the path with the lowest edge weight sum is the one connecting nodes 1, 4 and 7, with  $SPL_{1,7} = 2|z|$ . In practice, computation of the SP is performed using a computational algorithm such as Dijkstra's

algorithm, which belongs to the class of labelling algorithms [164][169] and has been widely used in the study of large networks. In particular, for a given vertex, Dijkstra's algorithm finds the SPLs to every other vertex considering the edge weights. In simple terms, the algorithm starts with an array of distances assuming each  $SPL = \infty$ ; then, finds the distance to each vertex, in an iterative way, updating the distances whenever it finds an SPL smaller than a previously found [164].

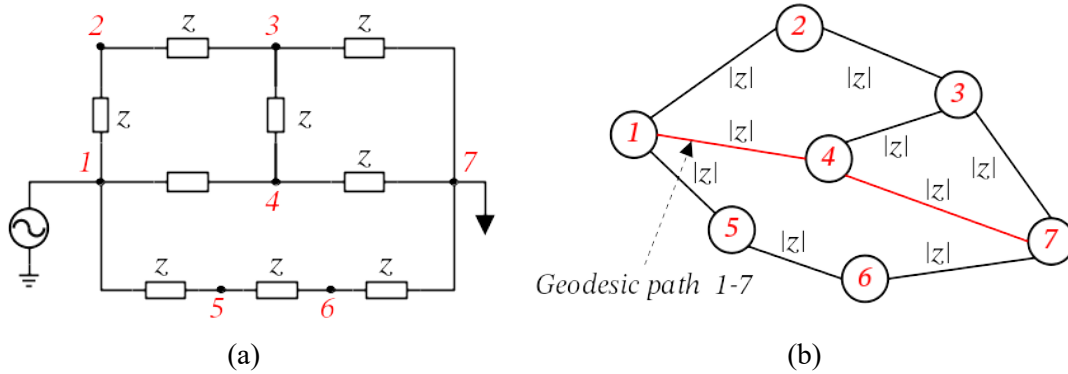


Figure 2.10: Impedance-based circuit (a) and geodesic path between nodes 1 and 7 (b) (adapted from [164])

The computation of SPL between two nodes in a graph where the weights are the magnitude of the line series impedances allows the identification of the circuit with the smallest series impedance. Assuming that a network has multiple strictly parallel paths between a given pair of buses, the computation of the SPL between those buses finds the circuit that carries the most significant proportion of current. Commonly, there is only one SP between any pair of nodes in weighted graphs; this fact makes the resulting impedance-based proximity metric in the form of SPL less susceptible to topological changes.

## 2.3 Short circuit and line-switching modelling techniques

### 2.3.1 Short circuit modelling using admittance matrices

The admittance matrix is a common mathematical representation of networks in power systems, introduced in Section 2.2.1; particularly, the  $Y_{bus}$  matrix reflects the topology and parameters of the network. In this thesis the  $Y_{bus}$  matrix is used to quantify the impact of the large disturbances in the topology of the system. Assuming the worst-case scenario, a three-phase fault, the  $Y_{bus}$  can be modified to account for the fault condition; at the same time, other topological changes like line-switching can be introduced, enabling the study of different network structures and adding flexibility to the analysis. In particular, the following modification procedures have been defined to model the fault

condition when the fault location is on a busbar or on a single/parallel connection between two busbars.

Starting with a fault in a busbar, Figure 2.11 illustrates a simplified topology, including a fault on a single node. Considering a fault on busbar  $k$ , first procedure starts with the admittance matrix of the pre-fault condition  $Y^{pf}$  and introduces the following changes:

- i.  $Y_{kk}^f = \alpha Y_{kk}^{pf}$
- ii. All other shunt or series elements connected to node  $k$  remain unchanged.

Here the coefficient  $\alpha$  is a very large number, e.g.,  $10^6$  p.u., and amplifies the self-admittance  $Y_{kk}^{pf}$ , which implies that the node  $k$  has been merged with the reference node. The resulting admittance matrix has a large admittance  $Y_{kk}^f$  between the faulted node and the reference. Other modification procedures [14][19] eliminate the row and column of the faulted node, which disable further computations considering the specific busbar.

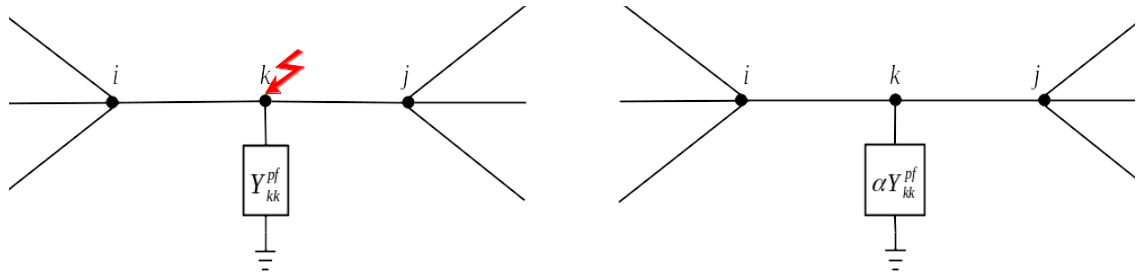


Figure 2.11: Simplified topology with a fault on a busbar of a transmission network

The second procedure starts with the admittance matrix of the pre-fault condition  $Y^{pf}$  to model a fault on single transmission circuits. For a three-phase fault in the middle of the line between busbars  $i$  and  $j$ , with series admittance  $y_{ij}^{series}$ , the procedure modifies the admittance matrix of the pre-fault condition  $Y^{pf}$  as follows (the post-fault admittances are denoted as  $Y^f$ ):

- i.  $Y_{ij}^f = Y_{ji}^f = 0$
- ii.  $Y_{ii}^f = Y_{ii}^{pf} - y_{ij}^{series} + 2y_{ij}^{series} = Y_{ii}^{pf} + y_{ij}^{series}$
- iii.  $Y_{jj}^f = Y_{jj}^{pf} - y_{ij}^{series} + 2y_{ij}^{series} = Y_{jj}^{pf} + y_{ij}^{series}$
- iv. All other shunt or series elements connected to nodes  $i$  and  $j$  remain unchanged.

Figure 2.13(a) shows the simplified topology considering a fault on a link with a single transmission line. Due to the fault, half-line impedances  $z_{ij}^{series}/2$  are added as shunt admittances  $2y_{ij}^{series}$  to both nodes  $i$  and  $j$ , i.e., increasing pre-fault shunt admittances  $Y_{ii}^{pf0}$  and  $Y_{jj}^{pf0}$ ; as half-line impedances are relatively small, shunt admittances can be

large, which implies that both nodes are electrically closer to the reference node. Moreover, mutual admittances  $Y_{ij}^f$  and  $Y_{ji}^f$  are eliminated to account for the disconnection between both nodes.

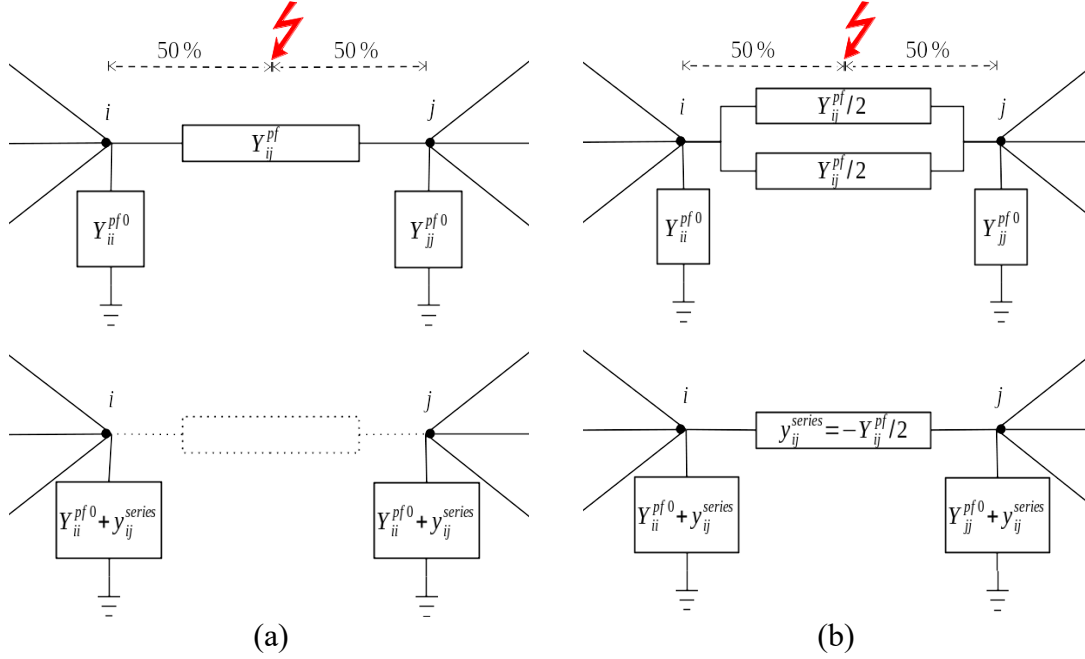


Figure 2.12: Simplified topology for single circuit (a) and double circuit (b) with faults in the middle (50% of line length) of transmission lines

The third procedure also starts with the admittance matrix of the pre-fault condition  $Y^{pf}$  to model a fault on a transmission link with double (identical) circuits. For a three-phase fault in the middle of one line between busbars  $i$  and  $j$ , with series admittance  $y_{ij}^{series}$ , the procedure modifies the admittance matrix of the pre-fault condition  $Y^{pf}$  as follows:

- i.  $Y_{ij}^f = Y_{ji}^f = -y_{ij}^{series} = Y_{ij}^{pf}/2$
- ii.  $Y_{ii}^f = Y_{ii}^{pf} - y_{ij}^{series} + 2y_{ij}^{series} = Y_{ii}^{pf} + y_{ij}^{series}$
- iii.  $Y_{jj}^f = Y_{jj}^{pf} - y_{ij}^{series} + 2y_{ij}^{series} = Y_{jj}^{pf} + y_{ij}^{series}$
- iv. All other shunt or series elements connected to nodes  $i$  and  $j$  remain unchanged.

Due to a fault only in one of the two lines, half-line impedances  $z_{ij}^{pf}/2$  are added to both nodes  $i$  and  $j$  as shunt admittances  $2y_{ij}^{series}$ , increasing pre-fault shunt admittances  $Y_{ii}^{pf0}$  and  $Y_{jj}^{pf0}$ ; besides, absolute values of mutual admittances  $Y_{ij}^f$  and  $Y_{ji}^f$  decrease by half, in comparison with the pre-fault condition, to account for the disconnection of one line.

### 2.3.2 Short circuit modelling in simulation environments

A deterministic approach was used throughout this thesis to assess the effect of line-switching actions on transmission networks with further consequences on the transient

stability of power systems. Within the deterministic framework, the study of transient stability effects related to different network topologies involves the analysis of severe disturbances. For instance, Chapter 5 includes a study based on test cases, possibly due to the discrete and finite number of combinations between line-switching actions defining network topologies and fault locations.

For TDS studies, the modelling of faults in computational tools is typically restricted to three parameters: type, duration, and location [170]. Firstly, self-clearing bolted three-phase fault is the fault type used within this work, which is the worst-case scenario that provides conservative results in terms of security. Secondly, fault duration can be defined within a set of realistic clearing times; for instance, 100, 110, and 120 ms of fault duration used in chapters 4 and 5 are longer than the 100 ms for 275 kV on the GB network [24]. Finally, the fault location is defined by the selection of busbars or transmission lines; particularly, studies in Chapter 3 use faults on busbars, whereas those in Chapter 5 include faults in the middle of transmission lines, i.e., 50% of line length. In case transmission lines are available for fault cases, considering the number of transmission lines and single line-switching actions defining a network topology, the number of available fault locations on transmission lines for any given topology is one less than the number of transmission lines.

### 2.3.3 Line-switching modelling using admittance matrices

The combination of the transmission line model and the network model based on admittances enables the representation of line-switching actions by introducing changes to the  $Y_{bus}$  matrix. In mathematical terms, a line-switching action is a binary operation that changes the status of a transmission line, i.e., *on* or *off*; in practice, switching off a line removes the asset temporarily from service, whilst switching-on a line changes its status from out-of-service to in-service. These actions have significant implications not only on the impedance of the network but also on the network topology and the system's stability, as analysed in chapters 3 and 5 through empirical test cases.

Line-switching actions like fault clearing can be applied as corrective control actions. However, in this thesis, the focus is on preventive control actions where the disconnection (switching-off) of a line can be considered a form of preventive control against a high probability event (fault) on another asset of the network that may cause more harm to the system from the transient stability perspective. In this context, assuming a high probability of a fault event on a transmission line  $f$ , the modification of

the  $Y_{bus}$  matrix due to a switching action on a transmission line  $s$ , different from line  $f$ , is introduced. In particular, the line-switching action will affect the pre-fault admittance matrix  $Y^{pf}$ , which can improve or reduce the transient stability of a system.

A simple procedure starts with the admittance matrix of the pre-switching condition  $Y^{ps}$  to model a switching action on a transmission circuit. For a switching action on a transmission line between busbars  $p$  and  $q$ , with series admittance  $y_{pq}^{series}$  and shunt admittance  $y_{pq}^{shunt}$ , the procedure generates an after-switching matrix  $Y^s$  following the steps below:

- i.  $Y_{pq}^s = Y_{qp}^s = Y_{pq}^{ps} + y_{pq}^{series} = 0$  (for single circuits)
- ii.  $Y_{pp}^s = Y_{pp}^{ps} - y_{pq}^{series} - y_{pq}^{shunt}/2$
- iii.  $Y_{qq}^s = Y_{qq}^{ps} - y_{pq}^{series} - y_{pq}^{shunt}/2$
- iv. All other shunt or series elements connected to nodes  $p$  and  $q$  remain unchanged.

Figure 2.13 illustrates a simplified topology considering changes due to a switching-off action on a single transmission line. Due to the switching-off action, the line series admittance  $y_{pq}^{series}$  is added to both pre-switching mutual admittances  $Y_{pq}^{ps}$  and  $Y_{qp}^{ps}$ ; moreover, half-line shunt admittance  $y_{pq}^{shunt}/2$  and series admittance  $y_{pq}^{series}$  are subtracted from pre-switching shunt admittances  $Y_{pp}^{ps0}$  and  $Y_{qq}^{ps0}$ , removing the transmission line from the network representation. Particularly, a switching-on action can be modelled simply by changing the addition operation for subtractions, and vice versa, to incorporate a transmission line on the  $Y_{bus}$  matrix. For TDS, the modelling of line-switching actions in computational tools is done by simply changing the service status of a line [170].

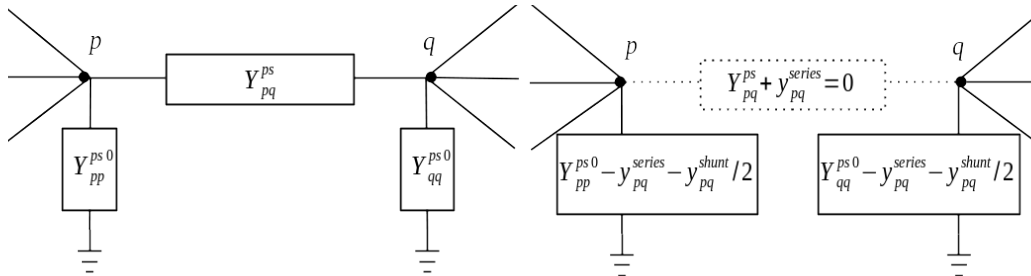


Figure 2.13: Simplified topology representing a switching-off action of a transmission line.

## 2.4 Power system optimisation techniques

This section briefly introduces three types of optimisation techniques used in this thesis, that is, optimal power flow, dynamic optimisation, and genetic algorithms. The purpose



is to describe the tools in terms of general concepts that will be later used in chapters 4 and 5.

### 2.4.1 Optimal power flow

First introduced in 1962, the purpose of optimal power flow (OPF) is to find the best settings of a given power system to optimise a single or several objective functions such as total generation cost, system losses, voltage deviations, number of control actions, or load shedding. Furthermore, those objectives must be fulfilled so that requirements regarding power flow, system security and equipment operational limits are met [171]. Moreover, OPF problems can be formulated by defining control variables like the generator's real power outputs and voltages, transformers tap changing settings, switched capacitors and reactors to find the optimal network setting. In particular, the alternating current optimal power flow (ACOPF) has been used throughout this thesis; the terms ACOPF and OPF have been used interchangeably. The ACOPF provides information related to active and reactive power flows over all network branches connecting any pair of nodes; similarly, it gives the magnitude and phase angle of the voltage at each network bus [172].

Equality constraints (2.17) and (2.18) model the active and reactive power balance at node  $i$  [171].

$$P_{Gi} - P_{Di} - \sum_{ij} P_{ij}(\cdot) = 0 \quad (2.17)$$

$$Q_{Gi} - Q_{Di} - \sum_{ij} Q_{ij}(\cdot) = 0 \quad (2.18)$$

Additionally, inequality constraints (2.19) and (2.20) represent limits on the active and reactive power production, whilst inequality (2.21) and (2.22) are node and line security constraints in terms of node voltage and line active power limits (related to boiler operation and generator thermal limits), respectively [171].

$$P_{Gi}^{min} \leq P_{Gi} \leq P_{Gi}^{max} \quad (2.19)$$

$$Q_{Gi}^{min} \leq Q_{Gi} \leq Q_{Gi}^{max} \quad (2.20)$$

$$V_i^{min} \leq V_i \leq V_i^{max} \quad (2.21)$$

$$P_{ij}^{min} \leq P_{ij}(\cdot) \leq P_{ij}^{max} \quad (2.22)$$

Here,  $P_{Gi}$  and  $Q_{Gi}$  are the real and reactive power output of a generator connected to bus  $i$ ;  $P_{Di}$  and  $Q_{Di}$  are the real and reactive power load connected to bus  $i$  and  $P_{ij}$  is the power flow at a branch connecting nodes  $i$  and  $j$ . The subscripts “min” and “max” in the above equations represent the lower and upper limits of constraints, respectively. Furthermore, expressing the voltage at node  $i$  in polar coordinates  $V_i = V_i(\cos \theta_i + j \sin \theta_i)$ , the active and reactive power flowing at a branch connecting nodes  $i$  and  $j$  can be given as equations (2.23) and (2.24) [171].

$$P_{ij}(\cdot) = V_i^2 g_{ij} - V_i V_j [g_{ij} \cos(\theta_i - \theta_j) + b_{ij} \sin(\theta_i - \theta_j)] \quad (2.23)$$

$$Q_{ij}(\cdot) = -V_i^2 b_{ij} - V_i V_j [g_{ij} \sin(\theta_i - \theta_j) - b_{ij} \cos(\theta_i - \theta_j)] \quad (2.24)$$

Here,  $V_i$ ,  $V_j$ ,  $\theta_i$ , and  $\theta_j$  are magnitudes and phase angles of voltages at bus  $i$  and  $j$ , respectively. Besides,  $g_{ij}$  and  $b_{ij}$  are branch conductance and susceptance associated with transmission network assets.

For a multi-machine system with  $NG$  generators, an ACOPF problem can minimize the total generation cost  $f(P_{Gk})$ , typically known as economic dispatch, given by (2.25) [171].

$$\begin{aligned} \min F &= \sum_k^{NG} f(P_{Gk}) \\ \text{Subject to} & \text{ (2.17)-(2.22)} \end{aligned} \quad (2.25)$$

The first-order optimality conditions for the static non-linear problem defined above are given by well-known Karush-Kuhn-Tucker relations [171]. However, they are not discussed here because solution algorithms used in this thesis do not solve these relations.

### 2.4.2 Dynamic optimisation and optimal control

Though the underlying principles of static and dynamic optimisation are similar, the main difference is the nature of the optimal solution. On the one hand, static optimisation provides an optimal solution in the form of a point, which gives the minimum (or maximum) value of a cost function; on the other hand, in dynamic optimisation the solution is a function, which is the optimal solution of an integral cost function, known as cost functional [173][174]. A particular case of dynamic optimisation is optimal control, which studies optimisation problems integrating two components. Firstly, a cost functional in the form of a Lagrange problem (2.26) defined by the integral over time  $[t_0, t_f]$  of a cost function  $L$ ; and secondly, a dynamic system (2.27) in the form of state-

space equations, where  $\mathbf{x}$  and  $\mathbf{u}$  are vectors of state variables and control actions, respectively. It is assumed that the state of the system is known at  $t_0$ .

$$\min_{\mathbf{x}, \mathbf{u}} \left\{ J = \int_{t_0}^{t_f} L(t, \mathbf{x}(t), \mathbf{u}(t)) dt \right\} \quad (2.26)$$

$$\begin{aligned} \text{Subject to: } \dot{\mathbf{x}} &= f(t, \mathbf{x}, \mathbf{u}); \\ \mathbf{x}(t_0) &= \mathbf{x}_0 \end{aligned} \quad (2.27)$$

In this case, the optimal control actions  $\mathbf{u}^*(t)$  minimise the cost given by (2.26), where the dynamic system (2.27) is a point-wise-time non-integral constraint [173].

In the general case of the constrained dynamical optimisation problems, the mathematical model with a single variable, control and one constraint can be set as follows [173][174].

$$\begin{aligned} \min_{x, u} \left\{ J(x) = \int_{t_0}^{t_f} F(t, x(t), \dot{x}(t)) dt \right\} \\ \text{Subject to: } G(t, x(t), \dot{x}(t)) = 0; \\ x(t_0) = x_0; x(t_f) = x_f \end{aligned} \quad (2.28)$$

The combination of the argument of the functional  $F(t, x(t), \dot{x}(t))$  with the equality constraint  $G(t, x(t), \dot{x}(t))$  in (2.29) is called Lagrangian [173]. In particular,  $\lambda$  is a Lagrange multiplier.

$$L(t, x(t), \dot{x}(t)) = F(t, x(t), \dot{x}(t)) + \lambda \cdot G(t, x(t), \dot{x}(t)) = 0 \quad (2.29)$$

The first-order optimality conditions, presented in (2.30), are called the Euler-Lagrange equations, and they are the first-order necessary condition to have  $x^*(t)$  as optimal curve; moreover,  $J(x^*(t))$  is a stationary value of the integral, i.e., it makes the first variation equal to zero [174]. Additionally,  $x^*(t)$  has to fulfil the constraint  $G(\cdot) = 0$ , and initial and final conditions.

$$\begin{aligned} \frac{\partial L(\cdot)}{\partial x} - \frac{d}{dt} \frac{\partial L(\cdot)}{\partial \dot{x}} &= 0; \\ \frac{\partial L(\cdot)}{\partial \lambda} &= G(t, x(t), \dot{x}(t)) = 0; \\ x(t_0) &= x_0; x(t_f) = x_f \end{aligned} \quad (2.30)$$

Note that for the problem (2.28), the initial and final conditions  $x_0$  and  $x_f$  are given in (2.30).

In case of unknown final condition  $x(t_f)$ , constrained dynamical optimisation problem, with  $n$  state variables and  $m$  differential equations as constraints, can be given as follows:

$$\min_{x,u} \left\{ J(x) = \int_{t_0}^{t_f} F(t, x_1(t), x_2(t), \dots, x_n(t), \dot{x}_1(t), \dot{x}_2(t), \dots, \dot{x}_n(t)) dt \right\}; \quad (2.31)$$

$$\text{Subject to: } G_j(t, x(t), \dot{x}(t)) = 0; j = 1, 2, \dots, m$$

$$x_1(t_0) = \alpha_1, x_2(t_0) = \alpha_2, \dots, x_n(t_0) = \alpha_n$$

$$L(\cdot) = F(t, x_1, x_2, \dots, x_n, \dot{x}_1, \dot{x}_2, \dots, \dot{x}_n) + \sum_{j=1}^m \lambda_j(t) \cdot G_j(t, x_1, x_2, \dots, x_n, \dot{x}_1, \dot{x}_2, \dots, \dot{x}_n) = 0 \quad (2.32)$$

Here  $\mathbf{x}$  and  $\dot{\mathbf{x}}$  are vectors of state variables and first-order derivatives with respect to time, respectively, and  $\boldsymbol{\alpha}$  is a vector of initial conditions; besides,  $\mathbf{G}$  and  $\boldsymbol{\lambda}$  are vectors of equality constraints and Lagrange multipliers, respectively. In this case, Lagrange multipliers in (2.32) are functions of time. Moreover, the optimal solution  $\mathbf{x}^*(t)$  has to satisfy not only the Euler-Lagrange equation (2.33) and differential constraints (2.34) but also each partial derivative of the Lagrangian with respect  $\dot{x}_i$  to must be zero at  $t = t_f$  (2.35) [173].

$$\frac{\partial L(\cdot)}{\partial x_i} - \frac{d}{dt} \frac{\partial L(\cdot)}{\partial \dot{x}_i} = 0; i = 1, \dots, n \quad (2.33)$$

$$\frac{\partial L(\cdot)}{\partial \lambda_j} = G_j(t, \mathbf{x}(t), \dot{\mathbf{x}}(t)) = 0; j = 1, \dots, m \quad (2.34)$$

$$\left. \frac{\partial L(\cdot)}{\partial \dot{x}_i} \right|_{t=t_f} = 0; i = 1, \dots, n \quad (2.35)$$

Inequality constraints in the form  $x(t) \leq \varphi(t)$  are modelled in the form of equality  $x(t) + z^2(t) = \varphi(t)$  where  $z(t)$  is a new unrestricted variable. In this way, inequality constraints are modelled as equalities in (2.31) and (2.34).

A simple inspection of the constraints in sections 2.4.1 and 2.4.2 can give insight into the number of equality constraints of an optimisation problem combining both approaches. On top of OPF constraints and constraints in the form of SGs differential equations, an optimisation approach using the topology of the transmission system needs to include discrete variables to model line-switching actions, which makes the problem

even harder to solve. An iterative solution for a preventive optimal control problem will be described in Chapter 5.

### 2.4.3 Genetic algorithms

Genetic algorithms are heuristic search methods based on the mechanics of nature and natural genetics [175]. In simple terms, it is a search technique to find an approximate solution to optimisation problems using a fitness function instead of an objective function, as in classic optimisation methods. Notably, a GA uses the fitness function to direct the search; thus, there is no need for derivatives which is more convenient to solve highly non-linear problems. A GA provides a solution to a problem by evaluating a population of individuals, also called generation; each individual is represented by a collection of numbers, known as a chromosome, characterising a potential solution [171]. GA operations such as evaluation, selection, reproduction and replacement define new potential individuals in the search space.

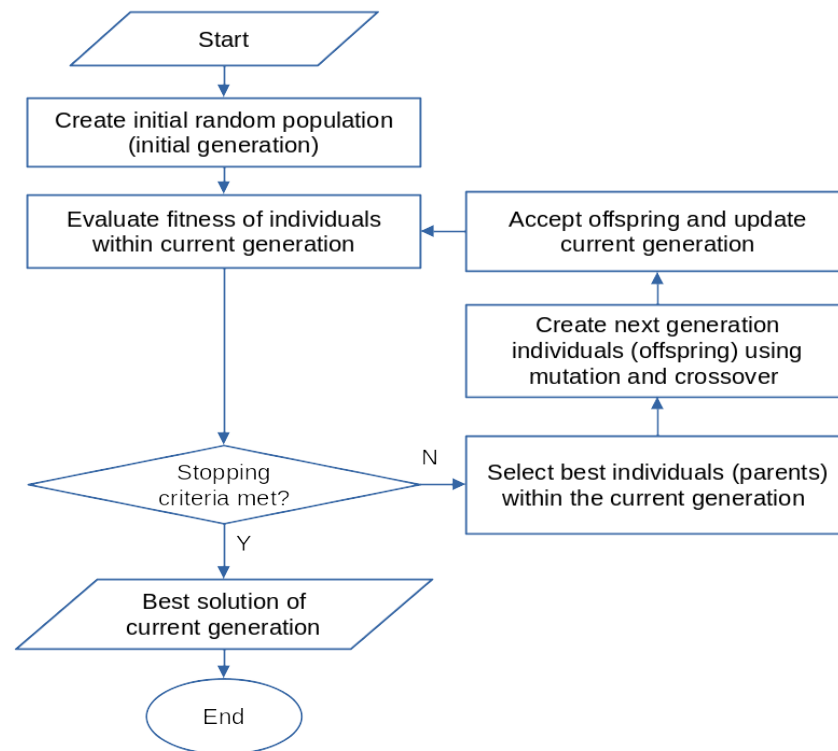


Figure 2.14: Simplified flow chart of a GA (Adapted from [176]).

A flow chart of a GA is shown in Figure 2.14 [176]; the figure illustrates an iterative algorithm combining a series of steps to reach the optimal solution. In particular, the creation of the next generation of individuals, known as children, is produced mainly by three operators. Firstly, applied with a pre-defined probability, the crossover is the primary search operator; it creates a new child based on the information of two parent chromosomes. Secondly, the mutation is a secondary search operator, also applied with

a pre-defined probability, randomly changing a child's chromosome component to provide a characteristic different from the parents. Finally, an elitist strategy can be applied to preserve the fittest individuals within each generation. In summary, the operators allow the production of an offspring with new characteristics but preserve the information of the best individual from previous iterations [171].

## **2.5 Overview of computational tools**

Results presented in this thesis have been produced by integrating several computational tools to automate different processes by selecting the most suitable software for a given purpose within the research. A comprehensive view of the computational tools is illustrated in Figure 2.15; the figure shows the interaction of different software components to automate preparation, optimisation, and validation processes. In particular, three software components have been used as main tools in this thesis; PowerFactory DIgSILENT as power system simulation and computational engine, MATLAB as the main component for technical computing, and Python as an integration tool to provide the communication layer between software components.

Firstly, the computation of electrical power flow and transient stability simulation are performed using PowerFactory DIgSILENT 2020 version SP3 [170]; the scripting capabilities within the software, provided by the DIgSILENT Programming Language (DPL) and PowerFactory Python module, enable the automation of computation of initial conditions for dynamical models and the execution of TDS. All the models described in Chapter 2, including test systems used in chapters 3 and 5, are available or have been implemented using PowerFactory Simulation Language (DSL). Secondly, the data processing considering mathematical operations, including the optimisation based on GA [177], has been done using MATLAB version 9.10.0 R2021a [178]; particularly, the economic dispatch solution to determine the active power output and terminal voltages of SGs has been solved using MATPOWER version 7.0 [179]. Finally, Python version 3.7.11 [180] has been used to enable the integration of the software components utilizing the Application Programme Interfaces (APIs) of MATLAB and PowerFactory.

The complete process automation is shown in Figure 2.15. The figure shows that data processing is done in MATLAB by running OPF, obtaining the best topology using GA, and validating the best solution by transient stability assessment; besides, PowerFactory is used to compute steady state variables by computing initial conditions and to obtain

generator responses by running RMS simulation. It can also be seen that Python is mainly used as a communication layer to transport data structures between MATLAB and PowerFactory.

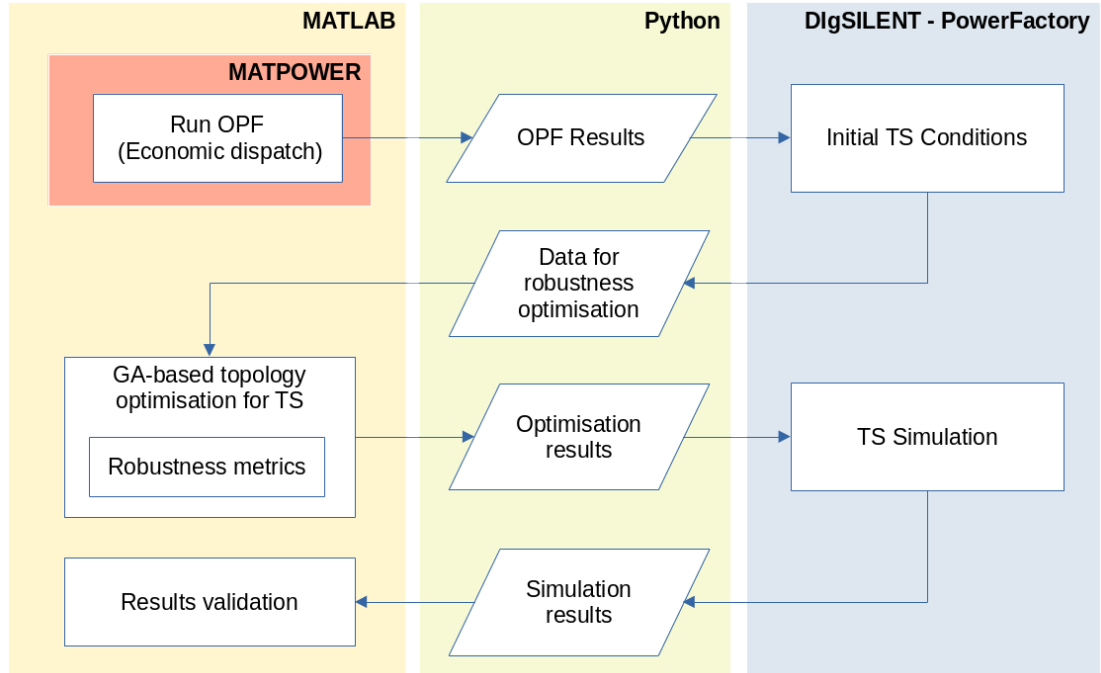


Figure 2.15: Simplified flow chart of data for the proposed topology optimisation.

## 2.6 Summary

This chapter has presented the essential modelling, procedures and techniques used throughout this dissertation. The chapter introduces the details of the mathematical models of components typically found in power systems; these include synchronous generators with standard controllers influencing their behaviour during electromechanical transients, i.e., AVR and PSS. Moreover, the matrix representation of the power system network was introduced considering branch elements such as power transformers, transmission lines and loads.

As the focus of the work presented in this thesis is the study of the effect of network topology on transient stability, procedures modifying the admittance matrix of transmission networks were described in detail. The inclusion of line-switching actions on transmission lines and the integration of fault conditions on busbars or transmission lines were defined mainly by the removal (or addition) of the admittances related to the corresponding component. The procedures are simple enough to produce a fast computation process modifying the network representation. The theoretical framework

of optimisation techniques used in power systems was described with special attention to static and dynamic problems, like OPF and optimal control, respectively.

Finally, the chapter describes the computational environment used to produce the results included in this thesis. Notably, the integration of two software components, PowerFactory and MATLAB, was possible due to the flexibility provided by Python. Particularly, the corresponding Python API of both software packages allowed seamless integration to run different processes.



## **3 Assessment of the Impact of Line-Switching Actions on Transient Stability**

---

This chapter introduces the assessment of the effect of line-switching actions on changing the structure and properties of transmission networks. Switching off a transmission line directly impacts the impedance seen from SGs, with consequences on the stability of power systems. In particular, the assessment of switching actions is done by two impedance-based proximity metrics using two small test systems; the purpose is to provide a clear evaluation of the impact of switching actions avoiding the complexity of large systems.

The chapter includes two parts. Firstly, a definition of a Single Machine Infinite Bus (SMIB) system is used to introduce an in-depth analysis, using theoretical and simulation tools, of the effect of line-switching actions changing the impedance between generators and fault locations. Secondly, an adaptation of the Anderson and Fouad 9 bus (AF9B) system was made to provide a detailed analysis of line-switching actions using a simulation tool. Theoretical and simulation results are used in both parts to verify topology-related findings.

### **3.1 Effect of line-switching actions between generators and fault location on transient stability**

#### **3.1.1 SMIB test system**

The concept of the SMIB network introduced in Section 1.3.2 provides the building blocks to define the test system shown in Figure 3.1. The SMIB test system is used to analyse the impact of line-switching actions on the network structure and the effects on

the impedance between the SG and the fault location. In particular, the generation plant includes a single generator  $G$  and a step-up transformer  $T$ . The SG has a direct-axis transient reactance  $x'_d = 0.462$  p.u. and inertia constant  $H = 3.7143$  s; it is represented by a sixth-order model equipped with a generic governor and a slow DC exciter (IEEE-DC1A). The generator  $G$  operates at 90% of nominal capacity with a constant operating power factor of 0.915 lagging. The step-up transformer has a series reactance of  $x_T = 0.15$  p.u. Besides, the connection between the single SG and the infinite bus is through 6 double-circuit transmission lines with a reactance of  $0.5 \Omega/\text{km}$ , which is a typical value for 220 kV networks. The transmission network includes only inductive series components to represent transmission branches. Other relevant network parameters are shown in Figure 3.1 and can be found in Appendix A.1.

A distinctive feature of the test system is the 150 km of physical distance between busbars 2 and 4. Furthermore, the main difference between the SMIB test system defined in this chapter and a typical SMIB network (see Section 1.3.2) is the topology of the transmission network. The SMIB test system has more transmission circuits and an intermediate busbar (bus 3), as seen in Figure 3.1, so that the effect of line switching can be analysed by gradual disconnection of the circuits, i.e., varying the network impedance, resembling what happens on actual networks. Additionally, the test system enables the analysis of disturbances with and without power transfer during fault., if the status of the double-circuit Line1 is *on*, the network allows the power transfer during a three-phase bolted fault on busbar 3; on the contrary, switching-off Line1, the electrical power output of the generator is zero.

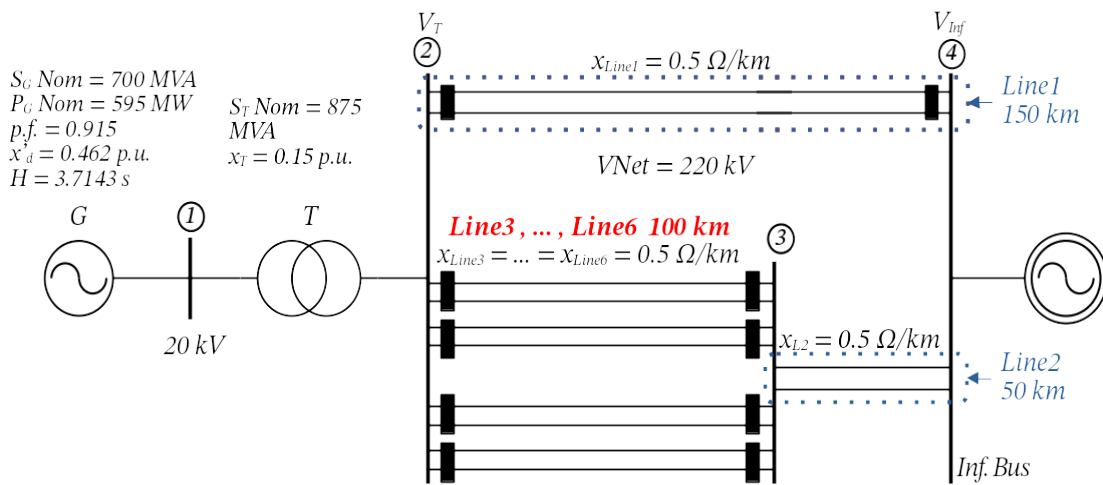


Figure 3.1: SMIB test system (100KM-SMIB) with double circuit transmission lines

A variant of the SMIB test system can be defined by reducing the distance between busbars 2 and 3 to 50 km (see Figure 3.2); the change reduces the reactances of the transmission links between busbars 2 and 3 whilst increasing the reactance of the double-circuit Line2 from 12.5  $\Omega$  to 25  $\Omega$ . Based on the connection between busbar 2 and 3, the SMIB variant in Figure 3.2 is identified as 50KM-SMIB, whilst the network shown in Figure 3.1 is identified as 100KM-SMIB.

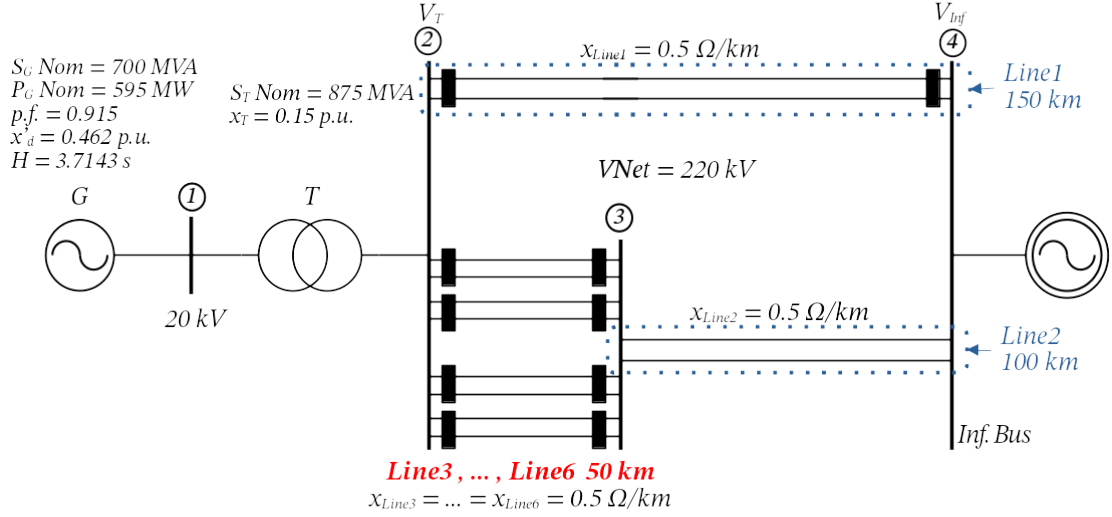


Figure 3.2: SMIB test system variant (50KM-SMIB) with double circuit transmission lines

### 3.1.2 Considerations for the analysis based on the SMIB test system with the classical model of SG

A preliminary approach considers the analysis of the transient stability level of the 100KM-SMIB test system by the computation of Critical Clearing Time (CCT) based on the Equal Area Criterion (EAC), both described in Section 1.3. The critical clearing angle  $\delta_{cr}$  obtained by the EAC can be used in equation (1.4) to obtain the expression for CCT, repeated here for clarity.

$$CCT = \sqrt{\frac{4H(\delta_{cr} - \delta_0)}{\omega_r(P_M - P_E)}} \quad (3.1)$$

The ratio of parameters  $4H/\omega_r$  in equation (3.1) gives an insight into the effect of the size of an SG; the constant inertia value  $H$  reflects the designed SG nominal capacity; hence with a larger  $H$  the more likely the SG will remain stable, which is reflected by longer CCTs. Similarly, a longer CCT will require a large angle difference  $\delta_{cr} - \delta_0$  and a small accelerating power  $P_A = P_M - P_E$ . The angle difference  $\delta_{cr} - \delta_0$  is influenced by the characteristics of the fault, pre-fault operating conditions, and the post-fault network structure, which determines the size of the decelerating area. Though the angle difference

is affected by the generator's active and reactive power production, *the structure of the network significantly impacts its magnitude*. For the accelerating power  $P_A$ , the mechanical power can be considered constant and equal to the pre-fault dispatch, whereas the electrical power will be greatly influenced by the post-fault network and by the structure of the transmission system during the fault condition.

An estimation of the average accelerating power  $P_A^{avg}$  can be obtained by the average of discrete successive evaluations (sampling) of  $P_M - P_{E,max}^{fault} \sin \delta$ . Similarly, as the accelerating area and clearing angle can be calculated by applying the EAC,  $P_A^{avg}$  (3.2) can be expressed as a function of the accelerating area and the angle difference  $\delta_{cr} - \delta_0$ , when  $P_E$  is not constant during fault condition. Results based on the test system described in the previous section indicate that the calculation of  $P_A^{avg}$  based on (3.2) or using successive evaluations have highly similar results.

$$P_A^{avg} = \frac{1}{\delta_{cr} - \delta_0} [P_M(\delta_{cr} - \delta_0) + P_{E,max}^{fault}(\cos \delta_{cr} - \cos \delta_0)] \quad (3.2)$$

In the EAC context, the transient power-angle characteristic, described in Section 1.3.3, is valid for the representation of SG using the classical second-order model; the equation is reproduced below to illustrate the network effect.

$$P_E^{fault} = \frac{E' \times V_{Inf}}{x_{Eq}^{fault}} \sin \delta'_0$$

Here, the equivalent impedance  $x_{Eq}^{fault}$  considers the impedance of the transmission system, step-up transformer, and the internal transient reactance of an SG during the fault. Particularly, the ratio  $E' \sin \delta'_0 / x_{Eq}^{fault}$  governs the magnitude of the power output of the SG; since  $E'$  is constant in the model, the numerator  $E' \sin \delta'_0$  is also constant. In the SMIB context,  $x_{Eq}^{fault}$  is the only parameter effectively influencing  $P_E^{fault}$ , hence, a larger  $x_{Eq}^{fault}$  will reduce the magnitude of active power transfer. In the case of a radial connection, for faults that completely interrupt the flow of power during the fault, e.g., at busbar 3 of the SMIB test system when Line1 is switch-off, the equivalent impedance  $x_{Eq}^{fault}$  can be considered infinite (or extremely large for analysis purposes), making  $P_E^{fault} = 0$ . Nevertheless, a radial connection is not typical for transmission systems; they are usually the resulting condition after several line outages.

### 3.1.3 Preliminary analysis using the EAC and CCT based on the SMIB system

To focus on the effect of line-switching actions, parameters like line status change to emphasise their influence on transient stability, whilst parameters unrelated to the transmission network are kept constant. In addition, changes in line impedances are included according to changes in physical distances, as seen in Figure 3.1 and Figure 3.2. An initial approach considers the analysis of the transient stability level of the 100KM-SMIB test system by the computation of CCT based on the EAC. The transient stability is studied using the classical second-order model of the SG (1.3), and disturbances are simulated in the form of three-phase self-clearing bolted faults in busbar 3. Moreover, changes in the network are introduced as line-switching actions, reducing the number of available transmission links between busbars 2 and 3 from 4 to 1 pair, i.e., having 8, 6, 4 or 2 circuits in service. An essential change is incorporated by the outage of Line1, which creates the condition where the SG is connected radially to the infinite bus; particularly, test cases with Line1 in service are identified as type “A”, whereas Line1 status is *off*, i.e., a radial connection with Line1 out of service, for test cases belonging to type “B”. The two types represent two extreme cases; type A is a meshed topology, which is commonly found in transmission systems, whereas type B is a radial connection less frequent in transmission systems.

Based on the 100KM-SMIB test system, the described topological changes enable the definition of preliminary test cases included in Table 3.1; for instance, the test case A-8Lines considers Line1 in service and four double circuits (8 lines) in the link between busbars 2 and 3, whereas case B-2Lines has Line1 under outage and only one double circuit (2 lines) between busbars 2 and 3. The naming convention for test cases is used consistently throughout this chapter.

Table 3.1 Transfer impedances of the 100KM-SMIB Cases A-B with 8 and 2 parallel lines

Test Case	$x_{Eq}^{pre-fault}$ (p.u.)	$x_{Eq}^{fault}$ (p.u.)	$x_{Eq}^{ratio}$ (p.u.)	CCT (s.) Eq (3.1)
A-8Lines	0.109	0.659	6.045	0.285
A-2Lines	0.122	0.285	2.336	0.493
B-8Lines	0.122	Inf	Inf	0.206
B-2Lines	0.161	Inf	Inf	0.150

The 100KM-SMIB test system is used to introduce changes in the network structure; impedance diagrams of the preliminary test cases in Table 3.1 are shown in Figure 3.3. In every test case, the SG dispatch is 90% of its nominal active power (595 MW) with a constant operating power factor of 0.915 to avoid changing the active and reactive power

injections. The generator's parameters, such as inertia constant and d-axis transient reactance are 3.714 s and 0.462 p.u., respectively. Figure 3.3 illustrates the impedance diagram with 8 and 2 parallel lines, between busbars 2 and 3, for test cases type A and B, respectively; the impedances are in p.u. in a typical 100 MVA base. In Figure 3.3,  $Q_{load}$  changes due to the change in the losses associated to the number of transmission lines in service. The figure reveals changes in impedance when 8 or 2 lines are in service between busbars 2 and 3, i.e., the comparison between having all lines in service (8 lines) or switching off three double circuits (2 lines) between busbar 2 and 3, resulting in a 300% increase of the impedance.

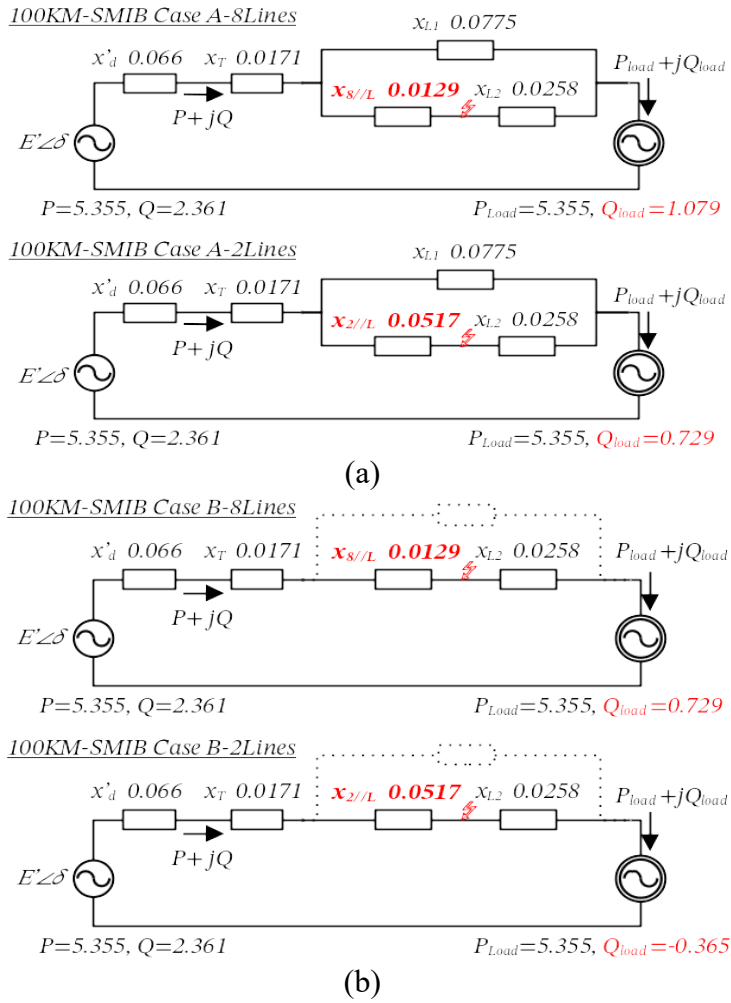


Figure 3.3: Impedance diagram of cases type A (a) and B (b) of the 100KM-SMIB test system with 8 and 2 parallel lines.

A summary of the transfer impedances,  $X_{Eq}$  in the power angle characteristic equation, shown in Table 3.1, shows the effect of line-switching actions on transfer impedance associated with each test case. In general, test cases type A have a smaller pre-fault impedance  $x_{Eq}^{pre-fault}$  due to the higher number of available (parallel) lines, whilst cases type B have a larger impedance due to the *off* status of Line1. Additionally, a substantial difference can be seen in the ratio of during-fault over pre-fault transfer impedances,

identified as the transfer impedance ratio  $x_{Eq}^{ratio} = x_{Eq}^{fault} / x_{Eq}^{pre-fault}$ , which account for the relative impedance size between under fault and pre-fault conditions. A comparison between 8 and 2 parallel lines for cases type A reveals that  $x_{Eq}^{ratio}$  is smaller when only 2 lines are in service; Table 3.1 shows that a lower number of parallel lines in service has a lower during-fault transfer impedance  $x_{Eq}^{fault}$ , which enables a larger power transfer during fault condition. The lower  $x_{Eq}^{ratio}$  of the case A-2Lines produces a longer CCT, which reflects a better transient stability level in comparison with the case A-8Lines. For cases type B, an infinite impedance is used because there is no power transfer due to the radial connection, i.e., the fault on busbar 3 is located on the only available path between the SG and the infinite busbar.

Based on the power-angle characteristic (1.2), the computation of the critical clearing angle  $\delta_c$  enables the analysis of the transient stability level of switching-line actions of each test case. Figure 3.4 compares the two types of test cases where all parameters are based on a typical 100 MVA base and plotted at scale. Pairs of power-angle curves (pre-fault and during fault) of each test case are shown in blue and green colours, with 8 and 2 available parallel lines between busbars 2 and 3, respectively. The figure reveals that test cases type B (radial connection) are more critical than type A because angle differences  $\delta_{cr} - \delta_0$  are significantly smaller, resulting in shorter CCTs; this fact is intrinsically related to the power transfer capability during the fault condition. Notably, the pre-fault equivalent impedance  $x_{Eq}^{pre-fault}$  influences the smaller amplitude of the power-angle characteristic of cases type B in comparison with cases type A; smaller transfer capabilities after the fault of cases type B are defined by pre-fault transfer impedances of higher magnitude (see Table 3.1), which causes shorter CCTs.

Figure 3.4 shows a different tendency when comparing the clearing angle among different types of test cases. For example, Figure 3.4(a) suggests that the clearing angle of the test case with two parallel lines is larger than the case with eight parallel lines for cases type A. Conversely, for the radial connection in Figure 3.4(b), the clearing angle of the case with eight parallel lines is the largest for test cases type B. In particular, the test case A-2Lines with larger pre-fault impedance, in comparison with A-8Lines, has a larger angle difference and longer CCT (see Figure 3.4(a)); this indicates that the system can be more stable even with fewer lines in the network, for configurations and faults similar to case type A in Figure 3.4(a), which may sound contradictory at first. Therefore, line-switching can be advantageous and used to improve transient stability.

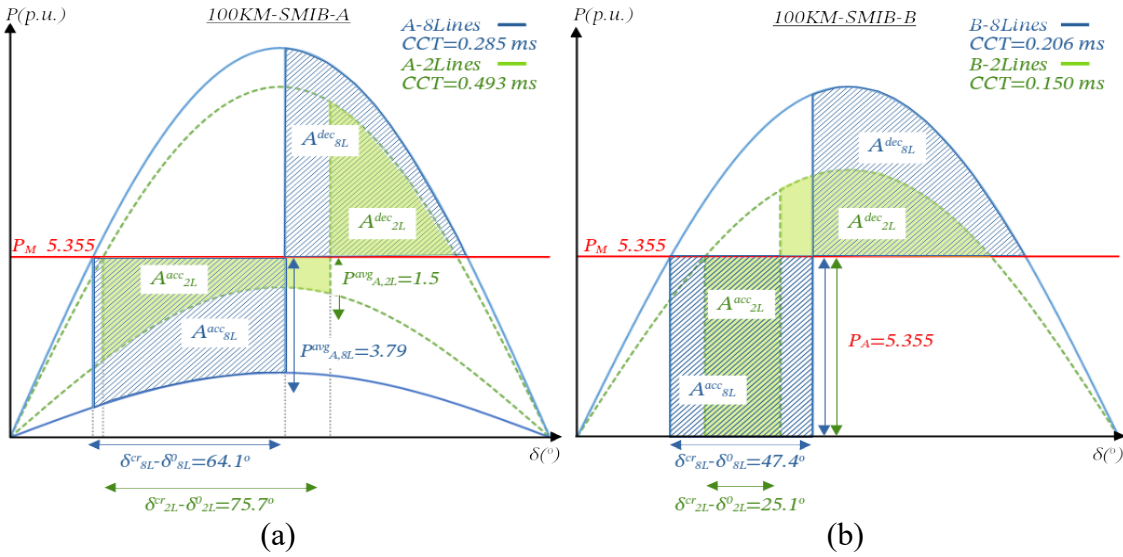


Figure 3.4: Power angle characteristics of cases type A (a) and B (b) of the 100KM-SMIB test system with 8 and 2 parallel lines.

Insight can be obtained by complementing the evidence shown in Figure 3.4 with the data of factors influencing the CCT shown in Table 3.2. In the table, the accelerating area  $A^{acc}$  in  $p.u. rad$  is the area between mechanical power of the SG and its electrical power output characteristics during the fault in the interval between  $\delta_0$  and  $\delta_{cr}$  (equal to the corresponding decelerating area, see Figure 3.4), the average accelerating power  $P_A^{avg}$  in  $p.u.$  is an approximation by the mean of successive evaluations of  $P_M - P_E^{fault}$ , and the CCT in seconds is based on (3.1). Notably, for a constant ratio of  $4H/\omega_r$  in equation (3.1), the CCT is directly proportional with the angle difference  $\delta_{cr} - \delta_0$ ; moreover, the CCT has an inversely proportional relationship with the accelerating power  $P_M - P_E$ , which is estimated by  $P_A^{avg}$  for the purpose of this analysis.

Table 3.2 CCT factors of the 100KM-SMIB Cases A-B with 8 and 2 parallel lines

Test Case	$A^{acc}$ (p.u. rad)	$P_A^{avg}$ (p.u.)	$\delta_{cr} - \delta_0$ (deg.)	CCT (s.)
A-8Lines	4.240	3.790	64.10	0.285
A-2Lines	1.985	1.502	75.71	0.493
B-8Lines	4.430	5.355	47.39	0.206
B-2Lines	2.348	5.355	25.12	0.150

The data in Table 3.2 indicate that for cases type B (radial connection), the reduction from 8 to 2 available parallel lines between buses 2 and 3 decreases the accelerating area that the system can develop before losing synchronism. This effect is due to having a smaller decelerating area because of the higher post-fault (pre-fault) impedance; as the accelerating power is constant and equal for both test cases, the angle difference of the case B-2Lines is smaller, which produces a shorter CCT. Though the reduction of parallel lines also decreases the accelerating area, a conversely effect can be seen for cases type



A. The reduction of parallel lines increases the impedance between busbars 2 and 3; however, it produces a 56.7% reduction of the transfer impedance between pre-fault and during fault conditions (see Table 3.1). As a result, for cases type A the case with two lines has a larger angle difference providing a longer CCT.

A similar analysis is done using the 50KM-SMIB test system based on analogous test cases (see Figure 3.5) as a sensitivity analysis. The difference is the reduction (50KM) on the transmission link between busbars 2 and 3 and the corresponding increase in length of Line2. Compared with the 100KM-SMIB system, the topological change introduced in the 50KM-SMIB system increases or maintains the corresponding pre-fault and fault transfer impedances (see Table 3.1 and Table 3.3).

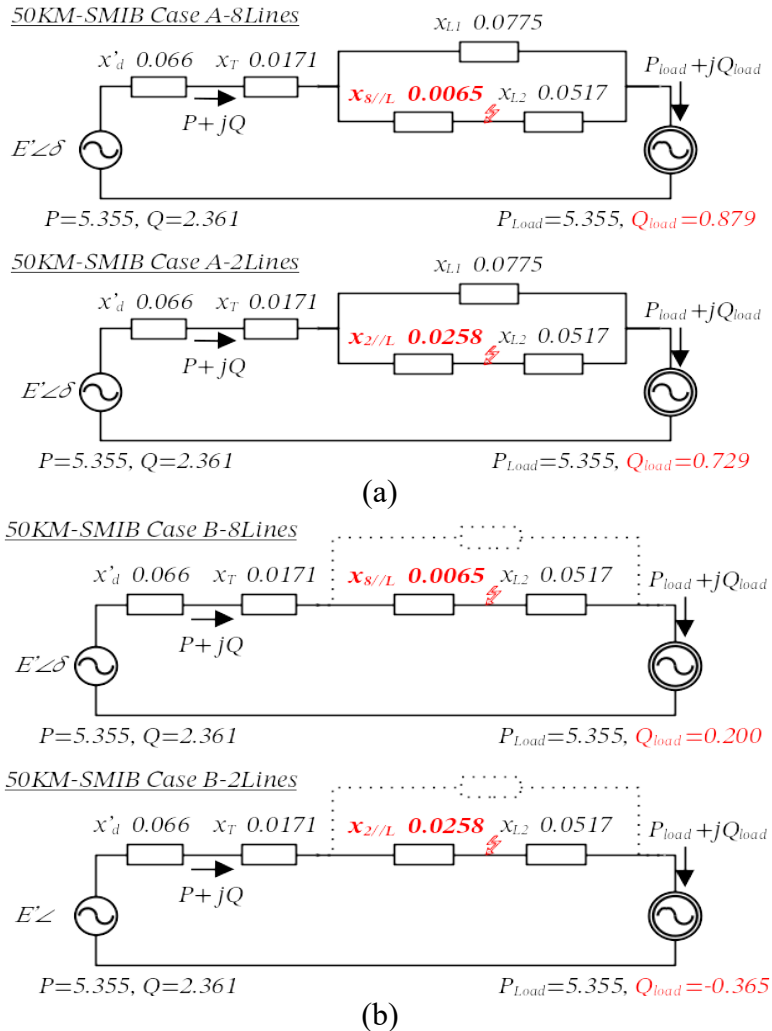


Figure 3.5: Impedance diagram of cases type A (a) and B (b) of the 50KM-SMIB test system with 8 and 2 parallel lines.

A comparison of test cases type A of both test systems indicates that test cases of the 50KM-SMIB system have higher  $x_{Eq}^{ratio}$ ; overall, this fact reveals that even though the reduction of distance (from 100 to 50 km) reduces the impedance between busbar 2 and 3, the change is not beneficial from the transient stability perspective because it increases

$x_{Eq}^{ratio}$ , which indicates an increase in the equivalent impedance during the fault reducing the active power output. Though there is a slight increase of  $x_{Eq}^{pre-fault}$ , the main reason behind the increase of  $x_{Eq}^{ratio}$  is an increase of more than 40% of  $x_{Eq}^{fault}$  for the 50KM-SMIB system in comparison to the 100KM-SMIB. In simple terms, the fault location is closer to the SG for the 50KM-SMIB system, which makes the disturbance on busbar 3 more severe from the transient stability viewpoint; the opposite can be said if the distance between busbars 2 and 3 increases like for the 100KM-SMIB system. Overall, the CCTs for the 100KM-SMIB are higher or equal compared to the 50KM-SMIB system, which indicates that smaller impedances are not always beneficial from the transient stability viewpoint.

Table 3.3 Transfer impedances of the 50KM-SMIB Cases A-B with 8 and 2 parallel lines

Test Case	$x_{Eq}^{pre-fault}$ (p.u.)	$x_{Eq}^{fault}$ (p.u.)	$x_{Eq}^{ratio}$ (p.u.)	CCT (s.)
A-8Lines	0.116	1.158	9.983	0.244
A-2Lines	0.122	0.410	3.361	0.333
B-8Lines	0.141	Inf	Inf	0.180
B-2Lines	0.161	Inf	Inf	0.150

Table 3.4 CCT factors of the 50KM-SMIB Cases A-B with 8 and 2 parallel lines

Test Case	$A^{acc}$ (p.u. rad)	$P_A^{avg}$ (p.u.)	$\delta_{cr} - \delta_0$ (deg.)	CCT (s.)
A-8Lines	4.318	4.472	55.32	0.244
A-2Lines	3.034	2.744	63.36	0.333
B-8Lines	3.359	5.355	35.94	0.180
B-2Lines	2.348	5.355	25.12	0.150

Figure 3.6 compares power angle characteristics for 100KM-SMIB and 50KM-SMIB test systems; in combination with the data in Table 3.2 and Table 3.4, the comparison shows that the impedance reduction, due to the decrease in physical distance, increases the severity of the disturbance on busbar 3. For cases 50KM-SMIB type A (top row of Figure 3.6), though  $x_{Eq}^{pre-fault}$  are similar, the increase of  $x_{Eq}^{fault}$  are significant, which reduces the during-fault power transfer capability increasing the accelerating area especially on test cases with lower impedance, i.e., cases with eight parallel lines between busbars 2 and 3. As a consequence, cases 50KM-SMIB type A have larger  $P_A^{avg}$  and  $A^{acc}$  in comparison to those of the 100KM-SMIB; the increase of  $P_A^{avg}$  compared to the reduction  $\delta_{cr} - \delta_0$  decreases the corresponding CCT. In practical terms, the combination of larger accelerating area and power produces worse stability results for cases 50KM-SMIB type A. A different reason is behind the increase in CCT for the radial connection

in cases type B (bottom row of Figure 3.6) with a constant  $P_A^{avg}$ , the smaller post-fault power transfer capability of 50KM-SMIB cases reduces the decelerating area, also reducing  $A^{acc}$ . The reduction of  $A^{acc}$  on cases type B lowers the angle difference  $\delta_c - \delta_0$ , which produces smaller CCT; under this type, the lower decelerating area is the cause for worse stability results. Overall, the shorter fault distance of the 50KM-SMIB system produces smaller CCTs, i.e., it is detrimental to the stability of the system.

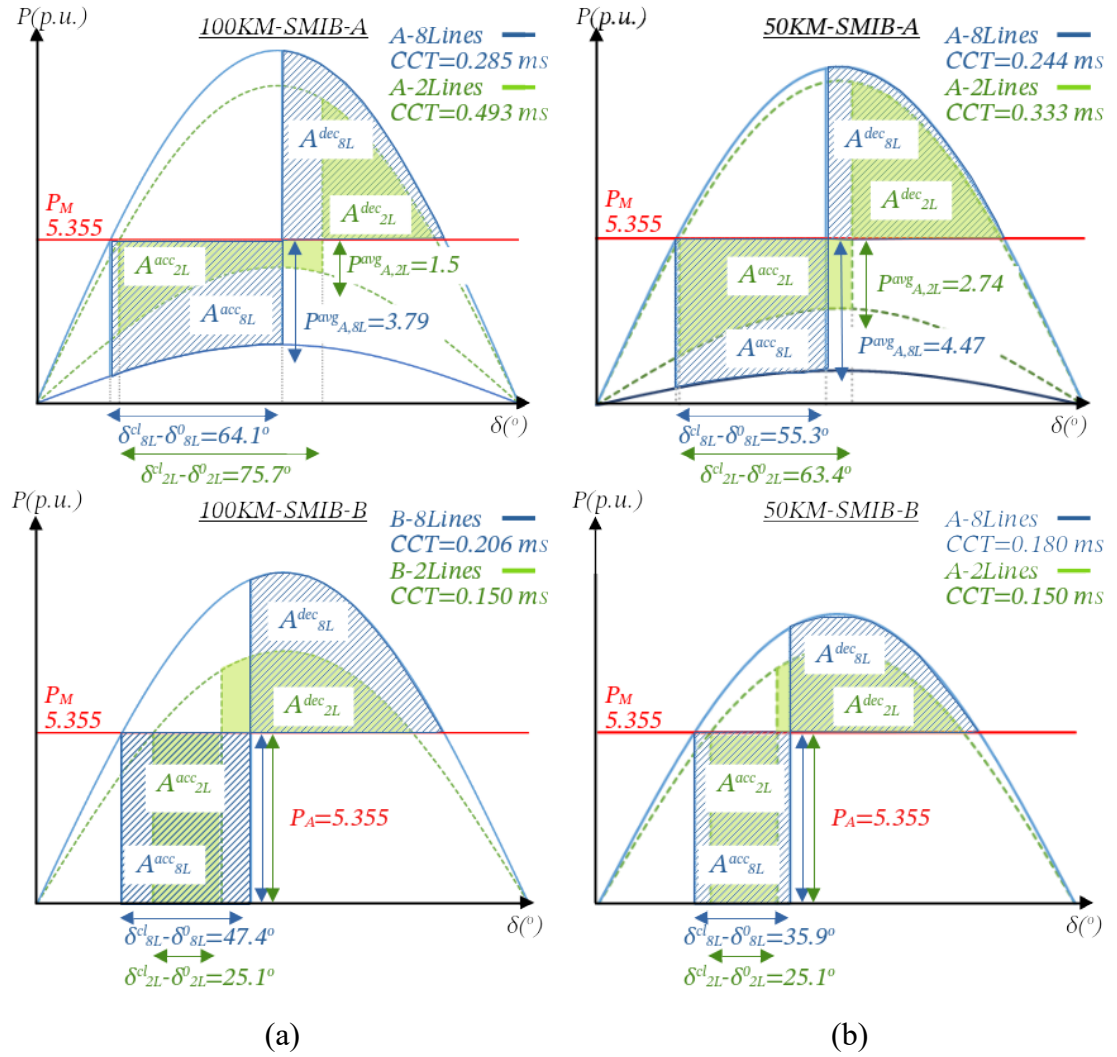


Figure 3.6: Power angle characteristics (in scale) of cases type A and B of the 100KM (a) and 50KM (b) SMIB test systems with 8 and 2 parallel lines.

The findings described above suggest that there are structural differences introduced by line-switching actions, which can have a positive impact on transient stability. Particularly, the impedance change between the SG and the fault location on busbar 3 produces a substantial difference, as shown for test cases with power transfer during the fault condition (non-radial connection Type A). Conversely, the reduction of impedance due to a shorter physical distance between busbars 2 and 3 (faults closer to the SG) negatively impacts transient stability for cases Type A and B. The following sections

comprehensively analyse the impedance between a generator and fault location and its influence on transient stability.

### 3.1.4 Impedance between a generator and fault location

A broader analysis must consider more test cases than those provided in the preliminary analysis of the previous section. For that purpose, eight more test cases are added to the 100KM-SMIB system and 50KM-SMIB system, which consider 4 and 6 parallel lines (2 and 3 double circuits) on the link between busbars 2 and 3 for case type A and B; the purpose is to demonstrate that discrete changes affecting the impedance can have a different effect on the transient stability response of the system. Table 3.5 includes all test cases used within this section. Prefixes 100KM and 50KM associate the test cases with their corresponding test system; letters A or B indicate the status of Line1 (type B is a radial connection with an outage on Line1), and the suffixes with the number of lines are related to the number of lines available in the transmission link between busbars 2 and 3.

Table 3.5 Test cases Type A and B of SMIB-Based test systems

Test Case	$x_{Eq}^{pre-fault}$ (p.u.)	$x_{Eq}^{fault}$ (p.u.)	$x_{Eq}^{ratio}$ (p.u.)	ZFG (p.u.)	CCT (s.)
100KM-A-2Lines	0.122	0.285	2.336	0.118	0.493
100KM-A-4Lines	0.114	0.410	3.596	0.104	0.344
100KM-A-6Lines	0.111	0.535	4.820	0.098	0.304
100KM-A-8Lines	0.109	0.659	6.046	0.095	0.285
100KM-B-2Lines	0.161	Inf	Inf	0.135	0.150
100KM-B-4Lines	0.135	Inf	Inf	0.109	0.189
100KM-B-6Lines	0.126	Inf	Inf	0.100	0.201
100KM-B-8Lines	0.122	Inf	Inf	0.096	0.206
50KM-A-2Lines	0.122	0.410	3.361	0.105	0.333
50KM-A-4Lines	0.118	0.659	5.585	0.095	0.272
50KM-A-6Lines	0.117	0.909	7.769	0.091	0.253
50KM-A-8Lines	0.116	1.158	9.983	0.089	0.244
50KM-B-2Lines	0.161	Inf	Inf	0.109	0.150
50KM-B-4Lines	0.148	Inf	Inf	0.096	0.170
50KM-B-6Lines	0.143	Inf	Inf	0.092	0.177
50KM-B-8Lines	0.141	Inf	Inf	0.090	0.180

As seen in the previous section, the transfer impedance ratio  $x_{Eq}^{ratio}$  can provide insight into the changes affecting pre-fault and during-fault transfer impedances with consequences on the power transfer capability; in practical terms,  $x_{Eq}^{ratio}$  provides information on the relative importance of the fault impedance with respect to the pre-fault impedance. Figure 3.7 shows the relationship between  $x_{Eq}^{ratio}$  and the CCT; it can be observed that cases type A have an exponentially-like decreasing relationship where

line-switching actions removing lines from service in the test system have a positive effect on transient stability, i.e., increasing the CCT; it can also be seen that the reduction of impedance due to a shorter physical distance between busbar 2 and 3 (100 to 50 km) increases  $x_{Eq}^{ratio}$ , which produces a reduction of CCT. Though it is not possible to assess the influence of line-switching action based on  $x_{Eq}^{ratio}$  for cases type B (radial connection), an increase in pre-fault impedance  $x_{Eq}^{pre-fault}$  shortens the CCT, which is negative from the transient stability perspective, with even worse results for test cases of the 50KM-SMIB test system.

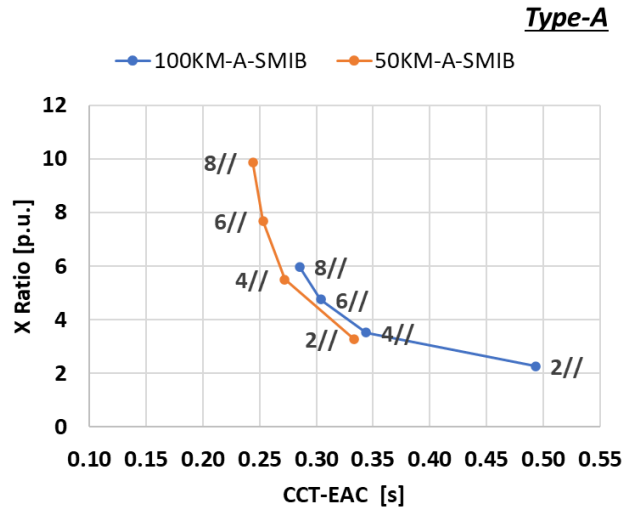


Figure 3.7: Transfer impedance ratio of cases type A of the 100KM-SMIB and 50KM-SMIB test systems.

In the context of the analysed line-switching actions, the characteristics of the fault and the network configuration of the system can make the fault to be “electrically” closer to the generator, which will make the system less stable; particularly, line-switching actions in a direct path (between the SG and fault location) have significant positive (or negative) effects depending on the structure of the transmission network. Based on the concept of electrical distance introduced in Section 2.2.3.1, the impedance between an SG and a fault location  $ZFG_{kj}$  (3.3) is an impedance-based metric that quantifies the magnitude of the Thevenin impedance between a generator node  $k$  and a fault location in node  $j$ ; in practical terms, it represents the magnitude of the electrical distance between a generator and a fault location considering all available parallel paths.

$$ZFG_{kj} = |Z_{kk} + Z_{jj} - 2Z_{kj}| \quad (3.3)$$

The effect of line-switching action on  $ZFG$  for each test case in Table 3.5, illustrated in Figure 3.8, shows a similar effect as the one seen for  $x_{Eq}^{ratio}$  and  $x_{Eq}^{pre-fault}$ ; there are radically different CCT responses for cases type A and B. In general, test cases type A

have better stability results with CCT values concentrated above 240 milliseconds, whereas for cases type B, CCT is below 210 milliseconds; therefore, it can be seen that radially connected cases type B are more critical from the stability viewpoint. In contrast to the tendency of  $x_{Eq}^{ratio}$  (see Figure 3.7), the  $ZFG$  of cases type A in Figure 3.8(a) exhibits a growing tendency, which implies that line-switching actions increasing  $ZFG$  have longer CCT. Similarly, in Figure 3.8(b) the  $ZFG$  of cases type B reveals a decreasing tendency implying that switching off lines reduces the CCT.

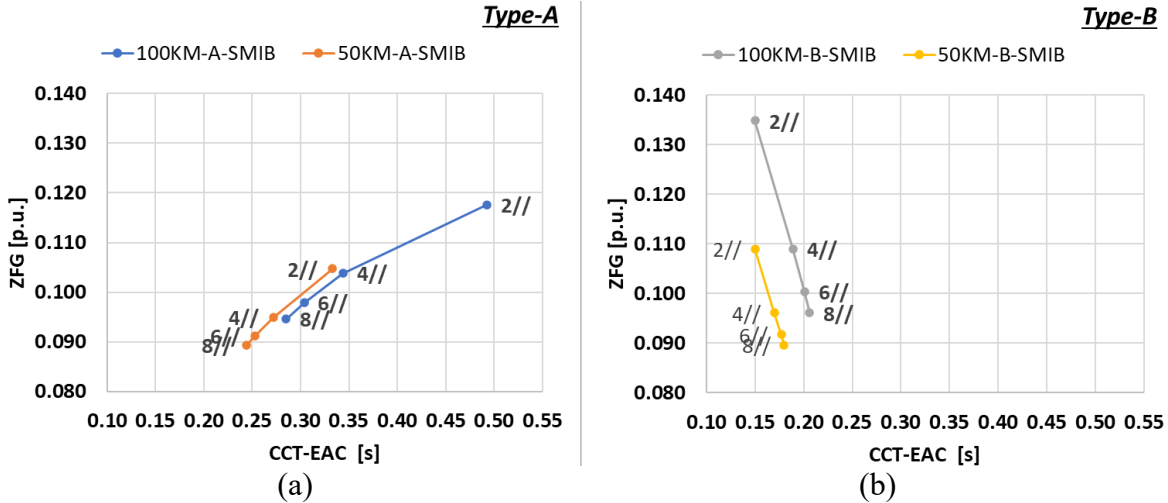


Figure 3.8:  $ZFG$  of cases type A (a) and B (b) of the 100KM-SMIB and 50KM-SMIB test systems.

From Figure 3.7,  $x_{Eq}^{ratio}$  may seem more useful to work as a predictor of CCT because the larger  $x_{Eq}^{ratio}$  it can be considered worse for transient stability. However, the main drawback of  $x_{Eq}^{ratio}$  with respect to  $ZFG$  is the fact that it is not possible to compare test cases type B with  $x_{Eq}^{ratio}$  because of infinite values, which conceals the effect of the impedance between the SG and fault location during the fault condition. A disadvantage of  $ZFG$  is the fact that for different type of cases it can have similar magnitudes with different CCTs; however, this inconvenience can be overcome by determining the type of the topology (meshed or radial) before the assessment with  $ZFG$ . Figure 3.8 indicates that an increase of  $ZFG$  can positively influence the stability for meshed networks (type A). Consequently, the selected impedance metric is  $ZFG$ ; therefore, subsequent analyses in this chapter use  $ZFG$  as the impedance-based proximity metric between the SG and the fault location.

### 3.1.5 Analysis of the effect of $ZFG$ with the aid of EAC

The EAC and CCT introduced in Section 1.3 serve as a theoretical basis for analysing the effect of line-switching actions on transient stability. In this section, examining the effect of  $ZFG$  on the stability results, combined with the factors affecting the CCT,

provides the tools to review the preliminary findings of the previous section. Furthermore, the additional test cases considering 4 and 6 parallel lines extend the preliminary analysis shown in Section 3.1.3.

The focus of the analysis is to illustrate the effect of discrete topological changes, given by line-switching action, increasing the number of lines in service in the transmission link between busbars 2 and 3. The effect can be observed by four factors (see Figure 3.9) with different magnitudes and units. Firstly, the average accelerating power  $P_A^{avg}$  provides an estimation of the difference between the mechanical power and electrical power output of the SG during the fault condition. Secondly, the difference between the critical and pre-fault angles  $\delta_{cr} - \delta_0$  gives an insight in the increase or reduction of the stability level. Thirdly, the CCT is used to assess the transient stability level of each test case; and finally, the *ZFG* can highlight the effect of the switching action on the electrical distance between the SG and the fault location. Particularly, the combination of the average accelerating power  $P_A^{avg}$  and angle difference  $\delta_{cr} - \delta_0$  gives insight into the growth of the accelerating area; the combination of these factors and the CCT equation (3.1) provide the building blocks of the assessment. For instance, a sharp growth of  $P_A^{avg}$  combined with a virtually constant  $\delta_{cr} - \delta_0$  account for a larger accelerating area; this will produce a smaller CCT due to the faster increase of the denominator with respect to the numerator in equation (3.1).

In particular, Figure 3.9(a)(c) shows test cases type A of 100KM-SMIB and 50KM-SMIB test systems. The figure reveals an overall decreasing tendency of *ZFG* when the number of lines in service increases, which is aligned with the reduction of the impedance of the transmission link between busbars 2 and 3. Conversely, the average accelerating power has an increasing trend, also increasing the accelerating area; however, the rapid increase of  $P_A^{avg}$  with a slowly decreasing  $\delta_{cr} - \delta_0$  reduces the CCT. For both test systems, *ZFG* and CCT have the same decreasing tendency, which suggests that for cases type A the larger electrical distance between the SG and the fault location provides longer CCT. Notably, for test cases with power transfer capability during fault conditions, a longer electrical distance *ZFG* helps to reduce the accelerating power  $P_A^{avg}$ , which means that for meshed networks switching-off transmission lines can improve the stability of the system.

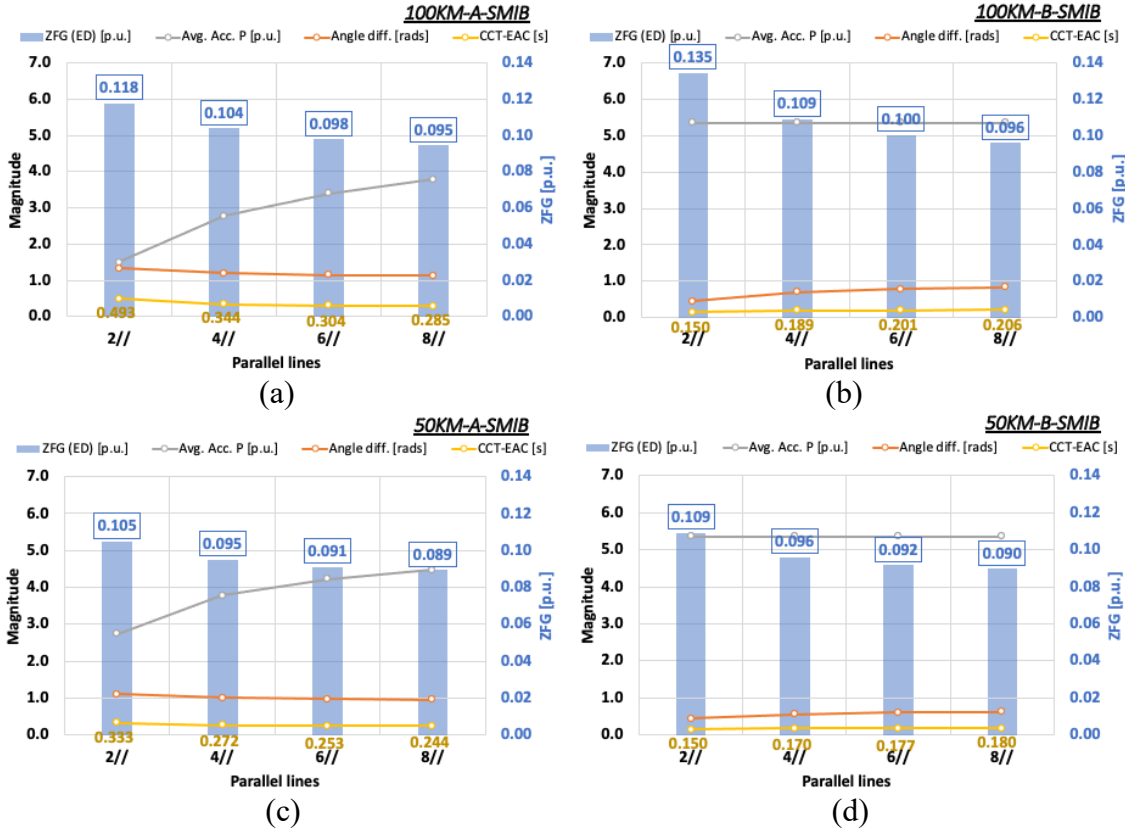


Figure 3.9: CCT factors and ZFG of cases type A (a)(c) and B (b)(d) of SMIB-based test systems with 2, 4, 6 and 8 parallel lines.

A different effect can be seen for test cases with the radial connection (type B in Figure 3.9(b)(d)); the fact that there is no other path for the current to flow produces a reduction of the electrical power output to zero, making the accelerating power  $P_A^{avg}$  maximum and equal to the turbine mechanical power of the SG. For cases type B, the increasing number of available lines reduces the impedance, which in time makes the decelerating area larger, increasing the CCT; in this case, a growing angle difference  $\delta_{cr} - \delta_0$  combined with a constant accelerating power  $P_A^{avg}$  produces longer CCT. In Figure 3.9(b)(d),  $ZFG$  exhibits a different trend in comparison to the CCT; the increase of available lines decreases the electrical distance from the generator to the fault location, whilst the CCT increases. In this case, an increase of  $ZFG$ , by reducing the number of lines in service, reduces the post-fault transfer capability and decelerating area; thus, the CCT diminishes, reflecting a reduction in the stability level. The result was expected for a radial connection between the SG and the infinite bus. This type of connection is not common in transmission networks; they are more likely found on distribution networks. As this thesis focuses on the topology of transmission networks, the analysis focuses on cases type A to provide relevant insight into the topological effect of the network structure on transient stability.



Notably, the comparison of *ZFG* and CCT between 100KM-SMIB (top row Figure 3.9) and 50KM-SMIB (bottom row Figure 3.9) test systems indicates that for all test cases the reduction of the impedance to the fault, due to a shorter physical link between busbars 2 and 3 (from 100 to 50 km), reduces the electrical distance *ZFG* and also reduces the CCT. Though the reduction of a physical link may not be considered a line-switching action, the evidence shows that the reduction of *ZFG* decreases the corresponding CCT; this fact confirms the idea that a shorter electrical distance between SG and fault location, due to shorter physical distance, can be considered adverse from the transient stability perspective. Notably, the effect of line-switching actions removing lines, typically considered harmful for transient stability, can improve stability under certain conditions (non-radial connections) by increasing the electrical distance between an SG and a fault location.

### 3.1.6 Verification of the effect of ZFG with the aid of TDS

The analysis based on the theoretical approach applying the EAC and CCT provides valuable insight into the effect of line-switching actions and structural changes of the transmission network on the impedance of the system and the subsequent impact on the stability level of the system. Analysing the effect under study by TDS offers a more detailed view of the implications of line-switching actions. Integrating mathematical models of power system components described in Section 2.1, like the sixth-order model of SG and AVR, provides a more realistic perspective of the impact of discrete structural changes on the system.

The effect of line-switching was analysed using three mathematical representations of the SG, implemented in the computational tools described in Section 2.5. In addition to the assessments of the stability level of test cases by the EAC-based CCT (see Figure 3.9), three additional evaluations of the CCT were computed using TDS results by increasing the complexity of the SGs modelling. Firstly, the second-order model was used in simulation to test the accuracy of the EAC-based CCT; secondly, the sixth-order model of SG, also called the standard model, was used to increase the level of detail of the modelling of SG; finally, the standard model was used in combination with AVR and governor to obtain a more realistic response, increasing the accuracy of the assessment of stability level by CCT.

CCT results with multiple SG models are shown in Figure 3.10. The figure illustrates the changes of *ZFG* by line-switching action in blue bars for test cases type A and B of both

SMIB test systems. Similarly, the figure shows the evaluations of CCT using EAC, classical model, standard model, and standard model with controllers in colours grey, orange, yellow and blue, respectively. In general, the comparison between CCT results based on EAC and TDS reveal a similar tendency, which implies that the rate of change of impedance due to switching is similar. The differences between CCT results for cases type B are almost identical, with at most 2 ms of difference, which is the reason for the overlap between orange and grey lines in Figure 3.10(b) and Figure 3.10(d).

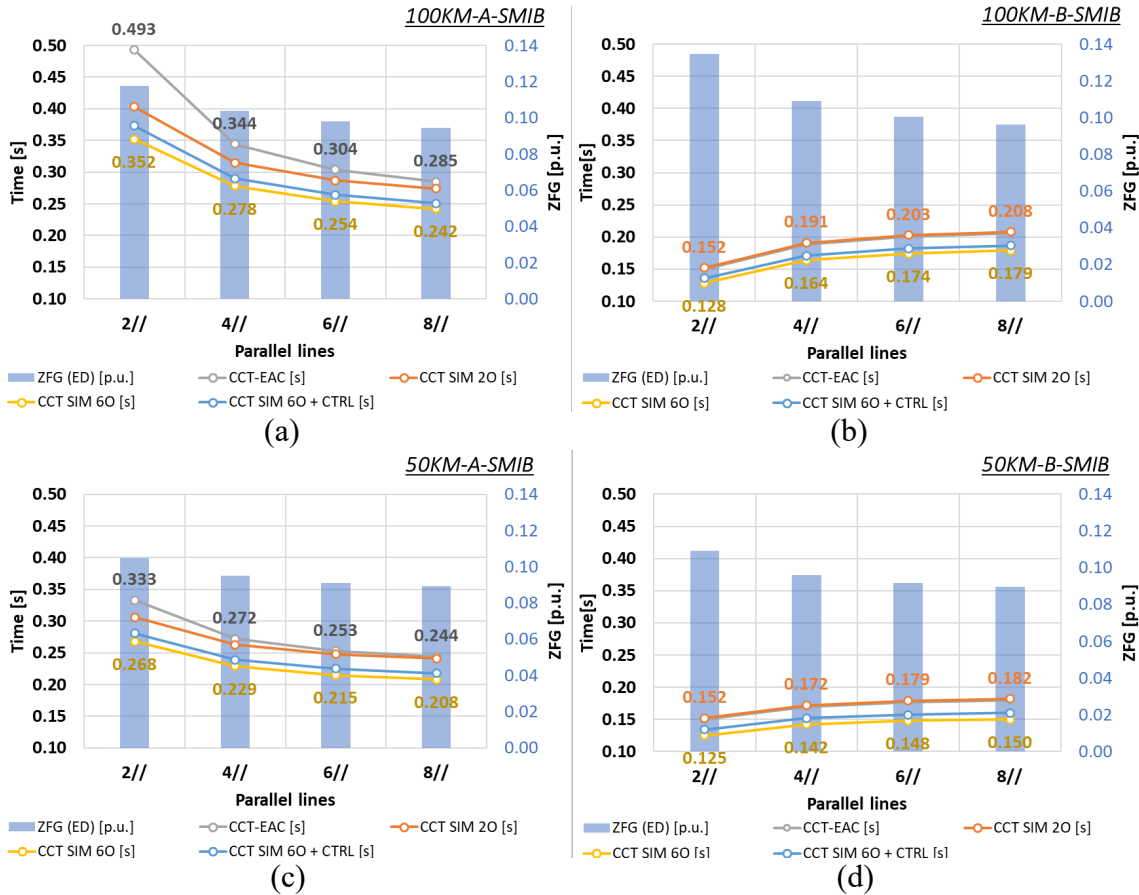


Figure 3.10: CCT-based stability level of cases type A (a)(c) and B (b)(d) of SMIB-based test systems with 2, 4, 6 and 8 parallel lines.

Overall, Figure 3.10 provides evidence that the tendency of CCT results related to line-switching actions found in the previous section using EAC-based CCT is highly similar to the assessments using TDS, based on the 100KM-SMIB system. In particular, simulation results confirm that for cases type A, increasing *ZFG* by line-switching produces longer CCTs, which improves the stability level. A different tendency was found for the radial connection of cases type B; however, those results are based on a radial connection which is less common in transmission networks.

Simulation results provide the dynamic response of the generator's variables, such as rotor angle and active power output. In particular, the results below were obtained using the sixth-order model representation of the SG, integrating AVR and governor control to

provide an accurate and realistic assessment. In addition, to study the stability during the first swing of each test case, the corresponding CCT was used as the simulation clearing time. Beginning with the study of rotor angle responses, Figure 3.11 illustrates the behaviour of the rotor angle considering step changes in the number of parallel lines in service (2 to 8) for cases type A and B of SMIB-based test systems.

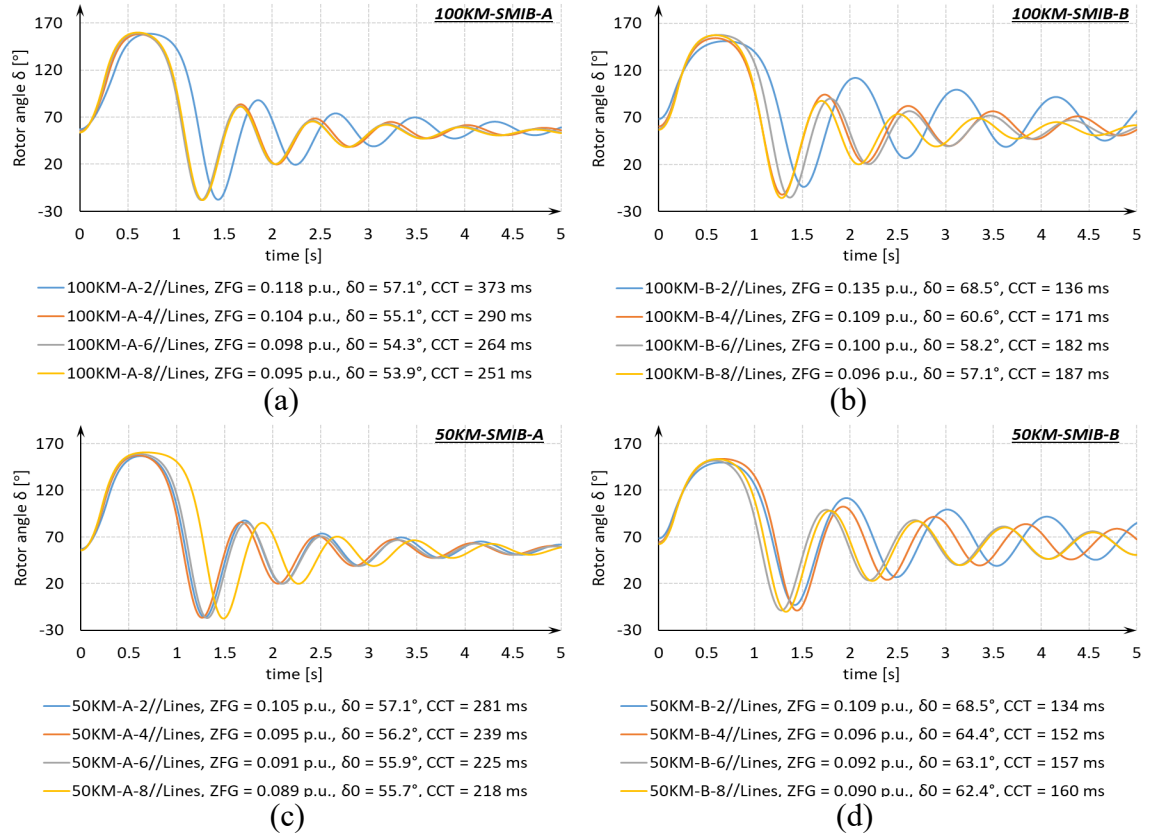


Figure 3.11: Generator rotor angles of cases type A (a)(c) and B (b)(d) of SMIB-based test systems with 2, 4, 6 and 8 parallel lines.

Along with the previously highlighted trend difference of CCT, there are three key differences between cases type A and B. Firstly, Figure 3.11 shows that cases type B have higher corresponding pre-fault rotor angles  $\delta_0$  in comparison with cases type A (e.g., test case A-2//Lines and B-2//Lines), which suggests that the network topology for case type A is better from the stability perspective even prior to the fault. Secondly, there is less damping in the rotor angle responses in cases type B, compared to cases type A, because the SG has been exposed to a larger accelerating power in cases type B. Finally, even though it can be seen as an overall trend that increasing ZFG causes an increase of  $\delta_0$ , simulation results indicate that within cases type A larger  $\delta_0$  have longer CCT. In particular, simulation results based on the SMIB test system suggest that larger  $\delta_0$  can produce longer CCTs which is counterintuitive. The key finding on the studied test cases is that initial conditions  $\delta_0$  are less influential than the transient conditions  $P_A^{avg}$  and  $\delta_{cr} - \delta_0$  for cases with power transfer during the fault condition, this aspect opens a

range of possibilities for using network switching as a preventive measure to improve transient stability. These key effects can be seen in test cases of the 100KM-SMIB system and the 50KM-SMIB system; though valid for the SMIB system under study, those effects must be studied for the particular network under analysis.

The final part of the study of generator variables considers the analysis of  $ZFG$  and the active power output of the SG. Figure 3.12 illustrates the effect of  $ZFG$  on the active power output immediately after the fault  $P_0^+$  in MW; the figure confirms the fundamental difference between cases type A and B in terms of active power transfer during the fault condition.

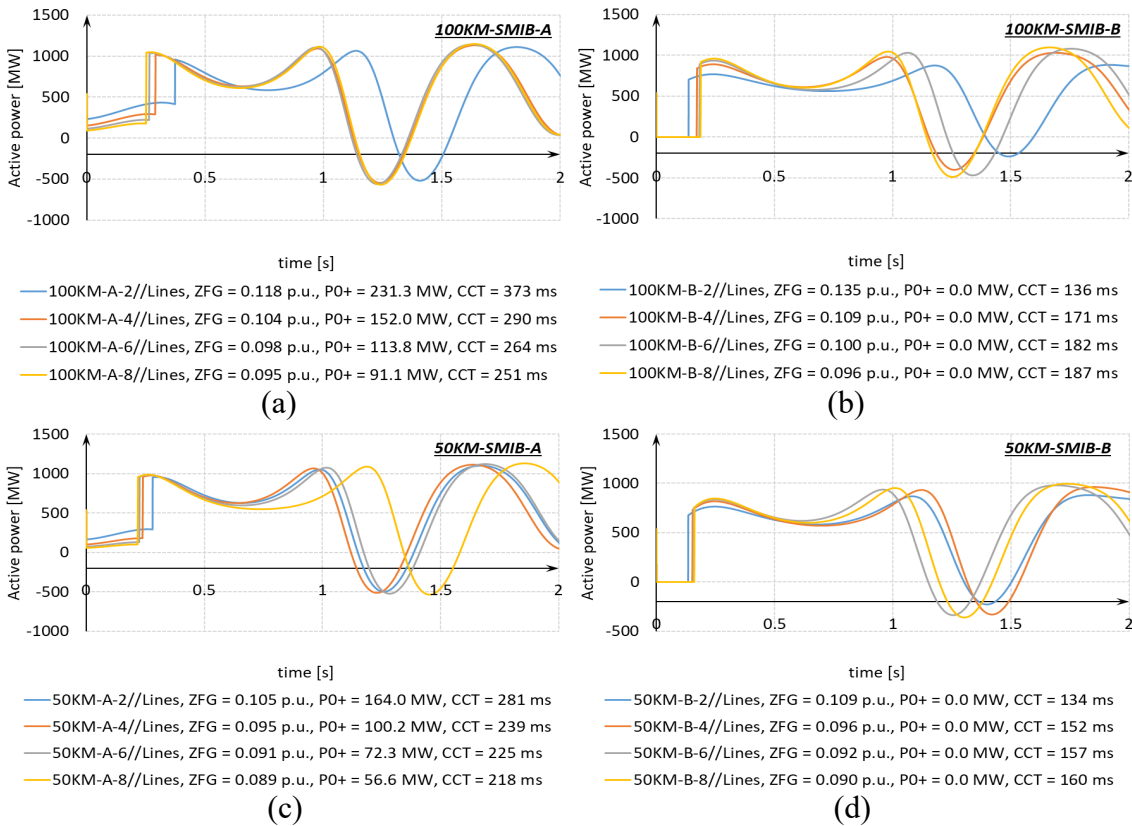


Figure 3.12: Generator active power output of cases type A (a)(c) and B (b)(d) of SMIB-based test systems with 2, 4, 6 and 8 parallel lines.

Considering both SMIB-based test systems, for cases type A, an increase of  $ZFG$  is negatively correlated with the during-fault transfer impedance  $x_{Eq}^{fault}$  (see Table 3.5); the reduction of  $x_{Eq}^{fault}$  related to the line-switching actions removing lines from service between busbars 2 and 3 causes the growth of  $P_0^+$ , which helps reducing the accelerating power. On the contrary, in cases type B, the increase of  $ZFG$  does not cause any effect on  $P_0^+$ , which is equal to zero making the accelerating power maximum and equal to the mechanical power input. Notably, the largest  $ZFG$  is correlated with the smallest  $x_{Eq}^{fault}$  providing the longest CCT, which reflect its positive impact on transient stability.

## 3.2 Effect of line-switching between generators on transient stability

### 3.2.1 AF9B modified test system and test cases

The multi-machine test system introduced in Chapter 2 of [17] was modified to study the impact of line-switching actions on impedance between SGs. Structural modifications of the Anderson and Fouad 9 bus test system (AF9B) are twofold; firstly, all physical distances (impedances) between busbars have been doubled; and secondly, all transmission links were changed to double circuits, except for transmission links between busbars 5 and 7 and between busbars 8 and 9, which have been modified to have triple circuits. In terms of generation, the test system includes three generating plants where  $G1$  is the reference machine.

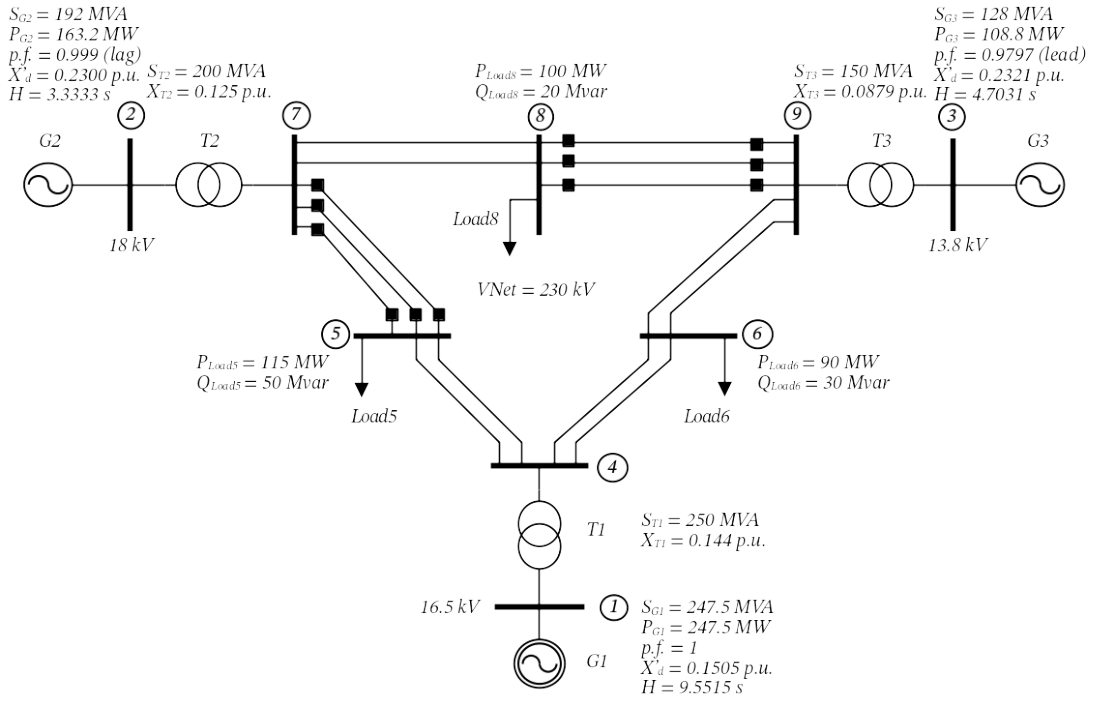


Figure 3.13: Modified AF9B test system

Notably, the introduced changes did not alter the impedance of the transmission links, which remain similar to the original test system; moreover, the definition of double circuits for each transmission link increases the redundancy, which is a traditional approach used in real networks. The network structure and other relevant details of the proposed variation of the Anderson and Fouad test system can be seen in Figure 3.13 and found in Appendix A.2.

Based on the AF9B test system, the study of the effect of line-switching action on the impedance between generators and its consequences on the stability of the system is presented. The approach considers the analysis of the transient stability level of the AF9B

test system by computing the CCT through time-domain simulations; for that purpose, generating plants include SGs represented using the sixth order model and equipped with the Mag-A IEEE Type 1 DC Exciter [17], described in Section 2.1.2.1. In particular, the dispatch of  $G2$  is 163 MW with a constant power factor of 0.999 lagging, whilst for  $G3$  is 108 MW with a constant power factor of 0.979 leading. Furthermore, the influence of increasing impedance between busbars 7 and 9 is analysed by simulating large disturbances in the form of three-phase self-cleared bolted faults in busbar 5.

In realistic meshed networks, line-switching actions can have a significant impact not only on the impedance between a generator and the fault location but also on the impedance between generators. Particularly, the test cases presented in this section provide the basis for analysing the effect of line-switching actions on transient stability. Though the focus is on the effect on the impedance between generators, test cases also address the effect between generators and fault location in a multi-machine environment.

Test cases in Table 3.6 reflect changes in the AF9B network, changing the number of available lines on transmission links between busbars 5 to 7 and busbars 7 to 9. Test case types A, B, and C are defined by the type of circuit in the link between busbars 5 and 7, which can be a triple, double, or single circuit, respectively. Moreover, test cases belonging to a case type are defined by switching actions reducing the number of lines between busbars 7 and 9, which can be done by reducing from 5 to 3 lines opening the circuit breakers up to 2 lines on the link between busbars 8 and 9. For instance, the test case AF9B-B-4Lines differs from the original AF9B network by line-switching actions removing from service one line on the link between busbars 5 and 7; and removing one line on the link between busbars 8 and 9.

Table 3.6 Test cases type A, B, and C of the AF9B test system

Test Case	Lines BB5 to BB7	Series Impedance between busbars 5 and 7			Lines BB7 to BB9	Series Impedance between busbars 7 and 9		
		$R$ (Ohm)	$X$ (Ohm)	$Z$ (p.u.)		$R$ (Ohm)	$X$ (Ohm)	$Z$ (p.u.)
A-5Lines	3	11.2853	56.7793	0.1094	5	8.6932	73.6368	0.1402
A-4Lines	3	11.2853	56.7793	0.1094	4	10.7916	91.4112	0.1740
A-3Lines	3	11.2853	56.7793	0.1094	3	17.0867	144.7344	0.2755
B-5Lines	2	16.9280	85.1690	0.1641	5	8.6932	73.6368	0.1402
B-4Lines	2	16.9280	85.1690	0.1641	4	10.7916	91.4112	0.1740
B-3Lines	2	16.9280	85.1690	0.1641	3	17.0867	144.7344	0.2755
C-5Lines	1	33.8560	170.3380	0.3283	5	8.6932	73.6368	0.1402
C-4Lines	1	33.8560	170.3380	0.3283	4	10.7916	91.4112	0.1740
C-3Lines	1	33.8560	170.3380	0.3283	3	17.0867	144.7344	0.2755

Using a common 100 MVA base, Figure 3.14 illustrates the impedance diagram of test case types (A/B/C-5Lines) having a constant number of lines between busbars 7 and 9 (5 lines), whilst the number of lines in service between busbars 7 and 5 is reduced from 3 to 1. The lines belonging to a transmission link are identical; therefore, the equivalent impedance is calculated by dividing the line impedance by the number of lines in service. In this setting, the impedance between generators  $G2$  and  $G3$  is constant, but the impedance between  $G2$  and the fault location increases. The figure shows a growth of 200% of impedance on the link connecting busbars 5 and 7, reducing the circuit from a triple to a single line.

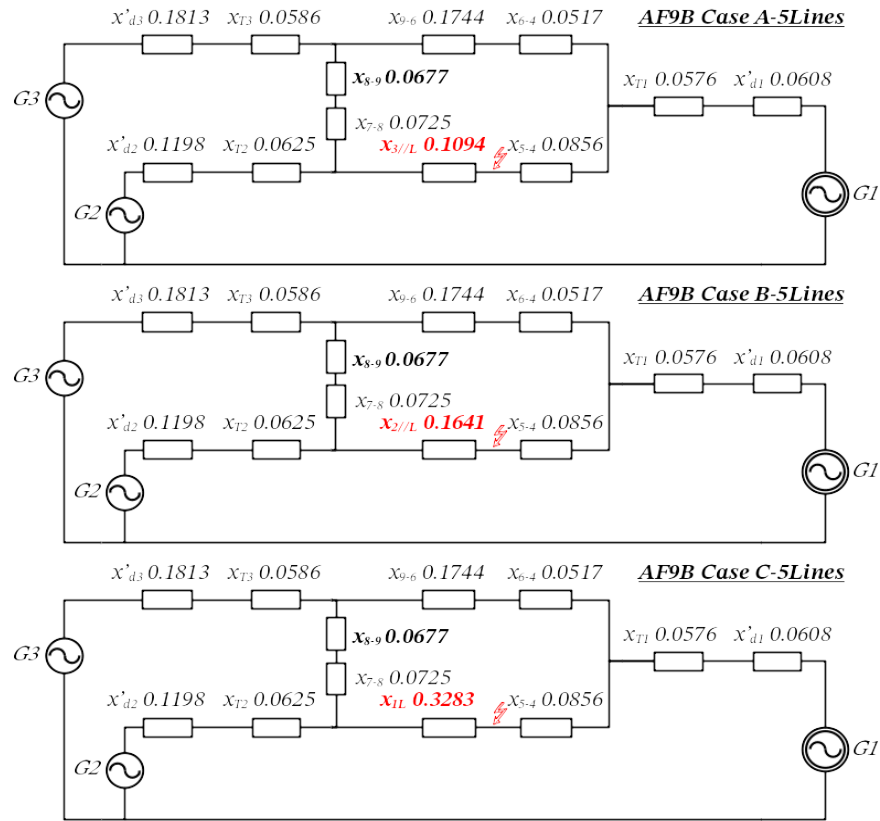


Figure 3.14: Impedance diagram of types A, B and C of the AF9B test system with 5 lines.

Test cases A-5Lines/4Lines/3Lines can be seen in Figure 3.15; in this figure, the impedance between generator and fault location is constant (type A with three lines in service between busbars 5 and 7), whilst the impedance between generators increases due to line-switching actions on the link between busbars 8 and 9; the series impedance between busbars 7 and 9 grows 96.5% when the number of lines on the transmission link decreases from 5 to 3. As described above, test cases are defined by the combination of line-switching actions; the detail of changes in impedance of each test case can be found in Table 3.6.

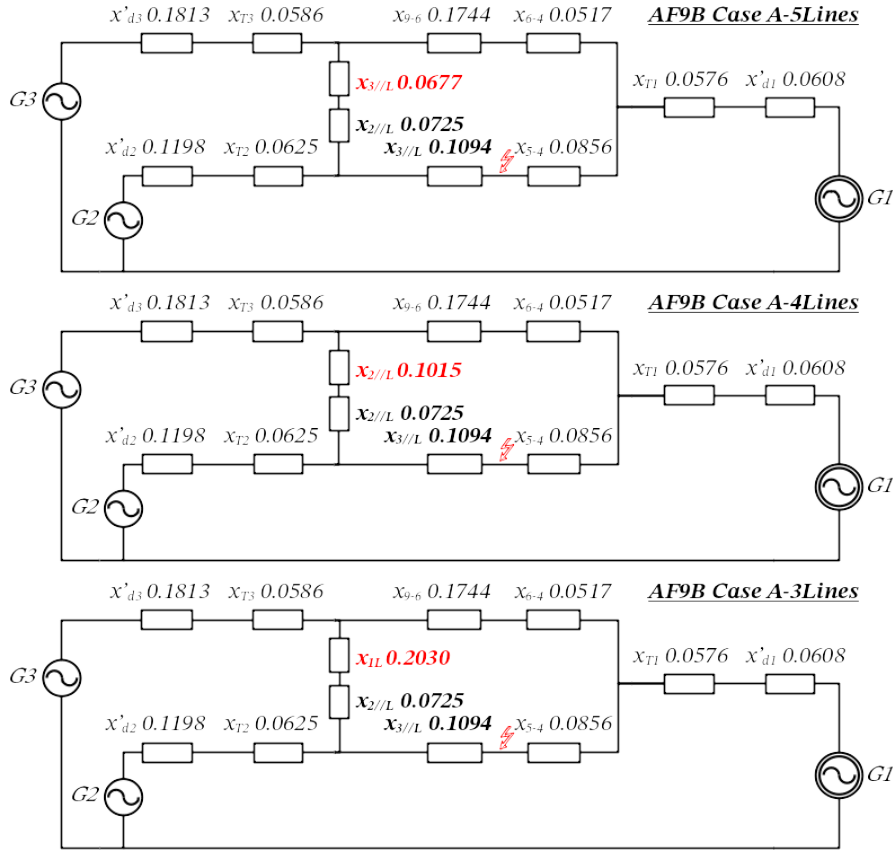


Figure 3.15: Impedance diagram of cases type A of the AF9B test system with 5, 4 and 3 lines.

### 3.2.2 Impedance between generators

The previous section describes the effect of discrete changes, such as line-switching actions, on impedances in the test system; in fact, combinations of those changes were used to define 9 test types/cases. With the main focus on the proximity between generators, this section applies two measures to quantify the effect of line-switching actions. First, based on the concept of electrical distance ( $ED$ ) introduced in Section 2.2.3.1, the impedance between generators  $ZBG(ED)$  (3.4) is an impedance-based metric that quantifies the magnitude of the Thevenin impedance between a generator internal node  $k$  and another generator internal node  $j$ ; in practical terms, it represents the magnitude of the electrical distance between a generators considering all available parallel paths.

$$ZBG(ED)_{k,j} = |Z_{kk} + Z_{jj} - 2Z_{kj}| \quad (3.4)$$

Similarly, using the series impedance-based graph representation and the concept of shortest path length ( $SPL$ ) introduced in Section 2.2.3, the  $ZBG(SPL)_{kj}$  (3.5) is the impedance of the path with the minimum sum of series impedances between one generator internal node  $k$  and another internal node  $j$ . Notably, in large and meshed networks the  $SP$  between two generators is typically unique and considers a limited



number of branch elements of the network; therefore,  $SPL$  focuses only on the path with the lowest impedance. This fact makes the  $ZBG(SPL)_{kj}$  less susceptible to non-relevant topological changes (changes in other parts of the network) in comparison to  $ZBG(ED)_{kj}$ .

$$ZBG(SPL)_{k,j} = \min_{paths\ k,j} \left\{ \sum_{pq \in path\ k,j} |z_{pq}| \right\} \quad (3.5)$$

Another relevant aspect is the relationship between  $SPL$  and the transient synchronising power coefficient  $K_S$  (1.6), repeated below for clarity. As the computation of  $SPL$  identifies the path with lowest impedance between two nodes of a network, the identified path (shortest path) is the circuit with the largest influence on the magnitude of  $K_S$ . In cases where two paths have similar and low impedance, the computation of  $ZBG(SPL)_{kj}$  can identify the impedance of the most significant path in terms of synchronising power between generators; particularly, any change in the path with the lowest impedance will produce significant changes in  $K_S$ , and consequently in the ability of the system to maintain synchronism.

$$K_S = \left. \frac{\partial P_{E'}}{\partial \delta'} \right|_{\delta'=\delta'_0} = \frac{E' \times V_{Inf}}{x_{Eq}} \cos \delta'_0$$

Depending on the location, the impact of line-switching actions on multi-machine systems like the AF9B can change the topology affecting SGs in different ways. Particularly, switching actions can impact not only the relative distance between generators  $ZBGs$ , but also the distance between each generator and the fault location  $ZFGs$ . Here, using simple network metrics, the impact of line-switching can be quantified by impedance-based proximity metrics between generators  $ZBG(ED)$  (3.4) and  $ZBG(SPL)$  (3.5), and the metric between generators and the fault location  $ZFG$  (3.3). For instance, the effect of line-switching actions of a few test cases shown in Figure 3.16. The figure illustrates the effect of increasing the impedance between busbars 7 and 9 using  $ZBG$  based on  $ED$  (3.4) and  $SPL$  (3.5) in orange and green colour, respectively; additionally, Figure 3.17 shows the effect of increasing the impedance between busbars 5 and 7 using  $ZFGs$  between  $G2$  and  $G3$  to busbar 5 in yellow and grey colour, respectively. In particular, Figure 3.16 illustrates how the proximity measures based on  $ZBG(ED)$  (3.4) and  $ZBG(SPL)$  (3.5) increase due to switching-off lines between busbars 7 and 9, which reflect a longer distance between generators; furthermore, the evidence indicates that the magnitude of the total series impedance is larger than the Thevenin

impedance between  $G2$  and  $G3$ , especially for case with large impedance such as the one with only 3 lines in service between busbars 7 and 9.

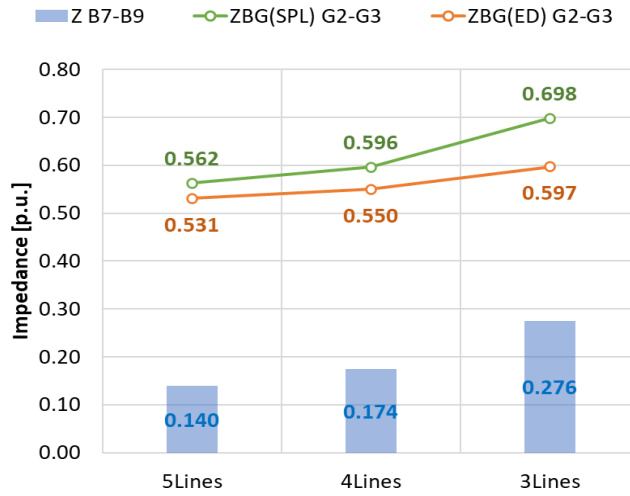


Figure 3.16: Impedance-based proximity metrics between generators: ZBG(SPL), ZBG(ED), and impedance between busbars 7 and 9 of the AF9B test system.

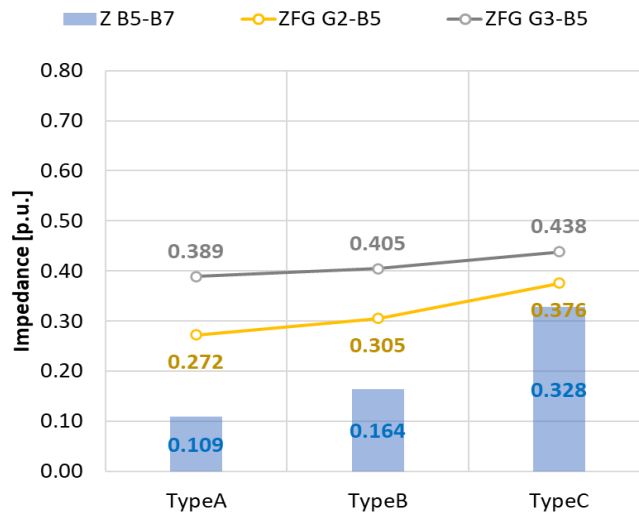


Figure 3.17: Impedance-based proximity metrics between generators and fault location: ZFG from  $G2$ , ZFG from  $G3$ , and impedance between busbars 5 and 7 of the AF9B test system.

Furthermore, Figure 3.17 shows a growing  $ZFG$  between  $G2$  (and  $G3$ ) and the fault location on busbar 5 by switching-off lines between busbars 5 and 7, which defined test case types (A-B-C); the figure indicates that removing lines increases the distance between SGs and fault location. Finally, the comparison between ZBG and ZFG metrics (see Figure 3.16 and Figure 3.17) reveals that for the AF9B network, the magnitude of the impedance between generators is larger than the impedances between generators and the fault location, which can result in different stability results when combining line-switching actions in the system; the details of the effect of different magnitudes is described in the following sections.

In the context of the small system under analysis, a preliminary analysis of the effect of  $ZBG(ED)$  and  $ZBG(SPL)$  reveals that line-switching actions increasing the impedance

between generators can be considered harmful from the stability perspective. Comparing CCT of test cases with 3 and 5 Lines in service, between busbars 7 and 9, shown in Figure 3.18, results in a reduction of at least 50 ms when two lines are removed, which increases the impedance between generators and deteriorates the stability of the system.

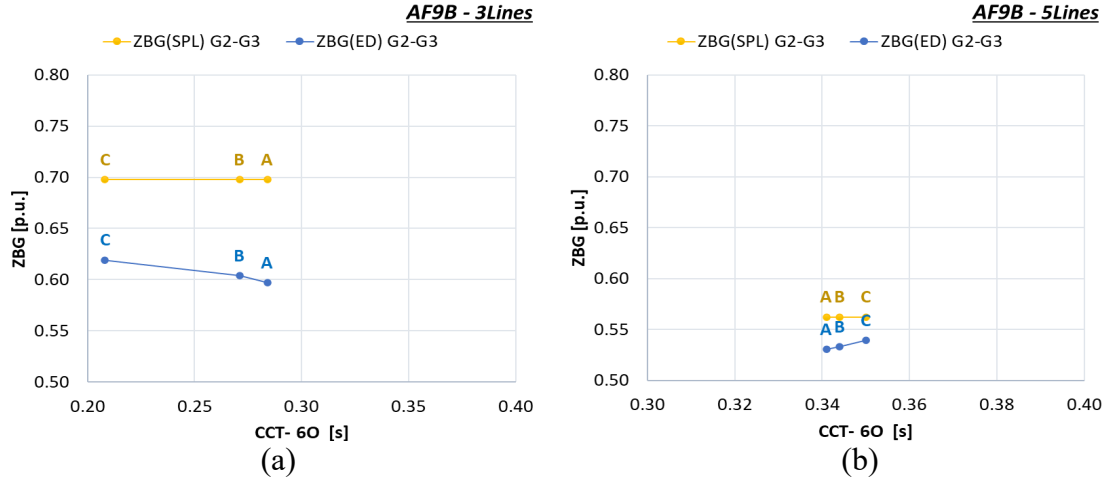


Figure 3.18:  $ZBG(ED)$  and  $ZBG(SPL)$  for cases with 3 Lines (a) and 5 Lines (b) between busbars 7 and 9 of the AF9B test system.

Figure 3.18 also reveals that  $ZBG(SPL)$  varies only due to changes on the path with the lowest total impedance between  $G2$  and  $G3$ , whilst  $ZBG(ED)$  varies due to switching actions on different parts of the network.  $ZBG(SPL)$  remains constant because it is affected only by changes on lines between busbar 7 and 9, whereas  $ZBG(ED)$  varies due to changes in the transmission link between busbars 5 and 7 defining types of test cases (A-B-C). This fact shows an advantage of the  $SPL$  method over the  $ED$  because  $ZBG(SPL)$  is able to avoid potential errors induced by changes in network locations that are irrelevant for the analysis of the impedance between generators. Even though this observation is based on a small test system (AF9B), a more comprehensive analysis in Section 5.4.5.2 based on a realistic test system confirms the benefits of the  $SPL$  method. As  $ZBG(SPL)$  can be considered a more reliable computation method, and it will be used in the remainder of the chapter denoted as  $ZBG$ .

### 3.2.3 Analysis of ZBG based on AF9B with the aid of TDS

Though defined in the context of SMIB systems and based on the classical model of SGs, the transient synchronising power coefficient can be used as a conceptual approach to analyse the effect of line-switching actions on the stability of the AF9B test system. The transient synchronising power coefficient  $K_S$  (1.6) affects the provision of synchronising torque immediately after the fault, which helps to avoid aperiodic drifts. According to the definition of  $K_S$  in [21], the influence of the network is accounted by the equivalent

impedance  $x_{Eq}$ , which consider series impedance of branch elements including the SG d-axis transient reactance. As shown in Figure 3.19, repeated below for clarity, an increase of  $x_{Eq}$  reduces the maximum  $K_S$  diminishing the synchronising component of the electrical torque; in practical terms, generators electrically closer to the infinite bus in a SMIB system will have larger synchronising torque improving first-swing stability. Moreover, changes in the network may also increase the pre-fault rotor angles, which can also reduce the provision of synchronising torque, shown as the difference between  $K_S(01)$  and  $K_S(02)$  in Figure 3.19.

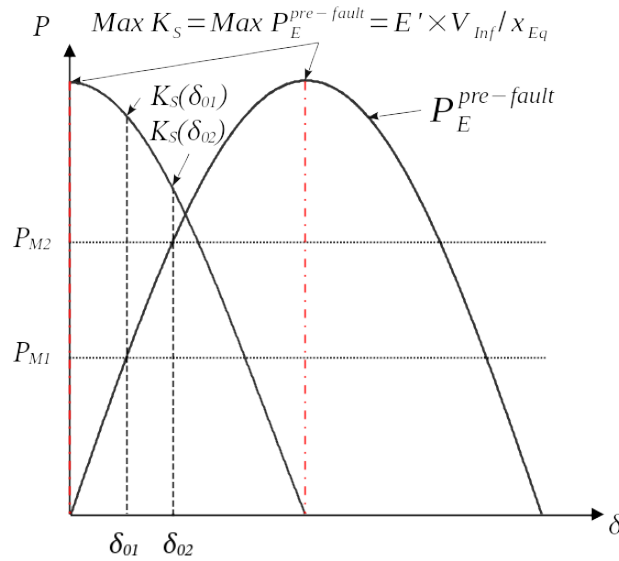


Figure 3.19: Transient synchronising power coefficient and power-angle characteristic (adapted from [21])

In multi-machine systems, the transient stability is measured in terms of the relative rotor angle separation, known as coherence [36]; a higher coherence implies a larger synchronising power enabling rotor angles to remain close to each other during a large disturbance. Even though the transient synchronising power coefficient  $K_S$  in (1.6) is strictly valid for SMIB systems and the classical model, the concept can be used to explain the change in the level of synchronising torque provided to a given SG by a neighbouring generator(s) in multi-machine systems due to a change in the equivalent impedance between them; an increase of  $ZBG$  between a pair of SGs will reduce the synchronising torque between them lowering the coherence level, which diminishes the stability level of the entire system.

The effect of increasing  $ZBG$  is confirmed by simulation results representing the SGs with the standard model (sixth-order). Figure 3.20(a) illustrates CCTs based on TDS results for test cases with 5, 4 and 3 lines between busbars 7 and 9 in grey, green, and orange, respectively. Moreover, Figure 3.20(b) shows the effect of  $ZFG$  for a fault

condition in busbar 5. The evidence, shown in Figure 3.20(a), confirms that the increase of  $ZBG$  reduces the stability level. The figure indicates that test cases with three lines between busbars 7 and 9 have the highest  $ZBG$  and shortest CCTs; on the contrary, cases with 5 lines have at least 50 ms longer CCT with 19.4% smaller  $ZBG$ . Results associated with each test case can be found in Table 3.7.

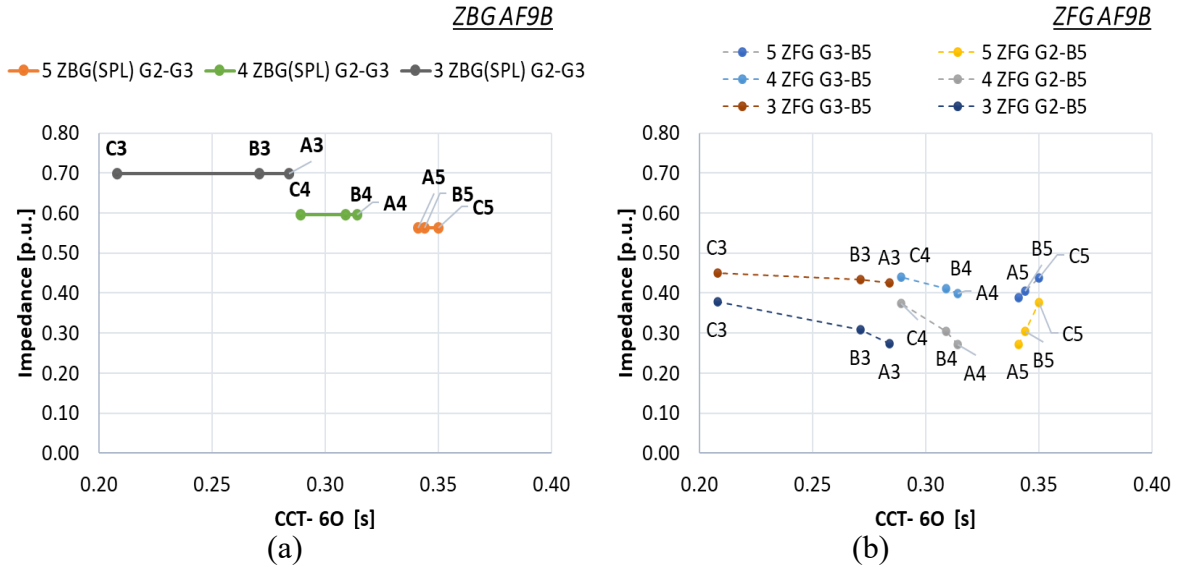


Figure 3.20:  $ZBG(SPL)$  (a) and  $ZFG$  (b) of test cases of the AF9B test system.

Notably, combined line-switching actions on busbars 5-7 and 8-9 have a different impact on CCTs. On the one hand, for the lowest value of  $ZBG$  (test cases 5Lines A5, B5, C5), the effect of the impedance between fault and generators  $ZFG$  has a similar impact on CCTs as the one seen in Section 3.1.5, where larger  $ZFG$  was found beneficial for transient stability. On the other hand, for higher  $ZBG$  (test cases A4, B4, C4 and A3, B3, C3), the effect of increasing  $ZFG$  is detrimental from the stability viewpoint. Though observations suggest a consistent effect of  $ZBG$ , a combination of transient stability factors, analysed later in Section 5.4, is required to improve the accuracy of the assessment. The comparison between the magnitudes of  $ZFG$  and  $ZBG$  in Figure 3.20 reveals that  $ZBG$  is always larger than  $ZFG$ ; however it is also possible to observe that small changes in  $ZFG$  have a large influence on CCT (slopes). In particular, for the AF9B test cases, the  $ZBG$  overcomes the effect of  $ZFG$ , changing how  $ZFG$  influences the stability behaviour. The analysis of combined effects of  $ZBG$  and  $ZFG$  suggest that an adequate balance is needed to harness the best possible line-switching action to enhance the stability of the system.

The details associated with each test case can be found in Table 3.7. The table contains topological information of test cases concerning the  $ZBG$  between G2 and G3,  $ZFG$  between SGs and a fault location on busbar 5. Moreover, the table includes the CCTs in

seconds based on TDS for SGs represented with and without AVR, as CCT TDS and CCT TDS wAVR, respectively.

Table 3.7 *ZBG* and *ZFG* of test cases type A, B, and C of the AF9B test system

Test Case	ID	Lines BB5 to BB7	Lines BB7 to BB9	<i>ZBG</i> G2-G3 (p.u.)	<i>ZFG</i> G2 (p.u.)	<i>ZFG</i> G3 (p.u.)	<i>CCT</i> TDS (s.)	<i>CCT</i> TDS wAVR (s.)
A-5Lines	A5	3	5	0.562	0.272	0.389	0.341	0.356
B-5Lines	B5	2	5	0.562	0.305	0.405	0.344	0.363
C-5Lines	C5	1	5	0.562	0.376	0.438	0.350	0.377
A-4Lines	A4	3	4	0.596	0.272	0.398	0.314	0.327
B-4Lines	B4	2	4	0.596	0.306	0.412	0.309	0.326
C-4Lines	C4	1	4	0.596	0.375	0.439	0.289	0.313
A-3Lines	A3	3	3	0.698	0.274	0.425	0.284	0.295
B-3Lines	B3	2	3	0.698	0.308	0.435	0.271	0.285
C-3Lines	C3	1	3	0.698	0.378	0.451	0.208	0.231

In particular, the combination of switching-off lines between busbars 5 and 7, whilst maintaining the original number of lines between busbars 7 and 9, i.e., Case C-5Lines in Table 3.7 (C5 in Figure 3.20), has the best stability performance; the effect can be understood as an improvement of stability level by increasing the impedance between generators and fault location, whilst maintaining the impedance between generators. From a more general perspective, Chapter 5 includes a broader analysis of the combined effect of both network metrics based on a more realistic system, such as the IEEE-68Bus test system.

### 3.2.4 Verification of the effect of *ZBG* with the aid of TDS

The effect of line-switching actions on the impedance between generators was studied using the standard mathematical representations of the SG (sixth-order model) implemented in the computational tools described in Section 2.5. Though the analysis is focused on the effect of *ZBG*, for completeness it also considers the effect of *ZFG*. Similar to the study of the effect of *ZFG*, TDS results considering a fault in busbar 5 were used to analyse the effect of *ZBG* between *G2* and *G3*; to analyse the first swing stability behaviour, the corresponding CCT was used as clearing time for each test case.

The assessment of the stability level of test cases included two types of evaluations of the CCT using TDS results. The first group of results was obtained using the standard model to focus on the response based only on generator parameters, and the second group of results considered the effect of voltage control action by including the Mag-A IEEE Type 1 DC Exciter [17] described in Section 2.1.2.1. The two groups of simulation-based CCT results, presented in Figure 3.21, illustrate the effect of *ZBG*. The blue bars

represent the magnitude of  $ZBG$  for a given number of lines in service between busbars 7 and 9; similarly, data points in yellow colour represent the CCT results using the standard TDS model, whilst the data points in orange colour correspond to results integrating voltage control action to the standard TDS model.

Regardless of the test case type, i.e., level of  $ZFG$ , there is a consistent effect of  $ZBG$  on stability, as seen in Figure 3.21. The figure reveals that the effect of line-switching actions involving an increase of the impedance between SGs is detrimental to transient stability; the effect can be corroborated with and without the influence of AVRs. The evidence suggests that the improvement given the AVR effect is almost constant among different test cases with 5, 4 or 3 lines within each test type (A, B, C); however, there are more significant improvements in CCT due to control action for cases of test type C. For test cases type C, there is a combination of smaller voltage drop but longer  $ZFG$ ; the voltage drop is rapidly corrected by the AVR, which is beneficial for the first swing stability, but it increases the oscillatory behaviour of later swings, as explained in Section 1.3.7 and seen in Figure 3.22(a)(b).

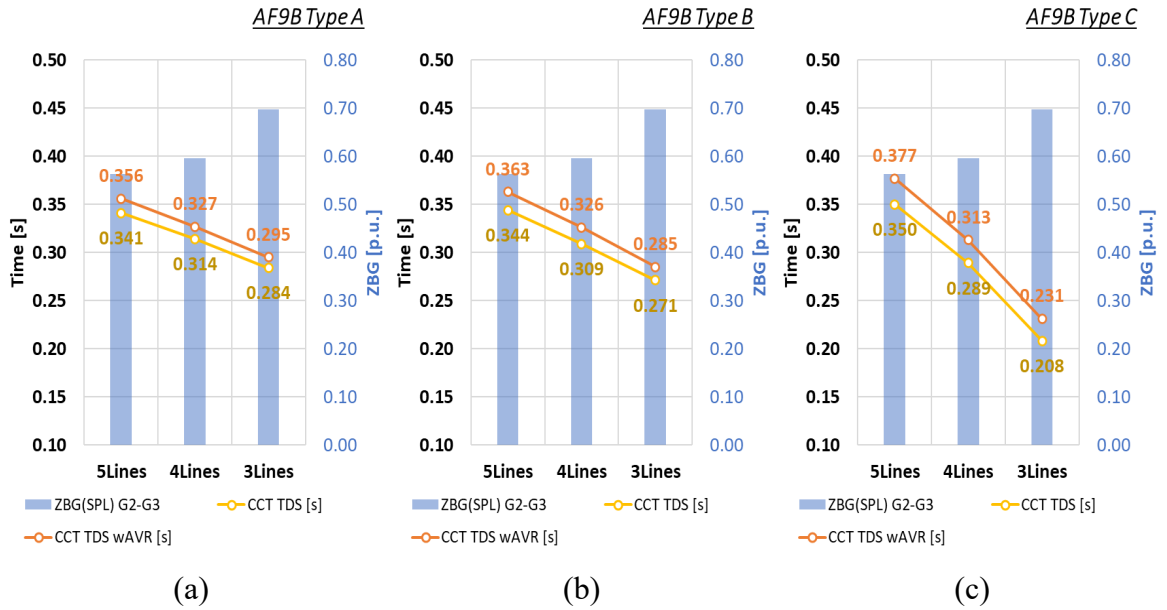


Figure 3.21: Simulation-based CCTs of test cases type A(a), B(b), and C(c) of the AF9B test system.

A broader study of the effect of discrete topological changes on  $ZBG$  considers the analysis of dynamic responses of SGs reflected in two key variables: rotor angle and active power output. Beginning with the study of rotor angle responses, Figure 3.22 illustrates the responses of test cases type A in Figure 3.22(a)(b) and type C in Figure 3.22(c)(d), with a different number of lines in service between busbars 7 and 9; particularly, test cases with 5, 4, and 3 lines are coloured in grey, orange and blue, respectively. Moreover, Figure 3.22(a)(c) shows rotor angle responses for  $G2$  and  $G3$

with continuous and dashed lines, respectively; whilst Figure 3.22(b)(d) illustrates the deviation between rotor angles using the difference  $\delta^{G2}(t) - \delta^{G3}(t)$ .

The evidence shows a consistent effect of line-switching action increasing  $ZBG$  reduces the coherence level of the system, which means that larger  $ZBG$  reduces the ability to maintain rotor angle responses closer together; more specifically, the comparison between cases with 5 and 3 lines shows an increase of rotor angle deviation of 84.79% and 92.12% for cases type A and C, respectively. Additionally, from  $ZFG$  perspective, it can be seen that cases type C have a higher oscillatory behaviour compared to cases type A; this is related to the combination of the AVR effect and higher impedance for cases type C. The effect of the combination of  $ZBG$  and  $ZFG$  on rotor angles indicates that smaller  $ZBG$  and larger  $ZFG$  provides the smallest rotor angle difference between  $G2$  and  $G3$ , which gives the best stability result with longer CCT.

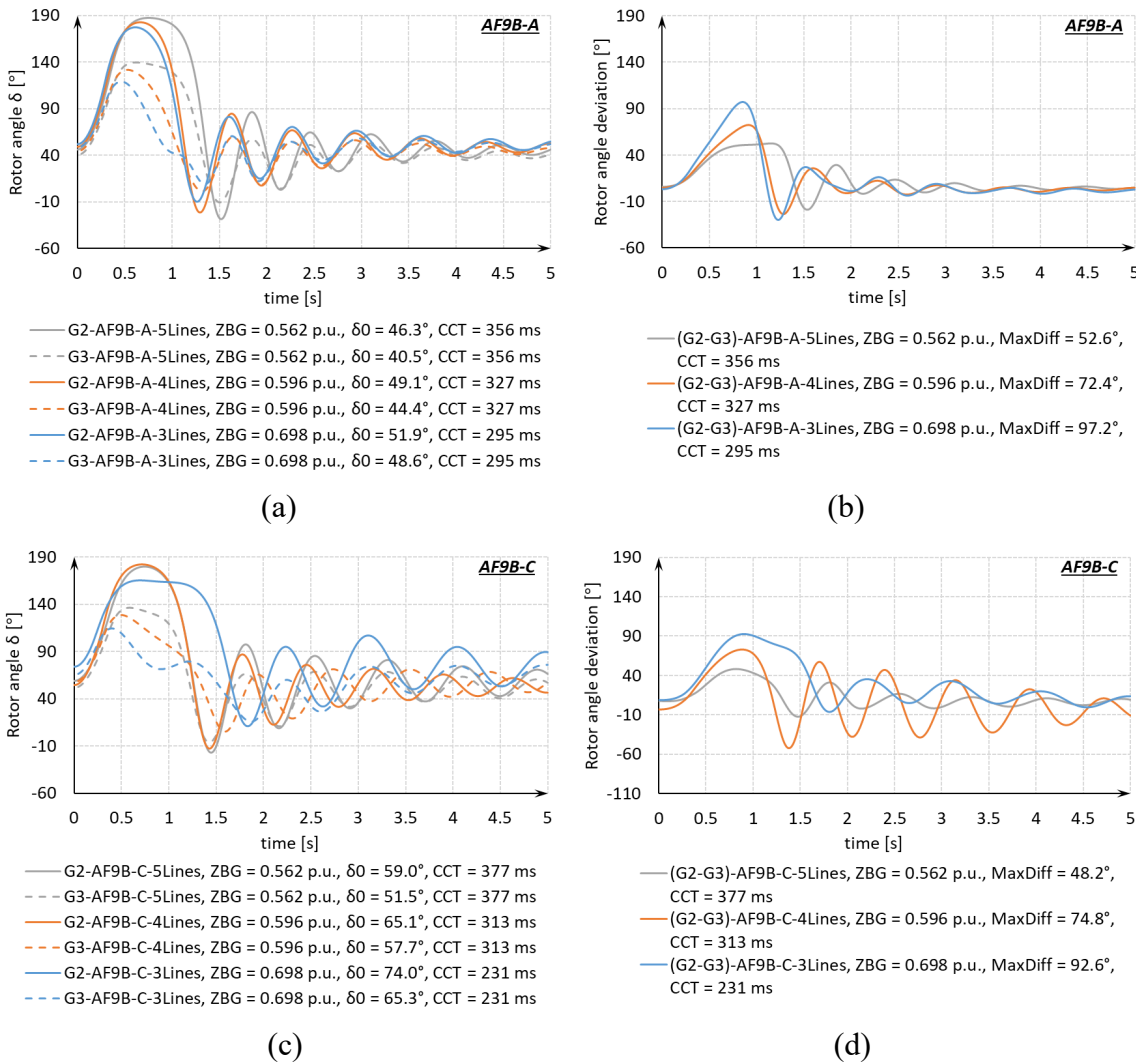


Figure 3.22: Generator rotor angles of cases type A (a)(b) and C (c)(d) of the AF9B-based test systems with 3, 4, and 5 lines.



Following the investigation of generator variables, the effect of  $ZBG$  and  $ZFG$  on the active power output of  $G2$  and  $G3$  is depicted in Figure 3.23 in the form of power-angle curves. Based on simulation results related to  $G2$ , Figure 3.23(a)(c) illustrates active power output as a function of the rotor angle for test cases with different  $ZBG$ , grouped by cases type A in Figure 3.23(a) and type C in Figure 3.23(c); particularly, test cases with 5, 4, and 3 lines in service between busbars 7 and 9 are coloured in grey, orange and blue, respectively. The same applies to simulation results of  $G3$  in Figure 3.23(b)(d).

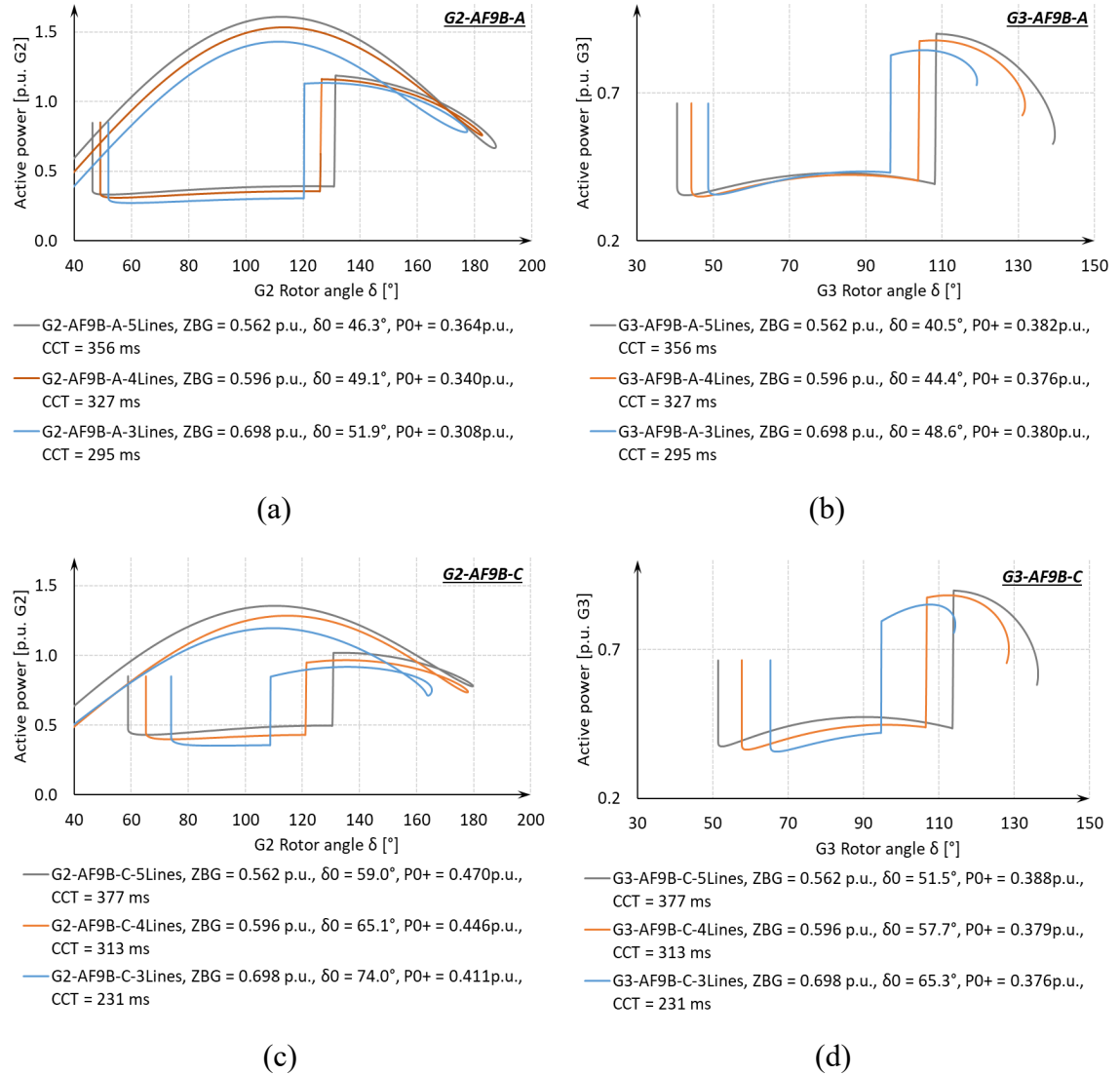


Figure 3.23: P-delta curves of  $G2$  and  $G3$  for test cases type A (a)(b) and C (c)(d) of AF9B-based test systems with 3, 4, and 5 lines between busbars 7 and 9.

The evidence consistently suggests that line-switching actions increasing  $ZBG$  reduce the active power injection from SGs during the fault; this fact is particularly true for  $G2$ , with larger drops of  $P_0^+$  in comparison to  $G3$  for both test types (see Figure 3.23(a)(c)). The lower active power injection during faults reinforces the influence of  $ZBG$  on the provision of synchronising power, which is smaller due to the increase of impedance between generators; in fact, the smaller active power injection during faults increases the

accelerating power, which is detrimental from the stability perspective. Moreover, the combination of higher  $\delta_0$  with bigger *ZBG* reducing the synchronising effect reduces the CCT, which is the consequence of a smaller capacity of the system to absorb the kinetic energy stored in the generator during the fault; the reduction of potential energy is reflected in the corresponding reduction of the accelerating area  $A^{acc}$  in Figure 3.23(a)(c). A similar effect can be seen for *G3* (see Figure 3.23(b)(d)), but in smaller magnitude because it is electrically further away from the fault location in busbar 5, i.e., *G3* has larger *ZFG* in comparison to *G2* (see Figure 3.20(b)).

From the *ZFG* viewpoint, line-switching actions increasing the impedance between SGs and the fault location (cases type C have larger *ZFG* in comparison with type A) reduces the active power drop during the fault condition, which is consistent with the findings described in Section 3.1.6. Aligned with the findings above, the combined effect of *ZBG* and *ZFG* on the active power output suggests that the line-switching action reducing *ZBG* and increasing *ZFG* have larger  $P_0^+$  and better active power transfer during the fault condition, which produces a longer CCT.

### 3.3 Summary

This chapter studied the effect of line-switching actions on the impedance of the transmission network by using two impedance-based proximity metrics: the first is the impedance between generators and the fault location, whilst the second is between generators. The impedance-based metrics provide insight into the effect of discrete topological changes on the transient stability level. Furthermore, the study involved the specification of two test systems and test cases to describe and demonstrate the switching action effect on the impedance of specific transmission links and how it affects transient stability.

The first study included in this chapter analysed the effect of line-switching actions on the stability of a SMIB test system; particularly, the use of EAC and CCT allowed the assessment of the transient stability impact for changes in the impedance between a generator and a fault location. In the context of the analysed SMIB system, the study of a network structure that allowed active power transfer during the fault revealed that switching actions, removing circuits from service, between the generator and fault location increased the CCT. Though it sounded contradictory at first, the increase in impedance, removing parallel circuits between the SG and fault location, produced a

56.7% reduction of the transfer impedance during the fault condition, resulting in a longer CCT. Moreover, the initial study using the classic model of SG showed that structural changes could positively impact transient stability, especially if those changes diminish the average accelerating power, decreasing the accelerating area. Furthermore, it was found that the impedance increase between a generator and a fault location can be accurately measured by an impedance-based proximity measure called ZFG. Even though the positive effect of increasing ZFG by line switching actions cannot be guaranteed based only on observations using small test systems (SMIB and AF9B), it was found a consistent effect of ZFG on both test systems, which suggests that the effect can apply in different network structures. A study based on a realistic test system is presented in Chapter 5, confirming the positive effect of increasing the impedance between generators and fault location.

The finding relating to the increase of ZFG and better transient stability results were confirmed by TDS using different SG models, including AVR and governor control. Simulation results showed that increasing the electrical distance between an SG and a fault due to physical change or line-switching action improved the stability of the system with longer CCTs for all SG models. Furthermore, simulation results of test cases with active power transfer during the fault condition showed that even though the increase of ZFG produces larger pre-fault rotor angles, the increase of electrical distance to the fault reduced the accelerating area, overcoming the effect of the pre-fault condition. The effect of ZFG was also analysed from the active power perspective; simulation results also showed that increasing ZFG reduces the active power drop immediately after the fault, which confirms the reduction of accelerating area increasing the CCT.

The second part of the chapter included the study of the impact of line-switching actions on the transient stability of a modified version of the Anderson and Fouad 9 bus system (AF9B), which contains three generators; particularly, the purpose was to analyse the impact of switching actions on impedance between generators. A comparison between the two computation procedures to calculate the impedance between SGs revealed that the impedance-graph-based shortest path length provided better accuracy because it focuses only on the lowest impedance path; hence, it was selected as the proximity-based impedance metric to calculate the impedance between SGs (ZBG).

The initial study of the effect of ZBG on the transient stability of the AF9B showed that line-switching actions increasing the impedance between generators has a detrimental

effect. On the contrary, increasing the impedance between SGs and fault location whilst reducing the impedance between SGs provided the largest CCT. The initial finding was confirmed by TDS using the SG sixth-order model, with and without AVR. Simulation results revealed a consistent detrimental effect of line-switching actions increasing ZBG; in fact, the results showed the largest CCT for the combination of the largest ZFG and smallest ZBG, which is the network structure with the best transient stability performance for the analysed fault condition. Furthermore, further evidence of the negative effect of the largest ZBG was shown with the level of coherence; the maximum difference between rotor angles increased by at least 84%, which reveals a significant detriment of transient stability. Moreover, the effect was also corroborated with plots showing active power as a function of rotor angle; the analysis revealed that as ZBG increases, the active power drops immediately after the fault grow, with a corresponding reduction of CCT.

In summary, the relevant studies performed with the SMIB and AF9B verified that line-switching actions increasing ZFG are beneficial from the transient stability viewpoint; similarly, the studies confirmed that the increase in ZBG has a detrimental stability effect. Furthermore, theoretical and TDS results corroborate both effects based on switching actions.

Particularly, the contributions of the present chapter are:

- *Identification and definition of impedance-based proximity metrics to evaluate the effect of line-switching actions on the impedance of a transmission network. In particular, ZFG and ZBG have not been used before to evaluate the topological effect of the network structure on the transient stability behaviour of power systems.*
- *Quantitative analysis of the effect of line-switching actions on the impedance between generators and fault locations, as well as between generators, with further implications on transient stability based on small test systems; this was done by confirming the quantitative effects of ZFG and ZBG on transient stability using TDS in the context of small-size test systems.*

## **4 Modelling Framework for Transient Stability Preventive Control via Rescheduling and Switching**

---

The previous chapter demonstrated the positive effect of line-switching actions on transient stability in the context of small test systems. The findings provided insight to formulate an optimisation problem that uses the concept of line switching as a measure that can improve transient stability, although that stability benefits can be counterintuitive at first. In particular, this chapter presents an optimisation framework to minimise generation production costs whilst meeting stability and security constraints. The framework introduces a cost functional subject to base-case and N-1 algebraic security constraints, along with transient stability constraints in the form of dynamic equations and stability limits for all credible fault locations, which can be applied to the base-case network and N-1 networks. Within the framework, line-switching actions are used as binary (discrete) controls to change the topology and improve the transient stability response of the system in the presence of large disturbances.

This chapter includes four parts. Firstly, the proposed framework's starting point is the description of the classical multi-machine model with the reduced network for transient stability analysis. Secondly, a detailed explanation of a new model for transient stability assessment called the classical multi-machine model with structure-preserving network and network switching; the new model enables to study of the impact of different topologies on the transient stability performance of a power system. Thirdly, a study of transient stability indicators to determine the most suitable to define stability limits. Finally, a general dynamic optimisation model is proposed as an optimum power flow

with transient stability and security constraints; the objective functional is the minimum operation or bid costs appended with the potential cost of unsupplied demand. The objective is subjected to system security and transient stability constraints based on binary variables.

#### 4.1 Classical multi-machine model for transient stability analysis

For transient stability studies focusing on the first swing, an overview of a multi-machine system is depicted in Figure 4.1 [17][22]. The model includes internal generator nodes indexed  $i$  or  $j = 1, 2, \dots, NG$ , where  $NG$  is the number of generators; the model considers the classical representation of SGs, introduced in Section 1.3.1. The network has different types of nodes, such as transition nodes and loads; particularly, load nodes are indexed  $m = 1, 2, \dots, NL$ , where  $NL$  is the number of loads. The transmission system box in Figure 4.1 represents passive branch elements connecting various nodes in the network, whilst only internal generator nodes and load nodes are extracted. In transient stability studies, all physical quantities are often related to the positive-sequence network because only three-phase faults, the worst-case scenario, are considered [22].

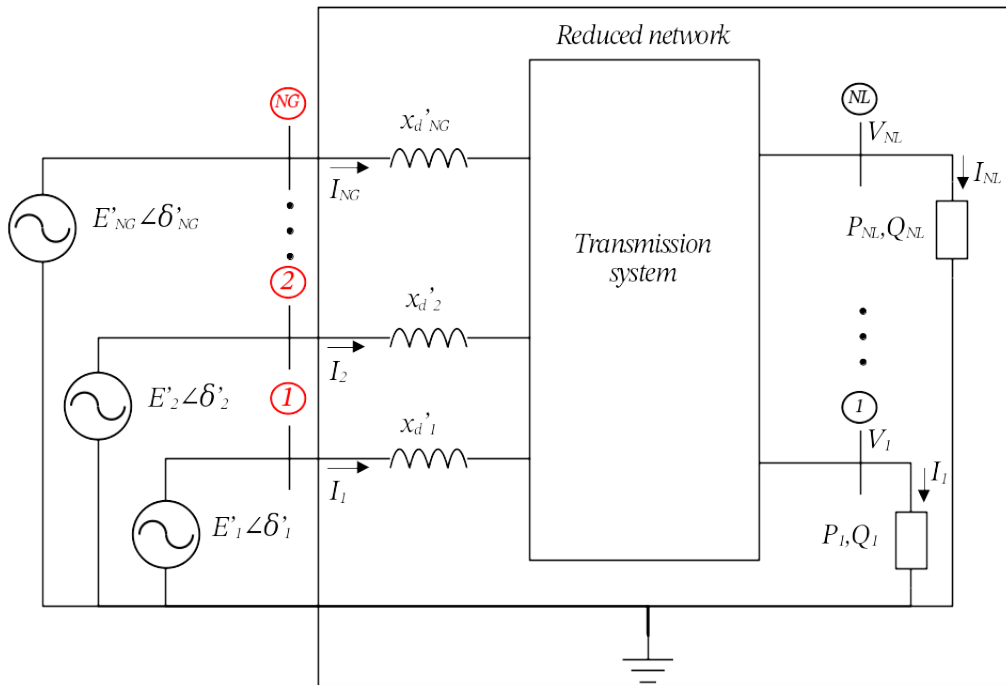


Figure 4.1: Multi-machine system with network reduction (adapted from [17])

#### 4.1.1 Network modelling and reduction

In transient stability studies, the loads can be represented as passive impedances allowing them to be integrated as shunt admittances, which are constant through the transient period [17]. With the classical model, internal transient reactances and loads can be easily included in the admittance matrix; besides, after node elimination, the network is reduced only to the internal generator nodes resulting in the so-called reduced network [17][23]. A method of network formation and reduction considers the following steps [17][181]:

- i. All network data are converted to p.u. values using base voltage levels and a single MVA base.
- ii. The loads are converted to equivalent shunt admittances using the load-flow solution of the pre-disturbance condition. Assuming the complex voltage  $V_m$  at node  $m$  is known from a load-flow solution, with active power  $P_m$  and reactive power  $Q_m$  as input load data, the load admittance  $Y_m = G_m + jB_m$  can be derived. The shunt admittance  $Y_m$  representing the constant impedance can be obtained using (4.1) [17]

$$Y_m = \frac{P_m - jQ_m}{V_m^2} \quad (4.1)$$

- iii. The internal EMF of generators can also be calculated using the load-flow results in the pre-disturbance state. The transient rotor angle  $\delta'_i$  of the generator connected to node  $i$  (i.e. angle of the internal voltage) can be computed with respect to the terminal voltage  $V_i \angle \alpha_i$ . Using the expression for the complex current  $I = (P - jQ)/V^*$ , it is possible to compute the phasor  $E'_i \angle \delta'_i$  (4.2) for each generator in the system.

$$E_i \angle \delta'_i = (V_i + Q_i x'_{d,i}/V_i^*) + j(P_i x'_{d,i}/V_i^*) \quad (4.2)$$

Here,  $x'_{d,i}$  is the direct axis transient reactance of generator  $i$ .

- iv. The system admittance matrix must be calculated for each network condition defined by loads, transmission line statuses and generator's availability. Particularly, the direct axis transient reactance is used to connect generators to the network through the series impedance of the form  $x'_{d,i} + x_{Ti}$ , where  $x_{Ti}$  is the impedance of the step-up transformer of generator  $i$  [23].
- v. Finally, the procedure to obtain the reduced network is described as follows, assuming that the network has only generation and load nodes [181]:

- a) All branch and load impedances are converted into admittances.
- b) The self-admittances  $Y_{ii}$  of the  $Y_{bus}$ , are the summation of all series and shunt admittances connected to node  $i$ ; and non-diagonal (mutual) admittances  $Y_{ij}$  are the negative values of the series admittances connecting nodes  $i$  and  $j$ . The matrix  $Y_{bus} \in \mathbb{C}^{(NG+NL) \times (NG+NL)}$  includes all network load nodes and generation internal nodes.
- c) In the last step, the entire network is partitioned into two clusters:
  - The first contains all internal generation nodes; there are  $NG$  such nodes,
  - The second contains all the rest of the original nodes; there are  $NL$  such nodes accounting for load and transition nodes.

The complex admittance matrix (2.12) can be written in the compact form:

$$\begin{bmatrix} I_{NG \times 1} \\ 0_{NL \times 1} \end{bmatrix} = \begin{bmatrix} Y_{NG \times NG} & Y_{NG \times NL} \\ Y_{NL \times NG} & Y_{NL \times NL} \end{bmatrix} \begin{bmatrix} V_{NG \times 1} \\ V_{NL \times 1} \end{bmatrix} \quad (4.3)$$

Where  $I_{NG \times 1}$  correspond to the current injections at internal generator nodes and  $0_{NL \times 1}$  is related to original nodes without external current injection, including load nodes, which are converted into shunt admittances. By expanding (4.3), it is possible to eliminate  $V_{NL \times 1}$ , which gives voltage-current relationship between  $NG$  internal generator nodes.

$$I_{NG \times 1} = (Y_{NG \times NG} - Y_{NG \times NL} Y_{NL \times NL}^{-1} Y_{NL \times NG}) V_{NG \times 1} \quad (4.4)$$

Here, the matrix  $Y_{bus}^r = (Y_{NG \times NG} - Y_{NG \times NL} Y_{NL \times NL}^{-1} Y_{NL \times NG})$  is the reduced admittance matrix  $Y_{bus}^r \in \mathbb{C}^{NG \times NG}$ , which contains only internal generator nodes.

After the reduction, the power network can be represented by a network structure having only  $NG$  generator internal nodes; these nodes are highlighted in red in Figure 4.1.

#### 4.1.2 Classical multi-machine model with network reduction

According to [22], the classical power system representation for a multi-machine system is restricted to the period immediately after the fault. The model enables the representation of  $NG$  generators in a set of generators  $\Omega_g$ ; the dynamics of the generators indexed by  $i = 1, \dots, NG$  are given as follows:

$$\frac{2H_i}{\omega_r} \frac{d\omega_i}{dt} + D_i \omega_i = P_{Mi} - P_{Ei}(\cdot) \quad (4.5)$$



$$\frac{d\delta_i}{dt} = \omega_i - \omega_r$$

The assumptions and parameters of the model have been explained in detail in Section 1.3.1.

When the entire transmission network has been reduced, using the method described in Section 4.1.1, the electrical power output of generator  $i$  in an  $NG$ -machine system, is given by the following expression [17]

$$P_{Ei}(\cdot) = E_i^2 G_{ii}^r + \sum_{\substack{j=1 \\ j \neq i}}^{NG} E_i E_j Y_{ij}^r \cos(\theta_{ij}^r - \delta_{ij}); \forall i, j \in \Omega_g$$

$$P_{Ei}(\cdot) = E_i^2 G_{ii}^r + \sum_{\substack{j=1 \\ j \neq i}}^{NG} E_i E_j [B_{ij}^r \sin(\delta_{ij}) + G_{ij}^r \cos(\delta_{ij})]; \forall i, j \in \Omega_g$$
(4.6)

Here,  $\delta_{ij}$  is the rotor angles difference  $\delta_i - \delta_j$ ;  $Y_{ij}^r = G_{ii}^r + jB_{ii}^r = Y_{ii}^r \angle \theta_{ii}^r$  and  $Y_{ij}^r = G_{ij}^r + jB_{ij}^r = Y_{ij}^r \angle \theta_{ij}^r$ , are driving point admittance and negative transfer admittance of the complex matrix of the reduced network  $Y_{bus}^r$ , respectively.

Notably, prior to the disturbance ( $t = 0^-$ ), the steady state condition of (4.5) is given by (4.7) for each generator; the subscript “0” denotes the pre-fault condition, which applies to network parameters  $Y_{ij0}^r$ , i.e., pre-fault network topology, and generator rotor angles  $E_{i0} \angle \delta_{i0}$  [17][35]. The inclusion of network changes on admittance matrices are explained in detail in Section 2.3.

$$P_{Mi0} = E_{i0}^2 G_{ii0}^r + \sum_{\substack{j=1 \\ j \neq i}}^{NG} E_{i0} E_{j0} Y_{ij0}^r \cos(\theta_{ij0}^r - \delta_{ij0}); \forall i, j \in \Omega_g$$
(4.7)

## 4.2 Classical multi-machine model for transient stability with structure-preserving network and switching

The multi-machine system introduced in Section 4.1 relies on the representation of constant impedance loads, which are included in the admittance matrix and later reduced to build the reduced network  $Y_{bus}^r$ . Though convenient to diminish the complexity, the network reduction suppresses the network's topology; therefore, the reduction hides the role of structural aspects in stability assessment [162][161]. Structure-preserving

network models date from the 1980s and have been scarcely used for stability analysis, mainly because they were used in transient energy function methods [162][161], which are known to have high complexity because they require information about unstable equilibrium points. In particular, the novelty in the proposed framework is the integration of line-switching actions in the context of transient stability assessment using a structure-preserving network model.

#### 4.2.1 Structure-preserving network model

Similar to the network definition in Section 4.1.1, the power network can be represented by  $NG + NL + 1$  nodes or buses connected by lossless transmission lines, as shown in Figure 4.2. The transmission system can be modelled by the node admittance matrix  $Y_{bus}$ . The first  $NG$  nodes are generator terminal nodes with busbar  $NG + 1$  as the reference; these nodes are indexed with  $gi$  or  $gj = 1, \dots, NG + 1$ . The remaining  $NL$  nodes are load buses, which are indexed by  $dm$  or  $dn = NG + 2, \dots, NG + NL + 1$ . Figure 4.2 illustrates the generator internal EMFs where  $E'_{gi} \angle \delta'_{gi}$  is the voltage phasor of the  $i$ -th generator; similarly,  $V_{dm} \angle \varphi_{dm}$  is the voltage phasor at the  $dm$ -th load bus. All angles are measured relative to the reference node  $NG + 1$ , which has an angle  $\vartheta_{NG+1} = 0^\circ$ , and voltage magnitude  $V_{NG+1} = 1 \text{ p.u.}$

In terms of branch elements, the network contains several branches connecting pairs of buses; therefore, considering only transmission lines, it is possible to define a set of branches  $\Omega_l$ , where branches are indexed  $(dm, dn) = 1, \dots, L$ , with  $L$  transmission lines. This definition implies that there is a map that uniquely relates a line index with the pair of load buses connected by the given line. As seen in Figure 4.2, each generator is connected to the system through a fictitious lossless transmission line indexed  $(gi, dm) = 1, \dots, NG$  in the set generator lines  $\Omega_{gl}$ , with reactance  $x'_{dgi} + x_{Tgi}$  combining the transient reactance of the generator  $gi$  and the reactance of the corresponding step-up transformer. An overview of the component of the model can be seen in Figure 4.2. In particular, busbars connected to the HV side of the transformers are the corresponding point of connection of each generator; these buses are considered “load” nodes, as shown later in Figure 4.3.

One of the fundamental differences between the reduced network and the model presented in this section is the load model. For instance, the work presented in [162] uses a linear model to represent the loads as frequency-dependent power loads assuming

constant bus voltages. Within the proposed framework, loads are modelled as constant active power demand  $P_{Ddm}(V_{dm}^0)$ , where the superscript “0” denotes the pre-fault (steady state) voltage, as shown in Figure 4.2. The loads are not incorporated into the transmission system admittance matrix; consequently, the original network topology is preserved so that the model has structural integrity [162].

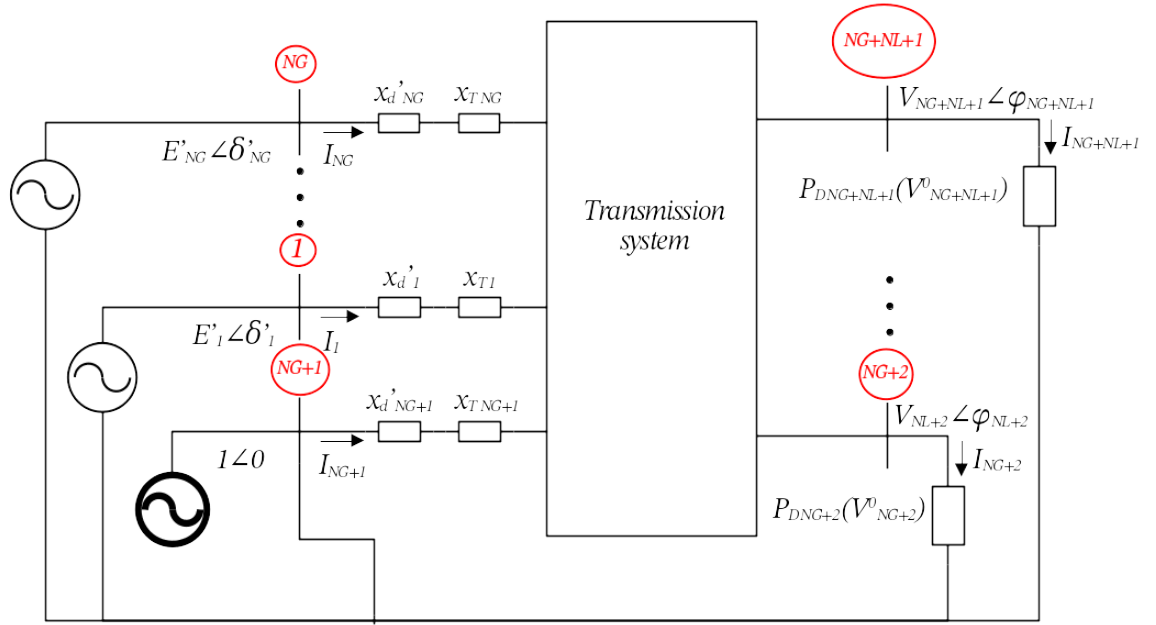


Figure 4.2: Multi-machine system with structure-preserving network (adapted from [17])

#### 4.2.2 Security, fault and switching modelling

Within the proposed framework, security and fault cases involving transmission lines are optimisation parameters required as inputs, whereas the switching scenarios are output variables related to topological changes, based on line-switching actions, that can increase the robustness of a power system from the transient stability perspective [183][184]. In particular, the security of the system can be defined by single outages changing the topological structure of a transmission network, which is the typical approach considering the N-1 security condition [69][73][91]; it is possible to define a set of single-branch-outages  $\Omega_k$  with outages indexed with  $k = 1, \dots, L$ . Moreover, each single outage has a probability of occurrence  $\pi^k$ , which can be obtained from a given probability density function. A security case  $k$  represents a single outage on a transmission line  $dmdn$  of the network, hence, it is possible to uniquely define a binary parameter vector for security case  $x^k \in B^{L \times 1}$  representing the outage status ( $B = \{on = 1, off = 0\}$ ) of each transmission line. For instance, a security case with a single outage on Line1 connecting busbars 1 and 2, will have the component  $x_{1,2}^{k=1} = 0$ , whilst

$x_{dmdn}^{k=1} = 1$  for all other components. To simplify the notation, case  $k = 0$  denotes the base-case with the intact network, i.e., no outage, where all  $x_{dmdn}^{k=0} = 1$ .

A power system can be subjected to several faults, which can be evaluated individually using assessments based on transient stability indicators [36][37][185] or risk-based methods [186]. The assessment provides a list of events ranked by severity, e.g., shorter CCT, as in [186], which has a probability of occurrence associated with each event. Within the proposed framework, the robustness of a power system is analysed for a set of single-branch-faults  $\Omega_f$ , where each fault indexed  $f = 1, \dots, L$  has a probability of occurrence  $\pi^f$ . The work presented in this thesis studies the effect of self-cleared three-phase bolted faults with procedures described in detail in Sections 2.3.1 and 2.3.2. Particularly, the single-branch-faults  $\Omega_f$  and the probability of occurrence  $\pi^f$  are also input parameters in the optimisation framework.

In the reviewed literature [47][96][72], a small number of switching actions usually provide the most significant improvements in comparison with actions involving multiple switching at the same time. Therefore, the proposed framework uses line-switching actions as a control to improve transient stability. In particular, a switching case, also called a switching scenario, can be defined by a set of switching actions on available transmission lines, i.e., lines which are not in the set of single-branch-faults  $\Omega_f$ . A switching scenario indexed by  $s = 1, \dots, L$ , in the set of switching scenarios  $\Omega_s$ , can be modelled as a binary vector  $oc^{k,f} \in B^{L \times 1}$  representing the switching status ( $on = 1$ ,  $off = 0$ ) of all transmission lines. A component of the switching case vector is a binary switching variable  $oc_{dmdn}^{k,f}$  related to the transmission line  $dmdn$ , in security case  $k$  and fault  $f$ , such that (4.8) holds. The constraint (4.8) indicates that a line  $dmdn$  can be switched-off if it is not considered on an outage or fault case.

$$x_{dmdn}^{k,f} \geq oc_{dmdn}^{k,f} \quad (4.8)$$

### 4.2.3 Classical multi-machine model with structure-preserving network and line switching

Within the proposed optimisation framework, the representation of a multi-machine system uses the classical model, restricted to the “first swing”, as typically described in the literature [22][17]. The novelty of the model is the introduction of parameters associated with security and fault cases, as well as (unknown) variables related to switching scenarios. The notation used here is consistent with [22]. The first part of the

model represents generator dynamics up to the point of connection (POC); a POC is a demand node belonging to the transmission network model. The set of generators is denoted as  $\Omega_g$  with SGs indexed as  $gi$  or  $gj = 1, \dots, NG$ . The dynamic model is given via relations (4.9)–(4.11), where (4.9) gives mechanical motion, (4.10) denotes electrical MW power delivered from an internal generator node to a POC (“load” node), and (4.11) shows relation between the generator angle and speed.

The assumptions of the model (4.9)–(4.13) are described below, which are similar to those in [33], except for the load representation.

- i. Mechanical power inputs are constant.
- ii. Damping or asynchronous power is neglected.
- iii. Based on the constant flux linkage model, a generator is represented by a constant EMF behind the direct axis transient (unsaturated) reactance.
- iv. The mechanical rotor angle of a synchronous generator can be represented by the angle of the voltage behind direct transient reactance.
- v. Loads are represented by constant power demands.

For an internal generator node  $gi \in \Omega_g$  connected to a “load” node  $dm \in \Omega_d$  through an internal generator branch (or fictitious transmission line)  $gidm \in \Omega_{gl}$ , its dynamical behaviour is defined as follows:

$$\frac{2H_{gi}}{\omega_r} \frac{d\omega_{gi}^{k,f}}{dt} = P_{M,gi}^k - P_{E,gidm}^{k,f}(\cdot); \quad (4.9)$$

$$\forall gi \in \Omega_g; \forall dm \in \Omega_d; \forall k \in \Omega_k; \forall f \in \Omega_f$$

$$P_{E,gidm}^{k,f}(\cdot) = (E_{gi}^{k,f})^2 G_{gidm} - E_{gi}^{k,f} V_{dm}^{k,f} \cdot [G_{gidm} \cos(\delta_{gi}^{k,f} - \varphi_{dm}^{k,f}) + B_{gidm} \sin(\delta_{gi}^{k,f} - \varphi_{dm}^{k,f})]; \quad (4.10)$$

$$\forall gidm \in \Omega_{gl}; \forall k \in \Omega_k; \forall f \in \Omega_f$$

$$\frac{d\delta_{gi}^{k,f}}{dt} = \omega_{gi}^{k,f} - \omega_r; \forall gi \in \Omega_g; \forall k \in \Omega_k; \forall f \in \Omega_f \quad (4.11)$$

Here,  $H_{gi}$  is the inertia constant of generator  $gi$  in its MVA base  $S_{gi}$ ;  $\delta_{gi}^{k,f}$  and  $\omega_{gi}^{k,f}$  are the angle and angular velocity of the machine rotor in security case  $k$  and fault case  $f$ , respectively;  $D_{gi}$  is a damping constant and  $\omega_r$  is the reference speed.  $P_{M,gi}$  and  $P_{E,gidm}$  are the mechanical power input and electrical power output of the synchronous generator  $gi$ . Moreover,  $\delta_{gi}^{k,f} - \varphi_{dm}^{k,f}$  is the angle difference between generator and “load” node

voltages;  $G_{gidm}^{k,f} + jB_{gidm}^{k,f}$  is the positive non-diagonal admittance (i.e., the admittance of the lossless fictitious branch  $gidm$ ) of the complex admittance matrix of the structure-preserving network. In particular,  $P_{E,gidm}^{k,f}(\cdot)$  is the active power flowing in the fictitious generator branch.

For all transmission network nodes, called load nodes  $dm, dn \in \Omega_d$ , which are connected via transmission lines  $dmdn \in \Omega_l$ , the nodal balance is given below

$$P_{Ddm} = P_{E,gidm}^{k,f}(\cdot) - \sum_{dmdn \in \Omega_l} oc_{dmdn}^{k,f} \cdot x_{dmdn}^{k,f} \cdot P_{dmdn}^{k,f}(\cdot); \quad (4.12)$$

$$\forall dm \in \Omega_d; \forall dn \in \Omega_d; \forall dmdn \in \Omega_l; \forall k \in \Omega_k; \forall f \in \Omega_f$$

$$P_{dmdn}^{k,f}(\cdot) = (V_{dm}^{k,f})^2 G_{dmdn}^{k,f} - V_{dm}^{k,f} V_{dn}^{k,f} \cdot [G_{dmdn}^{k,f} \cos(\varphi_{dm}^{k,f} - \varphi_{dn}^{k,f}) + B_{dmdn}^{k,f} \sin(\varphi_{dm}^{k,f} - \varphi_{dn}^{k,f})]; \quad (4.13)$$

$$\forall dm \in \Omega_d; \forall dn \in \Omega_d; \forall dmdn \in \Omega_l; \forall k \in \Omega_k; \forall f \in \Omega_f$$

Here,  $P_{Ddm}$  is the constant active power demand at node  $dm$  (if any); besides,  $\varphi_{dm}^{k,f} - \varphi_{dn}^{k,f}$  is the angle difference between “load” node voltages at nodes  $dm$  and  $dn$ ;  $P_{dmdn}^{k,f}(\cdot)$  is the active power flowing on a transmission line  $dmdn$  connecting demand nodes  $dm$  and  $dn$  with security-fault parameter  $x_{dmdn}^{k,f}$  and switching variable  $oc_{dmdn}^{k,f}$ . Moreover,  $G_{dmdn}^{k,f} + jB_{dmdn}^{k,f}$  is the positive admittance of transmission line  $dmdn$ .

A partial representation of a power system using the proposed classical model with structure-preserving network and switching is shown in Figure 4.3. The figure highlights the connection of generator nodes  $gi$  and  $gj$  to the system through fictitious transmission lines and the connection between load nodes  $dm$  and  $dn$  through a transmission line; actual transmission lines can be subjected to a switching-action. In a normal regime, transmission line  $dmdn$  is in service; however, if the parameter  $x_{dmdn}^{k,f}$  or variable  $oc_{dmdn}^{k,f}$  is equal to zero, then the power flowing on the line  $dmdn$  is equal to zero, like having a line with infinite impedance. The remainder of the network, considering other generators, load nodes and transmission lines, is represented by the transmission system box.

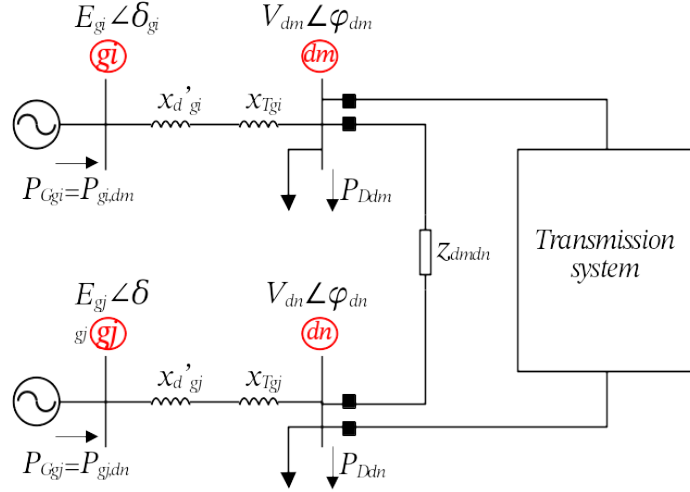


Figure 4.3: Partial representation of a power system with structure-preserving network

### 4.3 Study of time-domain transient stability indicators for constraint modelling

As described in Section 1.4.5, transient stability thresholds have been introduced in optimisation methods; in TSC-OPF, a transient stability constraint can be set via a limit on rotor angle deviation with respect to the COI, with the threshold angle of 100-180 degrees [121][123]–[125][181]. An accurate stability threshold value of relative rotor angle differences, i.e., the difference between pair SGs, was found to be 240 degrees [188]. In the work presented in this thesis, TDS were used for the verification of the developed transient stability constraint; particularly, transient stability indicators are calculated based on simulation results using the time interval  $T_{sim} = [0, t_{cl} + \Delta t]$ , where  $t_{cl}$  is the clearing time and  $\Delta t$  is a short period after the clearing. Transient stability indicators shown in Table 4.1 are investigated to understand their quality and consistence; a brief description of the studied indicators is given below.

- i. Coherence (COH): Formulated on the COI reference, COH measures how close generator rotor angles remain after the fault clearing. COH is defined by the difference between the maximum and minimum of each generator rotor angle [36].
- ii. Dot products (DOT1, DOT2, DOT3): Based on the kinetic and potential energy, they are defined using the maximum and minimum of three functions. Firstly, *dot1* characterises the maximum potential energy of the post-fault network; it is defined by the dot product between the vector of power mismatches  $f$  and the vector of rotor speeds determined by the fault condition [22][36]. Secondly, *dot2* focuses on the transient potential energy, which varies with the rotor angles; it is defined by the dot product between the vector of power mismatches  $f$  and the vector of

rotor angles [36]. Finally,  $dot3$  combines effect of changes in rotor angles and speeds by the dot product between the vector of rotor speeds  $\tilde{\omega}$  and the vector of rotor angle differences  $\theta(t) - \theta(t^{cl})$  [36]

- iii. Integral of squared generator rotor angles (ISGA): Also formulated on the COI reference, ISGA measures the lack of coherence between rotor angles during steady state and transient conditions [136][189][190]. Though ISGA is not an energy function, it is intrinsically related to the potential energy [37], which influences the oscillatory level of rotor angle responses.
- iv. Transient stability index (TSI): By measuring the maximum relative (pairwise) difference between generator rotor angles [191], TSI provides an accurate estimation not only of the stability level but also of the characteristic of the rotor angle response, i.e., stable or unstable [137]. Among the studied indicators, TSI is the only indicator that incorporates a stability threshold of  $360^\circ$ , which reflects that there is a cycle difference between rotor angles of two SGs [137][192][193].

Table 4.1 Time-domain transient stability indicators

Indicator	Calculation
COH	$Max\{Max\{\theta_{gi}(t)\} - Min\{\theta_{gi}(t)\}\}; \forall gi \in \Omega_g$
DOT1	$dot1 = \sum_{gi \in \Omega_g} f_{gi} \cdot \tilde{\omega}_{gi}(t); \forall gi \in \Omega_g$ $f_{gi} = P_{M,gi} - P_{E,gi} - \frac{M_{gi}}{M_T} \sum_{gi \in \Omega_g} P_{M,gi} - P_{E,gi}$ $Max\{dot1(t)\} - Min\{dot1(t)\}$
DOT2	$dot2 = \sum_{gi \in \Omega_g} f_{gi} \cdot \theta_{gi}(t); \forall gi \in \Omega_g$ $Max\{dot2(t)\} - Min\{dot2(t)\}$
DOT3	$dot3 = \sum_{gi \in \Omega_g} \tilde{\omega}_{gi}(t) \cdot (\theta_{gi}(t) - \theta_{gi}(t^{cl})); \forall gi \in \Omega_g$ $Max\{dot3(t)\} - Min\{dot3(t)\}$
ISGA	$\int_0^{t_{cl}+\Delta t} \frac{1}{M_T(t_{cl} + \Delta t)} \sum_{gi \in \Omega_g} M_{gi} \cdot (\theta_{gi}(t))^2 dt; \forall gi \in \Omega_g$
TSI	$\frac{360 -  Max\{\Delta\delta_{gi,gj}(t)\} }{360 +  Max\{\Delta\delta_{gi,gj}(t)\} } \times 100; \forall gi, gj \in \Omega_g$

Here,  $M_{gi} = 2H_{gi}/\omega_r$  and  $M_T$  are the inertia constant of the  $i$ -th generator and the total inertia of the system, respectively. Most of the indicators are based on the definition of



the rotor angle and speed  $(\theta_{gi}, \tilde{\omega}_{gi})$  with respect to the Centre of Inertia (COI), whilst TSI uses the relative pairwise difference between rotor angles  $\Delta\delta_{gi,gj} = \delta_{gi} - \delta_{gj}$ .

The quality of time-domain TS indicators was investigated under different fault locations, switching scenarios, and clearing times (15,339 valid cases were analysed based on the combination of 72 line-switching actions, 72 fault locations, and three clearing times). The simulation interval was 10 s, with a step size of 0.01 s. Whilst TSI was calculated over the entire simulation period, the computation of dot products, coherence and ISGA indicators was done between fault initiation and clearing, less than 0.12 s. Initially, correlation analysis was used to identify the relationship and tendency between transient stability indicators. The Kolmogorov-Smirnov tests showed that TS indicator results are not normally distributed; therefore, the Spearman correlation is more suitable for analysing the monotonic strength of relations [194]. The findings revealed by Spearman rank coefficients in Table 4.2 are threefold: firstly, TSI has a strong negative correlation with dot products and moderate with ISGA. Secondly, as expected, there is a very strong positive correlation among dot products. Finally, there is also a moderate positive correlation between dot products and ISGA. The correlation analysis of TSI shows a negative correlation with dot products, which suggests that for simulation results with a higher TSI, simulations showed that the system can have higher post-fault potential energy or absorb less kinetic energy during the fault condition. Similarly, the negative correlation coefficient between TSI and ISGA suggests that rotor angle oscillations are smaller in magnitude for cases with higher TSI. Though the analysis based on Spearman correlation coefficients may not be an exact measure of the relationship between indicators, it provides meaningful insight into the monotonicity of the relationship trends.

Table 4.2 Spearman correlation coefficient of transient stability indicators

TDS TS Indicator	COH	DOT1	DOT2	DOT3	ISGA
TSI	-0.08	-0.81	-0.74	-0.83	-0.52
COH	1.00	-0.02	0.09	0.00	0.05
DOT1		1.00	0.88	0.96	0.52
DOT2			1.00	0.85	0.48
DOT3				1.00	0.53
ISGA					1.00

Previous work investigating the effect of different levels of RES penetration [137][192][193] and the study presented in this thesis have confirmed that TSI can be selected as the reference transient stability indicator. In particular, Monte-Carlo

simulations in [188] indicate that a stability threshold of  $240^\circ$  has a 99% accuracy in identifying unstable results. Though results based on TSI with the original angle threshold of  $360^\circ$  [137] can be considered more relaxed, they take between 0.13 – 0.21 s longer simulation time in comparison with a threshold of  $240^\circ$  [188]. Furthermore, TSI is less computationally expensive than other indicators in Table 4.1 because it does not require the representation of rotor angles and speeds in the COI reference frame. In summary, previous and current studies support the selection of TSI as main stability indicator.

Within the work presented in this thesis, TSI was selected as the reference transient stability indicator to assess the stability performance in the proposed framework. Consequently, with the reformulated TSI in (4.14), considering rotor angles in security case  $k$  and fault case  $f$  and the maximum pairwise rotor angle deviation  $\max\{\delta_{gigj}^{k,f}\}$ , it is possible to define the transient stability constraint (4.15) in terms of a parameter  $\varepsilon$ . Through  $\varepsilon$  it is possible to change the stability threshold of (4.15) increasing the flexibility of (4.14); moreover, a larger  $\varepsilon$  reduces threshold. For instance, with  $\varepsilon = 0$  the stability threshold is  $360^\circ$ , whereas with  $\varepsilon = 0.2$  the threshold is  $240^\circ$  as suggested in [188].

$$TSI^{k,f} = \frac{360 - \max\{|\delta_{gi}^{k,f}(t) - \delta_{gj}^{k,f}(t)|\}}{360 + \max\{|\delta_{gi}^{k,f}(t) - \delta_{gj}^{k,f}(t)|\}} = \frac{360 - \max\{\delta_{gigj}^{k,f}\}}{360 + \max\{\delta_{gigj}^{k,f}\}}, \quad (4.14)$$

$$\forall gi, gj \in \Omega_g$$

$$TSI^{k,f} \geq \varepsilon \text{ or } \max\{\delta_{gigj}^{k,f}\} \leq \frac{360 \cdot (1 - \varepsilon)}{(1 + \varepsilon)} \quad (4.15)$$

#### 4.4 General transient stability and security constrained optimal power flow with switching actions

In a broader sense, the purpose of the optimisation framework is to provide the tools to find the best combination of network topology and active power dispatch such that the production cost is minimal and the power system is able to remain stable and secure while subjected to a selection of probable fault conditions. In particular, the framework includes not only fault conditions and security constraints (N-1 reliability criterion) but also uses the available line-switching capabilities, described in Section 4.2.2., to increase the robustness of a power system from the transient stability point of view. Figure 4.4 shows the components of the optimisation framework; the figure illustrates the

integration of the classical multi-machine model, the structure-preserving network with switching capabilities, and the TSI-based constraint into the different constraints of a dynamic optimisation problem. The definition of the dynamic optimisation components is discussed in Section 4.4.1; moreover, a detailed formulation is described in Section 4.4.2.

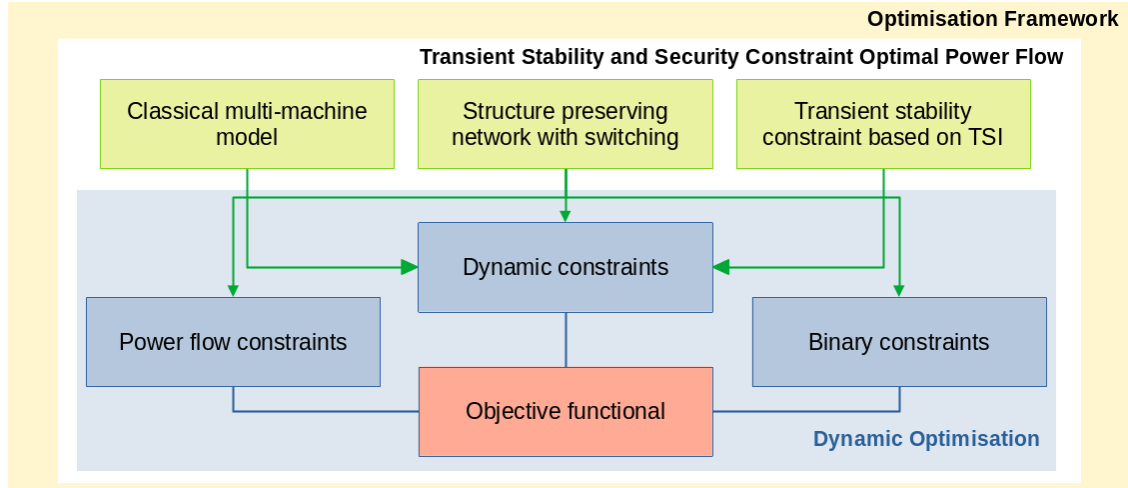


Figure 4.4: Components of the optimisation framework

From a mathematical perspective, the optimisation problem is a minimisation of generation production costs (or bids) and unreliability costs, i.e., the cost of non-delivered energy, in the considered post-fault interval subject to the base-case network topology considering N-1 security constraints (pre-specified transmission branch outages), as well as transient stability constraints for all probable fault locations; hence, faults can be applied to the base-case network and all N-1 networks. Within the so-defined framework, the optimisation problem is called *transient stability and security constraint optimal power flow with switching* (TSSC-OPFwS). The priority of the approach is on stability/security over economics, which means that once stability and security are satisfied, the focus is on economics; this is done by maximising the stability by changing the topology and generation dispatch with an incremental cost increase. In the case of an unfeasible solution, the problem considers load curtailment as the last recourse.

The TSSC-OPFwS model encompasses two significant aspects, power system security and transient stability in a preventive control mode. The idea of power system security, in a preventive mode, is to satisfy all operational constraints for the original network (security case  $k = 0$ ) and all assumed N-1 outages ( $k > 0$ ). Modelling security in the preventive mode can generally be done in two ways. First, if it is assumed that controls

can be changed following an assumed single outage, they are dependent on outage  $k$ ; for example, if generation can be changed after the outage of one line, there is a *capability of corrective (re)dispatch* in the preventive mode. Secondly, if there is no possibility to change the controls following an assumed branch outage, the same controls, e.g., generation dispatch, need to be used for intact and N-1 networks; then, the controls are not dependent on security case  $k$ .

Though the mathematical definition of the TSSC-OPFwS problem is given in this chapter, the solution is presented separately in Chapter 5. A traditional solution approach would include the discretisation of dynamic equations [122][124]–[126] in combination with a set of probable faults applied to the base-case and N-1 networks. Hence, the TSSC-OPFwS problem is a large-scale mixed-integer non-linear multi-stage (i.e., discretised temporal relations) optimisation, which commercial tools cannot solve. Consequently, the solution strategy will be iterative, and it will be fully described in Chapter 5.

#### 4.4.1 Condensed formulation of the general problem

In a general form, the optimisation model is presented via vector functions, states, controls, and parameters. The standard SC-OPF model [122] has been modified so that the line switching can be modelled. For instance, a binary control variable  $ub_{dmdn}$  multiplies branch  $dmdn$  admittance to model branch switching, as described in Section 4.2. The equality constraints of the model are in the form:

$$\mathbf{h}_a(\mathbf{x}^k, \mathbf{uc}^k, \mathbf{ub}^k, \mathbf{p}^k) = \mathbf{0} ; \forall k \in \Omega_k \quad (4.16)$$

Where subscript  $\mathbf{a}$  denotes “algebraic”;  $\mathbf{h}_a(\cdot)$  are nodal power flow equations;  $\mathbf{x}^k$  is a vector of states, typically nodal voltage magnitudes and angles, tap-changer ratios, in security case  $k$  ( $k = 0$  for base-case and  $k > 0$  for single outages);  $\mathbf{uc}^k$  is a vector of continuous control variables in case  $k$ , typically active and reactive power generations, load curtailments, AVR and tap-changer settings, reactive power compensation;  $\mathbf{ub}^k$  is a vector of binary control variables in case  $k$  (*on/off* statuses of network branches, shunt capacitance/inductance in discrete steps); and  $\mathbf{p}^k$  is a vector of parameters in case  $k$ , e.g., admittance matrices. Branch switching is modelled as in [183][184], whilst control vectors  $\mathbf{uc}^k$  and  $\mathbf{ub}^k$  are defined by envisaged security cases  $k$  indicating that corrective security control capabilities are available. For the preventive control, on the other hand, vectors  $\mathbf{uc}$  and  $\mathbf{ub}$  for all security cases  $k \in \Omega_k$  need to be defined. They,

however, could lead to infeasible problems [195], hence the use of control vectors  $\mathbf{uc}^k$  and  $\mathbf{ub}^k$  in the model.

Inequality constraints of the SC-OPF model are in the form:

$$\mathbf{g}_a(\mathbf{x}^k, \mathbf{uc}^k, \mathbf{ub}^k, \mathbf{p}^k) \leq \mathbf{0} ; \forall k \in \Omega_k \quad (4.17)$$

Where subscript  $\mathbf{a}$  refers to “algebraic”;  $\mathbf{g}_a(\cdot)$  denotes power flow inequality constraints, and the same vectors as in (4.16) are used. Inequalities (4.17) describe active and reactive generation limits, load curtailment limits, branch thermal limits, tap-changer, shunt compensation ranges, and limits on nodal voltages. They need to be extended with the logical constraints on binary variables  $\mathbf{ub}^k$ . For instance, network connectivity, or switching in MVAr compensation, or switching a branch out:

$$\mathbf{g}_{a,D}(\mathbf{ub}^k) \leq \mathbf{0} ; \forall k \in \Omega_k \quad (4.18)$$

Where subscript  $\mathbf{D}$  denotes discrete form and  $\mathbf{g}_{a,D}(\cdot)$  stands for logical (in)equality relations.

The classical multi-machine model with structure-preserving network, introduced in Section 4.2, is used to investigate network switching. The network model consists of all original network nodes, as load nodes and internal generator nodes. The first part of the model is given by differential equations (4.19).

$$\dot{\mathbf{y}}^{k,f}(t) = \mathbf{d}_d(\mathbf{y}^{k,f}(t), \mathbf{z}^{k,f}(t), \mathbf{uc}^k, \mathbf{ub}^k, \mathbf{p}^{k,f}) ; \forall k \in \Omega_k ; \forall f \in \Omega_f \quad (4.19)$$

Where subscript  $\mathbf{d}$  denotes differential (dynamic) model;  $\mathbf{d}_d(\cdot)$  stands for state-space equations;  $\mathbf{y}^{k,f}(t)$  is a vector of dynamic state variables, typically rotor angles and speeds [17], in the security case  $k \in \Omega_k$  and credible fault  $f \in \Omega_f$ ;  $\mathbf{z}^{k,f}(t)$  is a vector of “non-dynamic” state variables whose first derivative is negligible (typically, nodal voltage angles at nodes where generators are not connected) and  $\mathbf{p}^{k,f}$  is a vector of parameters. Vector  $\mathbf{p}^{k,f}$  also contains some components of the vector  $\mathbf{x}^k$  (e.g. nodal voltage magnitudes), which are assumed constant in the classical model [17]. Control vectors  $\mathbf{uc}^k$  and  $\mathbf{ub}^k$  are not dependent on the considered faults  $f \in \Omega_f$ , that is, a single network topology and other controls apply for all fault locations.

Equations (4.19) are set for all internal generator nodes, whilst equations in the form:

$$\mathbf{0} = \mathbf{h}_d(\mathbf{y}^{k,f}(t), \mathbf{z}^{k,f}(t), \mathbf{uc}^k, \mathbf{ub}^k, \mathbf{p}^{k,f}) ; \forall k \in \Omega_k ; \forall f \in \Omega_f \quad (4.20)$$

Need to be set for all load nodes. Initialization of vectors  $\mathbf{y}^{k,f}(t)$  and  $\mathbf{z}^{k,f}(t)$  is based on the steady state just before a fault at  $t = 0^-$ . Limitations on rotor angle differences or TS indices in the time domain need to be included to complete the constraints of the dynamic optimisation model.

$$\mathbf{g}_d(\mathbf{y}^{k,f}(t), \mathbf{z}^{k,f}(t), \mathbf{u}^k, \mathbf{u}^b, \mathbf{p}^{k,f}) \leq \mathbf{0} ; \forall k \in \Omega_k; \forall f \in \Omega_f \quad (4.21)$$

The objective functional reflects minimum operation or bid costs whilst meeting the system security and transient stability constraints; however, these limitations can lead to infeasible problems. It is for this reason that the objective function also contains the cost of load curtailments [195]:

$$\begin{aligned} z = & \int_0^{T_{sim}} \sum_k \pi_k \sum_{gi} c_{gi}(P_{M,gi}^k(t)) \cdot dt \\ & + \int_0^{T_{sim}} \sum_k \pi_k \sum_{dm} c_{dm}(PLC_{dm}^k(t)) \cdot dt \end{aligned} \quad (4.22)$$

Here, the time period  $T_{sim} = [0, t_{cl} + \Delta t]$  is typically one second;  $\pi_k$  is security case  $k$  probability;  $c_{gi}(\cdot)$  is generator  $gi$  cost/bid function;  $P_{M,gi}^k(t) \in \mathbf{u}^k$  is mechanical power of unit  $gi$  in case  $k$ , and it does not depend on failure case  $f$ ;  $c_{dm}(\cdot)$  is cost function of load curtailment at node  $dm$ ; and  $PLC_{dm}^k(t) \in \mathbf{u}^k$  is load curtailment at node  $dm$  at case  $k$ . All controls ( $P_{M,gi}^k$  and  $PLC_{dm}^k$ ) are applied in the preventive mode, as it was envisaged that they cannot be changed in the corrective mode realistically. Mechanical power and load curtailments in (4.22) are kept constant in the considered time interval. Note that (4.22) is not a function of credible faults  $f \in \Omega_f$ , because identical controls are applied for all of them. The unknown variables of the optimisation model (4.16)-(4.22) are vectors  $\mathbf{x}^k, \mathbf{u}^k, \mathbf{u}^b, \mathbf{y}^{k,f}(t)$  and  $\mathbf{z}^{k,f}(t)$ ,  $k \in \Omega_k ; f \in \Omega_f$ . The model is general in the sense that it includes preventive controls (generation dispatch) in conjunction with network switching and both security and transient stability constraints.

#### 4.4.2 Detailed formulation of preventive TSSC-OPFwS

The preventive TSSC-OPFwS problem is presented in detail in this section and will be solved in Chapter 5. The formulation includes the assumptions used to define the classical multi-machine model with structure-preserving network, described in Section 4.2.3; they are extended by considering aspects like security and operating constraints. The proposed model extends previous formulations of the OPF approaches with the inclusion of the structure-preserving network within the classical TS model, as well as

line-switching control actions, while subjected to a set of credible faults. The TSSC-OPFwS model incorporates power system security and transient stability in the preventive control mode. The aim of power system security in a preventive mode is to fulfil all operational constraints for the original network, and all assumed N-1 networks (with security cases  $k$  in the set of single-branch-outages  $\Omega_k$ ).

The optimisation problem is based on the following assumptions:

- i. This is a general formulation in which it is assumed there is a possibility for corrective control actions following assumed security (N-1) outages in the preventive control mode. Active and reactive power generations, switching actions, and load curtailments are functions of security case  $k$ .
- ii. The classical model is used to represent SGs.
- iii. Generation is divided into dispatchable and non-dispatchable generation. Dispatchable generations are available controls, whilst non-dispatchable generations are not controls; they are constants injections like negative demands. Wind, solar, nuclear and distributed generation are usually considered non-dispatchable generation.
- iv. The model is valid for the first-swing period consisting of several cycles; however, the studied time of generator dynamics is 1 second.
- v. Mechanical power inputs do not change within the studied time interval of 1 second and are not time functions; this is a simplifying assumption used in the classical TS model [17] so that the modelling of governors is avoided.
- vi. The classical TS model does not use the reactive power–voltage phenomena. Consequently, their dynamics are not modelled. The classical TS model, which is one part of the general model, focuses on active power and voltage angles; therefore, reactive power injections and voltage magnitudes are considered constant (i.e., they are not variables) within the studied time.
- vii. The unknown load shedding is modelled as active power injection; therefore, the curtailed reactive power is also injected and assumed to be proportional to the power factor of the original demand.
- viii. Loads are represented by constant power demands.
- ix. Load curtailments at demand nodes are also included in the model, and they are the results of the optimisation model.

- x. Based on the classical TS modelling, voltage angles and magnitudes do not change over time. Therefore, it was assumed that the SCOPF gives the initial point at  $\theta^+$ , and voltages magnitudes and angles are kept constant.
- xi. All actual transmission branches are modelled with a single switching device.

Equality and inequality constraints of the preventive TSSC-OPFwS problem are classified into two groups: a) Power flow and b) Transient Stability and Binary constraints; they are presented in groups below.

#### 4.4.2.1 Power flow constraints

AC load-flow nodal active and reactive power balances in security case  $k$  are defined by (4.23) and (4.24), respectively. Here,  $P_{Ggi}$  and  $Q_{Ggi}$  are active and reactive power injections from SGs, equal to the power flowing through the fictitious transmission line  $gidm$ , whilst  $P_{DGdm}$  and  $Q_{DGdm}$  represent injections from non-dispatchable generation. Besides,  $P_{Ddm}$  and  $Q_{Ddm}$  are the constant active and reactive power demands at load nodes.  $PLC_{dm}$  is the amount of active power injection due to load curtailment; particularly, the curtailed reactive power is proportional to the power factor of the original demand  $Q_{Ddm}/P_{Ddm}$ . Additionally,  $P_{dm,dn}^k(\cdot)$  and  $Q_{dm,dn}^k(\cdot)$  are the active and reactive power flowing on actual transmission lines, respectively.

$$P_{Ggi}^k(\cdot) + P_{DGdm} - P_{Ddm} + PLC_{dm} - \sum_{dm, dn \in \Omega_l} oc_{dm, dn}^k \cdot x_{dm, dn}^k \cdot P_{dm, dn}^k(\cdot) = 0; \quad (4.23)$$

$$\forall gi \in \Omega_g; \forall dm \in \Omega_d; \forall k \in \Omega_k$$

$$Q_{Ggi}^k(\cdot) + Q_{DGdm} - Q_{Ddm} + PLC_{dm} \cdot \left( \frac{Q_{Ddm}}{P_{Ddm}} \right) - \sum_{dm, dn \in \Omega_l} oc_{dm, dn}^k \cdot x_{dm, dn}^k \cdot Q_{dm, dn}^k(\cdot) = 0; \quad (4.24)$$

$$\forall gi \in \Omega_g; \forall dm \in \Omega_d; \forall k \in \Omega_k$$

Constraints (4.23) and (4.24) include  $P_{dm, dn}^k(\cdot)$  and  $Q_{dm, dn}^k(\cdot)$  which are active and reactive power flow on branch components described by (4.25) and (4.26); they also consider active and reactive power injections  $P_{Ggi}(\cdot)$  and  $Q_{Ggi}(\cdot)$  defined by the power flow on fictitious lines in (4.27) and (4.28), respectively. Considering the type of transmission line, (4.25) and (4.26) specify that only the flow on actual transmission lines  $P_{dm, dn}^k(\cdot)$  and  $Q_{dm, dn}^k(\cdot)$  can experience a step change according to a security case  $k$ ,



whilst the active and reactive power injection from SGs  $P_{Ggi}(\cdot)$  and  $Q_{Ggi}(\cdot)$  can vary because of changes in voltage but not due to an outage (see (4.27) and (4.28)). Here,  $E_{gi}^k \angle \delta_{gi}^k$  and  $V_{dm}^k \angle \varphi_{dm}^k$  are generator and load node voltages; moreover,  $G_{gidm} + jB_{gidm}$  and  $G_{dmdn}^k + jB_{dmdn}^k$  are branch reactances related to fictitious and actual transmission lines; note that actual branch parameters are functions of security case  $k$ , because the branch can be put on an outage.

$$P_{dmdn}^k(\cdot) = (V_{dm}^k)^2 G_{dmdn}^k - V_{dm}^k V_{dn}^k \cdot [G_{dmdn}^k \cos(\varphi_{dm}^k - \varphi_{dn}^k) + B_{dmdn}^k \sin(\varphi_{dm}^k - \varphi_{dn}^k)]; \quad (4.25)$$

$$\forall dmdn \in \Omega_l; \forall dm \in \Omega_d; \forall dn \in \Omega_d; \forall k \in \Omega_k$$

$$Q_{dmdn}^k(\cdot) = -(V_{dm}^k)^2 B_{dmdn}^k + V_{dm}^k V_{dn}^k \cdot [B_{dmdn}^k \cos(\varphi_{dm}^k - \varphi_{dn}^k) - G_{dmdn}^k \sin(\varphi_{dm}^k - \varphi_{dn}^k)]; \quad (4.26)$$

$$\forall dmdn \in \Omega_l; \forall dm \in \Omega_d; \forall dn \in \Omega_d; \forall k \in \Omega_k$$

$$P_{Ggi}^k(\cdot) = (E_{gi}^k)^2 G_{gidm} - E_{gi}^k V_{dm}^k \cdot [G_{gidm} \cos(\delta_{gi}^k - \varphi_{dm}^k) + B_{gidm} \sin(\delta_{gi}^k - \varphi_{dm}^k)]; \quad (4.27)$$

$$\forall gidm \in \Omega_{gl}; \forall gi \in \Omega_g; \forall dm \in \Omega_d; \forall k \in \Omega_k$$

$$Q_{Ggi}^k(\cdot) = -(E_{gi}^k)^2 B_{gidm} + E_{gi}^k V_{dm}^k \cdot [B_{gidm} \cos(\delta_{gi}^k - \varphi_{dm}^k) - G_{gidm} \sin(\delta_{gi}^k - \varphi_{dm}^k)]; \quad (4.28)$$

$$\forall gidm \in \Omega_{gl}; \forall gi \in \Omega_g; \forall dm \in \Omega_d; \forall k \in \Omega_k$$

The current magnitude on actual transmission lines under security case  $k$  is defined in (4.29). In particular,  $I_{REdmdn}^k(\cdot)$  and  $I_{IMdmdn}^k(\cdot)$  are the real and reactive components of the complex current flowing on a branch connecting nodes  $dm$  and  $dn$ , which are functions of terminal voltage magnitudes and angles as defined in (4.30) and (4.31), respectively.

$$I_{dmdn}^k(\cdot) = [I_{REdmdn}^k(\cdot)^2 + I_{IMdmdn}^k(\cdot)^2]^{0.5}; \forall dmdn \in \Omega_l \quad (4.29)$$

$$I_{REdmdn}^k(\cdot) = G_{dmdn}^k [V_{dm}^k \cos(\varphi_{dm}^k - \varphi_{dn}^k) - V_{dn}^k \cos(\varphi_{dm}^k - \varphi_{dn}^k)] - B_{dmdn}^k [V_{dm}^k \sin(\varphi_{dm}^k - \varphi_{dn}^k) - V_{dn}^k \sin(\varphi_{dm}^k - \varphi_{dn}^k)]; \quad (4.30)$$

$$\forall dmdn \in \Omega_l; \forall dm \in \Omega_d; \forall dn \in \Omega_d$$

$$I_{IMdmdn}^k(\cdot) = G_{dmdn}^k [V_{dm}^k \sin(\varphi_{dm}^k - \varphi_{dn}^k) - V_{dn}^k \sin(\varphi_{dm}^k - \varphi_{dn}^k)] + B_{dmdn}^k [V_{dm}^k \cos(\varphi_{dm}^k - \varphi_{dn}^k) - V_{dn}^k \cos(\varphi_{dm}^k - \varphi_{dn}^k)]; \quad (4.31)$$

$$\forall dmdn \in \Omega_l; \forall dm \in \Omega_d; \forall dn \in \Omega_d$$

Thermal constraints of transmission lines are given in (4.32). The explicit inclusion of parameter  $x_{dmdn}^k$  and variable  $oc_{dmdn}^k$  in (4.32) indicates that an actual transmission line connecting load nodes  $dm$  and  $dn$  is equipped with a switchgear.

$$oc_{dmdn}^k \cdot x_{dmdn}^k \cdot \left(I_{dmdn}^k(\cdot)\right)^2 \leq \left(I_{dmdn}^{k,max}\right)^2; \forall dmdn \in \Omega_l \quad (4.32)$$

Limits on nodal voltage magnitudes are defined in (4.33). Those limits can differ for the base-case  $k = 0$ , i.e., intact network, and security cases  $k > 0$ . In particular, there are no limits on the magnitude of generator internal node voltages because internal EMFs are kept constant.

$$V_{dm}^{k,min} \leq V_{dm}^{k,max} \leq V_{dm}^{k,max}; \forall dm \in \Omega_d \quad (4.33)$$

Finally, limits on apparent power generation  $S_{Ggi}$  are given in (4.34). Notably, there are no limits related to reactive power because they are not modelled.

$$S_{Ggi}^{min} \leq S_{Ggi}(\cdot) \leq S_{Ggi}^{max}; \forall gi \in \Omega_g \quad (4.34)$$

#### 4.4.2.2 *Dynamic and binary constraints*

Described in detail in Section 4.2.3, repeated here for completeness and clarity, (4.35)-(4.39) define constraints related to generator dynamics and loads under security case  $k$  and fault case  $f$ , respectively. The pair of first order differential equations (4.35) and (4.37) enables the state-space representation of a generator connected at node  $gi$  with state variables rotor speed  $\omega_{gi}^{k,f}$  and angle  $\delta_{gi}^{k,f}$ , whilst a load at node  $dm$  is defined by a constant active power demand  $P_{Ddm}$  as shown in the algebraic equation (4.38). The active power injection flows through the lossless fictitious transmission line  $gidm$  according to (4.36), neglecting the armature resistance; hence, the active power flow  $P_{E,gidm}^{k,f}(\cdot)$  is equal to the active power injection  $P_{Ggi}(\cdot)$  used in power flow constraints in Section 4.4.2.1. Moreover, (4.39) defines the active power flow on actual transmission lines  $P_{dmdn}^{k,f}(\cdot)$ , which can be subjected to switching. In particular, the active power balance in demand nodes (4.38) follows the network modelling described in Figure 4.3.

$$\begin{aligned} \frac{2H_{gi}}{\omega_r} \frac{d\omega_{gi}^{k,f}}{dt} + D_{gi} \cdot \omega_{gi}^{k,f} &= P_{M,gi}^k - P_{E,gidm}^{k,f}(\cdot); \\ \forall gi \in \Omega_g; \forall dm \in \Omega_d; \forall k \in \Omega_k; \forall f \in \Omega_f \end{aligned} \quad (4.35)$$

$$\begin{aligned}
P_{E,gidm}^{k,f}(\cdot) &= (E_{gi}^k)^2 G_{gidm} - E_{gi}^k V_{dm}^{k,f} \\
&\cdot [G_{gidm} \cos(\delta_{gi}^{k,f} - \varphi_{dm}^{k,f}) + B_{gidm} \sin(\delta_{gi}^{k,f} - \varphi_{dm}^{k,f})]; \quad (4.36) \\
&\forall gidm \in \Omega_{gl}; \forall k \in \Omega_k; \forall f \in \Omega_f
\end{aligned}$$

$$\frac{d\delta_{gi}^{k,f}}{dt} = \omega_{gi}^{k,f} - \omega_r; \forall gi \in \Omega_g; \forall k \in \Omega_k; \forall f \in \Omega_f \quad (4.37)$$

$$P_{Ddm} = P_{E,gidm}^{k,f}(\cdot) - \sum_{dmdn \in \Omega_l} oc_{dmdn}^{k,f} \cdot x_{dmdn}^{k,f} \cdot P_{dmdn}^{k,f}(\cdot); \quad (4.38)$$

$$\forall dm \in \Omega_d; \forall dn \in \Omega_d; \forall dmdn \in \Omega_l; \forall k \in \Omega_k; \forall f \in \Omega_f$$

$$\begin{aligned}
P_{dmdn}^{k,f}(\cdot) &= (V_{dm}^{k,f})^2 G_{dmdn} - V_{dm}^{k,f} V_{dn}^{k,f} \\
&\cdot [G_{dmdn} \cos(\varphi_{dm}^{k,f} - \varphi_{dn}^{k,f}) + B_{dmdn} \sin(\varphi_{dm}^{k,f} - \varphi_{dn}^{k,f})]; \quad (4.39) \\
&\forall dm \in \Omega_d; \forall dn \in \Omega_d; \forall dmdn \in \Omega_l; \forall k \in \Omega_k; \forall f \in \Omega_f
\end{aligned}$$

The transient stability limit (4.40), explained in Section 4.3, establishes the stability boundary characterising stable and unstable behaviour. In particular, if the relative rotor angle between a given pair of SGs is lower than the limit, the system remains stable after a severe fault case  $f$ .

$$\begin{aligned}
TSI^{k,f} &\geq \varepsilon \text{ or } \max\{\delta_{gigj}^{k,f}\} \leq \frac{360 \cdot (1 - \varepsilon)}{(1 + \varepsilon)}; \quad (4.40) \\
&\forall gi, gj \in \Omega_g; \forall k \in \Omega_k; \forall f \in \Omega_f
\end{aligned}$$

Finally, switching constraints (4.41), described in Section 4.2.2, define the relationship between the security-fault parameter  $x_{dmdn}^{k,f}$  and switching variable  $oc_{dmdn}^{k,f}$  for actual transmission lines.

$$x_{dmdn}^{k,f} \geq oc_{dmdn}^{k,f}; \forall dmdn \in \Omega_l; \forall k \in \Omega_k; \forall f \in \Omega_f \quad (4.41)$$

#### 4.4.2.3 Objective functional

An optimal solution of the objective functional (4.42), subject to constraints (4.23)-(4.41), is a function that reflects the minimum operation bid cost whilst satisfying dynamic and transient stability constraints; load curtailments are also available in case of infeasible problems. In (4.42), the integration is done over a time period  $[0, T_{sim}]$ , which is up to one second.  $\pi_k$  is security case  $k$  probability. Moreover,  $c_{gi}(\cdot)$  is generator  $gi$  cost/bid function with  $P_{m,gi}^k(t)$  as the mechanical power of unit  $gi$  in case  $k$ ;  $c_{dm}(\cdot)$  is the cost function of load curtailment at node  $dm$  with  $PLC_{dm}^k(t)$  as load curtailment at node  $dm$  at case  $k$ . Mechanical power is kept constant and no change in load curtailments

is considered within the time interval of eq. (4.42). The preventive control actions in the form of line-switching actions are applied for all credible faults  $f \in \Omega_f$ ; therefore, (4.42) is not a function of  $f \in \Omega_f$ , because identical controls are applied for all of them (see also equation (4.35)).

$$\begin{aligned} \mathbf{z} = & \int_0^{T_{sim}} \sum_k \pi_k \sum_{gi} c_{gi}(P_{M,gi}^k(t)) \cdot dt \\ & + \int_0^{T_{sim}} \sum_k \pi_k \sum_{dm} c_{dm}(PLC_{dm}^k(t)) \cdot dt \end{aligned} \quad (4.42)$$

The unknown variables of the optimisation model (4.23)-(4.42) are machine rotor angles  $\delta_{gi}^{k,f}$  and angular velocities  $\omega_{gi}^{k,f}$ , as well as nodal voltage magnitudes and angles  $V_{dm}^{k,f} \angle \varphi_{dm}^{k,f}$ . Moreover, continuous control variables are in the form of active and reactive power generations  $P_{M,gi}^k(\cdot)$  and  $Q_{G,gi}^k(\cdot)$  for security case  $k$ ; and discrete controls are in the form of line-switching variables  $oc_{dm}^{k,f}$ , related to actual transmission lines for security case  $k$  and fault  $f$ . When necessary, all variables are defined for a security case  $k$  in the set of envisaged outages  $\Omega_k$ , and fault case  $f$  in the set of credible faults  $\Omega_f$ .

## 4.5 Summary

This chapter introduced a framework for the optimisation of the operation costs considering the security and transient stability of power systems. In particular, the framework uses line-switching actions as a discrete control to change the topology and improve the transient stability response of the system in the presence of large disturbances. The framework includes the modelling of multi-machine systems with switching capabilities of transmission lines. Moreover, the modelling of security, fault and switching cases affecting the service status of lines are also included in the framework

In this chapter, two network representations were studied to define the proposed *classical multi-machine model for transient stability with structure-preserving network and line switching*. Initially, the traditional formulation of the classical multi-machine with network reduction, based on the representation of loads as constant impedances, was introduced to highlight that network reduction creates a network representation where internal generator nodes are connected in an all-to-all topology. Conversely, the structure-preserving network relies on the representation of loads as active power

injections; in this way, loads are not incorporated into the admittance matrix, and the original topology is preserved. Keeping a non-reduced network representation is key for line-switching modelling. With the addition of security parameters and switching variables, it was possible to extend previous models incorporating the line-switching capability, which is one of the novel aspects of the proposed framework. In the proposed dynamical model, generators are connected to a POC, a load node, through a lossless non-switchable branch impedance; on the contrary, load nodes are connected through actual transmission lines with switching capabilities. In particular, switching capabilities are modelled by security parameters and switching variables, which enables the representation of different network structures to analyse their transient stability behaviour.

Based on TDS results, a comparison of different transient stability indicators was made to find the best stability indicator in terms of accuracy and efficiency. The study revealed that the transient stability index (TSI) had one of the highest levels of correlation with other indicators, while it also has an embedded stability threshold; The transient stability threshold was a characteristic not found in other studied indicators. Therefore, due to its accurate assessment and low computational complexity, TSI was selected as the main stability indicator; the selection of TSI allowed the definition of a transient stability constraint.

The final component of the proposed framework, which incorporates the previously described parts, is a dynamic optimisation problem called *transient stability and security constraint optimal power flow with switching* (TSSC-OPFwS). The problem is a minimisation of generation production and load curtailment costs in a considered post-fault interval. The problem considers N-1 security and transient stability constraints for all probable fault locations. Therefore, faults can be applied to the base-case network and all networks considering a single-line outage (N-1 networks). The focus is stability and security, achieved by changing the network structure and generation dispatch with the incremental cost increase. The problem formulation is general because it considers preventive and corrective actions for security and preventive actions such as line-switching for transient stability. The problem was initially presented in a condensed form, but the detailed formulation of preventive TSSC-OPFwS was later introduced. The detailed formulation highlighted the incorporation of dynamic equality constraints based on the proposed multi-machine model with a structure-preserving network, line switching and an algebraic inequality constraint as a stability threshold using TSI.

In summary, the contributions of the present chapter are three:

- *The improvement of the classical multi-machine structure-preserving model by including switching capabilities of transmission lines. The novel representation, including security parameters and switching variables, enables more flexibility to use line-switching to represent different network structures. Moreover, the main benefit of the formulation is the inclusion of network switching as a controllable preventive action toward improving transient stability.*
- *A quantitative and qualitative analysis of transient stability indicators. Based on TDS results, it was possible to select TSI as the main indicator based not only on the findings of previous research but also because its assessment shares qualitative characteristics with other well-studied transient stability indicators. Besides, TSI was used as a base indicator to propose a new transient stability inequality constraint, which has not been used before in the context of TSC-OPF or line-switching methodologies.*
- *A novel optimisation problem called transient stability and security constraint optimal power flow with switching (TSSC-OPFwS) to find the best topology in the form of a switching solution. The optimal solution improves the transient stability response of a power system making it more robust against a set of credible faults.*

## **5 Transient Stability Preventive Control with Generation Dispatching and Network Optimisation**

---

This chapter introduces a methodology to solve the Transient Stability and Security Constraint Optimal Power Flow with Switching (TSSC-OPFwS) problem described in Section 4.4. The proposed approach is a two-stage method; the first stage is the solution of an SC-OPF for fixed network topology, whilst the second stage is a network topology optimisation to find the network structure with the best transient stability response, considering a set of credible faults. Particularly, the goal of the topology optimisation problem for transient stability is to find the network topology that maximises a network robustness metric, making the system less susceptible to unstable behaviour. The proposed robustness metric is designed as a proxy function to estimate, to a certain extent, the transient stability behaviour of a network topology. The assessment of the network robustness metrics is based on three studies considering a stable base-case, an unstable base-case, and the application of load curtailments.

The chapter includes four parts. Firstly, the description of the IEEE68 bus test system, which serves as a realistic power system with a relatively large and complex transmission network. Secondly, a detailed description of the two-stage solution method highlights the computational processes; the methodology is described in detail by a flow chart, which includes three components: pre-processing, topology optimisation and the validation of optimal solutions. Thirdly, a comprehensive study of impact factors relating topological effects, given by the network structure, to transient stability results; relative improvements or detrimental effects on Transient Stability Index (TSI) reflect the

influence of the network structure in combination with impact factors, such as inertia and synchronous generator (SG) pre-fault loading. Finally, the network robustness metric is defined in the form of two fitness functions; the functions are assessed to verify their accuracy in mapping combinations of switching scenarios and fault conditions to time-domain simulation (TDS) stability results. Notably, the fitness functions characterise the system's dynamic behaviour, removing the burden of solving differential equations within the optimisation.

## 5.1 IEEE68 bus test system.

The largest test system used in this thesis to study the effect of line-switching action on transient stability is the IEEE68 bus test system. Introduced in [160][161] for damping controller design and later used to study the penetration of CIG [162][163], the system is deemed to be a realistic abstraction of a large multi-machine power system; it represents a 60 Hz system with a 230 kV network including 68 buses, 72 transmission branches, and 16 generators. Figure 5.1 illustrates an overview of the test system showing the location of SGs; the figure highlights that the system is a combination of the New England Test System (NETS) and the New York Power System (NYPS), extended by three areas. As shown in Figure 5.1, the generation in the test system is distributed in five areas. For instance, conventional generators G1-G9 are within the NETS area, G10-G13 belong to the NYPS area, whilst equivalent generators G14, G15, and G16 represent additional areas. The parameters of each generator are given in Appendix A, Table A.7.

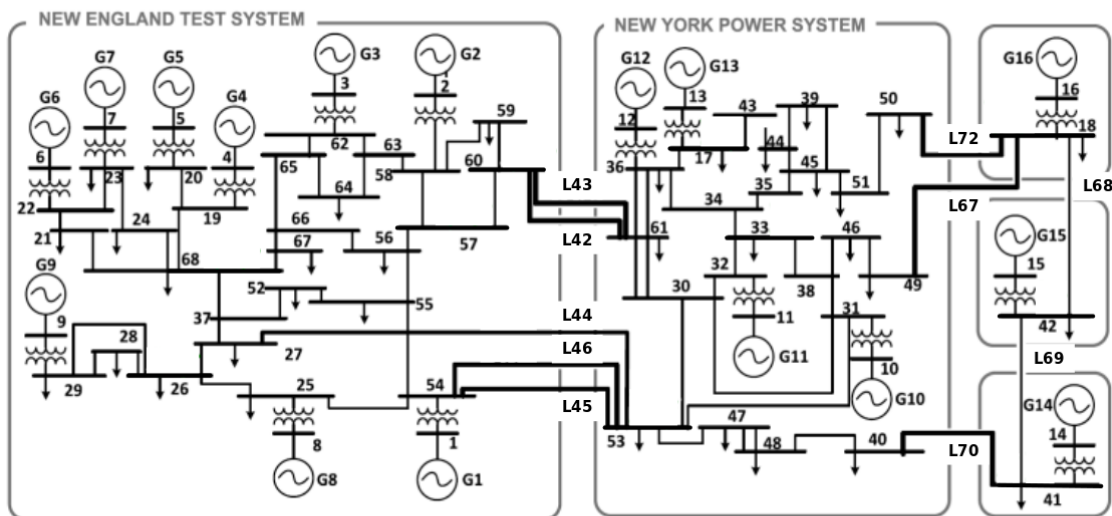


Figure 5.1: IEEE68 Bus Test System [148][149].

For stability studies, the implementation of the IEEE68 test system in PowerFactory DIgSILENT [170] considers the 16 conventional generation plants with synchronous



machines represented with the sixth-order model. To include the voltage regulation effect, all generating plants are equipped with IEEE DC1A exciters, except for G9, which has an IEEE ST1A fast-acting static exciter [100][156]. To model the (turbine) governor actions, generators G5 and G9 are equipped with IEEEG3 hydro governor, whilst generators G1 and G2 have gas turbine governor GAST [199]. The rest of the generator governors are general steam governors IEEEG1. Notably, G9 is the only plant with a power system stabiliser (PSS). The mathematical representation of the power system components mentioned above, except for governors, have been described in Section 2.1.

The transmission network contains 72 branches with ten inter-area ties interconnectors between five areas (see Figure 5.1). Lines 42-46 connect NETS and NYPS, while lines 67, 72 and 70 connect NYPS with Areas 5 and 3, respectively. Likewise, line 69 connects Area 3 to Area 4, while line 68 connects Area 4 to Area 5. The complete data of the transmission network are presented in Appendix A, Table A.5. Moreover, loads in the test system are spread throughout the entire network; particularly, the P and Q demands follow the 24-hour curve in [200]. The most substantial loads are connected to the buses in areas 3, 4, and 5 ranging from 600 to 1,800 MW. The full details of the loads are presented in Appendix A, Table A.6.

## 5.2 Solution of TSSC-OPFwS by topology optimisation for transient stability

The condensed formulation of the TSSC-OPFwS problem (4.16)-(4.22) introduced in Section 4.4.1 is a large-scale, dynamic model containing a set of integral-differential-algebraic equations in both continuous and discrete variables. In particular, a two-stage solution procedure is proposed, shown in Figure 5.2, to solve the TSSC-OPFwS problem. The logic behind the proposed solution procedure can be applied without loss of generality. For instance, assume that the aim is to solve the problem  $\min f\{\mathbf{x}_1; \mathbf{x}_2\}$ , where  $\mathbf{x}_1$  and  $\mathbf{x}_2$  denote sets of variables attributed to the first and the second stage, respectively. By keeping variables  $\mathbf{x}_2$  constant at  $\bar{\mathbf{x}}_2$  in the first stage and solving  $\min f\{\mathbf{x}_1; \bar{\mathbf{x}}_2\}$  in  $\mathbf{x}_1$ , “optimal” values  $\bar{\mathbf{x}}_1$  are obtained. Then in the second stage, by solving  $\min f\{\bar{\mathbf{x}}_1; \mathbf{x}_2\}$  in  $\mathbf{x}_2$  new “optimal” values  $\bar{\mathbf{x}}_2$  are obtained. The final optimal solution  $\mathbf{x}_1^*, \mathbf{x}_2^*$  is reached when there are no changes in both sets of variables and all constraints are met [21].

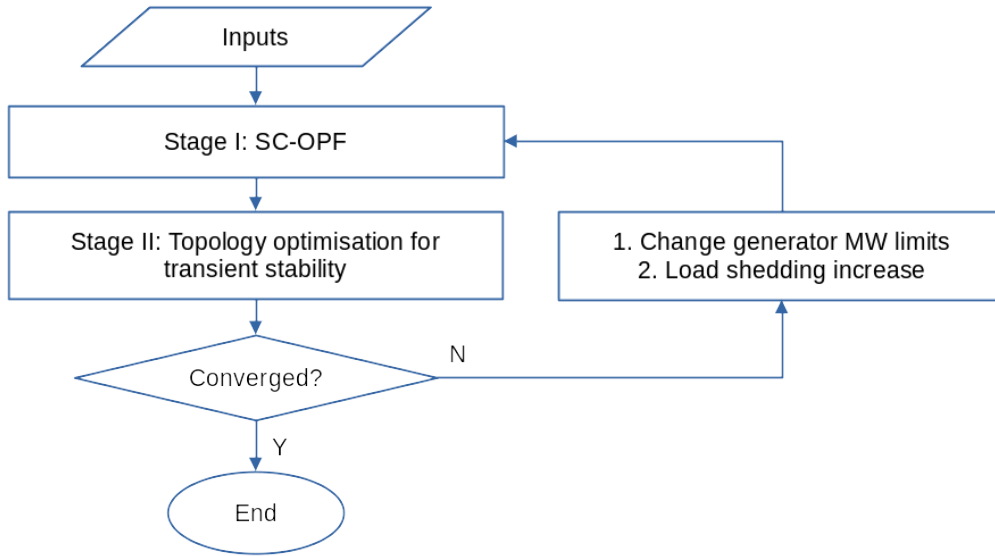


Figure 5.2: Two-stage solution procedure.

In solving the problem, the considered controls are active power dispatching with load curtailment as a last resort and network switching, both in preventive mode. In the first stage, the SC-OPF is solved for the fixed network topology, which is also obtained from the second stage during the iterative process. Optimal generations, load curtailments and nodal voltage magnitudes are input parameters, i.e., part of the vector  $\mathbf{p}^{k,f}$ , in the classical multi-machine structure preserving network model included (4.19) and (4.20); particularly, pre-fault SC-OPF generator voltage and active power dispatch are used to initialize the dynamical model (4.19). In the second stage, the network topology is optimised to achieve transient stability across all faults  $f \in \Omega_f$ . Iterative adjustments between the first and the second stage always consider generator MW rescheduling, i.e., reduction of MW limits/productions of unstable generators and possibly load shedding at centres close to unstable units. The convergence criteria are:

- i. There is no generation cost increase without additional load curtailment.
- ii. There is no change in the optimised network topology.

The output of the algorithm is a ranked list of solutions with minimum generation and load curtailment costs and network topologies, giving the best transient stability performance. The top solutions can be verified by running the full TDS.

An overview of the proposed optimisation using a genetic algorithm (GA) was introduced from the viewpoint of computational tools in Section 2.5; Figure 2.15 illustrates the processes involved in preparing, solving, and verifying optimisation results. Within this context, Figure 5.3 and Figure 5.4 describe the calculation of steady

state (pre-fault) data and the stability verification through TDS. For instance, the pre-fault data associated with different network structures are produced by the automated process shown in Figure 5.3; the figure illustrates how variables and parameters related to different network assets are generated as part of the OPF solution, that data is exported to the simulation engine to initialise dynamical models. In particular, parameters and variables from the initialised model are used to compute metrics later used in the methodology.

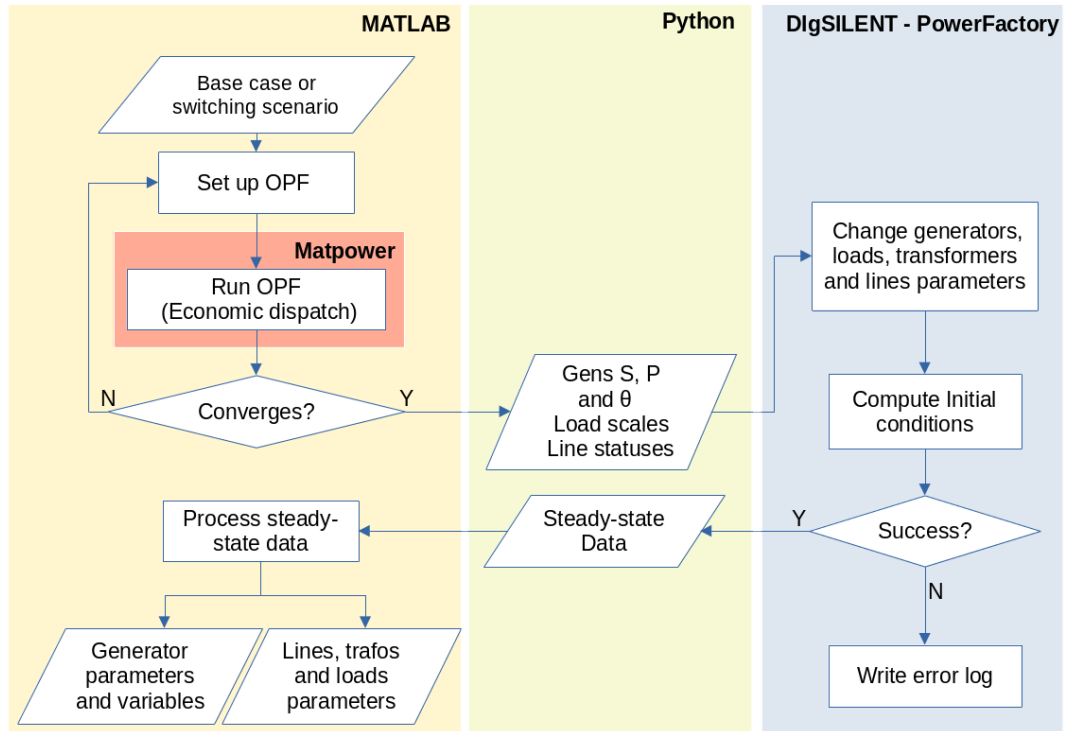


Figure 5.3: Flow chart of the pre-fault (steady state) data elaboration process

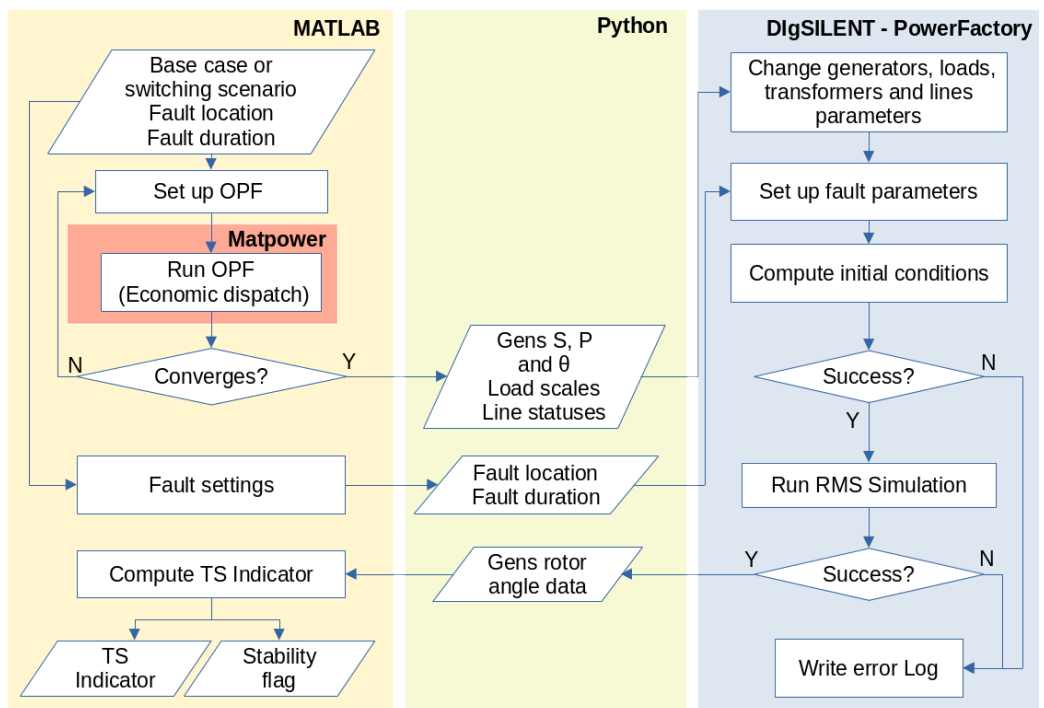


Figure 5.4: Flow chart of the transient stability verification process using TDS

Similarly, Figure 5.4 shows the automated process to validate an optimal network topology considering its transient stability level for a given fault condition and clearing time. The figure illustrates how the economic dispatch is used to define parameters which are input for the TDS; the simulation result given in the form of SGs rotor angle curves are used to calculate the transient stability level. Both processes are part of the method illustrated in Figure 5.5, shown as blue and green boxes.

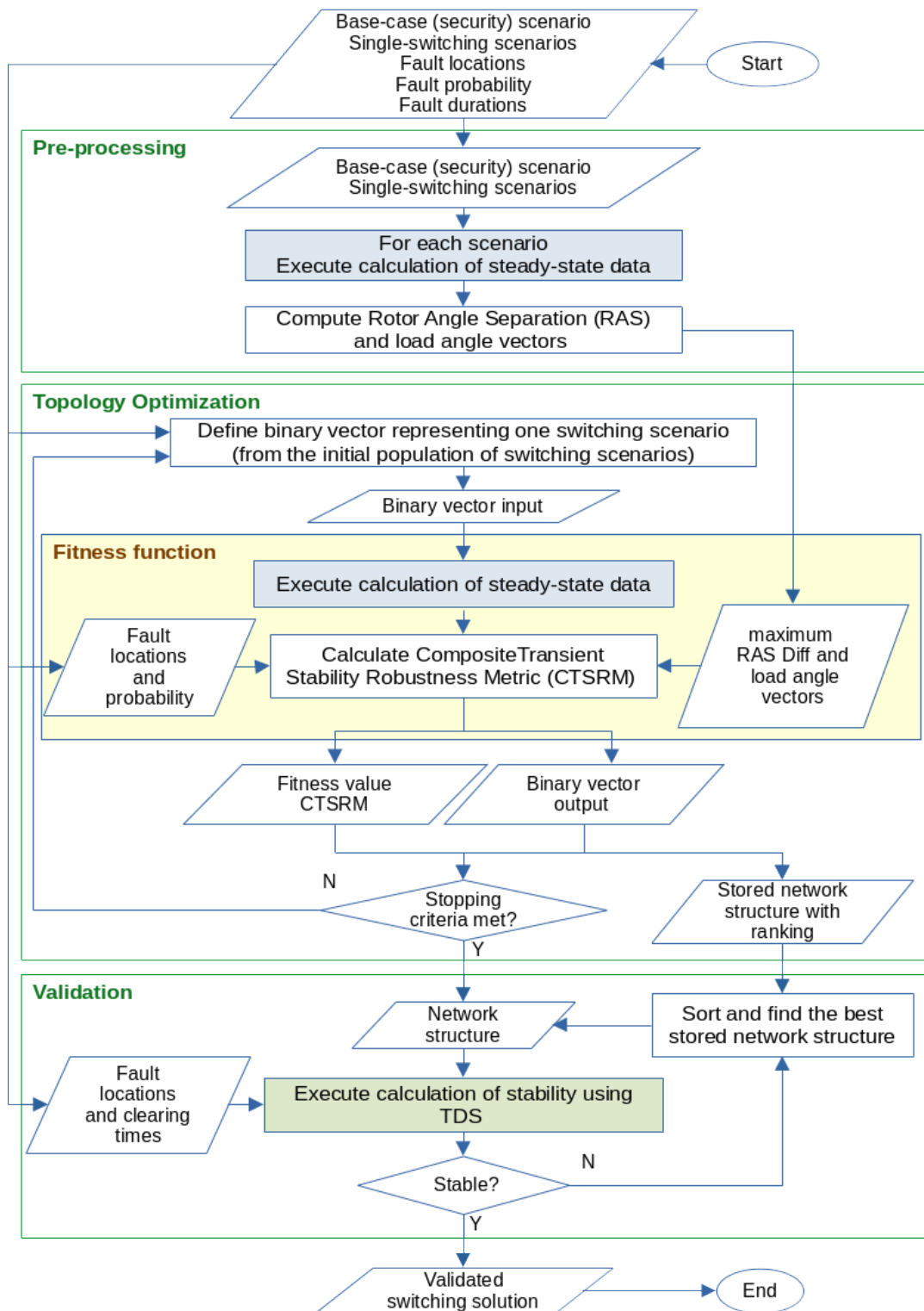


Figure 5.5: Flow-chart of topology optimisation for transient stability.

A simplified flowchart of the topology optimisation for transient stability is shown in Figure 5.5; the figure highlights three components (boxes with green borders), which are the building blocks of the proposed optimisation method. Firstly, the pre-process of steady state data block uses the process shown in Figure 5.3 to obtain SGs pre-fault variables, such as rotor angles with respect to the reference machine and loading angles, related to the base-case scenario (original topology) and different single-switching scenarios (original topology with different single-line-switching actions). Secondly, the topology optimisation block was designed to perform optimisation with GA. GA utilizes an initial population of switching scenarios, where each switching scenario is characterised by a vector of binary statuses of transmission lines; binary vectors are used to evaluate a fitness function, shown as a yellow box in Figure 5.5, which assigns a fitness value to each topology.

In particular, the GA stopping criteria are: when the maximum running time is reached, there are no more significant improvements on the solution, or there are no more potential switching scenarios to evaluate. Finally, the optimal topology (switching solution) validation using TDS is performed using the process illustrated in Figure 5.4. Particularly, the method ranks topologies using the fitness value; therefore, if the optimal network topology is not stable under the credible faults, the stored ranked topologies will be tested until finding a stable solution. More details about the components of the proposed method are given in sections 5.5 and 5.6.

### 5.3 Topology optimisation for transient stability

The topology optimisation problem for transient stability can then be stated as: find the network topology that maximizes the selected network robustness metric, i.e., improves transient stability, for all considered security cases and fault locations. Given that active power dispatch and load curtailments are determined in Stage I of Figure 5.2 and are constant in Stage II, the only available control is line-switching actions, so the objective function is:

$$z' = \max_{G^{k,f}(oc_{dmn}^k)} \left\{ \sum_k \pi^k \sum_f \pi^f \cdot R[G^{k,f}(oc_{dmn}^k)] \right\}; \quad (5.1)$$

$$\forall dmdn \in \Omega_l; \forall k \in \Omega_k; \forall f \in \Omega_f$$

Where the optimisation goes over all network graphs (or topologies)  $G^{k,f}(\cdot)$  defined by inputs  $k \in \Omega_k$  and  $f \in \Omega_f$ . As well as unknown branch statuses  $oc_{dmn}^k$  associated with

each branch  $dmdn \in \Omega_l$ ; a branch status  $oc_{dmdn}^k$  is one component of the switching vector  $\mathbf{oc}^k$  called switching scenario, which characterises the statuses (*on/off*) of all transmission lines in the system. Besides,  $\pi^k$  and  $\pi^f$  are security case  $k$  and fault  $f$  probabilities, respectively. In particular,  $R[\cdot]$  is a metric called *composite transient stability robustness metric* (CTSRM) that reflects the robustness of a network structure (topology) with respect to transient stability, which will be defined and assessed in sections 5.5 and 5.6.

For the topology optimisation, the following assumptions are used:

- i. To simplify the model, security cases  $k > 0$  are not initially studied. Base-case  $k = 0$  in conjunction with network faults  $f \in \Omega_f$  are analysed, which is often the practice in real-life. Modelling of cases  $k > 0$  in (5.1) may cause infeasible SC-OPF solutions [28] due to the formation of islands with unsupplied loads or the feasibility space being empty.
- ii. Metrics CTSRM,  $R[\cdot]$  in (5.1), described in detail in Section 5.5, are defined using the original network and the concept of composite robustness metrics [25].
- iii. Metrics CTSRM consists of two parts: the first quantifies the impact of topology changes on individual generators, including unit characteristics, whilst the second considers the impact of the network structure under a fault condition.
- iv. Within the discrete optimisation algorithm, infeasible switching scenarios, e.g., disconnected networks, are discarded from further analysis. The purpose is to provide a switching solution that maintains the integrity of a power system.
- v. All cases where the maximum rotor angle separation difference (see Section 5.4.3) is greater than the threshold value are excluded within the discrete optimisation.

## 5.4 Study of impact factors on transient stability

As explained in Section 2.4, the dynamic optimisation problem (4.16)-(4.22) is a hard problem to solve, especially due to the generator dynamics in the form of differential-algebraic constraints, described in Section 4.4.2, which also considers binary variables related to existing transmission lines. For this reason, a methodology requirement is that transient stability assessment (stage II of Figure 5.2) is completed without solving the dynamical model (4.19)(4.20) in the time domain.

A study based on the IEEE68 test system aimed to verify the influence of network structures reflected on transient stability impact factors to replace the transient inequality constraints (4.21); the idea is to select steady state variables and parameters (impact factors) influencing the transient stability performance of the system. To this end, the most important impact factors influencing transient stability are investigated to define a proxy measure in the form of the robustness function  $CTSRM, R[\cdot]$  in (5.1). Results from extensive probabilistic transient studies [187][192] are extended with additional simulations to capture the most important factors affecting transient stability; this was done only once in the research phase and is not repeated for different case studies. The studies of impact factors on transient stability are listed in Table 5.1.

Table 5.1 Studies of impact factors on transient stability

No.	Study
1	Impact of network structure
2	Impact of initial generation loading
3	Impact of rotor angle separation
4	Impact of inertia reduction
5	Impact of network topology metrics

The investigation of impact factors is based on TDS results using the IEEE68 Bus test system, described in Section 5.1; the analysis considered descriptive statistics and correlation analysis of impact factors with transient stability indicators, defined in Section 4.3 (see Table 4.1). The TDS settings were defined by combining three elements. Firstly, switching scenarios considering the original IEEE68 network structure (base-case identified as SWL0) and 72 derived topologies by introducing single-line-switching actions as switching scenarios (identified as SWL[Line number]). Though all possible line-switching actions were studied in this research, importance measures such as betweenness centrality [164] can be used to select relevant circuits in large scale networks. Secondly, 72 fault locations were defined by considering self-clearing bolted three-phase faults in the middle of each transmission line, as described in Section 2.3.2. Finally, fault durations equal to 0.10, 0.11, and 0.12 s, which are slightly longer than the 0.10 s specified in [24]. The number of simulations involved in the study is 15,339 cases; the original  $(72 \times 72 \times 3)$  cases had  $(71 \times 3)$  unfeasible switching scenarios. Correlation analyses between impact factors and transient stability indicators (see Table 4.1) are used to identify their influence on transient stability. Kolmogorov-Smirnov tests showed that transient stability indicators are not normally distributed, which means that commonly used Pearson correlation coefficients are not suitable; consequently, Spearman coefficients were selected as the correlation analysis tool. Spearman rank

coefficients provide a quantitative measure of the monotonic strength of relations; therefore, they are better suited for nonlinear correlations [194]. Notably, these results are used to define the proposed robustness metric CTSRM.

Specific test cases are used to demonstrate the influence of impact factors. For instance, fault cases with single-fault locations on Line47 and Line8 (marked in red in Figure 5.6) are used as test disturbances; these disturbances are combined with different topologies to highlight the effect of the network structure on a given factor. In particular, the comparison of different topologies uses the base-case scenario SWL0 and test switching scenarios with better transient stability performance, such as SWL4, SWL9 and SWL60 (marked in green in Figure 5.6), as well as SWL33, SWL26 and SWL70 with worse stability (marked in purple in Figure 5.6). Moreover, G14, G15, and G16 have been selected to verify the effect of inertia reduction as an impact factor (marked in light blue in Figure 5.6).

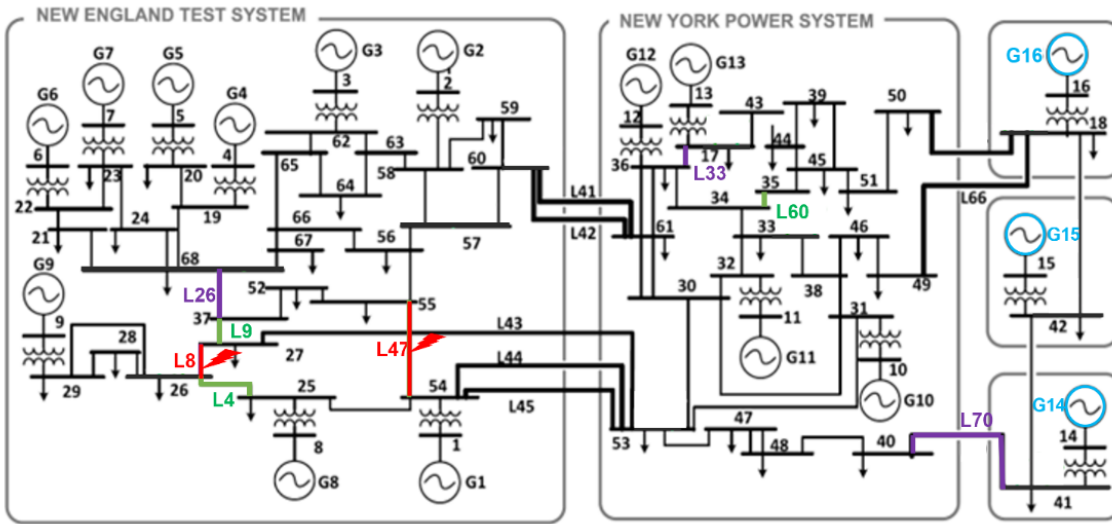


Figure 5.6: IEEE 68 bus test network showing line switching (purple and green), fault locations (red), and generation subject to inertia reduction (light blue) (adapted from [148][149]).

#### 5.4.1 Impact of network structure

The impact of different network structures has been assessed based on the same fault condition to identify relative differences in transient stability. A broad assessment considers the comparison of a base-case intact network (denoted as SWL0), the topology of the test system in Figure 5.1, and each derived switching scenario defined by 72 single-line-switching actions. The TSI defined in Section 4.3 is used as the stability indicator.

Figure 5.7 illustrates TSI results for  $t_{cl} = 100 \text{ ms}$ , where each row corresponds to a fault location and each column to a switching scenario. The colour scale on the right describes



TSI values  $[-100\%$  (*dark blue*),  $+100\%$  (*deep green*)] on steps of 20%; greener colour indicates more stable behaviour, whilst darker blue is more unstable. The green column on the left-hand side of Figure 5.7 displays TSIs for faults on the base-case network SWL0, whilst the yellow-green squares on the right-hand side represent TSIs of switching scenarios (columns). For instance, for a fault on Line47, the TSI for the base-case network is 57.28%, but for the network with Line4 switched off (SWL4), the TSI is 66.66%, which is an improvement of 9.38%. On the other hand, in the case of a fault on Line8, the TSI of the base-case is 56.89%, whereas, for the SWL33, the TSI is -53.42% indicating unstable behaviour. In particular, initial conditions switching out Line39 could not be obtained; therefore, the corresponding switching action was discarded, shown as a black column in Figure 5.7.

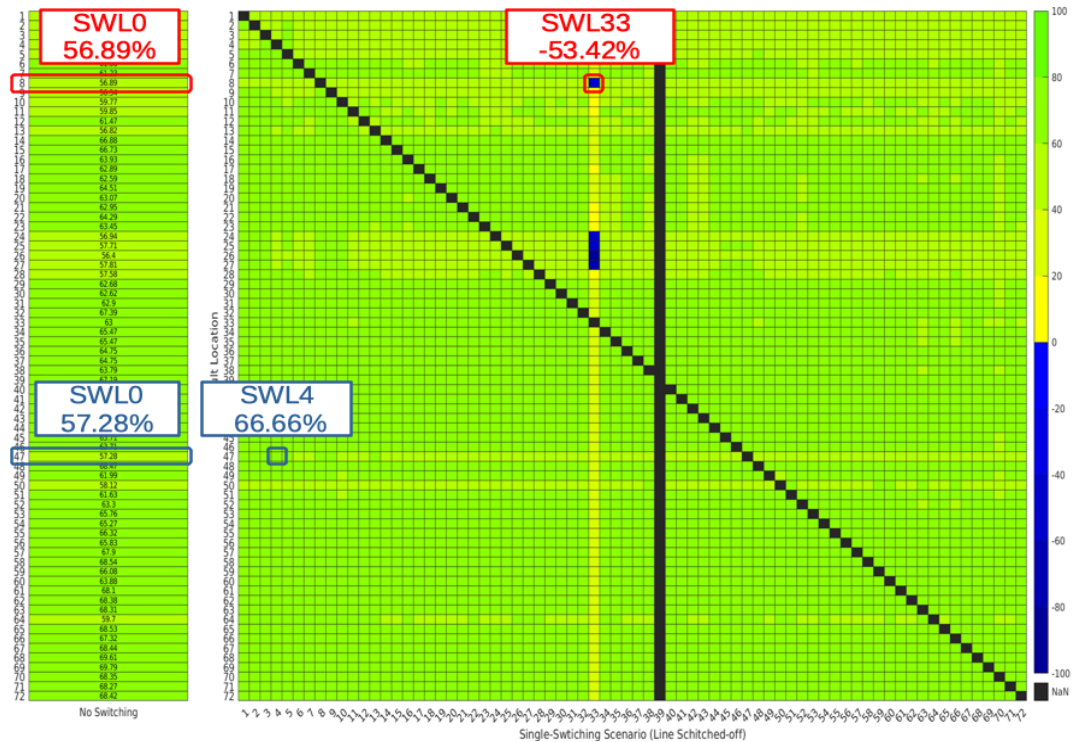


Figure 5.7: TSI results for different faults (y-axis) and switching scenarios (x-axis) of the IEEE68 Bus test system with clearing time of 100 ms.

A detailed comparison between each network structure and the base-case SWL0 considering a given fault can be seen in Figure 5.8. The figure illustrates the comparison of TSI results between each switching scenario and the base-case network using the difference between the two TSI evaluations; the colour scale on the right describes TSI difference values  $[-100\%$ ,  $+100\%$ ] on steps of 20%; greener colour indicates more positive difference (better improvement), whilst darker blue indicates a detrimental effect. For example, the TSI differences with 100 ms of fault clearing shown in Figure 5.8 depicts a similar proportion of fault cases with a positive (yellow-green colour) and negative (blue colour), which suggests that there are several switching scenarios

improving the stability level, in comparison with the original network structure of the IEEE68 bus test system. In particular, the methodology proposed in this thesis, described and assessed (see sections 5.5 and 5.6.), can capture transient stability improvement and deterioration.

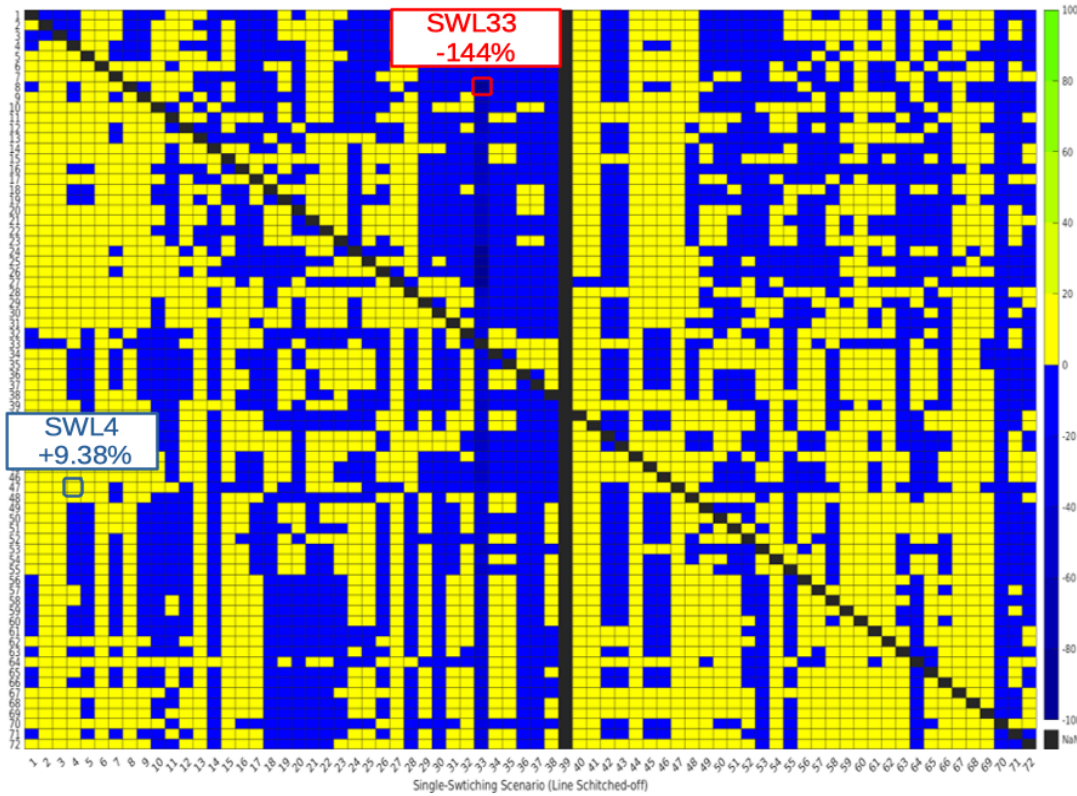


Figure 5.8: TSI difference between single-switching scenarios and SWL0 for the IEEE68 Bus test system with clearing time of 100 ms.

A summary of the time-domain TSI results considering three fault clearing times is shown in Table 5.2. The preliminary finding is that different network topologies can either reduce or improve transient stability results for a given fault case; therefore, there is a scope for topology optimisation. Time-domain analyses of a large number of switching scenarios (topologies) have shown that transient stability performance is better in more than 50% of cases, when compared with a base-case topology without analysing the magnitude of the improvements; therefore, line-switching can be considered as a preventive control measure with the potential of improving the network robustness from the transient stability viewpoint.

Table 5.2 Impact of switching scenarios based on TSI

$t_{cl}$ (ms)	Cases TS Increase	% Cases with better TS	Cases TS Reduction	% Cases with worse TS
100	2756	54.7	2285	45.3
110	2685	53.3	2356	46.7
120	2763	54.9	2278	45.1

### 5.4.2 Impact of initial generation loading

The steady state equilibrium requires that the mechanical power input must be equal to the electrical power output; therefore, a higher loading implies that an SG will operate closer to its maximum capacity [21]. Moreover, the effect of higher loading on synchronising power explained in Section 1.3.6 reduces the synchronising torque [21], which can lead to aperiodic drift [20]. The loading of SGs is reflected in the load angle, which is the angle between the internal EMF and terminal voltage [21]. In this thesis, the effect of pre-fault (steady state) generator loading was studied using the variable *fipol* (angle difference between the an SG q-axis and its terminal voltage) from DIgSILENT PowerFactory [170], which is the angle between a generator terminal voltage and its q-axis. Note that these angles can be retrieved by executing the process described in Figure 5.3.

Initially, differences in pre-fault load angles and TSI results between test switching scenarios and the base-case SWL0, for faults on lines 8 and 47, were used to analyse the effect of generator loading and its impact on transient stability. Figure 5.9(a) depicts the pre-fault load angles of switching scenarios reducing transient stability (dashed lines) and improving transient stability (solid lines). The figure shows that for some SGs, the topologies improving transient stability have smaller load angles, whereas those reducing the stability have larger angles compared to the base-case SWL0 (red line). Moreover, Figure 5.9(b) shows the difference between load angles corresponding to the test switching scenarios with respect to the base-case; it can be seen that most of the differences are negative for several test switching scenarios (solid lines), which means that there is a relationship between smaller load angles and stability improvements.

Comparison based on test switching scenarios is also presented in Table 5.3; relative differences are calculated between results of test switching scenarios (first column) and base-case SWL0. The table contains an aggregation in the form of a summation of pre-fault load angle differences (second column) and average TSI differences (third column) considering evaluations with fault on Line8 and Line47. As expected, results based on test switching scenarios presented in Table 5.3 suggest that there is an influence of the pre-fault load angles, considering the difference between a switching scenario and the base-case, on the stability result. For instance, unstable switching scenario SWL33 has a positive summation of *fipol* difference of 22.46 degrees, which implies an increase in machine loadings, with a negative effect on transient stability confirmed by the large

negative TSI difference of -72.67%. Conversely, SWL4 shows a negative summation of *fipol* differences -9.68 degrees with a positive TSI difference 4.53%, suggesting an improvement in transient stability. Notably, all test switching scenarios with positive TSI differences have negative pre-fault load angle differences (see Table 5.3), suggesting that switching scenarios reducing the load angles can have better transient stability compared to the base-case network. The finding aligns with the description of the initial loading effect on transient stability [20].

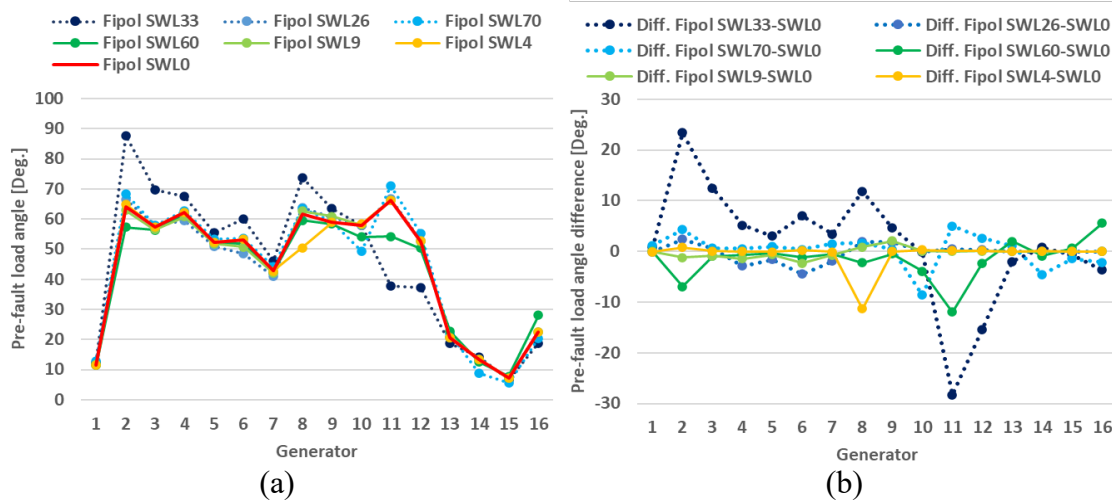


Figure 5.9: Generator pre-fault (steady state) load angles *fipol* (a) and *fipol* differences against base-case SWL0 (b) of IEEE68 test switching scenarios.

Table 5.3 Comparison of test switching scenarios based on summation of pre-fault load angle differences and TSI results for faults on Line8 and Line47

Switching scenario	Summation of load angle difference	Average TSI difference
SWL33	22.46	-72.67
SWL26	-3.35	-5.89
SWL70	3.64	-2.48
SWL60	-24.19	1.16
SWL9	-4.08	3.69
SWL4	-9.68	4.53

The preliminary finding of the effect of pre-fault loading on transient stability was also confirmed by a study considering TDS results. The impact of initial generator loading for unstable cases was analysed using the pre-fault load angles shown in the box plot of Figure 5.10. It was found that the highly loaded SGs lose stability in the first swing (“First Group” in Figure 5.10), whilst less loaded units can become unstable later (“Second Group” in Figure 5.10). The figure indicates that unstable switching scenarios with highly loaded SGs lose stability faster than those less loaded; in fact, it is possible to see that there is a pre-fault load angle band  $\sim[50^\circ - 60^\circ]$  separating the bulk of each group (dashed green lines in Figure 5.10), which will be later used for the CTSRM metrics to account for the effect of the initial loading threshold on the transient stability level. In

summary, that pre-fault steady state conditions can give invaluable insight into the potentially unstable generators; remarkably, a switching scenario increasing the pre-fault SG loading is more likely to have unstable results in comparison with the one where SGs are less loaded.

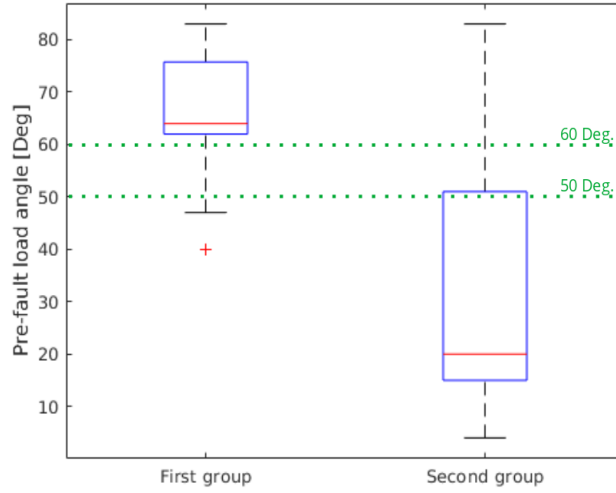


Figure 5.10: Box plot of pre-fault generator load angles.

### 5.4.3 Impact of rotor angle separation

In this thesis, for stability studies based on TDS, the angle difference between a unit  $q$ -axis and the reference unit  $q$ -axis is called rotor angle separation (RAS). In particular, the effect of RAS was studied using the variable *firel* (angle difference between the SG  $q$ -axis and the  $q$ -axis of the reference machine) from DIgSILENT PowerFactory [170], which follows the previous description; note that these angles can also be retrieved by executing the process described in Figure 5.4.

Initially, the effect of network structure on RAS was studied using the pre-fault difference of RAS between test switching scenarios and the base-case SWL0, called RAS Difference (5.2), which is related to each SG.

$$\Delta\delta_{gi}^{s,0}(t_0^-) = \delta_{gi}^{s>0}(t_0^-) - \delta_{gi}^{s=0}(t_0^-) \quad (5.2)$$

Here, superscript  $s \in \Omega_k$  is applied to differentiate between security cases  $k$  and single-line switching  $s$  ( $s = 0$  denotes base-case SWL0); and  $\delta_{gi}^{s>0}(t_0^-)$  is generator  $gi$  RAS for a switching scenario  $s > 0$  at steady state  $t_0^-$ . Accordingly, pre-fault RAS differences were calculated for test switching scenarios; results are shown in box plots of Figure 5.11(a). In particular, switching off Line 33 (denoted as SWL33) gives unstable topology and produces a large increase in RASs of all generators with a median of 67.8 degrees (left-side scale). All other switching scenarios are stable and have RAS differences within  $\sim \pm 5$  degrees (right-side scale). Moreover, negative differences in TSIs shown in

Figure 5.11(b) indicate that SWL33 has the worst performance reducing the stability level in all fault cases based on the IEEE68 test network; conversely, switching scenarios that improve transient stability, like SWL60, SWL9 and SWL4, have positive medians of TSI differences. Interestingly, two scenarios, SWL26 and SWL70, which have RAS differences similar to the scenarios with improved transient stability (see Figure 5.11(a)), have reduced stability and negative TSI medians; this is due to sustained or even growing long-term oscillations, which are difficult to predict using pre-fault SG variables.

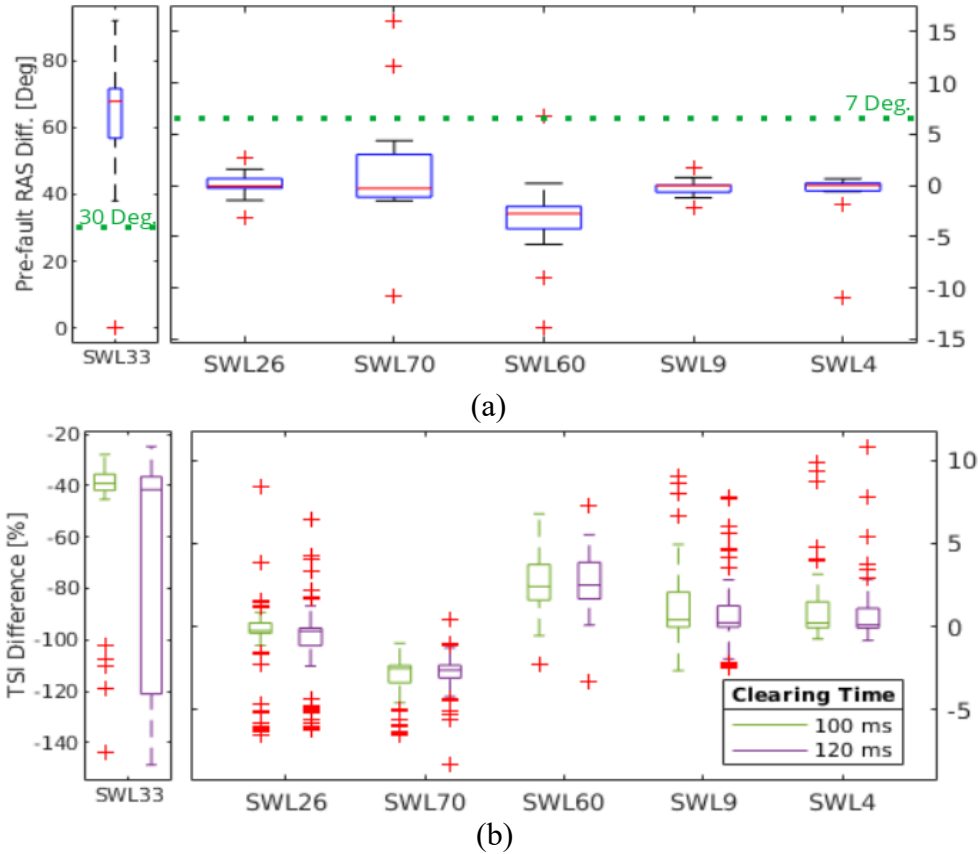


Figure 5.11: RAS difference (a) and TSI difference (b) between test switching scenarios and the base-case SWL0.

Results shown in Figure 5.11(a) indicate that it is possible to establish a threshold of around 7 degrees on the pre-fault RAS difference of SGs as a limit between stable and unstable results; in particular, pre-fault RAS difference of all stable test switching scenarios are under 7 degrees. Figure 5.11 also suggests a link between RAS differences and TSI; in practical terms, the switching will likely be detrimental to transient stability if a line switching action has a large RAS difference. Even though the observations apply to the IEEE68 system, a similar analysis can be performed on a different system to establish the pre-fault RAS difference threshold.

Moreover, a correlation analysis between RAS and ISGA gives a Spearman correlation coefficient of 0.59, whilst ISGA has a Spearman correlation coefficient of -0.52 with

TSI. These correlation results indicate that ISGA is negatively correlated with stability effects because highly oscillatory responses have large ISGA and smaller TSI; besides, RAS has a moderate positive correlation with ISGA, which means that having a larger RAS can produce higher oscillatory behaviour. Consequently, the analysis based on the IEEE68 test system suggests that a larger RAS influences oscillatory behaviour, which can be considered detrimental from the transient stability viewpoint.

As suggested above, the pre-fault RAS can impact the transient stability outcome, as they reflect the relative rotor position prior to the fault; this fact was confirmed with a comprehensive analysis comparing pre-fault RAS and TSI differences between all (72) switching scenarios and SWL0. The bar plot in Figure 5.12(a) illustrates the summation of pre-fault RAS differences (against the base-case SWL0) related to each switching scenario; the difference corresponding to each generator is shown in a different colour. Figure 5.12 shows how line-switching can increase or decrease the RAS difference; in particular, it can be seen that SWL33 has a significant impact on increasing the RAS of all generators, followed by SWL63, SWL66, SWL72, and SWL70.

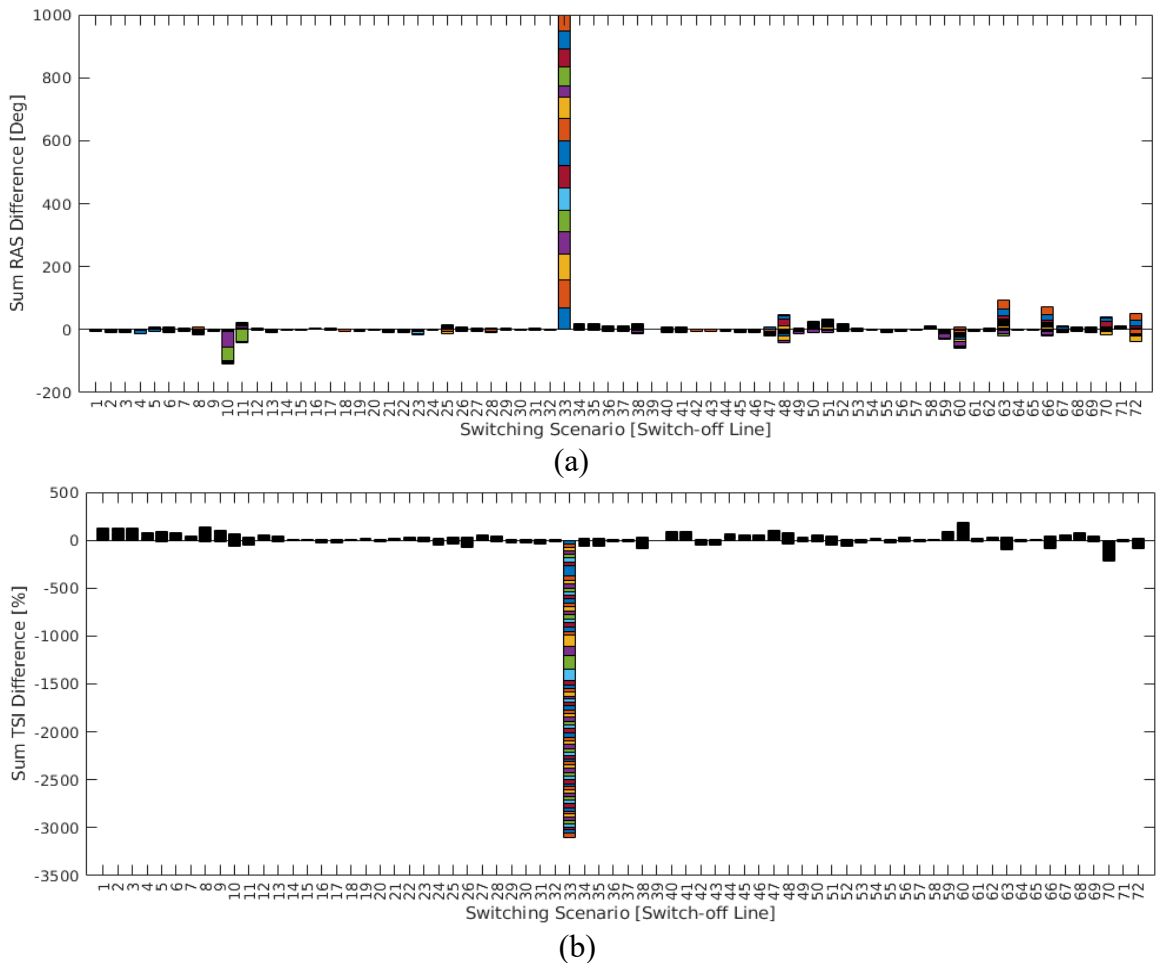


Figure 5.12 Bar plots of pre-fault RAS difference (a) with a different colour for each SG. TSI evaluations (b) where each colour represents a different fault location with  $t_{cl}=100$  ms.



The corresponding effect between pre-fault RAS and TSI differences (also against the base-case SWL0) can be seen in the bar plot in Figure 5.12(b), which has each fault location in a different colour. The comparison of TSI differences in Figure 5.12 indicates that SWL33 also has the largest pre-fault RAS and the worst performance from the TS perspective, with a similar assessment for SWL63, SWL66, SWL72, and SWL70. In summary, the RAS difference (5.2) is a good indicator for identifying the best switching scenarios candidates for improving transient stability for a given fault. Moreover, the comparison of all switching scenarios has shown that a significant difference in generator pre-fault rotor angles with respect to the base-case is a good indicator of unstable generators.

#### 5.4.4 Impact of inertia reduction

The analysis of inertia reduction was done by reducing the machine ratings of G14-G16 (blue colour in Figure 5.6) to 25%, 50%, and 75% of their original value; the study combined the analysis of the topological effect through switching scenarios with low inertia scenarios. Similar to the previous section, the combination of network structures and inertia reduction was analysed using RAS angles with quantity *firel* from DIgSILENT PowerFactory [170], obtained with the process described in Figure 5.4. In this case, the study involved the measurement of the maximum deviation between SG RASs called RAS coherence (5.3), which is the difference between the largest and the smallest SG RAS at a given point in time [36].

$$RAS\ Coherence^s = Max_{gi,t}\{\delta_{gi}^s(t)\} - Min_{gi,t}\{\delta_{gi}^s(t)\}; \forall gi \in \Omega_g \quad (5.3)$$

Here, superscript  $s \in \Omega_k$  identifies the switching scenario, and  $\delta_{gi}^s(t)$  is generator  $gi$  RAS as a function of time. Given that inertia is defined on machine levels, the inertia reduction was introduced by changing SG ratings of Gen14-Gen16 in proportion to the desired reduction.

From the pre-fault stage ( $t = 0^-$ ), the combination of line-switching actions with inertia reduction impacts the coherence, as depicted in Figure 5.13(a). For 25% of the original inertia ( $0.25J$  in blue bars), all RAS coherence are greater than 120 degrees, reflecting a significant increase compared with the original inertia ( $1J$  in purple bars). The figure also shows that the inertia reduction of smaller magnitude, such as 50% or 75% ( $0.5J$  and  $0.75J$  in orange and yellow bars, respectively) has a small effect on the coherence in the steady state of test switching scenarios with respect to SWL0, except for SWL33. As



described in the previous sections, SWL33 involves a line-switching action that imposes significant changes on SG loadings, which is consistent among different inertia levels.

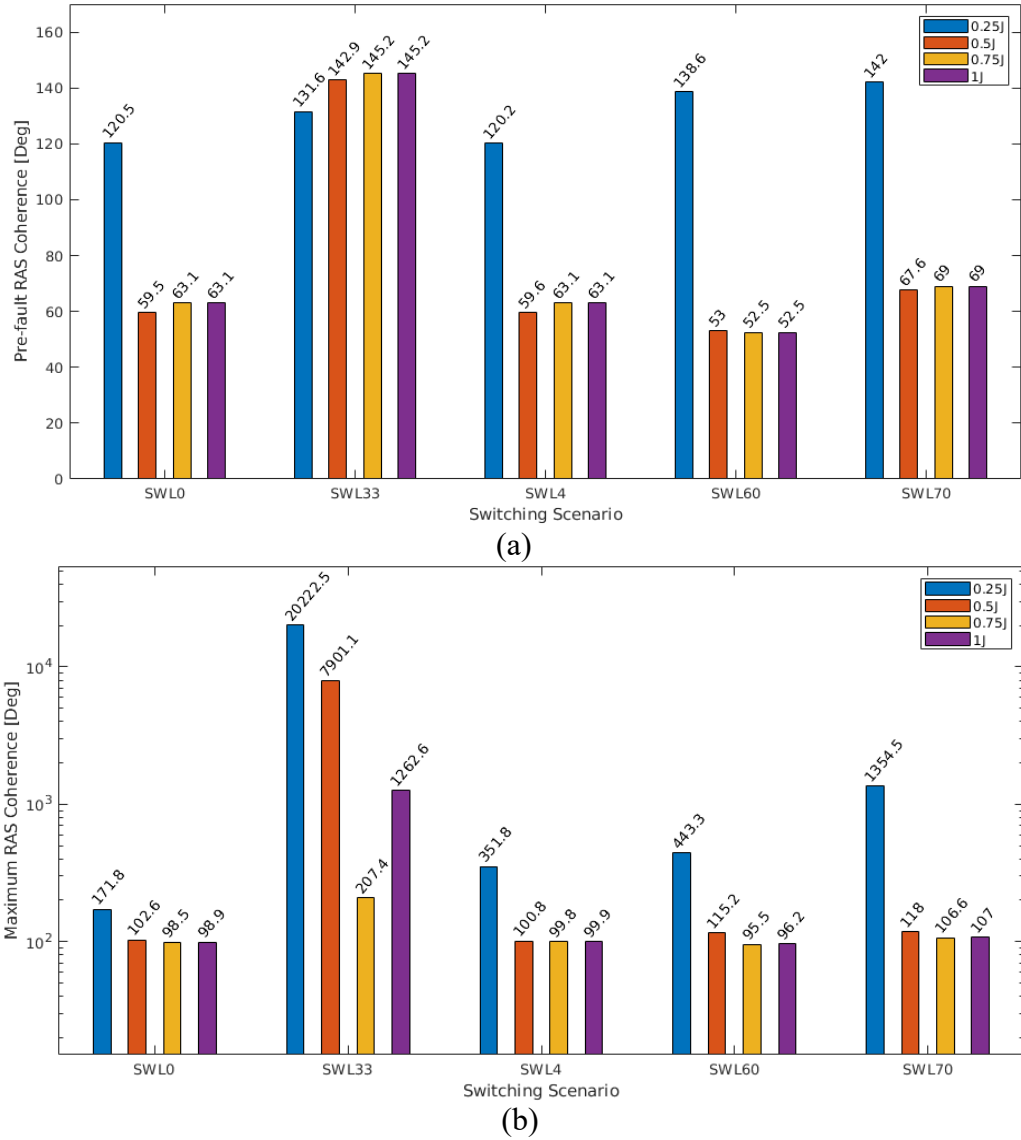


Figure 5.13: Pre-fault (a) and maximum (b) RAS coherence for a fault on Line8 with  $t_{cl}=100$  ms. considering inertia reduction of G14-G16. The y-axis of (b) is on a logarithmic scale.

Studying the post-fault period ( $t > 0$ ), the analysis of the maximum RAS coherence gives insight into the stability effect of the combination of topology and inertia factor; the maximum coherence is given for a time instant where (5.3) is the largest. Stable and unstable results can be seen in Figure 5.13(b) using a logarithmic scale. With the exception of SWL4, the maximum RAS coherence indicates that all test switching scenarios have unstable results for the scenario with 25% of original inertia (0.25J in blue bars) i.e., maximum relative angle difference greater than 360 degrees. In particular, for SWL33, the inertia reduction causes the loss of synchronism for the 25%, 50% and 100% levels of inertia, but the cause is intrinsically related to changes in machine loadings which push some machines closer to the instability boundary. In switching

scenarios like SWL60 and SWL70, the loss of synchronism is due to the deceleration of Gen16 and Gen14. On the other hand, stable results can be seen in cases of 50% and 75% of original inertia; all switching scenarios are stable, except for SWL33, for an inertia level of 50%. Figure 5.13(b) suggests that the stability level can be equal or even better for 75% of the original inertia in comparison with the original level; this finding is aligned with recent Monte Carlo studies indicating that up to 55% CIG penetration, replacing partial SG rating level with inertialess CIG, decreases the number of instabilities [26][192]. In summary, analysis of several switching scenarios has shown that inertia plays an important role in transient stability; however, scenarios with lower inertia do not always produce more unstable results. A combination of lower inertia and larger pre-fault RAS is an adverse factor that can lead to instability, as seen in Figure 5.13; therefore, the inertia level will be considered, combined with other factors, on the proposed CTSRM.

#### **5.4.5 Impact of network topology metrics**

Chapter 3 introduced the study of the topological effect based on two small test systems where it was possible to show the impact of line-switching actions, i.e., defining different topologies, on transient stability. On a larger scale, real networks have complex structures, usually providing more than one path between any given pair of buses; hence, foreseeing the impact of line-switching actions on transient stability is not a simple task. In particular, the study presented in this section aims to provide topology metrics useful to estimate stability results, which are included in the proposed CTSRM.

From the network theory perspective, network robustness can be defined as the ability to tolerate the loss of a fraction of vertices (nodes) or edges (branches) [164]; in other words, a network is robust if it can continue operating when it is subject to component failure. From the network perspective, paper [147] offers a comprehensive review of robustness metrics; similarly, in the power systems literature, the contributions presented in [149][153][154] introduced network metrics for the analysis of power systems robustness against cascading failures. Some of the most relevant topology metrics are presented in Table 5.4. Noteworthy is the fact that in the reviewed literature, the application of topology metrics in power systems is scarce; to the author's best knowledge, the use of topology metrics in the context of transient stability is virtually non-existent.

The purpose of the study of topology metrics was to verify how well a given metric can map the effect of a given network structure with a transient stability result, i.e., how well a topology metric can characterise the incremental or detrimental effect of a network structure from the transient stability viewpoint. The computational burden of topology metrics was also considered; thus, more straightforward metrics are preferred over those requiring longer computation time. In this thesis, relevant topology metrics found in power systems literature such as ADG, AEG, ABG, and ASPLG (see Table 5.4) were complemented with the average shortest path length between a fault location to all generator nodes (ASPLFG). Correlation analyses between transient stability indicators and relevant topology metrics using Spearman rank coefficients (see Table 5.5) provided insight into the monotonicity of the relationships based on 15,339 TDS results,  $(72 \times 72 \times 3)$  combinations with  $(71 \times 3)$  unfeasible switching scenarios.

Table 5.4 Network topology metrics

Metric	Id	Research area	Description
Average shortest path length [147]	ASPL	Network theory	Average of the minimum path distance between every pair of nodes. Each edge has its “length”, which is dependent on the application.
Average node degree [147]	AD	Network theory	Average of the number of links connected to every node.
Betweenness centrality [147][149]	BC	Network theory	A measure of the importance that a node plays between other nodes. Based on the number of shortest paths between any pair of nodes passing through the node under analysis.
Efficiency [147]	EFF	Network theory	Defined by the reciprocal of the shortest path distance between nodes, it reflects how efficiently the information is exchanged between nodes.
Average degree of generators [154]	ADG	Power systems	Average node degree of generator nodes.
Average efficiency of generators [154]	AEG	Power systems	Average shortest path distance between generators and all other nodes in the network.
Average betweenness of generators [154]	ABG	Power systems	Betweenness centrality of generator nodes.
Average SPL of generators [154]	ASPLG	Power systems	Average shortest path distance between all generator nodes.

Though the correlation coefficients are low, the assessment of relevant metrics in Table 5.5 indicates that comparatively, ASPLFG, ASPLG and ABG would be more appropriate to evaluate the effect of the network topology on TS. In particular, ASPLFG provides insight into the impedance between a fault location and generators; for instance, if the network structure increases the impedance between the fault and a critical generator, it will decrease the acceleration of the machine due to a smaller voltage drop, which

reduces the severity of the disturbance. Similarly, ASPLG provides information about the increase of the impedance between generators, which affects synchronising and damping power; in this case, if the network structure increases the impedance between close critical generators, the ability to synchronise and reduce rotor angle oscillations is going to decrease. Even though ABG has a better correlation with TSI in comparison to ASPLG, the latter is selected together with ASPLFG due to its simplicity.

Table 5.5 Spearman correlation coefficient between transient stability indicators and network topology metrics

Transient stability Indicator	ADG	ABG	AEG	ASPLG	ASPLFG
TSI	0.07	0.17	-0.04	-0.13	0.32
ISGA	-0.28	-0.22	0.24	0.18	-0.1
DOT1	0.06	-0.08	-0.11	0.01	-0.49
DOT2	0.15	0.04	-0.22	-0.09	-0.63
DOT3	0.07	-0.07	-0.1	-0.02	-0.51

#### 5.4.5.1 Distance between Fault and Generators

It is known that the larger the electrical distance between a fault location and generators, the more stable generators are [21]; this fact was analysed and confirmed in the context of SMIB test systems in Chapter 3. Moreover, results in Table 5.5 indicate that the shortest path distance between the generators and a given fault location is important. Nonetheless, the number and distances of other paths between them also play an important role in larger networks because multiple paths can increase the exposure of generators to the post-fault condition; therefore, a study based on a realistic network structure was needed. For clarity and following the naming convention of Chapter 3, the impedance between generators and a fault location is called *distance between fault and generators* (*DFG*).

The study included the comparison of three computations of *DFG*, to analyse the effect of considering a different number of parallel paths. For all computations of *DFG*, the fault location  $f$  is in the middle of an actual transmission line, with  $fta$ , and  $ftb$  as line terminals buses. As the fault is located in the middle of a line, the distance is calculated to the closest terminal bus ( $fta$  or  $ftb$ ). Based on the graph representation of a switching scenario under fault condition, *Avg. DFG 1SP* (5.4) is the average of distances between generators and a fault location based on the impedance of the shortest path computed by Dijkstra's algorithm, previously defined in Section 2.2.3. Similarly, *Avg. DFG 2SP* (5.5) is a similar average, but it is based on a parallel connection of two shortest paths to a faulty transmission branch, where the second shortest path  $[DFG1_{gi}^f(\mathbf{oc}^k)]''$  was again

calculated with Dijkstra's algorithm. The *Avg.DFG ED* (5.6) follows a different approach using the Thevenin equivalent impedance between nodes, described in detail in Section 2.2.3.1; it is the average of electrical distances between generators and fault locations end-nodes, which reflects all parallel paths.

$$\begin{aligned}
 Avg.DFG\ 1SP^{k,f} &= \frac{1}{NG} \sum_{gi \in \Omega_g} DFG1_{gi,lt}^f(\mathbf{oc}^k); \\
 &\forall gi \in \Omega_g; \forall f \in \Omega_l; \forall k \in \Omega_k; \forall f \in \Omega_f \\
 DFG1_{gi,f}^f(\mathbf{oc}^k) &= \min_{paths\ gi,(fta \vee ftb)} \left\{ |Z|_{gidm} \right. \\
 &\quad \left. + \sum_{dmdn \in path\ gi,(fta \vee ftb)} |Z^{k,f}|_{dmdn} oc_{dmdn}^k \right\}; \\
 &\forall gidm \in \Omega_{gl}; \forall gi \in \Omega_g; \forall dmdn, f \in \Omega_l; \forall k \in \Omega_k; \forall f \in \Omega_f
 \end{aligned} \tag{5.4}$$

$$\begin{aligned}
 Avg.DFG\ 2SP^{k,f} &= \frac{1}{NG} \sum_{gi \in \Omega_g} DFG2_{gi}^f(\mathbf{oc}^k); \\
 &\forall gi \in \Omega_g; \forall f \in \Omega_l; \forall k \in \Omega_k; \forall f \in \Omega_f \\
 DFG2_{gi,f}^f(\mathbf{oc}^k) &= [DFG1_{gi,f}^f(\mathbf{oc}^k)]' \wedge [DFG1_{gi,f}^f(\mathbf{oc}^k)]''; \\
 &\forall k \in \Omega_k; \forall f \in \Omega_f
 \end{aligned} \tag{5.5}$$

$$\begin{aligned}
 Avg.DFG\ ED^{k,f} &= \frac{1}{NG} \sum_{gi \in \Omega_g} DFG3_{gi}^f(\mathbf{oc}^k); \\
 &\forall gi \in \Omega_g; \forall f \in \Omega_l; \forall k \in \Omega_k; \forall f \in \Omega_f \\
 DFG3_{gi,f}^f(\mathbf{oc}^k) &= \min_{gi,f} \left\{ Z_{gi,gi}^f(\mathbf{oc}^k) + Z_{fta,fta}^f(\mathbf{oc}^k) - 2Z_{gi,fta}^f(\mathbf{oc}^k) \right\}; \\
 &\quad \left\{ Z_{gi,gi}^f(\mathbf{oc}^k) + Z_{ftb,ftb}^f(\mathbf{oc}^k) - 2Z_{gi,ftb}^f(\mathbf{oc}^k) \right\}; \\
 &\forall gi \in \Omega_g; \forall f \in \Omega_l; \forall k \in \Omega_k; \forall f \in \Omega_f
 \end{aligned} \tag{5.6}$$

The correlation analysis between *DFG* metrics and transient stability indicators, shown in Table 5.6, suggests a high positive monotonic correlation between *Avg.DFG ED* and TSI; it also reflects negative counterparts with dot products and ISGA. The monotonic correlation between *DFG* and transient stability indicators supports the finding that larger *DFG* improves transient stability.

Table 5.6 Spearman correlation coefficients between DFG metrics and transient stability indicators

DFG metrics	TSI	Dot1	Dot3	ISGA
Avg. DFG 1SP	0.37	-0.36	-0.36	-0.28
Avg. DFG 2SP	0.39	-0.35	-0.36	-0.27
Avg. DFG ED	0.80	-0.79	-0.78	-0.41

Based on the transient stability assessment presented in Section 5.4.1, it is possible to classify different combinations of switching scenarios and fault conditions into two groups. The group *BetterTSI* represent those switching scenarios with better transient stability, compared with SWL0, for a given fault location; the opposite applies for the combinations assigned to the group *WorseTSI*. The results of computation procedures of *DFG* are presented in Figure 5.14; they summarise fault cases with clearing times of 100, 110, and 120 ms; the figure shows the means and 95% confidence interval [178] of *DFG* metrics using 1SP, 2SP and ED. Figure 5.14(a) and (b) shows that the means related to *BetterTSI* and *WorseTSI* groups have a significant overlap for 1SP and 2SP, which makes transient stability improvement or deterioration harder to distinguish. On the contrary, differentiation between groups is more accurate using *Avg. DFG ED* due to the difference between the mean of the two groups in Figure 5.14(c).

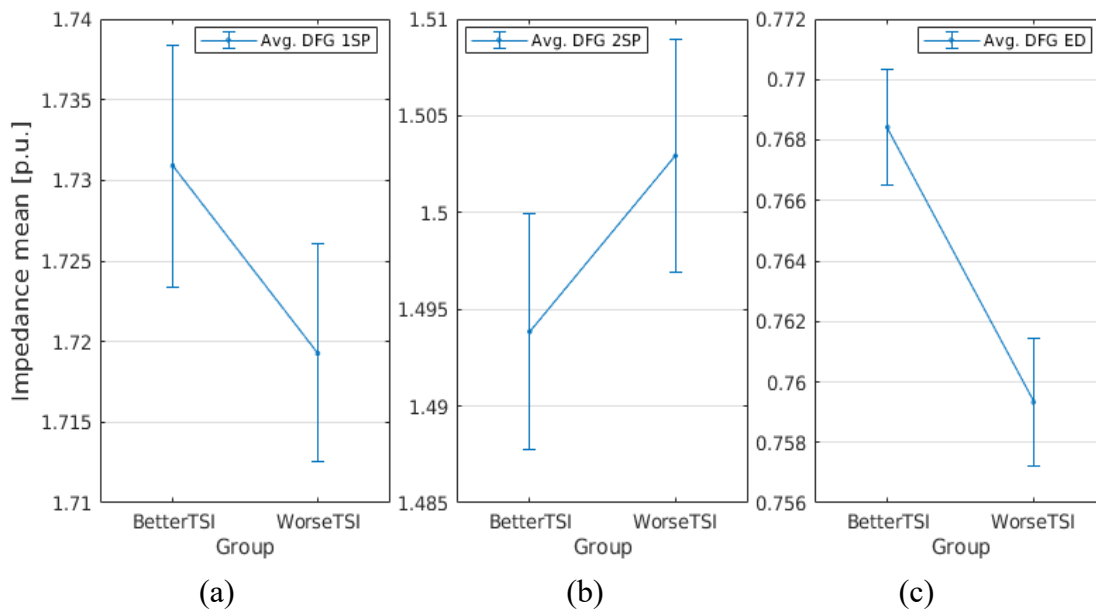


Figure 5.14: Average DFG impedance means of better and worse TSI groups with 95% confidence intervals based on shortest path (a), two shortest paths (b) and electrical distances (c).

The results in Figure 5.14 were also confirmed by two-sample (*BetterTSI* or *WorseTSI*) statistical *t-test* [178] to verify the difference between the mean of groups; it was found that within each computation the means were statistically different; however, higher support rejecting the null hypothesis, i.e., statistical difference between the means with  $p\text{-value } 5.47 \times 10^{-10}$  (the lower the  $p\text{-value}$ , the more significant the

difference between means) was found for *Avg.DFG ED*, confirming that it is better suitable to discriminate between groups. Consequently, *Avg.DFG ED* was selected as computation of *DFG* and will be later incorporated into the definition of CTSRMs.

#### 5.4.5.2 Distance Between Generators

The magnitude of the impedance between generators is a topological feature with a significant effect on synchronising and damping powers [21]. As described in Section 1.3.6, the impedance between generators has an inversely proportional effect on the provision of synchronising power; therefore, a line-switching action increasing the impedance between two relatively close SGs will reduce the maximum transient synchronising coefficient between them, which can be detrimental from the transient stability viewpoint. This fact was analysed and confirmed in the context of the AF9B test system in Chapter 3; particularly, the study of the impedance between generators based on a more realistic network, like the IEEE68 bus system, was performed to verify the generality of the initial findings. Moreover, a more detailed study is performed to find an accurate metric, which will be included later in CTSRMs.

Also, following the naming convention of Chapter 3, the impedance between generators is called *distance between generators (DBG)*, and it was also studied based on three calculation methods. In particular, *Avg.Min.DBG SP* (5.7) is the average of shortest path impedance, defined in Section 2.2.3, from any generator to its closest neighbour, which produces the average distance to the closest SGs, whereas *Avg.Mean DBG SP* (5.8) uses the mean shortest paths to all other SGs. *Avg.Min.DBG ED* (5.9) is also the average of the impedance to the closest generators, but it uses the components of the Thevenin equivalent impedance approach (electrical distance) defined in Section 2.2.3.1.

$$\begin{aligned}
 Avg.Min.DBG SP^{k,f} &= \frac{1}{NG} \sum_{gi \in \Omega_g} \min_{gj \in \Omega_g} \{DBG1_{gi,gj}^f(\mathbf{oc}^k)\}; \\
 &\quad \forall gi, gj \in \Omega_g; \forall k \in \Omega_k; \forall f \in \Omega_f \\
 &\quad DBG1_{gi,gj}^f(\mathbf{oc}^k) \\
 &= \min_{paths\ gi,gj} \left\{ |z|_{gidm} + |z|_{gjd n} \right. \\
 &\quad \left. + \sum_{dmdn \in path\ gi,gj} |z^{k,f}|_{dmdn} oc_{dmdn}^k \right\}; \\
 &\quad \forall gi, gj \in \Omega_g; \forall gidm, gjdn \in \Omega_{gl}; \forall dmdn \in \Omega_l; \forall k \in \Omega_k; \forall f \in \Omega_f
 \end{aligned} \tag{5.7}$$

$$Avg. Mean DBG SP^{k,f} = \frac{1}{NG^2} \sum_{gi \in \Omega_g} \sum_{gj \in \Omega_g} DBG1_{gi,gj}^f(\mathbf{oc}^k); \quad (5.8)$$

$$\forall gi, gj \in \Omega_g; \forall k \in \Omega_k; \forall f \in \Omega_f$$

$$Avg. Min. DBG ED^{k,f} = \frac{1}{NG} \sum_{gi \in \Omega_g} \min_{gj \in \Omega_g} \{DBG2_{gi,gj}^f(\mathbf{oc}^k)\};$$

$$\forall gi, gj \in \Omega_g; \forall k \in \Omega_k; \forall f \in \Omega_f \quad (5.9)$$

$$DBG2_{gi,gj}^f(\mathbf{oc}^k) = Z_{gi,gi}^f(\mathbf{oc}^k) + Z_{gj,gj}^f(\mathbf{oc}^k) - 2Z_{gi,gj}^f(\mathbf{oc}^k);$$

$$\forall gi, gj \in \Omega_g; \forall k \in \Omega_k; \forall f \in \Omega_f$$

A comparison using TDS results for *DBG* metrics based on *BetterTSI* and *WorseTSI* groups is depicted in Figure 5.15. The figure shows the mean and 95% confidence intervals suggesting that all the *DBG* means of *BetterTSI* group are smaller in comparison with the *WorseTSI* group. Figure 5.15 also suggests that the difference between the means of the stability groups is more significant for SP-based *DBG* metrics (5.7)(5.8); in particular, Figure 5.15(c) indicates that *Avg. Min. DBG ED* has a small overlap between group confidence intervals. The observation was confirmed with using two-samples t-test indicating that *Avg. Min. DBG ED* has a smaller statistical difference between the means of *BetterTSI* and *WorseTSI* groups with the largest p-value ( $5.4 \times 10^{-3}$ ) among *DBG* metrics; this fact confirms that this metric is the least suitable for discriminating between groups. Consequently, the use of *DBG* metrics based on *SP* (5.7)(5.8) provide better accuracy to discriminate stability results.

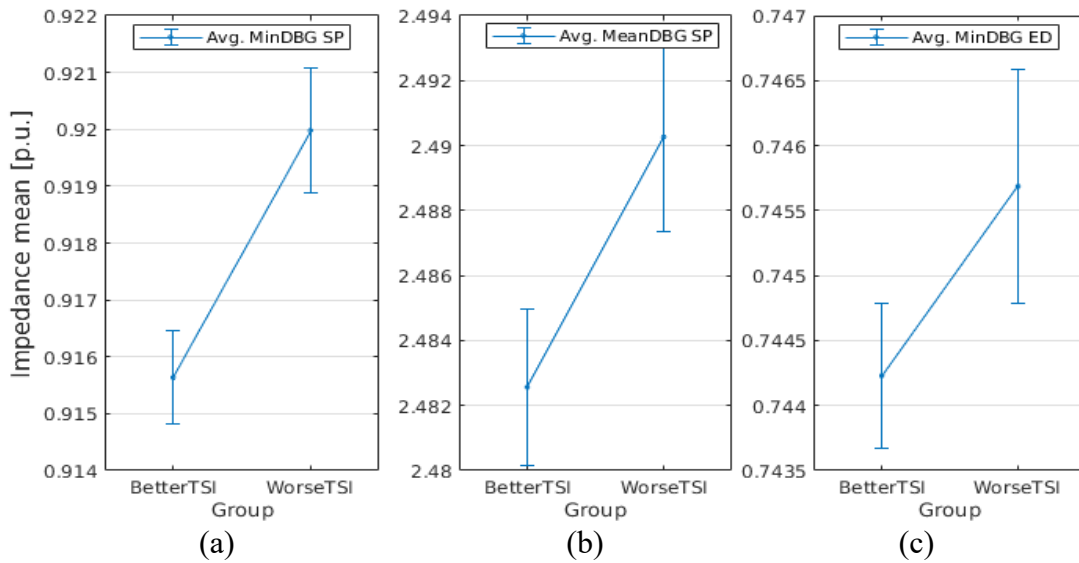


Figure 5.15: Average *DBG* impedance mean of better and worse TSI groups with 95% confidence intervals based on shortest path (a), mean of shortest paths (b) and electrical distances (c).



Further analyses using Spearman correlation coefficients between transient stability indicators and *DBG* metrics are shown in Table 5.7; correlation results indicate monotonic relations with different trends (increasing/decreasing) between *DBG* metrics and stability indicators. Even though results reveal low monotonic correlations with different tendencies, *Avg. Mean DBG SP* is the one with the smallest coefficients; this effect reveals that the inclusion of all SGs into the computation of *DBG* is not relevant because distant units have a small influence on synchronising power. The combination of correlation results with those shown in Figure 5.15 indicates that only *Avg. Min. DBG SP* has consistent results, with negative monotonicity for TSI and positive monotonicity for ISGA. Due to the low correlation, *Avg. Min. DBG SP* (5.7) cannot be used as standalone metric, it must be combined with other network metrics for the definition of CTSRMs.

Table 5.7 Spearman correlation coefficients between *DBG* metrics and transient stability indicators

DBG metrics	TSI	Dot1	Dot3	ISGA
Avg Min DBG SP	-0.23	0.11	0.09	0.22
Avg Mean DBG SP	0.00	-0.03	-0.08	0.17
Avg Min DBG ED	0.40	-0.38	-0.35	-0.04

## 5.5 Robustness metric for transient stability optimisation

Initially described in Section 5.3, the topology optimisation for transient stability, shown as “Stage II” in Figure 5.2, is carried out via the non-simulation-based methodology. The study of network robustness in relation to transient stability led to the analysis in the previous section, which identified and assessed impact factors to define a composite robustness metric. In the proposed optimisation, the objective function (5.1) includes the metric  $R[\cdot]$ , which is called *composite transient stability robustness metric* (CTSRM); it reflects the robustness of a network structure (topology) with respect to transient stability. The robustness metric CTSRM is a scalar function of transient stability impact factors and serves as a proxy for transient stability assessment; the metric quality is assessed by how accurately it maps TDS stability results into the scalar function. In particular, a proposed CTSRM consists of two parts: the first quantifies the impact of topology changes on individual generators, including unit characteristics, called nodal robustness, whilst the second encodes the network robustness considering the impact of the network structure, under fault condition, on individual SGs.

### 5.5.1 Nodal robustness

The nodal component of CTSRM considers the most important transient stability impact factors governing the behaviour of SGs prior to the fault. These impact factors are pre-fault rotor angle separation, generator inertia and pre-fault generator loading. Particularly, the first and third factors are strongly influenced by the network structure and related pre-fault operating conditions defined by the economic dispatch; the second factor provides a safeguard, influencing the rate of change of SGs rotor speed, protecting SGs from larger and faster rotor swings.

Results described in Section 5.4.3 indicate that pre-fault (steady state) conditions can give valuable insight into the potentially unstable generators. Differences in pre-fault RAS are directly related to the amount of power transmitted by the switched transmission branch, i.e., the higher power transfer through the branch in the original topology SWL0, the larger angle separation in the network structure with the branch switched off. In particular, the higher the RAS difference (5.2) due to topology change, the more likely a generator becomes unstable (see Figure 5.11). Therefore, a large RAS difference between a switching scenario and the base-case is a good indicator of unstable generators. Consequently, the first impact factor metric is defined in (5.10).

$$IFM1_{gi} = \begin{cases} \{1 + \|\Delta\delta_{gi}^{s,0}(t_0^-)\|_L\}^n & ; \|\Delta\delta_{gi}^{s,0}(t_0^-)\|_L > \Delta\delta_{thresh} \\ 1 & ; \text{otherwise} \end{cases}, \quad (5.10)$$

$$\forall gi \in \Omega_g, \forall s \in \Omega_k$$

Here,  $\|\cdot\|_L$  stands for the  $L$ -th norm (infinity norm  $L=inf$  and second norm  $L=2$  were tested), and  $n$  is a constant exponent.  $IFM1_{gi}$  is designed to give more weight to potentially unstable generators and can be controlled by exponent  $n$ ; besides, a comparison of  $L=inf$  and  $L=2$  norms has shown a better performance of the former, and it is used in the developed CTSRM. It is also possible to introduce a threshold value on maximum rotor angle separations defined in (5.10), which must be obtained for the system under study; for instance, the RAS difference threshold  $\Delta\delta_{thresh}$  was determined from TDS studies based on the IEEE68 system was around 7 degrees (see Figure 5.11).

Results described in Section 5.4.4 suggest that inertia plays an important role in transient stability; however, higher inertia does not always guarantee more stable results and vice versa. A harmful factor is the combination of inertia reduction and increased RAS angles, which can be found even in pre-fault conditions; this is why both aspects have been modelled in the robustness metric. Therefore, a linearly increasing function is used, as

seen in Figure 5.16. Accordingly, the inertia related impact factor is defined in (5.11). Generator inertia was studied at the machine level due to the smaller range (up to 9-10 s).

$$IFM2_{gi} = \begin{cases} IFM2_{thresh} + H_{gi} \cdot \frac{1 - IFM2_{thresh}}{H_{thresh}} & ; H_{gi} < H_{thresh} ; \\ 1 & ; H_{gi} \geq H_{thresh} \end{cases} \quad (5.11)$$

$$\forall gi \in \Omega_g$$

Here,  $IFM2_{thresh}$  and  $H_{thresh}$  are defined as limits according to Figure 5.16; and  $H_{gi}$  is generator  $gi$  inertia. The study based on the IEEE68 test system has shown that the range  $IFM2_{thresh} \in [0.7 - 0.9]$  and  $H_{thresh} = 5 \text{ or } 6 \text{ s}$  can be used. Having an inertia below a certain level can increase the likelihood of having unstable results, so the reciprocal  $1/IFM2_{gi}$  is used in the composite metric CTSRM, which assigns more weight to SG with lower inertia.

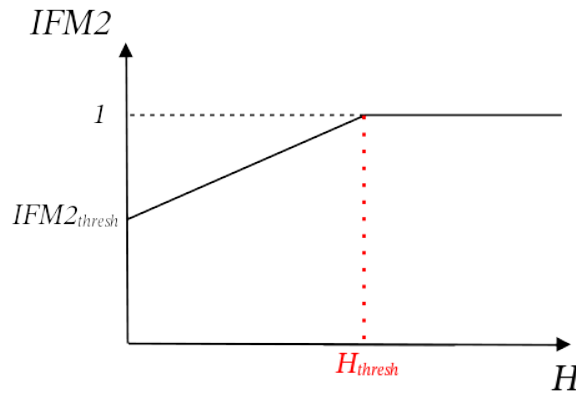


Figure 5.16: Generator inertia impact factor IFM2.

TDS results described in Section 0 suggest that higher pre-fault SG loading has a detrimental effect on transient stability (see Table 5.3); the finding is aligned with results reported in [127], indicating that a high initial loading of a generator (at  $t_0^-$ ) drives the unit towards instability and shortens critical clearing time. Consequently, the generator loading can be approximated via  $\sin\theta_{gi}$ , where  $\theta_{gi}$  is machine pre-fault load angle (the angle between the internal EMF and terminal voltage). The metric related to the generation loading is defined by (5.12).

$$IFM3_{gi} = \begin{cases} \frac{\sin\theta_{gi}}{\sin\theta_{thresh}} & ; \theta_{gi} > \theta_{thresh} ; \\ 1 & ; \theta_{gi} \leq \theta_{thresh} \end{cases} \quad \forall gi \in \Omega_g \quad (5.12)$$

Here,  $IFM3_{gi}$  increases the weight of all units loaded above the loading angle threshold  $\theta_{thresh}$ . Based on the IEEE68 test system, the range  $\theta_{thresh} \in [50^\circ - 60^\circ]$  was found (see Figure 5.10), characterising the loading angle of SGs likely to become unstable.

The combination of impact factors (5.10)-(5.12) allows the definition of the nodal robustness term of the CTSRM (5.13). Notably,  $NRM_{gi}$  is defined for each generator node  $gi \in \Omega_g$ , and is not a function of switching scenarios. The thresholds used in the study are related to the test system; a further analysis is required for their application on a different system.

$$NRM_{gi} = IFM1_{gi} \cdot IFM3_{gi} / IFM2_{gi}; \forall gi \in \Omega_g \quad (5.13)$$

### 5.5.2 Network robustness

The detailed study of the relation between topology metrics and transient stability effects of Section 5.4.5 revealed two network topology metrics having higher accuracy in mapping network structures under fault condition to TSI results. Therefore, the integration of the electrical distance-based  $DFG_{gi}^f(\mathbf{oc})$  (5.14) and the shortest path length-based  $DBG_{gi}^f(\mathbf{oc})$  (5.15) define the network robustness provided by the topology. In particular,  $DFG_{gi}^f(\mathbf{oc})$  represents the impedance between an SG and a fault location using Thevenin equivalent impedances, whilst  $DBG_{gi}^f(\mathbf{oc})$  represents the series impedance between an SG with its closest SG neighbour. Notably, both topology metrics are defined for each generator node  $gi \in \Omega_g$ , and include the topological changes introduced by the fault case  $f \in \Omega_f$ , using the procedure described in Section 2.3.1; besides, both metrics are functions of the optimisation variables represented via a switching vector  $\mathbf{oc}$ .

$$DFG_{gi}^f(\mathbf{oc}) = \min_{gi,f} \left\{ \begin{aligned} &Z_{gi,gi}^f(\mathbf{oc}) + Z_{fta,fta}^f(\mathbf{oc}) - 2Z_{gi,fta}^f(\mathbf{oc}) \\ &Z_{gi,gi}^f(\mathbf{oc}) + Z_{ftb,ftb}^f(\mathbf{oc}) - 2Z_{gi,ftb}^f(\mathbf{oc}) \end{aligned} \right\}; \quad (5.14)$$

$$\forall f \in \Omega_f; \forall gi \in \Omega_g; \forall f \in \Omega_f$$

$$DBG_{gi}^f(\mathbf{oc}) = \min_{gj \in \Omega_g} \{DBG1_{gi,gj}^f(\mathbf{oc})\}; \quad (5.15)$$

$$\forall gi, gj \in \Omega_g; \forall f \in \Omega_f$$

$$\begin{aligned}
 &DBG1_{gi,gj}^f(\mathbf{oc}) \\
 &= \min_{paths\ gi,gj} \left\{ |z|_{gidm} + |z|_{gjd n} \right. \\
 &\quad \left. + \sum_{dmdn \in path\ gi,gj} |z^f|_{dmdn}^{oc_{dmdn}} \right\}; \\
 &\forall gi, gj \in \Omega_g; \forall gidm, gjdn \in \Omega_{gl}; \forall dmdn, fl \in \Omega_l; \forall f \in \Omega_f
 \end{aligned}$$

### 5.5.3 Composite transient stability robustness metric

Optimal network topology is defined through a switching vector  $\mathbf{oc}^*$ , which contains binary values (*on/off*) of branch statuses. In particular, the maximisation of robustness index  $R[\cdot]$  is used in the general formulation (5.1); however, here, CTSRM needs to be minimised because they are designed to reflect potentially unstable switching solutions through large values. Consequently, the purpose of the optimisation is to find a switching vector  $\mathbf{oc}^*$  that provides the lowest possible value of CTSRM. As described in Section 5.4.5, the distance between a fault and a generator  $DFG$  works in opposite direction to distance between generators  $DBG$ ; hence, two CTSRMs (5.16) and (5.17) are defined to provide a comparison of different approaches.

$$\begin{aligned}
 z''(\mathbf{oc}^*) = \min_{\mathbf{oc}} &\left\{ \sum_f \pi^f \right. \\
 &\cdot \sum_{gi} NRM_{gi} \cdot \frac{1}{DFG_{gi}^f(\mathbf{oc}) + \alpha \cdot DBG_{gi}^f(\mathbf{oc})} \left. \right\}; \quad (5.16)
 \end{aligned}$$

$$\alpha = \begin{cases} 0 < \alpha < 1 ; DBG_{gi}^f(\mathbf{oc}) \leq DBG_{thresh} \\ 0 ; DBG_{gi}^f(\mathbf{oc}) > DBG_{thresh} \end{cases}; \forall gi \in \Omega_g$$

$$\begin{aligned}
 z'''(\mathbf{oc}^*) = \min_{\mathbf{oc}} &\left\{ \sum_f \pi^f \right. \\
 &\cdot \sum_{gi} NRM_{gi} \cdot \left[ \frac{1}{DFG_{gi}^f(\mathbf{oc})} - \beta \cdot DBG_{gi}^f(\mathbf{oc}) \right] \left. \right\}; \quad (5.17)
 \end{aligned}$$

$$\beta = \begin{cases} \beta > 1 ; DBG_{gi}^f(\mathbf{oc}) \leq DBG_{thresh} \\ 0 ; DBG_{gi}^f(\mathbf{oc}) > DBG_{thresh} \end{cases}; \forall gi \in \Omega_g$$

In the proposed approach, the metric  $DBG_{gi}^f(\mathbf{oc})$  had to be limited by an upper threshold value  $DBG_{gi}^f(\mathbf{oc}) \leq DBG_{thresh}$ . Thus, only the impact of a “sufficiently” close SG is considered. The threshold  $DBG_{thresh}$  can be directly associated with the length of

transmission lines with an impedance value of 0.06 p.u., which can be used for a voltage level of 230 kV of the IEEE68 transmission network; a revision of the threshold is required for a network with a different voltage level. As seen in (5.16), parameter  $\alpha < 1$  gives relative importance of  $DBG$  in relation to  $DFG$ . The term  $\alpha \cdot DBG_{gi}^f(\mathbf{oc})$  is added to  $DFG_{gi}^f(\mathbf{oc})$  only when it is under the threshold, which means that generator  $gi$  has a relatively close neighbour. In this case, the term  $\alpha \cdot DBG_{gi}^f(\mathbf{oc})$  increases the denominator and leads to a smaller network topology term associated with generator  $gi$  to account for the support provided from a close generator. Similarly, subtraction of the term  $\beta \cdot DBG_{gi}^f(\mathbf{oc})$  reduces the network topology term in (5.17) only when  $DBG_{gi}^f(\mathbf{oc})$  is below the threshold; in this case, factor  $\beta$  can vary in a much larger range.

The solution of the network topology optimisation is based on using CTSRMs metrics (5.16) and (5.17) as fitness functions; the solution can be obtained by applying the MATLAB built-in GA algorithm (function  $ga(\cdot)$ ), the technical documentation is found in [177]. Following a random generation of the switching solution vector  $\mathbf{oc}$ , robustness functions CTSRMs (5.16) and (5.17) are calculated if:

- i. The network is connected,
- ii. Maximum angle separation between generated network topology and intact network  $\max_s [\Delta \delta_{gi}^{s,0}(t_0^-)]$  is less than a pre-specified threshold, which was found to be around 30 degrees, as seen in Figure 5.11(a).

## 5.6 Assessment of switching solutions based on proposed CTSRMs

Initially, the purpose was to assess the accuracy of the proposed CTSRMs (5.16) and (5.17) based on the comparison against TDS stability evaluations based on TSI; at the same time, it was possible to verify which topology (among the test switching scenarios) has better transient stability robustness for a given set of fault conditions. The assessment of the proposed optimisation approach is based on three studies considering a stable base-case, an unstable base-case, and the application of load curtailments; these studies are based on the IEEE68 bus test system's original network from Figure 5.1.

Additionally, to avoid confusion between CTSRMs functions,  $z''(\mathbf{oc}^*)$  (5.16) is tested with parameter  $\alpha = 0.5$  and identified as Fitness Function 1 (FF1); likewise,  $z'''(\mathbf{oc}^*)$  (5.17) is identified as Fitness Function 2 (FF2) with parameter  $\beta = 10$ . Topology metrics

*DFG* and *DBG* can have different magnitude, especially in large networks; therefore, an adequate balance of the relative influence of both metrics is desired to avoid focusing only on one metric. In particular, the values of parameters  $\alpha$  and  $\beta$  used in this section were found through intensive testing, showing a reasonable balance between *DFG* and *DBG*.

### 5.6.1 Assessment of CTSRMs with stable base-case

The study considers the original network from Figure 5.1, which is stable, and does not require looping between stages I and II of the solution procedure described in Figure 5.2. Results comparing fitness values of different switching solutions against SWL0 (represented by a red line) for a fault on Line8 are shown in Figure 5.17(a) for FF1 with blue bars and in Figure 5.17(c) for FF2 with red bars. In the figures, the bar heights reflect fitness values; moreover, the switching scenarios are sorted from left to right by increased *instability* obtained by evaluations of TSI from simulation results. Only scenario SWL33 is unstable and is located on the far right of each plot.

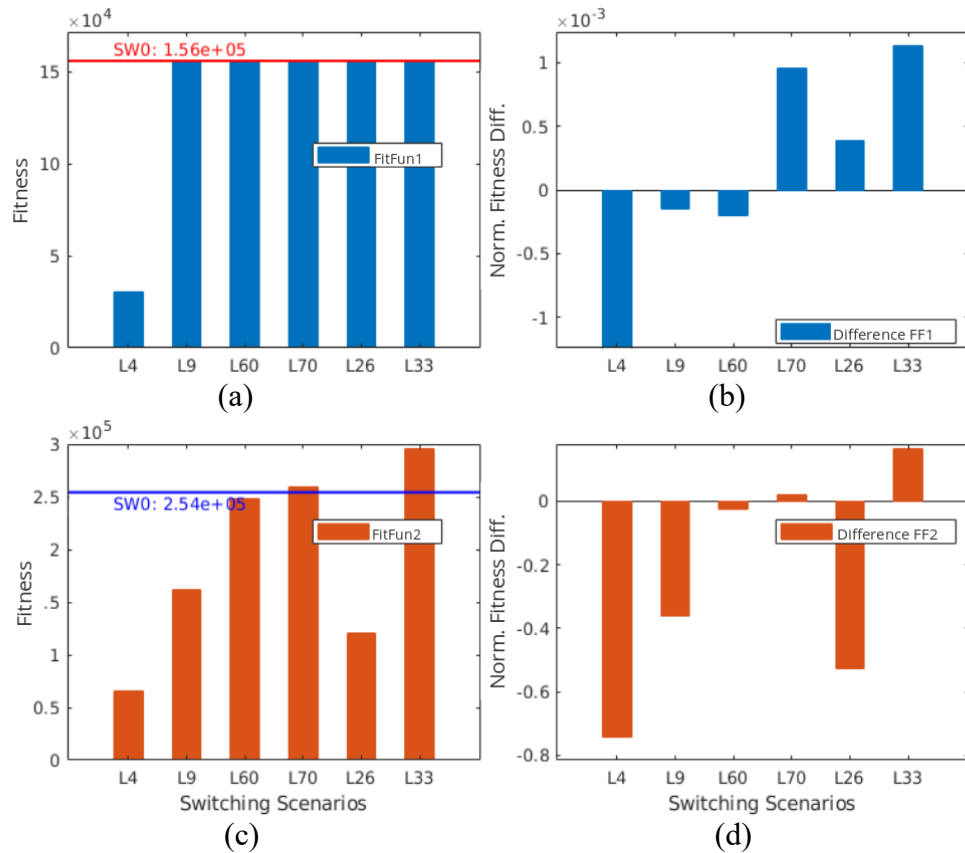


Figure 5.17: Fitness comparison of test switching scenarios for a fault on Line8 based on FF1 (a)(b) and FF2(c)(d).

A comparison of the difference between the fitness value corresponding to each switching scenario against the fitness value of SWL0 is shown in Figure 5.17(b) and Figure 5.17(d). As expected, from left to right, the bars reflect the largest negative values

on the left side, with the lower fitness value compared to the base-case SWL0, indicating better stability. On the contrary, the bars on the right side of the bar plots show a larger positive value, which reflects the worst transient stability. In particular, metric FF1 (5.16) performs better than FF2 (5.17) because the latter shows improved transient stability for SWL26, which is, in fact, less stable than SWL9, SWL60 and SWL70. Both metrics identify the best scenario, SWL4, the other stable cases, SWL9 and SWL60, and the unstable case, SWL33.

A broader assessment of robustness metrics (5.16) and (5.17) was done by comparing them with time-domain transient stability indicators for single faults and switching scenarios. Correlation analyses between robustness metrics and transient stability indicators shown in Table 5.8 indicate a similar tendency for both FFs, where less stable results have higher objective values; however, all coefficients are in the range of moderate-low correlation. Metric FF1 has a better correlation with TSI, which is based on longer simulation time; FF2 has similar correlations with all stability indicators. TSI correlation results suggest that FF1 better represents TDS stability results.

Table 5.8 Spearman correlation coefficients of objective functions and transient stability indicators

CTSRM metric	TSI	Dot2	ISGA
FF1	-0.56	0.25	0.26
FF2	-0.37	0.36	0.25

Further analysis of results based on both FFs can be done by comparing fitness differences between switching scenarios and the base-case SWL0 in Figure 5.18. In particular, Figure 5.18(a)(b) shows box plots of fitness differences in groups with *WorseTSI* and better *BetterTSI* for FF1 and FF2, respectively; though both FFs have substantial outliers above the third quartile, outliers are more condensed for FF1. Moreover, means of fitness differences between TSI stability groups of FF1 and FF2 illustrated in Figure 5.18(c)(d), reveal that for both FFs, the means of *BetterTSI* groups are smaller in comparison with the means of *WorseTSI* groups, which was expected.

There are two main differences between the results for both FFs. Firstly, the difference between medians for *WorseTSI* and *BetterTSI* groups is 5.4% in case of FF1 in Figure 5.18(a), whilst it is only 1.9% in case of FF2 in Figure 5.18(b), indicating that FF1 can be a better choice. Secondly, the box plots in Figure 5.18(a)(b) reveal a larger spread of results using FF2, whilst results with FF1 provide more concentrated results. In summary, metric FF1 can provide a better ranking of switching scenarios, but metric FF2 gives better differentiation between different cases.



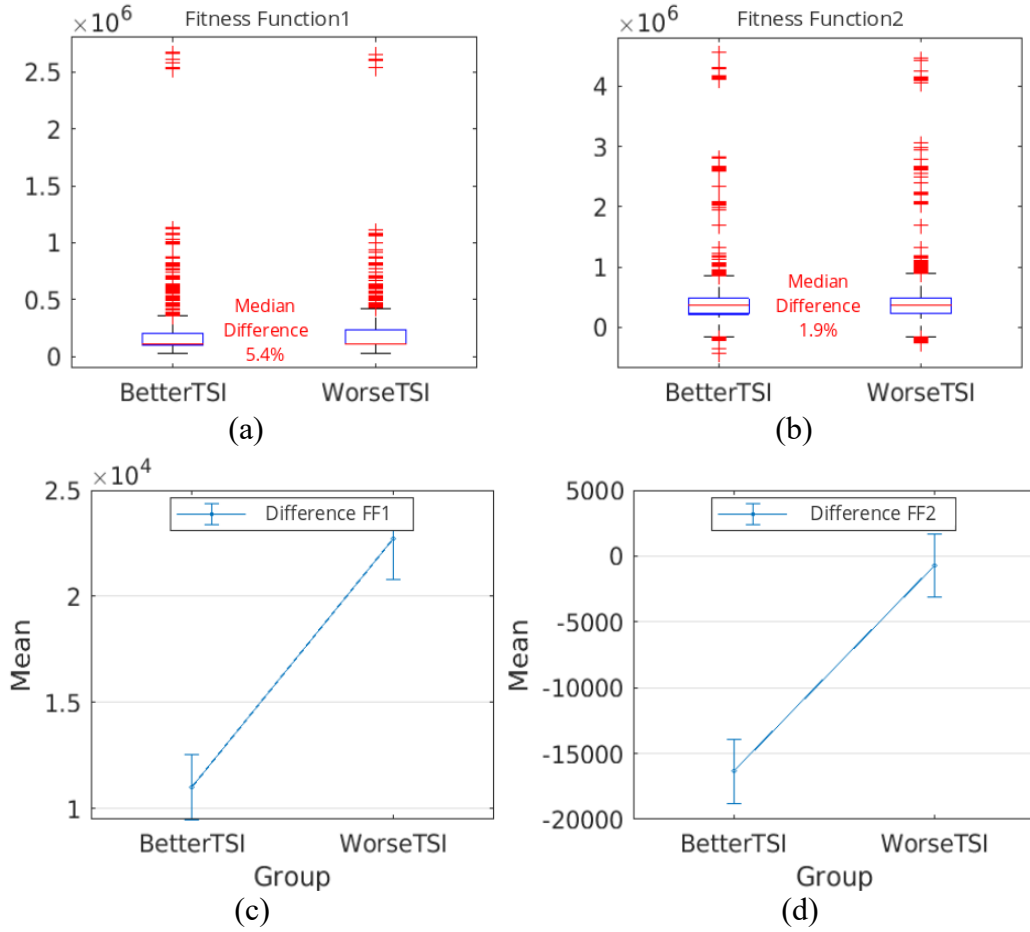


Figure 5.18: Box plots of fitness differences between all switching scenarios and SWL0 based on FF1 (a) and FF2 (b). Means of the fitness difference for evaluations using FF1 (c) and FF2 (d).

### 5.6.2 Network topology optimisation with unstable base-case

This study investigates whether an unstable baseline topology can be made stable by network switching and generation rescheduling (stages I & II in Figure 5.2). Results from Section 5.4.1 indicate that SWL33 is the only switching scenario with unstable results for a clearing time of 100 ms (see Figure 5.7); Therefore, Line33 is dropped from the network model with no possibility of reconnection, which means that in this context SWL33 is the base-case. With a new unstable base-case, the network topology is optimised via CTSRMs (5.16) and (5.17). Single and double switching scenarios are studied under a set of faults on Line24, Line25 and Line27. The analysis is performed with results considering a second single-line-switching of lines 23, 28, 13, 14, 18 and 16; for instance, SWL33-L23 denotes that the original test network (IEEE68) has been modified by switching-off lines 33 and 23.

Initial stability assessment is based on time-domain simulations and TSI, as shown in Figure 5.19; the  $x$ -axis denotes the baseline SWL33 with six switching scenarios superimposed, three faults (clearing time was 100ms) are on the  $y$ -axis, and the legend

shows better and worse TSI values in green and in blue, respectively. The baseline SWL33 is unstable for all three faults; however, scenarios SWL33-L23 and SWL33-L13 give stable results (green colour) in all 3 cases, whilst scenario SWL33-L28 is also stable but only for a fault on Line24. The positive impact of network switching is evident. Time-domain simulations confirmed that Gen2 is the weakest from the transient stability perspective; it also has the biggest RAS difference and loading angles in most switching scenarios. Notably, the difference in RAS is directly linked to the loading of transmission branches (in the base-case topology) that are switched *off/on*; the higher the branch loading, the higher the RAS difference. Moreover, TDS results confirmed that line-switching actions close to the fault location are more likely to stabilize the unstable baseline.

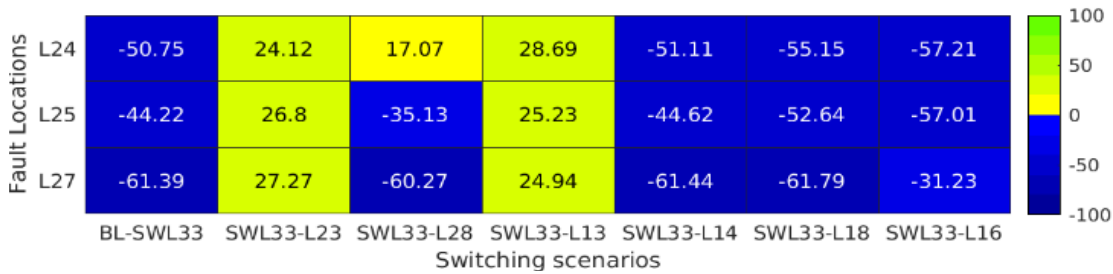


Figure 5.19: TSI results: switching scenarios with SWL33 as baseline (x-axis); fault locations on Line24, Line25, and Line27 (y-axis).

Results of both CTSRMs (5.16) and (5.17) for the double-switching scenarios and predefined single-fault conditions are shown in Table 5.9. The table follows the same colour pattern for stable (green) and unstable (blue) scenarios as TSI results in Figure 5.19, facilitating the comparison with stability results. CTSRMs are denoted by FF1 and FF2 in the first column, followed by the fault location. Results indicate that switching scenarios SWL33-L23, SWL33-L28 and SWL33-L13 are network structures with better transient stability because the CTSRMs have the lowest values among test switching scenarios. For instance, SWL33-L13 minimizes FF1 and FF2 for a fault on Line24, whereas SWL33-L23 minimizes both FFs for faults on lines 25 and 27. Closer inspection shows, for example, that the best switching scenario for a fault on Line24 is SWL33-L13, and the worst is SWL33-L16. The best transient stability performance of SWL33-L13 is due to the increase of the impedance between Gen2 and the fault location without increasing the impedance to Gen3. On the contrary, SWL33-L16 increases the impedance to the fault location in a smaller magnitude; however, it also increases the impedance between generators. Similar topological effects occur for a fault on Line27.

Table 5.9 Evaluation of FF1 and FF2 for double-switching scenarios with SWL33 as base-case

FF / Fault Loc.	BL SWL33	SW L33-L23	SW L33- L28	SW L33- L13	SW L33- L14	SW L33- L18	SW L33- L16
FF1/L24	<b>19500</b>	19138	19478	<b>19035</b>	19500	19499	24822
FF1/L25	<b>18679</b>	<b>18354</b>	18582	18381	18679	18678	24363
FF1/L27	<b>18753</b>	<b>18358</b>	18622	18429	18753	18752	24236
FF2/L24	<b>152767</b>	147720	147263	<b>143863</b>	152741	152155	160966
FF2/L25	<b>157045</b>	<b>149570</b>	153838	152123	157020	156636	164154
FF2/L27	<b>164892</b>	<b>154253</b>	162616	157709	164869	163825	172192

A comparison of Figure 5.19 and Table 5.9 reveals that both CTSRMs follow the TSI results very well for stable test cases; however, this may not always be the same for unstable cases. The proposed methodology is based on pre-fault conditions and network distances and captures synchronizing torque issues (first swing/initial swings stability) well; however, the methodology cannot identify loss of synchronism at later times beyond the first swing, caused by a lack of damping and sustained oscillations.

Findings in Section 5.6.1 revealed that robustness metrics (5.16) and (5.17) have different advantages; hence, the study of the combination of *normalised* values of FF1 and FF2 is done next. Figure 5.20 illustrates the normalised fitness values and the difference with respect to the fitness value of SWL33, obtained with both FFs (with blue and red bars). The affine combination  $0.66 * FF1_{nor} + 0.34 * FF2_{nor}$  was included to bring together the features of both fitness functions, shown in Figure 5.20 with yellow bars. The assessment includes the evaluation of switching scenarios for two combinations of single-fault conditions; the first combination (FC-A) consists of faults on Line24 and Line25 in Figure 5.20(a), whilst the second combination (FC-B) extends FC-A by adding a third fault on Line27, in Figure 5.20(b).

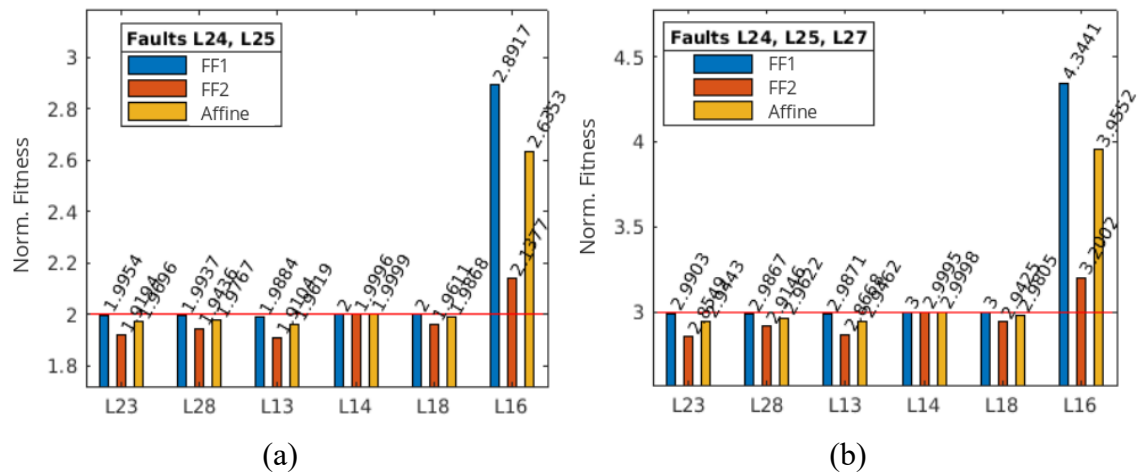


Figure 5.20: Normalised  $FF1_{nor}$  (blue),  $FF2_{nor}$  (red) and their affine combination (yellow). The x-axis contains switching scenarios with fault conditions FC-A (a) and FC-B(b).

Figure 5.20 reveals that all metrics identify the worst switching scenario SWL16 in fault conditions FC-A and FC-B; however, FF1 performs better, assigning the highest fitness value. The analysis of FC-A indicates that the affine combination selects SWL33-L13 as the best switching scenario ( $fit = 1.9819$ ) enhancing the same selection done with FF1 ( $fit = 1.9884$ ). Similarly, the analysis of FC-B suggests that while the selection based on FF1 is SWL28 ( $fit = 2.9867$ ), SWL23 ( $fit = 2.9443$ ) is selected as the best switching action using the affine combination of FFs. The comparison of these results with TSI values in Figure 5.19 shows a good alignment between the two; however, the affine combination selects SWL33-L13 and SWL33-L23 as the best switching scenarios for both fault cases, which is not the case with FF1 on its own. Therefore, the linear combination of normalized CTSRMs (5.16) and (5.17) can be considered the best choice.

### 5.6.3 Network topology optimisation with load curtailments

This study examines the effect of load curtailment as the last preventive recourse to improve the stability of an unstable baseline topology when generation rescheduling and network switching do not work (changes introduced by stages I & II in Figure 5.2 are not enough). For an initial total load of 12.4 GW, an increase of 7% and 10% raises the total load of the system to 13.2 and 13.6 GW, respectively. Under these new load scenarios, the base-case topology SWL33 is unstable for faults on Line24, Line25 and Line27. Although line switching can improve transient stability to some extent, the system remains unstable, and the problem has to be resolved with load curtailments. Stability outcomes with load curtailment for both increased load levels with the characteristic double-switching scenarios and predefined single-fault conditions are shown in Table 5.10; the table colour indicates stable and unstable results in green and blue, respectively. The load increase levels are denoted by 7% and 10% in the first column. In both increased load scenarios, load curtailment was done at load nodes 17, 25, and 28 to bring them down close to the non-increased values.

Table 5.10 Stability outcomes with load curtailment for total load increase of 7% and 10%

%Load Increase/ Fault Loc.	BL SWL33	SW L33- L23	SW L33- L28	SW L33- L13	SW L33- L14	SW L33- L18	SW L33- L16
7%/L24	Stable	Stable	Stable	Stable	Stable	Stable	Stable
7%/L25	Stable	Stable	Unstable	Stable	Stable	Unstable	Unstable
7%/L27	Unstable	Stable	Unstable	Stable	Unstable	Unstable	Unstable
10%/L24	Stable	Stable	Stable	Stable	Stable	Stable	Stable
10%/L25	Stable	Stable	Stable	Stable	Stable	Stable	Stable
10%/L27	Stable	Stable	Unstable	Stable	Unstable	Unstable	Unstable

As a result, the total load reduction in the two studied cases was 314 and 449 MW, respectively. Table 5.10 reveals that switching scenarios SWL33-23 and SWL33-13 give stable results in all studied cases. Consequently, load curtailment can effectively improve transient stability in a preventive mode; however, it should only be used as the last resource.

#### 5.6.4 Computation times

Finally, the performance of the proposed methodology was assessed by comparing the computation time against the time-domain-based assessments. The time-domain assessment considers OPF, full RMS simulation and TSI computation, whilst the CTSRM method considers OPF, initialization of dynamic RMS model and computation of the CTSRM metric FF1 (5.16). A series of tests using MATLAB provided the median computational time involved in both methods. The platform used was a Win10 virtual machine with 12GB of RAM and six processors; the host system is a Linux Fedora34 with an Intel Xeon 12 cores CPU of 3.6GHz.

The comparison of computation times between time-domain simulations (TDS) and the proposed CTSRM methodology is shown in Table 5.11; the number of branches is 72. Results show a significant reduction in computational time of 60% and 76% for single and two single faults, respectively. If extrapolated to faults in all branches, all single switching scenarios would require 766,800 s for the TDS and 10,650 s for the CTSRM method; the reduction goes up to 98.4%. Besides, TDS handles only a single fault condition, whereas the proposed method can integrate several fault conditions.

Table 5.11 Median computational time (seconds) for TDS and CTSRM using FF1 (5.16)

Single faults	1 TDS	71 TDS	1 CTSRM	71 CTSRM
L24	166.37	11379.7	66.9	5062.17
L24-L25	282.71	20151.5	67.7	4904.14

## 5.7 Summary

This chapter defined and analysed a method to solve the TSSC-OPFwS problem introduced in Section 4.4. The proposed solution is a two-stage methodology considering the solution of the economic dispatch problem for a fixed topology as the first stage, whilst in the second stage, the topology of the network is optimised to provide the best transient stability response, considering a set of credible faults. In particular, the topology optimisation problem for transient stability aimed to find the network structure that

maximizes a network robustness metric for a given fault scenario. The proposed robustness metric is called *composite transient stability robustness metric* (CTSRM), which was designed to serve as a proxy function to predict, to a certain extent, the transient stability behaviour for a given set of faults. The introduction of the proxy function replaced the solution of the multimachine model and verification of transient stability constraints in the time domain, reducing the complexity of solving the TSSC-OPFwS problem.

To build the network robustness metric, it was necessary to study multiple factors reflecting the influence of the network structure on the transient stability behaviour of power systems. The studies considered correlation analyses of TDS results, analyses of impact factors based on test switching scenarios, and the statistical analysis of impact factors using better and worse stability result groups. It was found that pre-fault variables such as generator loading and rotor angles encode valuable information which can be used to map the influence of network topology on the improvement or reduction of transient stability. Furthermore, to account for the fault conditions, the analysis of several network topology metrics allowed the selection of two metrics; impedance-based metrics like DFG and DBG, based on electrical distance and shortest path computation, respectively, enabled the discrimination between better and worse stability results more accurately in comparison with other metrics.

The definition of the network robustness metric CTSRM was based on combining a nodal and a network term. On the one hand, the nodal robustness of each SG was calculated based on the inertia, loading angle, and rotor angle; on the other hand, the network robustness incorporated the fault condition based on the equivalent impedance between individual SGs and a fault location, and the series impedances between SGs. Two CTSRMs were designed based on two different definitions of the network robustness term, identified as FF1 and FF2; they combine both nodal and network terms into robustness metrics, focusing on transient stability behaviour, to evaluate the fitness of a network structure. The accuracy of the proposed CTSRMs was evaluated by comparison against TSI results; simultaneously, it was possible to verify which test switching scenarios had better transient stability robustness for a given set of fault conditions. The assessment of the CTSRMs was based on three studies considering a stable base-case, an unstable base-case, and the application of load curtailments; it was found that metric FF1 can provide a better ranking of switching scenarios, but metric FF2 gives better differentiation between cases. Given that both robustness metrics showed certain

advantages, a study with *normalized* FF1 and FF2 was done, which indicated that a linear combination of normalized CTSRMs can be considered the best choice, adding more flexibility to the proposed approach to solve the TSSC-OPFwS problem.

In particular, the contributions of the present chapter are given as follows:

- *A two-stage methodology to solve the proposed TSSC-OPFwS problem, combining SC-OPF and topology optimisation for transient stability based on a general network robustness metric. In particular, two network robustness metrics in the form of fitness functions were designed to be used on a GA-based optimisation method.*
- *A study of transient stability impact factors, evaluating all possible single line-switching scenarios, revealed three main findings. Firstly, pre-fault (steady state) variables like loading and rotor angles can give invaluable insight into the potentially unstable generators. Secondly, line-switching actions, such as line disconnection defining different network topologies, can positively impact transient stability. Finally, a higher inertia level does not always guarantee more stable results and vice versa; a harmful factor is the combination of inertia reduction and increased rotor angle separation.*
- *A study of network topology metrics from network theory and power system literature provides high-quality metrics to capture the influence of network topology on transient stability. The analysis based on a realistic network suggested that the distance between generators and a fault location, and the distance between nearby generators, offer higher accuracy in discriminating between better and worse performance from the transient stability point of view.*





## 6 Conclusions and Future Work

---

### 6.1 Conclusions

Integration of Converter Interfaced Generation (CIG) in modern power systems is rapidly growing; hence the system's inertia is being reduced, resulting in increasingly faster system dynamics. The increasing integration of CIG is driven by the major commitment to remove carbon emissions in the production of electrical energy and to make power systems more sustainable; the cost reduction of CIG, especially photovoltaics (PV), has also boosted the growth. In addition, the integration of a large number of CIGs is decentralising the generation and shifting the balance to a converter-dominated grid; this phenomenon can be seen worldwide but predominantly in developed countries. Even though the current generation landscape is changing worldwide, in developing countries generation is still centralised and dominated mainly by conventional units; therefore, SGs will continue to be critical assets in power systems in the foreseeable future.

From a network perspective, the interconnections between power systems are expanding; hence, the integration of distant areas and markets will require significant transmission network reinforcements. Nevertheless, those changes will face growing environmental and budget restrictions; therefore, new approaches are needed to design flexible and cost-effective solutions. For example, one possibility is to use transmission lines as flexible (dispatchable) assets so that the network structure can be adjusted to operate under the expected conditions. In particular, this thesis has comprehensively evaluated how line-switching actions, like line disconnection or addition, can modify a network, how these discrete changes affect the network structure (topology), and the impact on the Transient Stability (TS) of power systems. In completing this research, a deterministic method, considering a comprehensive set of faults and switching scenarios, has been developed

to assess the transient stability performance of different network structures for a set of credible faults. The undertaken research is relevant because it focuses on improving transient stability with the aid of existing assets without the need for new capital investments; it is deemed that transient stability is likely to remain one of the key stability areas to be investigated in the following years.

The network structure has an essential role in dynamic processes; nonetheless, the power systems research community have not studied in detail the impact of the network topology (optimization) on transient stability. One of the contributions of this thesis is a comprehensive review of the literature surrounding the effect of the network structure on the stability of power systems. The review revealed that several approaches had been proposed, both deterministic and probabilistic in nature, to use the flexibility provided by the topology; however, the transient stability aspect has been overlooked. For instance, some TSOs are already taking advantage of changing the network's topology by procedures using commercial software to mitigate congestion on transmission lines. However, most of them do not apply systematic methodologies to harness all available benefits of topological changes; relevant challenges in adopting systematic approaches in the industry are often a lack of relevant data and appropriate software, lengthy computational times and studies of large-scale networks.

A successful approach using the network structure as a control means has been achieved in Optimal Transmission Switching (OTS), which focuses mainly on asset overloading, voltage violations, and reduction of operational costs. Very limited OTS literature addresses transient stability, focusing only on a regular topology or including restrictions on short-circuit currents. Similarly, Optimal Topology Control (OTC) literature incorporates the advantages of congestion reduction and investigates the integration of CIG. Among the small number of contributions considering transient stability within OTC, it is only possible to find corrective (optimisation) approaches based on transient energy functions; nonetheless, determining the controllable unstable equilibrium point is a typical drawback. Notably, the use of graph-based metrics is almost absent from the reviewed literature on optimisation techniques used in OTS and OTC; only in contingency analysis to avoid component overloading the graph-based electrical distance between generators and fault location has been previously used.

Another relevant reviewed topic was Transient Stability Constrained Optimal Power Flow (TSC-OPF); in this topic, dynamic equations of SGs are discretised, increasing the

dimension of the optimisation model or solved through Time-Domain Simulation (TDS). In both approaches modelling topological changes by switching would amplify scalability and complexity issues to the point that the optimisation problem becomes unsolvable; this indicates that a non-simulation-based approach can be an alternative way to reflect the effect of the network structure within the optimization problem. In the reviewed literature, topology metrics designed to assess the impact of the topology on the dynamic behaviour of SG during electromechanical transients are practically non-existent. Therefore, specific network topology metrics were investigated and developed, which is one of the central gaps that this thesis covers.

A summary of conclusions related to the contributions is given in the sections below. In addition, an overview of the contributions is given in Table 6.1.

Table 6.1 List of contributions

Id	Name	Description
C1	Optimisation framework TSSC-OPFwS	An optimisation framework combines a transient stability inequality constraint based on TSI, a classical multi-machine model based on a structure-preserving network, and line-switching actions. The integration is formulated in an optimisation problem called Transient Stability and Security Constraint Optimal Power Flow with Switching (TSSC-OPFwS).
C2	Two-stage solution of TSSC-OPFwS	A two-stage methodology to solve the proposed TSSC-OPFwS problem, which combines SC-OPF and topology optimisation for transient stability.
C3	Study of TS nodal impact factors	A study of generator transient stability impact factors, evaluating all possible single-line-switching scenarios, revealed pre-fault variables related to SGs that drive transient stability behaviour when there is a change in the network structure.
C4	Study of TS topological impact factors	The definition and study of two impedance-based proximity metrics to evaluate the effect of line-switching actions on the network structure of transmission networks and transient stability.
C5	Definition of TS robustness metrics	Two network robustness metrics, called Composite Transient Stability Robustness Metric (CTSRM) in the form of fitness functions, were designed to be used on a GA-based optimisation method.

### 6.1.1 Optimisation framework TSSC-OPFwS

An optimisation framework was proposed to provide the tool to find the best network controls, including branch switching, to improve the transient stability behaviour of power systems. The proposed framework addresses both transient stability and network security and is composed of several components: a) A classical multi-machine transient stability model making use of the structure-preserving network representation, including line switching; b) A transient stability inequality constraint formulated using TSI; c)

Network security model expressed via load-flow equations for intact and (N-1) networks; d) Network operational inequality constraints for intact and (N-1) network; and e) Objective function that contains costs of generations and possibly load curtailments; the envisaged controls, network switching and generation (re)dispatching, are used to improve the transient stability behaviour of power systems.

The first block of the proposed framework includes dynamic aspects of the power system transient stability. The details of two multi-machine models for transient stability analysis were developed within the optimisation framework. The first was the standard model based on the classical dynamic representation of SGs with network reduction, reducing the model's complexity but hiding the network's structural characteristics. The second model, also based on the classical dynamic representation of SGs, uses the network topology, where active power loads represent the demand at non-generation nodes. The novelty aspect of the second model is that it includes binary variables to represent the statuses of transmission lines. Next, the study of multiple transient stability indicators using TDS demonstrated that TSI is best suited to analyse the stability of fault cases. Using correlation analysis, it was possible to identify that TSI shares a similar qualitative assessment with other transient stability indicators; therefore, the selection of TSI as the base indicator was not only due to its accuracy reported in the literature but also because of its correlation level with other studied stability indicators. The second block of the proposed framework contains static aspects of the power system security; it was proposed to introduce network switching into the security model, which was again done using the branch status binary variables.

The two blocks are the basis of the proposed general dynamic optimisation problem called Transient Stability and Security Constraint Optimal Power Flow with Switching (TSSC-OPFwS); the formulation of the problem is general because it considers preventive controls, network switching and generation (re)dispatch, but also allows for the application of corrective remedies in the preventive mode. In other words, the preventive mode considers the premise “It will be possible to change a control following the system disturbance”, which is incorporated in the equations of the optimisation model.

*A novel optimization framework was proposed, which integrates transient stability and network security aspects with line switching as an available control. The transient stability block uses the classical multi-machine model with structure-preserving network*

and line switching, as well as an inequality constraint based on TSI. The combination of security and transient stability constraints defines the general dynamic optimisation problem called Transient Stability and Security Constraint Optimal Power Flow with Switching (TSSC-OPFwS).

### 6.1.2 Two-stage solution of TSSC-OPFwS

The TSSC-OPFwS problem is a large-scale mixed-integer non-linear multi-stage (i.e., discretised temporal relations) optimisation; therefore, instead of using traditional optimisation methods directly, a solution decoupling security from transient stability aspects was studied. The proposed solution is a two-stage methodology considering the solution of the economic dispatch problem for a fixed topology as the first stage, whilst in the second stage, the topology of the network is optimised to provide the best transient stability response, considering a set of credible faults. In the first stage, an SC-OPF is solved for the fixed network topology, which can also be obtained from the second stage during the iterative process; the output of the first stage is an optimal operating point considering pre-fault SC-OPF generator voltage and active power dispatch. In the second stage, a topology optimisation problem for transient stability finds the network structure that minimises a TS robustness metric (CTSRM) for a given set of fault scenarios. The proposed robustness metric uses pre-fault generator data and network structure metrics considering fault conditions, which can be computed using the computational methods described in this thesis. In summary, the proposed two-stage solution decouples the power flow (security) constraints from the dynamic and binary (transient stability) constraints; moreover, using a TS robustness metric within the topology optimisation reduces the complexity of the computational burden of solving the dynamical models is avoided.

*A two-stage methodology was defined to solve the proposed TSSC-OPFwS problem, combining SC-OPF and topology optimisation for transient stability based on a general network robustness metric. The proposed solution decouples the power flow (security) constraints from the dynamic and binary (transient stability) constraints; moreover, using a transient stability robustness metric within the topology optimisation reduces the complexity of solving the dynamical models in time domain.*

### 6.1.3 Study of TS nodal impact factors

A comprehensive study provided evidence that line-switching actions defining different network topologies can positively impact transient stability. The performance comparison between switching scenarios and a base-case topology, for all possible single-fault conditions, showed that improvements in transient stability could be found in more than 48% of cases. Moreover, the analysis of transient stability impact factors, evaluating all possible single line-switching scenarios, confirmed that pre-fault (steady state) conditions could give valuable insight into the potentially unstable generators. Line-switching actions can significantly impact pre-fault Rotor Angle Separation (RAS) difference and load angles, affecting the power transfer during faults. This thesis showed that such impact could be positive for highly oscillatory generators after faults, up to a certain degree; therefore, switching actions, leading to small changes in RAS differences and load angles, can be considered a preventive measure towards improving stability in the network. On the contrary, a large pre-fault difference in RAS between a switching scenario and the base-case can be considered a high-quality indicator of unstable generators; high pre-fault unit loading also contributes to the instability. The analysis also indicated that the difference in RAS is linked to the transmission branch loadings that are switched off/on; the higher the loading on the transmission branch, the higher the RAS difference, which is potentially detrimental from the transient stability perspective.

Furthermore, it was confirmed that generator inertia is a relevant impact factor on transient stability; however, a higher inertia level does not always guarantee more stable results and vice versa. A harmful factor is the combination of inertia reduction and increased RAS; hence, both factors are modelled in the proposed robustness metric. Finally, generator initial loading was also found to be an important factor in transient stability.

*A study of transient stability nodal (generator) impact factors evaluating single line-switching scenarios revealed three main findings related to switching actions. Firstly, pre-fault variables like generator loading and rotor angles can give invaluable insight into the potentially unstable generators. Secondly, line-switching actions defining different network topologies can positively impact transient stability. Finally, a higher inertia level does not always guarantee more stable results and vice versa; a harmful factor is the combination of inertia reduction and increased rotor angle separation.*

#### 6.1.4 Study of TS topological impact factors

The study of the effect of line-switching actions on impedance metrics in the transmission network was done based on two small-size test systems to avoid the complexity of large-size networks; impedance-based proximity metrics were used to provide insight into the effect of discrete topological changes on the transient stability level. Firstly, two SMIB test systems combined with the classical model of SG allowed the analysis of different network structures based on the EAC and CCT, with a focus on the impedance between a generator and the fault location, identified as *ZFG*. Based on a preliminary analysis, the *ZFG* was defined based on the electrical distance between an SG and a fault location, which was verified by running the TDS studies; depending on the network structure, the study showed that increasing the impedance between a generator and the fault location *ZFG* can improve the stability, increasing the CCT at least in 28% of cases.

In conjunction with TDS studies, a modified version of the Anderson and Fouad 9Bus test system (AF9B) served as a testing environment to study discrete topological changes focusing on the impedance between generators. The studies revealed that a graph-based proximity metric provides a higher focus on topological changes in the path between nearby SGs; therefore, the impedance between generators *ZBG* based on the geodesic distance was adopted. The analysis of simulation results revealed that line-switching actions increasing *ZBG* were detrimental from the stability perspective; remarkably, the combination of larger *ZFG* and smaller *ZBG* improved the stability by 20%, which was reflected by a longer CCT. Results based on SMIB and AF9B networks highlight the importance of the network structure and how line-switching actions impact dynamic responses of SGs; the topological effect was quantified by that two metrics (*ZFG* and *ZBG*), which have never been used before to provide a link between the network structure with the transient stability behaviour of power systems.

Furthermore, based on a realistic test system such as the IEEE68 bus network, the analysis of TDS results combining switching and fault scenarios allowed the selection of two network topology metrics; those impedance-based metrics, *DFG* and *DBG* based on electrical distance and shortest path computation, respectively, enabled the discrimination between better and worse stability results more accurately in comparison with other metrics. The study also revealed similar trends, in terms of the effect on transient stability behaviour, on the impedance between generators and fault locations

(DFG) and between generators (DBG) in comparison with those found using small test systems (SMIB and AF9B). The similarities in the effects, captured by the analysed topology metrics, lead to the conclusion that the network structure effect is general because it applies to systems of different sizes.

*The definition and study of two impedance-based proximity metrics, in the context of small test systems, to evaluate the effect of line-switching actions on the structure of a transmission network and how those discrete changes impact the transient stability behaviour of power systems. The analysis based on a realistic test system suggested that impedance-based distance between generators and a fault location DFG, and between nearby generators DBG, offer higher accuracy in discriminating between network structures with a better or worse performance from the transient stability point of view. In particular, the confirmation of the effects of DFG and DBG on transient stability based on a realistic test system, originally revealed on two small test systems using ZFG and ZBG, leads to the conclusion that the findings based on network topology metrics are general.*

#### **6.1.5 Definition of TS robustness metrics**

In particular, the solution of the TSSCOPFwS includes a network topology optimisation based on a Composite Transient Stability Robustness Metric (CTSRM); CTSRM was designed to serve as a proxy function to predict, to a certain extent, the transient stability behaviour for a given set of faults. Correlation analyses validated the selection of two impedance-based network topology metrics, namely, the impedance-based distance between generators and a fault location (DFG) and impedance between nearby generators (DBG), which both offer higher accuracy in discriminating between better and worse network topologies from the transient stability point of view. Network topology metrics, i.e., selected impedance-based proximity metrics, combined with transient stability “nodal” impact factors, i.e., RAS difference, generator inertia and initial loading, were used to define two networks CTSRMs in the form of fitness functions; the functions were designed to be used in a GA-based optimisation method. Both proposed robustness metrics, denoted as FF1 and FF2, discriminate well between better and worse stability performance. The studies showed that FF1 could provide a better ranking of switching scenarios, but FF2 showed better differentiation between the scenarios with worsened stability. However, TDS studies also revealed that the proposed methodology has a



limitation because it cannot capture instability beyond the first few swings, which is often of oscillatory nature.

The evaluation of the proposed robustness metrics did not exhibit scalability issues and can be applied to large systems; moreover, they lead to substantial computation time reductions and can be potentially exploited in real-time. The studies performed are comprehensive enough to test the proposed methodology; however, they are restricted to faults in the middle of transmission lines and for only a limited number of dispatch conditions. A more extensive set of fault conditions and variations in system loads will be necessary for the practical application of the proposed approach; nevertheless, the number and characteristics of scenarios used in the studies are enough for research purposes and to draw the most important conclusions.

*Within the proposed topology optimisation for transient stability, two network robustness metrics in the form of fitness functions were designed to be used in a GA-based optimisation method. In particular, the proposed robustness metrics are called Composite Transient Stability Robustness Metrics (CTSRMs), which serve as proxy functions to predict, to a certain extent, the transient stability behaviour of a power system for a given set of faults. The introduction of proxy functions replaced the solution of the multimachine model and verification of transient stability constraints in the time domain, reducing the complexity of solving the TSSC-OPFwS problem.*

## 6.2 Future work

The work presented in this thesis has fulfilled the research aims and objectives initially defined; nonetheless, there are several areas where the work included in this thesis can be extended. Some of the foreseeable extensions of the methods and concepts presented are described below:

- i. The proposed network topology optimisation method was defined as a deterministic approach; it was tested based on a specific load profile and fault location (in the middle of transmission lines) without including uncertainties. An extension of the work presented in this thesis is a probabilistic analysis of the effect of the network structure on transient stability, including uncertainties in different system parameters. The primary purpose is to test the accuracy of CTSRMs. A Monte Carlo (MC) simulation process can be implemented to incorporate load and fault location uncertainties into the analysis as a first step.

The MC method is simple and can provide accurate results; however, for large systems, the number of uncertainties must be kept low to avoid the need for a massive number of scenarios to capture a relevant range of parameters.

- ii. The study of the influence of generator inertia on transient stability in this thesis considered the reduction of the machine ratings. In the current and future scenarios, the inertia reduction is a consequence of the increasing penetration of CIG related to the integration of RES; therefore, extending the analysis of the impact of the network structure in combination with the penetration of RES is a highly relevant task. An initial approach to this work must consider the integration of wind and solar-based CIG into the AF9B to understand the effect under a discrete set of environmental conditions (wind and light availability). In particular, DFIG and FCC dynamic models are readily available in PowerFactory to integrate wind turbines and photovoltaic panels. In particular, the inclusion of CIG into the analysis opens a wide variety of options to define new operating scenarios due to the stochastic nature of RES.
- iii. Another extension of the work presented in this thesis is a probabilistic analysis based on MC simulation combining the effect of the network topology and penetration of RES. To accomplish this work, network models must be extended to integrate CIGs, and the computation of dispatch needs to include stochastic characteristics related to RES, like wind and solar uncertainties. An objective using a probabilistic approach can be to find the limits of the influence of the network structure on transient stability for a given level of CIG penetration; alternatively, to find the level of CIG penetration for which network switching is still effective.
- iv. The network topology optimisation based on the proposed CTSRMs was assessed based mainly on the performance of test switching scenarios. In particular, CTSRMs in the form of fitness functions were evaluated, and the IEEE68 transmission network was optimised for a set of switching scenarios. The work in this thesis can be extended by performing a comprehensive set of tests performing the GA-based optimisation defining different base-case scenarios of the IEEE68 test system. Moreover, the test set must be extended later to include publicly available test systems, such as the GB or Iceland transmission networks. For instance, the Iceland transmission system is a medium-sized network with 206 transmission branches connecting 189 buses with 35 generator nodes; besides, the GB network is a large network with 3207 transmission branches

connecting 2224 buses with 394 generation nodes. This work aims to increase the proposed methodology's testing environment to verify its performance and accuracy based on medium and large-scale networks.

- v. Another research possibility is the investigation of different metrics that can be incorporated within the CTSRM functions to improve the accuracy of the proposed methodology, for instance, the components of the matrix of the linearised classical TS model.



## References

- [1] GOV.UK, “Clean Growth Strategy - GOV.UK,” 2018. [Online]. Available: <https://www.gov.uk/government/publications/clean-growth-strategy>. [Accessed: 01-Feb-2022].
- [2] J. Watson *et al.*, “The Security of UK Energy Futures,” *UKERC Res. Rep.*, no. March, p. 44, 2018.
- [3] National Grid ESO, “FES 2019 document | National Grid - Future Energy Scenarios,” 2019.
- [4] National Grid ESO, “FES 2021 document | National Grid - Future Energy Scenarios,” 2021.
- [5] C. R. Gómez, S. Arango-Aramburo, and E. R. Larsen, “Construction of a Chilean energy matrix portraying energy source substitution: A system dynamics approach,” *J. Clean. Prod.*, vol. 162, pp. 903–913, Sep. 2017.
- [6] G. Strbac *et al.*, “Cost-effective decarbonization in a decentralized market: The benefits of using flexible technologies and resources,” *IEEE Power Energy Mag.*, vol. 17, no. 2, pp. 25–36, Mar. 2019.
- [7] F. Lamnabhi-Lagarrigue *et al.*, “Systems & Control for the future of humanity, research agenda: Current and future roles, impact and grand challenges,” *Annual Reviews in Control*, vol. 43. Pergamon, pp. 1–64, 01-Jan-2017.
- [8] L. Chang and Z. Wu, “Performance and reliability of electrical power grids under cascading failures,” *Int. J. Electr. Power Energy Syst.*, vol. 33, no. 8, pp. 1410–1419, Oct. 2011.
- [9] J. C. Araneda, H. Rudnick, S. Mocarquer, and P. Miquel, “Lessons from the 2010 Chilean earthquake and its impact on electricity supply,” in *2010 International Conference on Power System Technology: Technological Innovations Making Power Grid Smarter, POWERCON2010*, 2010, pp. 1–7.
- [10] C. Rodríguez-Monroy, G. Mármol-Acitores, and G. Nilsson-Cifuentes, “Electricity generation in Chile using non-conventional renewable energy sources – A focus on biomass,” *Renewable and Sustainable Energy Reviews*, vol. 81. Pergamon, pp. 937–945, 01-Jan-2018.
- [11] G. Jiménez-Estévez, R. Palma-Behnke, R. Román Latorre, and L. Morán, “Heat and Dust: The Solar Energy Challenge in Chile,” *IEEE Power Energy Mag.*, vol. 13, no. 2, pp. 71–77, Mar. 2015.
- [12] T. Ackermann, T. Prevost, V. Vittal, A. J. Roscoe, J. Matevosyan, and N. Miller, “Paving the Way: A Future Without Inertia Is Closer Than You Think,” *IEEE Power Energy Mag.*, vol. 15, no. 6, pp. 61–69, Nov. 2017.
- [13] B. Kroposki *et al.*, “Achieving a 100% Renewable Grid: Operating Electric Power Systems with Extremely High Levels of Variable Renewable Energy,” *IEEE Power Energy Mag.*, vol. 15, no. 2, pp. 61–73, Mar. 2017.
- [14] S. P. Burger, J. D. Jenkins, S. C. Huntington, and I. J. Perez-Arriaga, “Why distributed?: A critical review of the tradeoffs between centralized and decentralized resources,” *IEEE Power Energy Mag.*, vol. 17, no. 2, pp. 16–24, Mar. 2019.

- [15] PJM, "Monitoring Analytics - PJM State of the Market - 2021," 2021.
- [16] P. Kundur *et al.*, "Definition and classification of power system stability," *IEEE Trans. Power Syst.*, vol. 19, no. 3, pp. 1387–1401, Aug. 2004.
- [17] P. M. Anderson and A. A. Fouad, *Power system control and stability*. Piscataway, N.J: IEEE Press Wiley-Interscience, 2003.
- [18] N. Hatziargyriou *et al.*, "Definition and Classification of Power System Stability - Revisited & Extended," *IEEE Trans. Power Syst.*, vol. 36, no. 4, pp. 3271–3281, Jul. 2021.
- [19] IEEE, "Stability definitions and characterization of dynamic behavior in systems with high penetration of power electronic interfaced technologies," *Pes-Tr77*, no. April, pp. 1–42, 2020.
- [20] P. Kundur, *Power system stability and control*. New York: McGraw-Hill, 1994.
- [21] J. Machowski, Z. Lubosny, J. W. Bialek, and J. R. Bumby, *Power system dynamics : stability and control*, Third edit. Hoboken, NJ: John Wiley & Sons, Inc., 2020.
- [22] A. A. Fouad and V. Vittal, *Power system transient stability analysis using the transient energy function method*. Englewood Cliffs, N.J: Prentice Hall, 1992.
- [23] J. Grainger and W. J. Stevenson, *Power system analysis*. New York: McGraw-Hill, 1994.
- [24] National Grid Electricity System Operator, "The Grid Code Issue 5 Revision 7," 2021.
- [25] L. Freris, D. Infield, and M. Thomson, *Renewable Energy in Power Systems*, 1st ed. New York: John Wiley & Sons, Incorporated, 2008.
- [26] J. Morales Alvarado, "Probabilistic Transient Stability Assessment and Corrective Control of Power Systems with Increasing Penetration of Non-synchronous Generation." 2022.
- [27] A. N. Michel, A. A. Fouad, and V. Vittal, "Power System Transient Stability Using Individual Machine Energy Functions," *IEEE Trans. Circuits Syst.*, vol. 30, no. 5, pp. 266–276, 1983.
- [28] D. Z. Fang, T. S. Chung, Y. Zhang, and W. Song, "Transient stability limit conditions analysis using a corrected transient energy function approach," *IEEE Trans. Power Syst.*, vol. 15, no. 2, pp. 804–810, May 2000.
- [29] Y. Xue, T. Van Cutsem, and M. Ribbens-Pavella, "A simple direct method for fast transient stability assessment of large power systems," *IEEE Trans. Power Syst.*, vol. 3, no. 2, pp. 400–412, 1988.
- [30] C. K. Tang, C. E. Graham, M. El-Kady, and R. T. H. Alden, "Transient Stability Index from Conventional Time Domain Simulation," *IEEE Trans. Power Syst.*, vol. 9, no. 3, pp. 1524–1530, 1994.
- [31] P. W. Sauer, M. A. Pai, and J. H. Chow, *Power System Dynamics and Stability: With Synchrophasor Measurement and Power System Toolbox 2e*, Second edi. Hoboken, NJ, USA: IEEE Press, 2017.
- [32] P. M. Anderson and M. Mirheydar, "A low-order system frequency response model," *IEEE Trans. Power Syst.*, vol. 5, no. 3, pp. 720–729, 1990.

- [33] C. J. Távora and O. J. M. Smith, "Stability analysis of power systems," *IEEE Trans. Power Appar. Syst.*, vol. PAS-91, no. 3, pp. 1138–1144, 1972.
- [34] C. J. Távora and O. J. M. Smith, "Characterization of equilibrium and stability in power systems," *IEEE Trans. Power Appar. Syst.*, vol. PAS-91, no. 3, pp. 1127–1130, 1972.
- [35] A. A. Fouad and V. Vittal, "The transient energy function method," *Int. J. Electr. Power Energy Syst.*, vol. 10, no. 4, pp. 233–246, Oct. 1988.
- [36] C. Fu and A. Bose, "Contingency ranking based on severity indices in dynamic security analysis," *IEEE Trans. Power Syst.*, vol. 14, no. 3, pp. 980–986, Aug. 1999.
- [37] V. Brandwajn, A. B. R. Kumar, A. Ipakchi, A. Böse, and S. D. Kuo, "Severity indices for contingency screening in dynamic security assessment," *IEEE Trans. Power Syst.*, vol. 12, no. 3, pp. 1136–1142, 1997.
- [38] R. P. O'Neill, R. Baldick, U. Helman, M. H. Rothkopf, and W. Stewart, "Dispatchable transmission in RTO markets," *IEEE Trans. Power Syst.*, vol. 20, no. 1, pp. 171–179, Feb. 2005.
- [39] M. Abdi-Khorsand, M. Sahraei-Ardakani, and Y. M. Al-Abdullah, "Corrective Transmission Switching for N-1-1 Contingency Analysis," *IEEE Trans. Power Syst.*, vol. 32, no. 2, pp. 1606–1615, Mar. 2017.
- [40] P. A. Ruiz, E. Goldis, A. M. Rudkevich, M. C. Caramanis, C. R. Philbrick, and J. M. Foster, "Security-Constrained Transmission Topology Control MILP Formulation Using Sensitivity Factors," *IEEE Trans. Power Syst.*, vol. 32, no. 2, pp. 1597–1605, Mar. 2017.
- [41] K. W. Hedman, S. S. Oren, and R. P. O'Neill, "A review of transmission switching and network topology optimization," in *IEEE Power and Energy Society General Meeting*, 2011.
- [42] K. Purchala, M. Shinkai, and F. Regairaz, "Practices related to internal and cross-border congestion management," in *2005 CIGRE/IEEE PES International Symposium*, 2005, pp. 1–8.
- [43] PJM, "PJM - Switching Solutions," 2021. [Online]. Available: <https://www.pjm.com/markets-and-operations/etools/oasis/system-information/switching-solutions.aspx>. [Accessed: 11-Mar-2022].
- [44] ISO NE, "ISO New England Operating Procedure No. 19 - Transmission Operations," 2021. [Online]. Available: <https://www.iso-ne.com/participate/rules-procedures/operating-procedures>. [Accessed: 18-Mar-2022].
- [45] PJM, "PJM Manual 03: Transmission Operations," 2021. [Online]. Available: <https://www.pjm.com/directory/manuals/m03/index.html#about.html>. [Accessed: 21-Mar-2022].
- [46] NERC, "NERC | Hurricane Sandy Event Analysis Report | Hurricane Sandy Event Analysis Report," 2014.
- [47] X. Li, P. Balasubramanian, M. Sahraei-Ardakani, M. Abdi-Khorsand, K. W. Hedman, and R. Podmore, "Real-Time Contingency Analysis with Corrective Transmission Switching," *IEEE Trans. Power Syst.*, vol. 32, no. 4, pp. 2604–2617, Jul. 2017.
- [48] CAISO, "Stepped Constraint Parameters Issue Paper," 2016. [Online]. Available: <https://www.caiso.com/Documents/IssuePaper-SteppedConstraintParameters.pdf>. [Accessed: 30-Jan-2022].

- [49] A. S. Korad and K. W. Hedman, "Robust corrective topology control for system reliability," *IEEE Trans. Power Syst.*, vol. 28, no. 4, pp. 4042–4051, 2013.
- [50] K. W. Hedman, R. P. O'Neill, E. B. Fisher, and S. S. Oren, "Optimal transmission switching with contingency analysis," *IEEE Trans. Power Syst.*, vol. 24, no. 3, pp. 1577–1586, 2009.
- [51] M. Sahraei-Ardakani and S. A. Blumsack, "Transfer capability improvement through market-based operation of series FACTS devices," *IEEE Trans. Power Syst.*, vol. 31, no. 5, pp. 3702–3714, Sep. 2016.
- [52] M. Sahraei-Ardakani and K. W. Hedman, "A Fast LP Approach for Enhanced Utilization of Variable Impedance Based FACTS Devices," *IEEE Trans. Power Syst.*, vol. 31, no. 3, pp. 2204–2213, May 2016.
- [53] H. Glavitsch, "Switching as means of control in the power system," *Int. J. Electr. Power Energy Syst.*, vol. 7, no. 2, pp. 92–100, Apr. 1985.
- [54] C. Liu, J. Wang, and J. Ostrowski, "Heuristic prescreening switchable branches in optimal transmission switching," *IEEE Trans. Power Syst.*, vol. 27, no. 4, pp. 2289–2290, 2012.
- [55] G. Jacqueline, R. Luiz, and J. B. Machado, "A study of the use of corrective switching in transmission systems," *IEEE Trans. Power Syst.*, vol. 14, no. 1, pp. 336–341, 1999.
- [56] R. Bacher and H. Glavitsch, "Network topology optimization with security constraints," *IEEE Trans. Power Syst.*, vol. 1, no. 4, pp. 103–111, 1986.
- [57] A. A. Mazi, B. F. Wollenberg, and M. H. Hesse, "Corrective Control of Power System Flows By Line and Bus-Bar Switching," *IEEE Trans. Power Syst.*, vol. 1, no. 3, pp. 258–264, 1986.
- [58] A. G. Bakirtzis and A. P. S. Meliopoulos, "Incorporation of Switching Operations in Power System Corrective Control Computations," *IEEE Trans. Power Syst.*, vol. 2, no. 3, pp. 669–675, 1987.
- [59] H. E. Brown and K. P. Thornton, "Selection of lines to be switched to eliminate overloaded lines using a z-matrix method," *IEEE Trans. Power Syst.*, vol. 4, no. 2, pp. 653–661, 1989.
- [60] J. N. Wrubel, S. M. P. S. Rapcienski, and K. L. Lee, "Practical experience with corrective switching algorithm for on-line applications," *IEEE Trans. Power Syst.*, vol. 11, no. 1, pp. 415–421, 1996.
- [61] G. Schnyder and H. Glavitsch, "Security Enhancement Using An Optimal Switching Power Flow," *IEEE Trans. Power Syst.*, vol. 5, no. 2, pp. 674–681, 1990.
- [62] W. Shao and V. Vittal, "Corrective switching algorithm for relieving overloads and voltage violations," *IEEE Trans. Power Syst.*, vol. 20, no. 4, pp. 1877–1885, Nov. 2005.
- [63] A. Khodaei and M. Shahidehpour, "Transmission switching in security-constrained unit commitment," *IEEE Trans. Power Syst.*, vol. 25, no. 4, pp. 1937–1945, Nov. 2010.
- [64] E. B. Fisher, R. P. O'Neill, and M. C. Ferris, "Optimal transmission switching," *IEEE Trans. Power Syst.*, vol. 23, no. 3, pp. 1346–1355, 2008.
- [65] R. Bacher and H. Glavitsch, "Loss reduction by network switching," *IEEE Trans. Power Syst.*, vol. 3, no. 2, pp. 447–454, 1988.



- [66] G. Schnyder and H. Glavitsch, "Integrated security control using an optimal power flow and switching concepts," *IEEE Trans. Power Syst.*, vol. 3, no. 2, pp. 782–790, 1988.
- [67] F. Qiu and J. Wang, "Chance-constrained transmission switching with guaranteed wind power utilization," *IEEE Trans. Power Syst.*, vol. 30, no. 3, pp. 1270–1278, May 2015.
- [68] K. W. Hedman, R. P. O'Neill, E. B. Fisher, and S. S. Oren, "Optimal transmission switching - Sensitivity analysis and extensions," *IEEE Trans. Power Syst.*, vol. 23, no. 3, pp. 1469–1479, 2008.
- [69] K. W. Hedman, M. C. Ferris, R. P. O'Neill, E. B. Fisher, and S. S. Oren, "Co-optimization of generation unit commitment and transmission switching with N-1 reliability," *IEEE Trans. Power Syst.*, vol. 25, no. 2, pp. 1052–1063, May 2010.
- [70] G. Granelli, M. Montagna, F. Zanellini, P. Bresesti, R. Vailati, and M. Innorta, "Optimal network reconfiguration for congestion management by deterministic and genetic algorithms," *Electr. Power Syst. Res.*, vol. 76, no. 6–7, pp. 549–556, Apr. 2006.
- [71] J. D. Fuller, R. Ramasra, and A. Cha, "Fast heuristics for transmission-line switching," *IEEE Trans. Power Syst.*, vol. 27, no. 3, pp. 1377–1386, 2012.
- [72] C. Barrows and S. Blumsack, "Power engineering letters: Transmission switching in the RTS-96 test system," *IEEE Trans. Power Syst.*, vol. 27, no. 2, pp. 1134–1135, May 2012.
- [73] M. Khanabadi, H. Ghasemi, and M. Doostizadeh, "Optimal transmission switching considering voltage security and N-1 contingency analysis," *IEEE Trans. Power Syst.*, vol. 28, no. 1, pp. 542–550, 2013.
- [74] M. Soroush and J. D. Fuller, "Accuracies of optimal transmission switching heuristics based on DCOPF and ACOPF," *IEEE Trans. Power Syst.*, vol. 29, no. 2, pp. 924–932, Mar. 2014.
- [75] M. Sahraei-Ardakani, X. Li, P. Balasubramanian, K. W. Hedman, and M. Abdi-Khorsand, "Real-Time Contingency Analysis with Transmission Switching on Real Power System Data," *IEEE Trans. Power Syst.*, vol. 31, no. 3, pp. 2501–2502, May 2016.
- [76] Y. Bai, H. Zhong, Q. Xia, and C. Kang, "A Two-Level Approach to AC Optimal Transmission Switching with an Accelerating Technique," *IEEE Trans. Power Syst.*, vol. 32, no. 2, pp. 1616–1625, Mar. 2017.
- [77] B. Kocuk, S. S. Dey, and X. A. Sun, "New Formulation and Strong MISOCP Relaxations for AC Optimal Transmission Switching Problem," *IEEE Trans. Power Syst.*, vol. 32, no. 6, pp. 4161–4170, Nov. 2017.
- [78] M. Khanabadi, Y. Fu, and C. Liu, "Decentralized transmission line switching for congestion management of interconnected power systems," *IEEE Trans. Power Syst.*, vol. 33, no. 6, pp. 5902–5912, Nov. 2018.
- [79] X. Li and K. W. Hedman, "Enhanced Energy Management System with Corrective Transmission Switching Strategy - Part II: Results and Discussion," *IEEE Trans. Power Syst.*, vol. 34, no. 6, pp. 4490–4502, Nov. 2019.
- [80] W. E. Brown and E. Moreno-Centeno, "Transmission-Line Switching for Load Shed Prevention via an Accelerated Linear Programming Approximation of AC Power Flows," *IEEE Trans. Power Syst.*, vol. 35, no. 4, pp. 2575–2585, Jul. 2020.
- [81] S. Chen and H. Glavitsch, "Stabilizing switching," *IEEE Trans. Power Syst.*, vol. 8, no. 4, pp. 1511–1517, 1993.

- [82] Z. Yang, H. Zhong, Q. Xia, and C. Kang, "Optimal Transmission Switching with Short-Circuit Current Limitation Constraints," *IEEE Trans. Power Syst.*, vol. 31, no. 2, pp. 1278–1288, Mar. 2016.
- [83] M. Heidarifar and H. Ghasemi, "A network topology optimization model based on substation and node-breaker modeling," *IEEE Trans. Power Syst.*, vol. 31, no. 1, pp. 247–255, Jan. 2016.
- [84] E. A. Goldis, P. A. Ruiz, M. C. Caramanis, X. Li, C. R. Philbrick, and A. M. Rudkevich, "Shift Factor-Based SCOPF Topology Control MIP Formulations with Substation Configurations," *IEEE Trans. Power Syst.*, vol. 32, no. 2, pp. 1179–1190, Mar. 2017.
- [85] G. P. Granelli, M. Montagna, F. Zanellini, P. Bresesti, and R. Vailati, "A genetic algorithm-based procedure to optimize system topology against parallel flows," *IEEE Trans. Power Syst.*, vol. 21, no. 1, pp. 333–340, Feb. 2006.
- [86] P. A. Ruiz, J. M. Foster, A. Rudkevich, and M. C. Caramanis, "Tractable transmission topology control using sensitivity analysis," *IEEE Trans. Power Syst.*, vol. 27, no. 3, pp. 1550–1559, 2012.
- [87] J. Han and A. Papavasiliou, "The Impacts of Transmission Topology Control on the European Electricity Network," *IEEE Trans. Power Syst.*, vol. 31, no. 1, pp. 496–507, Jan. 2016.
- [88] J. C. Villumsen, G. Brønmo, and A. B. Philpott, "Line capacity expansion and transmission switching in power systems with large-scale wind power," *IEEE Trans. Power Syst.*, vol. 28, no. 2, pp. 731–739, 2013.
- [89] J. C. Villumsen and A. B. Philpott, "Investment in electricity networks with transmission switching," *Eur. J. Oper. Res.*, vol. 222, no. 2, pp. 377–385, Oct. 2012.
- [90] F. Kunz, "Improving congestion management: How to facilitate the integration of renewable generation in Germany," *Energy J.*, vol. 34, no. 4, pp. 55–78, Oct. 2013.
- [91] G. Poyrazoglu and H. Oh, "Optimal Topology Control with Physical Power Flow Constraints and N-1 Contingency Criterion," *IEEE Trans. Power Syst.*, vol. 30, no. 6, pp. 3063–3071, Nov. 2015.
- [92] P. Dehghanian and M. Kezunovic, "Probabilistic Decision Making for the Bulk Power System Optimal Topology Control," *IEEE Trans. Smart Grid*, vol. 7, no. 4, pp. 2071–2081, Jul. 2016.
- [93] A. S. Korad and K. W. Hedman, "Enhancement of Do-Not-Exceed Limits with Robust Corrective Topology Control," *IEEE Trans. Power Syst.*, vol. 31, no. 3, pp. 1889–1899, May 2016.
- [94] M. Alhazmi, P. Dehghanian, S. Wang, and B. Shinde, "Power Grid Optimal Topology Control Considering Correlations of System Uncertainties," *IEEE Trans. Ind. Appl.*, vol. 55, no. 6, pp. 5594–5604, Nov. 2019.
- [95] A. R. Escobedo, E. Moreno-Centeno, and K. W. Hedman, "Topology control for load shed recovery," *IEEE Trans. Power Syst.*, vol. 29, no. 2, pp. 908–916, Mar. 2014.
- [96] P. Dehghanian, Y. Wang, G. Gurralla, E. Moreno-Centeno, and M. Kezunovic, "Flexible implementation of power system corrective topology control," *Electr. Power Syst. Res.*, vol. 128, pp. 79–89, Nov. 2015.
- [97] J. Shi and S. S. Oren, "Stochastic Unit Commitment With Topology Control Recourse

- for Power Systems With Large-Scale Renewable Integration,” *IEEE Trans. Power Syst.*, vol. 33, no. 3, pp. 3315–3324, May 2018.
- [98] I. Aravena and A. Papavasiliou, “Renewable Energy Integration in Zonal Markets,” *IEEE Trans. Power Syst.*, vol. 32, no. 2, pp. 1334–1349, Mar. 2017.
  - [99] B. Perunicic, M. Ilic, and A. Stankovic, “Short time stabilization of power systems via line switching,” in *Proceedings - IEEE International Symposium on Circuits and Systems*, 1988, vol. 1, pp. 917–921.
  - [100] L. Chen, Y. Tada, H. Okamoto, R. Tanabe, and H. Mitsuma, “Optimal reconfiguration of transmission systems with transient stability constraints,” in *POWERCON 1998 - 1998 International Conference on Power System Technology, Proceedings*, 1998, vol. 2, pp. 1346–1350.
  - [101] S. Bruno, M. D’Aloia, G. De Carne, and M. La Scala, “Controlling transient stability through line switching,” in *IEEE PES Innovative Smart Grid Technologies Conference Europe*, 2012.
  - [102] W. Wang and G. M. Huang, “Impacts of smart grid topology control on power system stability with renewable integration,” in *NAPS 2016 - 48th North American Power Symposium, Proceedings*, 2016.
  - [103] T. Lan, W. Wang, and G. M. Huang, “A critical switching flow index for transient stability assessment in smart grid topology control,” in *2016 IEEE Power and Energy Society Innovative Smart Grid Technologies Conference, ISGT 2016*, 2016, pp. 1–5.
  - [104] T. Lan, W. Wang, and G. M. Huang, “Transmission Grid Topology Control Using Critical Switching Flow Based Preventive Stabilizing Redispatch,” *IEEE Trans. Power Syst.*, vol. 33, no. 3, pp. 2572–2582, May 2018.
  - [105] N. Senroy and G. T. Heydt, “A conceptual framework for the controlled islanding of interconnected power systems,” *IEEE Trans. Power Syst.*, vol. 21, no. 2, pp. 1005–1006, May 2006.
  - [106] F. Teymouri, T. Amraee, H. Saberi, and F. Capitanescu, “Toward controlled islanding for enhancing power grid resilience considering frequency stability constraints,” *IEEE Trans. Smart Grid*, vol. 10, no. 2, pp. 1735–1746, Mar. 2019.
  - [107] Q. Zhao, K. Sun, D. Z. Zheng, J. Ma, and Q. Lu, “A Study of System Splitting Strategies for Island Operation of Power System: A Two-Phase Method Based on OBDDs,” *IEEE Trans. Power Syst.*, vol. 18, no. 4, pp. 1556–1565, Nov. 2003.
  - [108] K. Sun, D. Z. Zheng, and Q. Lu, “Splitting strategies for islanding operation of large-scale power systems using OBDD-based methods,” *IEEE Trans. Power Syst.*, vol. 18, no. 2, pp. 912–923, May 2003.
  - [109] J. Li, C. C. Liu, and K. P. Schneider, “Controlled partitioning of a power network considering real and reactive power balance,” *IEEE Trans. Smart Grid*, vol. 1, no. 3, pp. 261–269, Dec. 2010.
  - [110] G. Xu and V. Vittal, “Slow coherency based cutset determination algorithm for large power systems,” *IEEE Trans. Power Syst.*, vol. 25, no. 2, pp. 877–884, May 2010.
  - [111] O. Gomez and M. A. Rios, “Real time identification of coherent groups for controlled islanding based on graph theory,” *IET Gener. Transm. Distrib.*, vol. 9, no. 8, pp. 748–758, May 2015.

- [112] P. A. Trodden, W. A. Bukhsh, A. Grothey, and K. I. M. McKinnon, "Optimization-based Islanding of power networks using piecewise linear AC power flow," *IEEE Trans. Power Syst.*, vol. 29, no. 3, pp. 1212–1220, 2014.
- [113] T. Amraee and H. Saberi, "Controlled islanding using transmission switching and load shedding for enhancing power grid resilience," *Int. J. Electr. Power Energy Syst.*, vol. 91, pp. 135–143, Oct. 2017.
- [114] L. Ding, F. M. Gonzalez-Longatt, P. Wall, and V. Terzija, "Two-step spectral clustering controlled islanding algorithm," *IEEE Trans. Power Syst.*, vol. 28, no. 1, pp. 75–84, Feb. 2013.
- [115] L. Ding, Z. Ma, P. Wall, and V. Terzija, "Graph Spectra Based Controlled Islanding for Low Inertia Power Systems," *IEEE Trans. Power Deliv.*, vol. 32, no. 1, pp. 302–309, Feb. 2017.
- [116] J. Quirós-Tortós, R. Sánchez-García, J. Brodzki, J. Bialek, and V. Terzija, "Constrained spectral clustering-based methodology for intentional controlled islanding of large-scale power systems," *IET Gener. Transm. Distrib.*, vol. 9, no. 1, pp. 31–42, Jan. 2015.
- [117] G. Isazadeh, A. Khodabakhshian, and E. Gholipour, "New intelligent controlled islanding scheme in large interconnected power systems," *IET Gener. Transm. Distrib.*, vol. 9, no. 16, pp. 2686–2696, Dec. 2015.
- [118] H. You, V. Vittal, and Z. Yang, "Self-healing in power systems: An approach using islanding and rate of frequency decline-based load shedding," *IEEE Trans. Power Syst.*, vol. 18, no. 1, pp. 174–181, Feb. 2003.
- [119] H. You, V. Vittal, and X. Wang, "Slow Coherency-Based Islanding," *IEEE Trans. Power Syst.*, vol. 19, no. 1, pp. 483–491, Feb. 2004.
- [120] B. Yang, V. Vittal, and G. T. Heydt, "Slow-coherency-based controlled islanding - A demonstration of the approach on the August 14, 2003 blackout scenario," *IEEE Trans. Power Syst.*, vol. 21, no. 4, pp. 1840–1847, Nov. 2006.
- [121] M. M. la Scala, "On-line dynamic preventive control: An algorithm for transient security dispatch," *IEEE Trans. Power Syst.*, vol. 13, no. 2, pp. 601–610, 1998.
- [122] D. Gan, R. J. Thomas, and R. D. Zimmerman, "Stability-constrained optimal power flow," *IEEE Trans. Power Syst.*, vol. 15, no. 2, pp. 535–540, May 2000.
- [123] Y. Kato and S. Iwamoto, "Transient stability preventive control for stable operating condition with desired CCT," *IEEE Trans. Power Syst.*, vol. 17, no. 4, pp. 1154–1161, 2002.
- [124] Y. Yuan, J. Kubokawa, and H. Sasaki, "A solution of optimal power flow with multicontingency transient stability constraints," *IEEE Trans. Power Syst.*, vol. 18, no. 3, pp. 1094–1102, Aug. 2003.
- [125] Q. Jiang and Z. Huang, "An enhanced numerical discretization method for transient stability constrained optimal power flow," *IEEE Trans. Power Syst.*, vol. 25, no. 4, pp. 1790–1797, Nov. 2010.
- [126] G. Geng, V. Ajjarapu, and Q. Jiang, "A hybrid dynamic optimization approach for stability constrained optimal power flow," *IEEE Trans. Power Syst.*, vol. 29, no. 5, pp. 2138–2148, 2014.
- [127] L. Tang and W. Sun, "An Automated Transient Stability Constrained Optimal Power

- Flow Based on Trajectory Sensitivity Analysis,” *IEEE Trans. Power Syst.*, vol. 32, no. 1, pp. 590–599, Jan. 2017.
- [128] A. Pizano-Martínez, C. R. Fuerte-Esquivel, E. A. Zamora-Cárdenas, and J. M. Lozano-Garcia, “Directional Derivative-Based Transient Stability-Constrained Optimal Power Flow,” *IEEE Trans. Power Syst.*, vol. 32, no. 5, pp. 3415–3426, Sep. 2017.
  - [129] S. Xia, Z. Ding, M. Shahidehpour, K. W. Chan, S. Bu, and G. Li, “Transient Stability-Constrained Optimal Power Flow Calculation with Extremely Unstable Conditions Using Energy Sensitivity Method,” *IEEE Trans. Power Syst.*, vol. 36, no. 1, pp. 355–365, Jan. 2021.
  - [130] D. Ruiz-Vega and M. Pavella, “A Comprehensive Approach to Transient Stability Control: Part I - Near Optimal Preventive Control,” *IEEE Trans. Power Syst.*, vol. 18, no. 4, pp. 1446–1453, Nov. 2003.
  - [131] A. Pizano-Martínez, C. R. Fuerte-Esquivel, and D. Ruiz-Vega, “A new practical approach to transient stability-constrained optimal power flow,” *IEEE Trans. Power Syst.*, vol. 26, no. 3, pp. 1686–1696, Aug. 2011.
  - [132] Y. Xu, J. Ma, Z. Y. Dong, and D. J. Hill, “Robust Transient Stability-Constrained Optimal Power Flow with Uncertain Dynamic Loads,” *IEEE Trans. Smart Grid*, vol. 8, no. 4, pp. 1911–1921, Jul. 2017.
  - [133] H. R. Cai, C. Y. Chung, and K. P. Wong, “Application of differential evolution algorithm for transient stability constrained optimal power flow,” *IEEE Trans. Power Syst.*, vol. 23, no. 2, pp. 719–728, May 2008.
  - [134] K. Y. Chan, S. H. Ling, K. W. Chan, H. H. C. Iu, and G. T. Y. Pong, “Solving multi-contingency transient stability constrained optimal power flow problems with an improved GA,” in *2007 IEEE Congress on Evolutionary Computation, CEC 2007*, 2007, pp. 2901–2908.
  - [135] O. Rattananatthaworn, “Transient Stability Constrained Optimal Power Flow by Particle Swarm Optimization with Time Varying Acceleration Coefficients,” in *2019 IEEE PES GTD Grand International Conference and Exposition Asia, GTD Asia 2019*, 2019, pp. 774–778.
  - [136] G. Li and S. M. Rovnyak, “Integral square generator angle index for stability ranking and control,” *IEEE Trans. Power Syst.*, vol. 20, no. 2, pp. 926–934, May 2005.
  - [137] D. Gautam, V. Vittal, and T. Harbour, “Impact of increased penetration of DFIG-based wind turbine generators on transient and small signal stability of power systems,” *IEEE Trans. Power Syst.*, vol. 24, no. 3, pp. 1426–1434, Aug. 2009.
  - [138] T. Liu, Y. Liu, L. Xu, J. Liu, J. Mitra, and Y. Tian, “Non-parametric statistics-based predictor enabling online transient stability assessment,” *IET Gener. Transm. Distrib.*, vol. 12, no. 21, pp. 5761–5769, Nov. 2018.
  - [139] F. Dorfler, M. Chertkov, and F. Bullo, “Synchronization in complex oscillator networks and smart grids,” *Proc. Natl. Acad. Sci.*, vol. 110, no. 6, pp. 2005–2010, 2013.
  - [140] A. E. Motter, S. A. Myers, M. Anghel, and T. Nishikawa, “Spontaneous synchrony in power-grid networks,” *Nat. Phys.*, vol. 9, no. 3, pp. 191–197, Mar. 2013.
  - [141] T. Nishikawa, F. Molnar, and A. E. Motter, “Stability landscape of power-grid synchronization,” in *IFAC-PapersOnLine*, 2015, vol. 28, no. 18, pp. 1–6.

- [142] L. Kempton, G. Herrmann, and M. di Bernardo, "Self-organization of weighted networks for optimal synchronizability," *IEEE Transactions on Control of Network Systems*, pp. 1–1, 2017.
- [143] T. Opsahl, F. Agneessens, and J. Skvoretz, "Node centrality in weighted networks: Generalizing degree and shortest paths," *Soc. Networks*, vol. 32, no. 3, pp. 245–251, Jul. 2010.
- [144] S. Boccaletti, V. Latora, Y. Moreno, M. Chavez, and D. U. Hwang, "Complex networks: Structure and dynamics," *Physics Reports*, vol. 424, no. 4–5. North-Holland, pp. 175–308, 01-Feb-2006.
- [145] V. Latora and M. Marchiori, "Efficient behavior of small-world networks," *Phys. Rev. Lett.*, vol. 87, no. 19, pp. 198701-1-198701-4, 2001.
- [146] Y. Hao, L. Jia, and Y. Wang, "Robustness of weighted networks with the harmonic closeness against cascading failures," *Phys. A Stat. Mech. its Appl.*, vol. 541, p. 123373, Mar. 2020.
- [147] D. F. Rueda, E. Calle, and J. L. Marzo, "Robustness Comparison of 15 Real Telecommunication Networks: Structural and Centrality Measurements," *J. Netw. Syst. Manag.*, vol. 25, no. 2, pp. 269–289, Apr. 2017.
- [148] F. Dorfler and F. Bullo, "Spectral Analysis of Synchronization in a Lossless Structure-Preserving Power Network Model," in *2010 First IEEE International Conference on Smart Grid Communications*, 2010, pp. 179–184.
- [149] J. V. Milanovic and W. Zhu, "Modeling of interconnected critical infrastructure systems using complex network theory," *IEEE Trans. Smart Grid*, vol. 9, no. 5, pp. 4637–4648, Sep. 2018.
- [150] W. Zhu and J. V. Milanović, "Assessment of the robustness of cyber-physical systems using small-worldness of weighted complex networks," *Int. J. Electr. Power Energy Syst.*, vol. 125, p. 106486, Feb. 2021.
- [151] W. Zhu and J. V. Milanovic, "Interdependency modelling of cyber-physical systems using a weighted complex network approach," in *2017 IEEE Manchester PowerTech, Powertech 2017*, 2017.
- [152] A. Dwivedi, X. Yu, and P. Sokolowski, "Identifying vulnerable lines in a power network using complex network theory," in *IEEE International Symposium on Industrial Electronics*, 2009, pp. 18–23.
- [153] X. Zhang and C. K. Tse, "Assessment of Robustness of Power Systems From a Network Perspective," *IEEE Journal on Emerging and Selected Topics in Circuits and Systems*, vol. 5, no. 3. Institute of Electrical and Electronics Engineers Inc., pp. 456–464, 01-Sep-2015.
- [154] H. Tu, Y. Xia, H. H. C. Iu, and X. Chen, "Optimal robustness in power grids from a network science perspective," *IEEE Trans. Circuits Syst. II Express Briefs*, vol. 66, no. 1, pp. 126–130, Jan. 2019.
- [155] R. Preece, *Improving the Stability of Meshed Power Networks: A Probabilistic Approach Using Embedded HVDC Lines*. University of Manchester, 2013.
- [156] IEEE, *IEEE Std 421.5-2016 (Revision of IEEE Std 421.5-2005) : IEEE Recommended Practice for Excitation System Models for Power System Stability Studies*. IEEE, 2016.

- [157] “Load representation for dynamic performance analysis,” *IEEE Trans. Power Syst.*, vol. 8, no. 2, pp. 472–482, May 1993.
- [158] Y. Zhu, J. V. Milanović, and K. N. Hasan, “Ranking and quantifying the effects of load model parameters on power system stability,” *IET Gener. Transm. Distrib.*, vol. 13, no. 20, pp. 4650–4658, Oct. 2019.
- [159] Y. Zhu, “Ranking of Power System Loads Based on Their Influence on Power System Stability,” 2019.
- [160] J. V. Milanović, K. Yamashita, S. Martínez Villanueva, S. Ž. Djokić, and L. M. Korunović, “International industry practice on power system load modeling,” *IEEE Trans. Power Syst.*, vol. 28, no. 3, pp. 3038–3046, 2013.
- [161] N. A. Tsolas, A. Arapostathis, and P. P. Varaiya, “A Structure Preserving Energy Function for Power System Transient Stability Analysis,” *IEEE Trans. Circuits Syst.*, vol. 32, no. 10, pp. 1041–1049, Oct. 1985.
- [162] A. R. Bergen and D. J. Hill, “A Structure Preserving Model for Power System Stability Analysis,” *Power Appar. Syst. IEEE Trans.*, vol. PAS-100, no. 1, pp. 25–35, Jan. 1981.
- [163] A. R. Bergen and V. Vittal, *Power systems analysis*, 2nd ed. Upper Saddle River, N.J.; Prentice Hall, 1999.
- [164] M. E. J. Newman, *Networks: an introduction*. Oxford New York: Oxford University Press, 2010.
- [165] P. Crucitti, V. Latora, and M. Marchiori, “Model for cascading failures in complex networks,” *Phys. Rev. E - Stat. Physics, Plasmas, Fluids, Relat. Interdiscip. Top.*, vol. 69, no. 4, p. 4, Apr. 2004.
- [166] F. Dörfler and F. Bullo, “Synchronization of power networks: Network reduction and effective resistance,” in *IFAC Proceedings Volumes (IFAC-PapersOnline)*, 2010, vol. 43, no. 19, pp. 197–202.
- [167] F. Dorfler and F. Bullo, “Topological equivalence of a structure-preserving power network model and a non-uniform Kuramoto model of coupled oscillators,” in *Proceedings of the IEEE Conference on Decision and Control*, 2011, pp. 7099–7104.
- [168] F. Dörfler and F. Bullo, “Kron reduction of graphs with applications to electrical networks,” *IEEE Trans. Circuits Syst. I Regul. Pap.*, vol. 60, no. 1, pp. 150–163, Jan. 2013.
- [169] E. W. Dijkstra, “A note on two problems in connexion with graphs,” *Numer. Math.*, vol. 1, no. 1, pp. 269–271, Dec. 1959.
- [170] DIgSILENTGmbH, “DIgSILENT PowerFactory User’s Manual (Version2020).” DIgSILENT GmbH, 2020.
- [171] J. Zhu, *Optimization of Power System Operation: Second Edition*, 2nd ed., vol. 47. New York: Wiley, 2015.
- [172] N. N. Mansor, “Integrated planning of modern distribution networks incorporating UK utility practices,” dissertation, University of Manchester, 2018.
- [173] D. Liberzon, *Calculus of variations and optimal control theory: A concise introduction*. Princeton, N.J: Princeton University Press, 2011.

- [174] A. M. Arthurs, *Calculus of variations*. London (etc.): Routledge and Kegan Paul, 1975.
- [175] G. B. Sheble and K. Brittig, “Refined Genetic Algorithm - Economic Dispatch Example,” *IEEE Trans. Power Syst.*, vol. 10, no. 1, pp. 117–124, 1995.
- [176] S. N. Sivanandam and S. N. Deepa, *Introduction to genetic algorithms*. Berlin, Heidelberg: Springer Berlin Heidelberg, 2008.
- [177] MathWorks Inc., “Mixed Integer ga Optimization - MATLAB & Simulink - MathWorks,” 2021. [Online]. Available: <https://uk.mathworks.com/help/gads/mixed-integer-optimization.html>. [Accessed: 29-Jun-2022].
- [178] MathWorks Inc., “MATLAB version 2021a Documentation - MathWorks,” 2021. [Online]. Available: <https://uk.mathworks.com/help/matlab/index.html>. [Accessed: 29-Jun-2022].
- [179] R. D. Zimmerman, C. E. Murillo-Sánchez, and R. J. Thomas, “MATPOWER: Steady-state operations, planning, and analysis tools for power systems research and education,” *IEEE Trans. Power Syst.*, vol. 26, no. 1, pp. 12–19, Feb. 2011.
- [180] Python Software Foundation, “The Python Language Reference — Python 3.7.11 documentation,” 2021. [Online]. Available: <https://docs.python.org/release/3.7.11/reference/index.html>. [Accessed: 23-Jun-2022].
- [181] N. Shams, “Analysis and response management of frequency events in low inertia power systems,” PhD Dissertation, University of Manchester, 2019.
- [182] T. Nishikawa and A. E. Motter, “Comparative analysis of existing models for power-grid synchronization,” *New J. Phys.*, vol. 17, no. 1, p. 015012, Jan. 2015.
- [183] N. N. Mansor and V. Levi, “Integrated Planning of Distribution Networks Considering Utility Planning Concepts,” *IEEE Trans. Power Syst.*, vol. 32, no. 6, pp. 4656–4672, Nov. 2017.
- [184] N. N. Mansor and V. Levi, “Operational planning of distribution networks based on utility planning concepts,” *IEEE Trans. Power Syst.*, vol. 34, no. 3, pp. 2114–2127, May 2019.
- [185] K. Sun, S. Likhate, V. Vittal, V. S. Kolluri, and S. Mandal, “An online dynamic security assessment scheme using phasor measurements and decision trees,” *IEEE Trans. Power Syst.*, vol. 22, no. 4, pp. 1935–1943, Nov. 2007.
- [186] Y. Mansour, F. E. Vaahedi, M. A. El-Sharkawi, F. A. Y. Chang, and M. B. R. Corns, “Large scale dynamic security screening and ranking using neural networks,” *IEEE Trans. Power Syst.*, vol. 12, no. 2, pp. 954–960, 1997.
- [187] P. N. Papadopoulos and J. V. Milanović, “Probabilistic Framework for Transient Stability Assessment of Power Systems with High Penetration of Renewable Generation,” *IEEE Trans. Power Syst.*, vol. 32, no. 4, pp. 3078–3088, Jul. 2017.
- [188] J. D. Morales and J. V. Milanovic, “Analysis of Angular Threshold Criteria for Transient Instability Identification in Uncertain Power Systems,” *2019 IEEE Milan PowerTech*, pp. 1–6, Jun. 2019.
- [189] S. M. Rovnyak, “Integral square generator angle index for stability assessment,” in *Proceedings of the IEEE Power Engineering Society Transmission and Distribution Conference*, 2001, vol. 3, no. WINTER MEETING, pp. 1052–1054.
- [190] U. Kerin, M. Bojan, and G. Bizjak, “Performance evaluation of indices for transient



- stability,” in *2009 IEEE Bucharest PowerTech: Innovative Ideas Toward the Electrical Grid of the Future*, 2009.
- [191] Powertech Labs Inc., “TSAT Transient Security Assessment Tool User Manual.” Surrey, British Columbia. Canada, 2011.
  - [192] J. D. Morales, J. V. Milanovic, and P. N. Papadopoulos, “Statistical Assessment of the Impact of Renewable Energy Sources on Transient Stability,” in *Proceedings - 2018 IEEE PES Innovative Smart Grid Technologies Conference Europe, ISGT-Europe 2018*, 2018, pp. 1–6.
  - [193] J. D. Morales and J. V. Milanovic, “Methodology for Optimal Deployment of Corrective Control Measures to Ensure Transient Stability of Uncertain Power Systems,” *IEEE Trans. Power Syst.*, vol. 36, no. 3, pp. 1677–1687, May 2021.
  - [194] W. Zhu, “Modelling of interconnected critical infrastructure systems using complex network theory,” dissertation, University of Manchester, 2019.
  - [195] F. Capitanescu, “Approaches to obtain usable solutions for infeasible security-constrained optimal power flow problems due to conflicting contingencies,” in *2019 IEEE Milan PowerTech, PowerTech 2019*, 2019.
  - [196] G. Rogers, “Power System Structure and Oscillations,” *IEEE Comput. Appl. Power*, vol. 12, no. 2, pp. 14–21, 1999.
  - [197] B. Pal, *Robust Control in Power Systems*. Boston, MA: Springer US, 2005.
  - [198] P. N. Papadopoulos, T. Guo, and J. V. Milanović, “Probabilistic framework for online identification of dynamic behavior of power systems with renewable generation,” *IEEE Trans. Power Syst.*, vol. 33, no. 1, pp. 45–54, Jan. 2018.
  - [199] P. Pourbeik and others, “Dynamic models for turbine-governors in power system studies,” *IEEE Task Force Turbine-Governor Model.*, no. 2013, 2013.
  - [200] National Grid ESO, “ESO Data Portal: Day Ahead Demand Forecast - Dataset| National Grid Electricity System Operator,” 2019. [Online]. Available: <https://data.nationalgrideso.com/demand/1-day-ahead-demand-forecast>. [Accessed: 27-Jun-2022].
  - [201] G. Rogers, *Power system oscillations*. Boston, MA: Springer US, 2000.



---

# Appendix A: Network Data

---

This appendix will provide the data corresponding to all the test networks used throughout this thesis.

## A.1 SMIB network

The data of the modified AF9B network described in Section 3.1.1 and used in the analysis of Chapter 3 are presented below:

- 220 kV transmission circuits impedance: 0.5 ohm/km, with 150, 100, and 50 km long each.
- 20/220 kV generator step-up transformer: 0.15 p.u., 875 MVA (nominal).
- 20 kV synchronous generator: the same parameters and controllers as G5 of the IEEE 68-bus test network. The nominal installed capacity rating data are 700 MVA and 595 MW.

## A.2 Modified AF9B network

The data of the modified AF9B network described in Section 3.2.1 and used in the analysis of Chapter 3 are presented below:

### A.2.1 Branch impedances

The branch impedance data for the network is presented in Table A.5 (100 MVA base), which includes transformers.

Table A.1 Branch data for the modified AF9B test network

From bus	To bus	R (p.u.)	X (p.u.)	B (p.u.)	Parallel circuits
1	4	0.0000	0.0576	0.0000	1
2	7	0.0000	0.0625	0.0000	1
3	9	0.0000	0.0586	0.0000	1
5	4	0.0200	0.1700	0.0880	2
6	4	0.0340	0.1840	0.0790	2
5	7	0.0640	0.3220	0.1530	3
9	6	0.0780	0.3400	0.1790	2
7	8	0.0170	0.1440	0.0745	2
8	9	0.0238	0.2016	0.1045	3

### A.2.2 Load flow data

The data required to complete the load power flow is included in Table A.6.

Table A.2 Load flow data for the modified AF9B test network

Bus	V (p.u.)	(°)	$P_G$ (MW)	$P_L$ (MW)	$Q_L$ (MVAR)
1	1.040	0.000	60.40		
2	1.111	6.420	163.00		
3	1.106	2.657	85.00		
5	1.068	147.167		115.00	50.00
6	1.069	146.331		90.00	30.00
8	1.113	149.374		100.00	20.00

### A.2.3 Generator dynamic data

The generator dynamic data are given in Table A.3 and Table A.4.

Table A.3 Generator dynamic data for the modified AF9B test network (1)

Gen.	Bus	Base (MVA)	$X_{lk}$ (p.u.)	$X_d$ (p.u.)	$X'_d$ (p.u.)	$X''_d$ (p.u.)	$T'_{do}$ (s)	$T''_{do}$ (s)
G1	1	247.5	0.08316	0.36135	0.1505	0.1	8.96	0.075
G2	2	192.	0.10003	1.7299	0.2300	0.2	6	0.0575
G3	3	128.	0.0949	1.68	0.2320	0.2	5.89	0.0575

Table A.4 Generator dynamic data for the modified AF9B test system (2)

Gen.	Bus	Rating (MVA)	$X_q$ (p.u.)	$X'_q$ (p.u.)	$X''_q$ (p.u.)	$T'_{q0}$ (s)	$T''_{q0}$ (s)	H (s)
G1	1	247.5	0.2398	-	0.1	-	0.15	9.55
G2	2	192.	1.6598	0.3780	0.2	0.535	0.0945	3.92
G3	3	128.	1.6099	0.32	0.2	0.6	0.08	2.76

Generators G1-G3 all use type Mag A exciter with the following parameters:

$$T_R = 0.0, K_A^{ex} = 400, T_A^{ex} = 0.05, E_{ex}^{min} = -3.5, E_{ex}^{max} = 3.5, T_E^{ex} = 0.95, K_E^{ex} = -0.17, A_E^{ex} = 0.0039, B_E^{ex} = 1.555.$$

### A.3 Modified IEEE 68-bus test network

This section provides the data for the IEEE 68-bus test network, described in Section 5.1. Full system details, generator, and exciter parameters are adopted from [197], with PSS settings for G9 obtained from [201].

#### A.3.1 Branch impedances

The branch impedance data for the network is presented in Table A.5 (100 MVA base), which includes transformers.

Table A.5 Branch data for the modified IEEE 68-bus test network

From bus	To bus	R (p.u.)	X (p.u.)	B (p.u.)	From bus	To bus	R (p.u.)	X (p.u.)	B (p.u.)
1	54	0.0000	0.0181	0.0000	38	31	0.0011	0.0147	0.2470
2	58	0.0000	0.0250	0.0000	39	44	0.0000	0.0411	0.0000
3	62	0.0000	0.0200	0.0000	39	45	0.0000	0.0839	0.0000
4	19	0.0007	0.0142	0.0000	41	40	0.0060	0.0840	3.1500
5	20	0.0009	0.0180	0.0000	42	41	0.0040	0.0600	2.2500
6	22	0.0000	0.0143	0.0000	43	44	0.0001	0.0011	0.0000
7	23	0.0005	0.0272	0.0000	43	17	0.0005	0.0276	0.0000
8	25	0.0006	0.0232	0.0000	44	45	0.0025	0.0730	0.0000
9	29	0.0008	0.0156	0.0000	45	51	0.0004	0.0105	0.7200
10	31	0.0000	0.0260	0.0000	45	35	0.0007	0.0175	1.3900
11	32	0.0000	0.0130	0.0000	47	48	0.0025	0.0268	0.4000
12	36	0.0000	0.0075	0.0000	47	48	0.0025	0.0268	0.4000
13	17	0.0000	0.0033	0.0000	48	40	0.0020	0.0220	1.2800
14	41	0.0000	0.0015	0.0000	49	46	0.0018	0.0274	0.2700
15	42	0.0000	0.0015	0.0000	50	51	0.0009	0.0221	1.6200
16	18	0.0000	0.0030	0.0000	52	37	0.0007	0.0082	0.1319
17	36	0.0005	0.0045	0.3200	52	55	0.0011	0.0133	0.2138
18	50	0.0012	0.0288	2.0599	53	54	0.0035	0.0411	0.6987
18	42	0.0040	0.0600	2.2500	53	27	0.0320	0.3200	0.4100
18	49	0.0076	0.1141	1.1600	53	47	0.0013	0.0188	1.3100
19	68	0.0016	0.0195	0.3040	54	53	0.0035	0.0411	0.6987
20	19	0.0007	0.0138	0.0000	55	54	0.0013	0.0151	0.2572
22	23	0.0006	0.0096	0.1846	56	55	0.0013	0.0213	0.2214
22	21	0.0008	0.0140	0.2565	57	56	0.0008	0.0128	0.1342
23	24	0.0022	0.0350	0.3610	58	57	0.0002	0.0026	0.0434
25	54	0.0070	0.0086	0.1460	59	60	0.0004	0.0046	0.0780
26	25	0.0032	0.0323	0.5310	59	58	0.0006	0.0092	0.1130
26	29	0.0057	0.0625	1.0290	60	61	0.0023	0.0363	0.3804
27	37	0.0013	0.0173	0.3216	60	61	0.0023	0.0363	0.3804
27	26	0.0014	0.0147	0.2396	60	57	0.0008	0.0110	0.1476
28	26	0.0043	0.0474	0.7802	61	30	0.0019	0.0183	0.2900
28	29	0.0014	0.0151	0.2490	61	30	0.0019	0.0183	0.2900

From bus	To bus	R (p.u.)	X (p.u.)	B (p.u.)	From bus	To bus	R (p.u.)	X (p.u.)	B (p.u.)
30	53	0.0008	0.0074	0.4800	62	65	0.0004	0.0043	0.0729
31	30	0.0013	0.0187	0.3330	62	63	0.0004	0.0043	0.0729
31	53	0.0016	0.0163	0.2500	63	58	0.0007	0.0082	0.1389
32	30	0.0024	0.0288	0.4880	63	64	0.0016	0.0435	0.0000
33	38	0.0036	0.0444	0.6930	65	66	0.0009	0.0101	0.1723
33	32	0.0008	0.0099	0.1680	65	64	0.0016	0.0435	0.0000
34	33	0.0011	0.0157	0.2020	66	67	0.0018	0.0217	0.3660
35	34	0.0001	0.0074	0.0000	66	56	0.0008	0.0129	0.1382
36	34	0.0033	0.0111	1.4500	67	68	0.0009	0.0094	0.1710
36	61	0.0022	0.0196	0.3400	68	24	0.0003	0.0059	0.0680
36	61	0.0022	0.0196	0.3400	68	37	0.0007	0.0089	0.1342
38	46	0.0022	0.0284	0.4300	68	21	0.0008	0.0135	0.2548

### A.3.2 Load flow data

The data required to complete the load power flow is included in Table A.6.

Table A.6 Load flow data for the modified IEEE 68-bus test network

Bus	V (p.u.)	(°)	$P_G$ (MW)	$P_L$ (MW)	$Q_L$ (MVAR)
1	0.91	57.27	222.29		
2	0.99	59.79	352.85		
3	0.90	62.67	436.73		
4	0.90	66.52	483.01		
5	0.92	65.54	407.01		
6	0.90	69.26	510.04		
7	0.91	71.93	425.55		
8	0.90	65.16	487.42		
9	0.93	72.94	712.69		
10	1.10	59.10	595.00		
11	1.09	62.78	1190.00		
12	1.10	48.14	161.50		
13	1.09	0.00	3543.45		
14	0.90	19.48	312.06		
15	0.90	25.20	491.45		
16	1.04	46.03	2762.40		
17	1.07	-5.78		4190.52	209.53
18	1.04	41.64		1873.57	93.30
19	0.90	61.66		0.00	0.00
20	0.90	60.48		525.82	79.65
21	0.89	59.34		198.05	83.12
22	0.90	64.08		0.00	0.00
23	0.90	63.84		181.33	62.15
24	0.91	56.94		209.58	-62.40

Bus	V (p.u.)	(°)	$P_G$ (MW)	$P_L$ (MW)	$Q_L$ (MVAR)
25	0.94	57.45		176.27	36.98
26	0.94	57.51		105.54	12.91
27	0.93	55.29		205.84	55.67
28	0.93	62.29		161.75	21.99
29	0.93	65.49		201.30	19.14
30	1.05	50.40		0.00	0.00
31	1.06	51.49		0.00	0.00
32	1.07	55.20		0.00	0.00
33	1.07	50.98		85.01	0.00
34	1.06	45.30		0.00	0.00
35	1.05	40.98		0.00	0.00
36	1.08	47.55		77.70	-14.49
37	0.92	55.34		0.00	0.00
38	1.07	49.78		0.00	0.00
39	0.99	9.70		207.92	9.81
40	1.05	34.25		47.44	16.79
41	0.90	19.15		753.16	188.29
42	0.90	24.68		829.31	180.29
43	1.00	3.90		0.00	0.00
44	1.00	4.32		200.54	3.64
45	1.04	30.58		164.16	16.57
46	1.07	45.85		109.82	20.87
47	1.05	42.33		154.37	24.33
48	1.05	38.44		179.70	1.49
49	1.08	43.60		127.75	22.59
50	1.09	35.10		72.42	-106.46
51	1.07	31.13		253.44	-91.75
52	0.92	54.18		120.86	22.95
53	1.03	49.47		208.27	97.52
54	0.95	54.60		0.00	0.00
55	0.94	53.38		241.40	1.50
56	0.94	53.78		153.79	56.60
57	0.96	53.96		0.00	0.00
58	0.96	54.43		0.00	0.00
59	0.97	52.55		184.43	66.21
60	0.98	52.12		163.53	55.03
61	1.04	49.48		81.78	98.30
62	0.93	56.70		0.00	0.00
63	0.94	55.91		0.00	0.00
64	0.92	56.00		6.92	67.67
65	0.93	56.22		0.00	0.00
66	0.93	55.12		0.00	0.00
67	0.90	55.10		248.60	118.86
68	0.91	56.67		253.09	24.62



### A.3.3 Generator dynamic data

The generator dynamic data are given in Table A.7 and Table A.8.

Table A.7 Generator dynamic data for the modified IEEE 68-bus test network (1)

Gen.	Bus	Base (MVA)	$X_{lk}$ (p.u.)	$X_d$ (p.u.)	$X'_d$ (p.u.)	$X''_d$ (p.u.)	$T'_{do}$ (s)	$T''_{do}$ (s)
G1	1	100	0.0125	0.1000	0.0310	0.025	10.2	0.05
G2	2	100	0.0350	0.2950	0.0697	0.05	6.56	0.05
G3	3	100	0.0304	0.2495	0.0531	0.045	5.7	0.05
G4	4	100	0.0295	0.2620	0.0436	0.035	5.69	0.05
G5	5	100	0.0270	0.3300	0.0660	0.05	5.4	0.05
G6	6	100	0.0224	0.2540	0.0500	0.04	7.3	0.05
G7	7	100	0.0322	0.2950	0.0490	0.04	5.66	0.05
G8	8	100	0.0280	0.2900	0.0570	0.045	6.7	0.05
G9	9	100	0.0298	0.2106	0.0570	0.045	4.79	0.05
G10	10	100	0.0199	0.1690	0.0457	0.04	9.37	0.05
G11	11	100	0.0103	0.1280	0.0180	0.012	4.1	0.05
G12	12	100	0.0220	0.1010	0.0310	0.025	7.4	0.05
G13	13	200	0.0030	0.0296	0.0055	0.004	5.9	0.05
G14	14	100	0.0017	0.0180	0.00285	0.0023	4.1	0.05
G15	15	100	0.0017	0.0180	0.00285	0.0023	4.1	0.05
G16	16	200	0.0041	0.0356	0.0071	0.0055	7.8	0.05

Table A.8 Generator dynamic data for the modified IEEE 68-bus test system (2)

Gen.	Bus	Rating (MVA)	$X_q$ (p.u.)	$X'_q$ (p.u.)	$X''_q$ (p.u.)	$T'_{q0}$ (s)	$T''_{q0}$ (s)	H (s)	D
G1	1	100	0.069	0.028	0.25	1.5	0.035	42	4
G2	2	100	0.282	0.06	0.05	1.5	0.035	30.2	9.75
G3	3	100	0.237	0.05	0.045	1.5	0.035	35.8	10
G4	4	100	0.258	0.04	0.035	1.5	0.035	28.6	10
G5	5	100	0.31	0.06	0.05	0.44	0.035	26	3
G6	6	100	0.241	0.045	0.04	0.4	0.035	34.8	10
G7	7	100	0.292	0.045	0.04	1.5	0.035	26.4	8
G8	8	100	0.28	0.05	0.045	0.41	0.035	24.3	9
G9	9	100	0.205	0.05	0.045	1.96	0.035	34.5	14
G10	10	100	0.115	0.045	0.04	1.5	0.035	31	5.56
G11	11	100	0.123	0.015	0.012	1.5	0.035	28.2	13.6
G12	12	100	0.095	0.028	0.025	1.5	0.035	92.3	13.5
G13	13	200	0.0286	0.005	0.004	1.5	0.035	248	33
G14	14	100	0.0173	0.0025	0.0023	1.5	0.035	300	100
G15	15	100	0.0173	0.0025	0.0023	1.5	0.035	300	100
G16	16	200	0.0334	0.006	0.0055	1.5	0.035	225	50

Generators G1-G8 and G10-G16 all use type DC1A exciters with the following parameters:

$T_R = 0.01$ ,  $K_A^{ex} = 40$ ,  $T_A^{ex} = 0.02$ ,  $E_{ex}^{min} = -10$ ,  $E_{ex}^{max} = 10$ ,  $T_E^{ex} = 0.785$ ,  $K_E^{ex} = 1$ ,  $A_E^{ex} = 0.07$ ,  $B_E^{ex} = 0.91$ .

Generator G9 uses a type ST1A exciter with the following parameters:

$T_R = 0.01$ ,  $K_A^{ex} = 200$ ,  $E_{fd}^{min} = -5$ ,  $E_{fd}^{max} = 5$ .

Generator G9 is also equipped with a PSS with the following settings:

$T_W^{PSS} = 10$ ,  $T_1^{PSS} = 0.05$ ,  $T_2^{PSS} = 0.01$ ,  $T_3^{PSS} = 0.05$ ,  $T_4^{PSS} = 0.02$ ,  $K_{PSS} = 10$ ,  $E_{PSS}^{min} = -0.5$ ,  $E_{PSS}^{max} = 0.5$ .

### A.3.4 Optimal power flow data

The Optimal Power Flow (OPF) formulation used for dispatch calculations in the IEEE 68-bus test system minimises the total cost of generation for the given loading scenario, where each generator is subject to the standard cost function  $Cost = c_0 + c_1 P_E + c_2 P_E^2$  \$/Hour. The coefficient values for each generator are given in Table A.9 and taken from [198]. Also included in the table are the constraints on active and reactive power for each generating unit. Furthermore, all bus voltages are constrained to between 0.9 and 1.1 p.u.

Table A.9 Data for optimal power flow solution for the IEEE 68-bus test system

Gen.	Bus	$c_0$	$c_1$	$c_2$	$p^{max}$ (MW)	$p^{min}$ (MW)	$Q^{max}$ (MVAR)	$Q^{min}$ (MVAR)
G1	53	0	6.9	0.0193	297.5	29.75	280	-210
G2	54	0	3.7	0.0111	637.5	63.75	600	-450
G3	55	0	2.8	0.0104	765	76.5	720	-540
G4	56	0	4.7	0.0088	765	76.5	720	-540
G5	57	0	2.8	0.0128	595	59.5	560	-420
G6	58	0	3.7	0.0094	850	85	800	-600
G7	59	0	4.8	0.0099	680	68	640	-480
G8	60	0	3.6	0.0113	637.5	63.75	600	-450
G9	61	0	3.7	0.0071	935	93.5	880	-660
G10	62	0	3.9	0.0090	595	59.5	560	-420
G11	63	0	4.0	0.0050	1190	119	1120	-840
G12	64	0	2.9	0.0040	1615	161.5	1520	-1140
G13	65	0	2.5	0.0019	3570	357	3360	-2520
G14	66	0	3.3	0.0033	2125	212.5	2000	-1500
G15	67	0	3.8	0.0050	1190	119	1120	-840
G16	68	0	3.5	0.0014	4717.5	471.5	4440	-3330

## Appendix B: List of Author's Thesis Based Publications

---

### B.1 International Journal Publications

- [B1] **J. Triviño**, V. Levi, J. Morales, R. Preece, and J. V. Milanović, "Network Robustness Based Transient Stability Optimisation via Scheduling and Switching," in *IEEE Transactions on Power Systems*, doi: 10.1109/TPWRS.2023.3238409.

### B.2 International Conference Publications

- [B2] **J. Triviño**, J. Morales, V. Levi, "Assessment of the Topological Impact of Line-Switching Actions on Transient Stability," in *2023 Belgrade PowerTech*, Belgrade, Serbia. (Submitted)